

University of Alberta

**Magnetization dynamics in magnetic
microdevices and hybrid materials.**

by

Alexander Krichevsky



A thesis submitted to the Faculty of Graduate Studies and Research in partial
fulfillment of the requirements for the degree of Doctor of Philosophy

Department of Physics

Edmonton, Alberta
Fall 2004



Library and
Archives Canada

Bibliothèque et
Archives Canada

Published Heritage
Branch

Direction du
Patrimoine de l'édition

395 Wellington Street
Ottawa ON K1A 0N4
Canada

395, rue Wellington
Ottawa ON K1A 0N4
Canada

Your file *Votre référence*
ISBN: 0-612-95957-0
Our file *Notre référence*
ISBN: 0-612-95957-0

The author has granted a non-exclusive license allowing the Library and Archives Canada to reproduce, loan, distribute or sell copies of this thesis in microform, paper or electronic formats.

L'auteur a accordé une licence non exclusive permettant à la Bibliothèque et Archives Canada de reproduire, prêter, distribuer ou vendre des copies de cette thèse sous la forme de microfiche/film, de reproduction sur papier ou sur format électronique.

The author retains ownership of the copyright in this thesis. Neither the thesis nor substantial extracts from it may be printed or otherwise reproduced without the author's permission.

L'auteur conserve la propriété du droit d'auteur qui protège cette thèse. Ni la thèse ni des extraits substantiels de celle-ci ne doivent être imprimés ou autrement reproduits sans son autorisation.

In compliance with the Canadian Privacy Act some supporting forms may have been removed from this thesis.

Conformément à la loi canadienne sur la protection de la vie privée, quelques formulaires secondaires ont été enlevés de cette thèse.

While these forms may be included in the document page count, their removal does not represent any loss of content from the thesis.

Bien que ces formulaires aient inclus dans la pagination, il n'y aura aucun contenu manquant.

Canada

Acknowledgements.

I would like to thank my colleagues Scott Zelakiewicz, Miroslav Belov, Kristen Buchanan and Heng Gong for their help in sample preparation, measurements, SEM imaging and numerous discussions throughout this project, and Mark Freeman for his supervision and full support of new ideas emerging during the experiment. I would also like to thank Mark Johnson, Al Meldrum and Antony S. Arrott for important discussions that contributed significantly to this project, and Michael Brett for his consultations on new lithography techniques. For administrative assistance and for her help in editing manuscripts I thank Lynn Chandler; for technical, electrical and machining assistance I'd like to thank Paul Zimmermann, Gilbert Lachat, Tony Walford, Jay Haverstock, Ken Marsh and (particularly) Greg Popowich and Don Mullin. I would like to thank Greg Popowich again for sharing his experience of electric circuitry design and consultation. For taking high-resolution SEM images I'd like to thank George Braybrook and Dong-Chan Lee. For thin-film characterization and deposition as well as for MFM imaging I'd like to thank Miroslav Belov, and Mirwais Aktary.

I thank the University of Alberta microfabrication facility, in particular Ken Westra, Stephanie Botic, Nicole Moreen, Keith Franklin for training in microfabrication and assistance and resources.

For financial support I thank the University of Alberta, Dept. of Physics, and Mark Freeman.

For their part in collaboration in recording heads characterization project I'd like to thank Heng Gong, Roger Beauregard and Andrzej Stankiewicz.

For preparing the ion-implantation sample I thank C. W. White in the Oak Ridge Laboratory.

For numerous scholarly discussions I'd like to thank Byoung-Chul Choi, Wayne Hiebert, Greg Ballentine, Miroslav Belov, Geoff Steeves, Andrzej Stanki-

ewicz, Marek Malac and Kristen Buchanan.

I would like to thank Mike Scheinfein, John Beamish, Frank Hegmann, James McMullin and Doug Schmitt for agreeing to comprise my defence committee.

Finally, my sincerest thanks to my advisor, Mark Freeman for his time, effort, mentoring and support.

Contents

1	Introduction.	1
1.1	Motivation.	1
1.2	Magnetic recording.	4
1.2.1	MRAMs	4
1.2.2	Recording heads and media.	11
1.3	Introduction to micromagnetics.	15
1.3.1	Weiss theory.	15
1.3.2	Different Hamiltonian terms.	19
1.3.3	Landau-Lifshitz wall.	28
1.3.4	Bloch and Néel walls.	31
1.3.5	Uniformly magnetized ellipsoid.	35
1.3.6	Stoner-Wohlfarth Astroid, half-select switching.	37
1.3.7	Landau-Lifshitz-Gilbert (LLG) equation.	41
1.3.8	Domain wall motion.	44
1.3.9	Kittel formula.	46
1.4	General idea of the project.	48
2	Experimental.	51
2.1	Vectorially resolved Kerr measurements.	51
2.2	System layout.	58
2.3	Time resolved measurements, triggering sequence.	67

2.4	Dual detector.	69
2.5	Garnet current sensor.	78
2.6	Lithography and tricks.	79
3	Characterization of commercial and prototype recording heads.	83
3.1	Recording head imaging.	83
3.2	The effect of pole-tip geometry on the flux rise time of write heads.	85
3.2.1	Motivation.	85
3.2.2	Experimental set-up.	86
3.2.3	Results.	91
3.3	Current onset.	96
3.4	Chapter summary.	101
4	Magnetization reversal with vector control of in-plane switching field.	102
4.1	Railway-cross element.	103
4.1.1	Swiss-cross and railway-cross samples.	103
4.1.2	Railway cross element: the effects of pulse amplitudes.	108
4.1.3	Railway cross: the effect of pulse overlap.	112
4.1.4	Spatial variations of magnetization during the switching. Arrott's wall.	115
4.2	Multi-junction crossed ("snake") wire structures	122
4.2.1	Snake sample preparation.	123
4.2.2	Antisymmetric switching.	127
4.2.3	Sample edge reluctance to switching.	133
4.2.4	Edge reluctance (simulations).	137
4.2.5	Precessional switching.	144

4.3	Chapter summary.	151
5	Magnetic implant sample.	155
5.1	Motivation.	155
5.2	Experiment.	158
5.2.1	Kerr measurement set-up.	158
5.2.2	In-plane magneto-optical response.	161
5.2.3	Out-of-plane signal.	163
5.2.4	Kerr and Faraday effects.	166
5.3	Simulations.	168
5.4	Chapter summary.	177
6	Conclusions.	178
A	Glancing angle deposition (GLAD).	191
A.1	Motivation.	191
A.2	Deposition of the crossed wires.	192
A.3	Thin wire deposition.	195
A.4	Helical and spiral structures.	197
A.5	Deposition system.	201
A.6	Experimental results.	201
A.7	Summary.	208
B	Local excitation by a split-pole head	211
C	Transmission lines.	218
C.1	General principles.	218
C.2	Impedance matching.	224
C.3	Summary.	231

List of Tables

1.1	Comparison of MRAMs and other random access memories . .	11
1.2	Demagnetizing factors factors N_x and N_y for uniformly magnetized ellipsoids. Factor $N_z = 1 - N_x - N_y$	36
3.1	Comparison of the geometrical parameters, inductance, and the resulting flux rise time for different designs.	89

List of Figures

1-1 Comparison of the rates of development of hardware and the software demands. (gray) Number of transistors of the PC CPUs (Intel). (black) Typical memory requirements for installation of the Windows operation system. 2

1-2 Schematic representation of a typical MRAM design. (a) Writing process. A current pulse propagating down the right Digit line half-selects the elements #3,6,9. Write current pulse flips the magnetization of the element #6 only. (b) Reading process, Digit lines are not shown. Transistors are open for the elements #2,5,8. Weak sense current pulses propagate down the top and bottom Word lines, and the magnetoresistance of the elements #2 and #8 is measured simultaneously. 5

1-3	One transistor per magnetic tunnel junction (1T1MTJ) architecture of MRAM (after Tehrani et. al.) (a) Read mode. Only one transistor along the Bit line is open allowing the current drain. The tunneling resistance to the sense current depends on the orientation of the free layer magnetization. (b) Write process. No current drain is allowed, as the top wire serves dual purpose (both Bit and Word) in this design. Combined action of Digit and Word pulses ensures the free layer orientation parallel to the Word pulse field. (After Tehrani <i>et.al.</i> , used with permission).	7
1-4	(a,c) Current-in-plane (CIP) geometry of magnetoresistive sensors. (b,d) Current perpendicular to the plane (CPP) geometry. In both cases parallel orientation of magnetization (a,b) in all layers results in lower resistance than antiparallel (c,d). (e) A spin valve (CIP) sandwich, similar to the ones actually used in contemporary designs. (f) Schematic energy diagram for the Magnetic Tunnel Junction (MTJ) CPP element (after Parkin et. al.).	8
1-5	Schematic design of longitudinal (a) and perpendicular (b) recording heads. (c) A complete head gimbal assembly (HGA) of a recording head.	13
1-6	(a) Schematic hysteresis loop observed in bulk materials. Enlarged section shows roughness associated with switching of individual domains or domain wall depinning. (b) Different switching regimes observed in scaled down particles: (b ₁) Few-domains sample; (b ₂) Nearly-single-domain particle; (b ₃) Molecular magnets. (after W. Wernsdorfer [14], used with permission).	16

1-7	(a) Magnetized (single domain) slab. Magnetic field emerges from the specimen ends. (b) Demagnetized sample. Magnetic flux is enclosed. Bold arrows represent the domain magnetizations, thin arrows schematically show the fringing magnetic fields.	26
1-8	(a) A schematic representation of a 180° domain wall. (b,c) The structure of the Landau-Lifshitz or Bloch walls, cross-section and plan view respectively. (c) Néel wall, plan view.	29
1-9	Comparison of Bloch (solid) and Neel (dashed) walls for permalloy (thick grey) and Cobalt (black). (a) Effective widths of the walls dependence on the film thickness. (b) Corresponding energy densities.	32
1-10	(a) Schematic illustration of the magnetization tilt under influence of the external magnetic field H . (b) The Astroid switching diagram, both hard- and easy-axis fields are normalized to the coercivity.	38
1-11	Switching diagrams for a single-domain elliptical samples perturbed by a finite duration sharp (left column) and half-sinusoidal (right column) pulses. In all cases the sample is initially magnetized to the left. Grayscale represents the final magnetization dark – unswitched, light – switched.	42
2-1	(a) General case of Kerr rotation. A polarized beam reflected from a magnetized sample experiences a small polarization shift δ . (b) Specific case of two symmetrical (mirrored) beams incident to the sample. (c) Bridge balancing set-up for detection of small polarization shifts.	53

2-2	(a) Normal set-up for measuring out-of plane (polar) Kerr shift. (b) Dual detector analyzing both polar and one of the in-plane components of magnetization. (c) Quadrant detector set-up for simultaneous mapping of all three magnetization components.	55
2-3	(a) Quadrant detectors' in-plane magnetization measurements (arbitrary units) of a horizontal sample. Solid line corresponds to M_x channel, dashed – to M_y . (b) Analogous measurement on the same sample rotated 90° . The channel readings are interchanged.	57
2-4	(a) A schematic layout of the stroboscopic measurements set up. (b) An example of an idealized domain structure of a rectangular sample. The central (gray) domain can be flipped back and force under influence of an appropriate magnetic field pulse. (c) Magnetization change in the case (b) as it would be seen by our system.	59
2-5	System layout. Details in the text.	62
2-6	A photograph of the actual sample holder and the objective assembly. Details in the text.	65
2-7	(a) Chopper modulation. The chopper wheel periodically blocks the beam triggering the pulse generator. The chopper circuitry sends the modulation frequency to the lock-in amplifier. (b) The lock-in sets the modulation frequency, flipping the switch between two positions and modulating the delay between optical and current pulses.	68

2-8	(a,b) Chopper modulation. (a) Schematic sequence of the optical pulses. (b) A sequence of the current pulses modulated by a chopper. (c,d) Delay modulation. (c) The same sequence of optical pulses as in case (a). (d) Sequence of the current pulses modulated by delay triggering (e) Corresponding Kerr signal for both modulation techniques. Whether the current pulses are turned off or mistimed, the probing laser pulses hit the sample alternately in the “high” and “low” magnetization states.	70
2-9	(a) The Insert part with a reflective metalized prism mounted at the bottom of the slot. (b) The Axis, holding both the inner Insert part and outer Ring part. (c) The Ring with PMT detectors and alignment screws.	71
2-10	(Top) A photograph of an assembled detector. Inset: enlarged central area. Reflections of halves of the PMT faces in the prism can be seen. Likewise, a beam emitted from the direction the observer sees the prism would be split in two and reach the corresponding PMTs. The entire assembly is mounted on a translation stage, whose micrometer screws can be seen in the background. (Bottom) Plan view, side view and cross-sections of the detector assembly.	73
2-11	(a) Schematic representation of the logic box design. The gain of each channel can be adjusted for proper balance with variable gain amplifiers, then two summers produce the outputs proportional to the polar and in-plane components of magnetization. (b) The circuitry of each amplifier. (c) The circuitry of the first summer (the second summer is the same up to the input channel permutation).	74

2-12	(a) Idealized cross-section of the garnet sensor. The beam is focused at the mirror adjacent to the active YIG layer between the WW creating an out-of plane magnetic field. The YIG layer magnetization is initially set by an in-plane bias field of a permanent magnet. (b) Schematic plan view of the sensor (rotated 90°).	76
2-13	Typical garnet sensor assembly. In this case the garnet sensor is mounetd in series with a recording head slider and terminated to 50 Ohms by surface-mounted resistors.	77
2-14	(a-h) A comparison of the etching and lift off techniques. Etching and ion milling result in a sharp step at the edge of the deposited structure (f,g) while a lifted-off structure may be thinner at the edges than in the middle (h). An example of sharp step coverage (i) by directional deposition and smooth step coating by spin-on glass (j).	80
3-1	Time-resolved polar Kerr images, rendered on a linear grayscale. Times are relative to the onset of a bipolar switching pulse of 10 ns duration. Each scan area is $6 \times 6 \mu m$	84
3-2	(a) SEM image of the slider air bearing surface (ABS). (b) SEM image of the same head cross section. The length L_p of the pedestal determines the throat height. (c) A typical Kerr imaging from ABS spatial scan. Both P_1 and P_2 poles demonstrate the highest magnetization (and hence the highest flux density) at the edges right across the write gap. Note that the horizontal scale of frame (c) has been stretched relative to the vertical (as indicated), for presentation purposes	87
3-3	Schematic plot of the front end pole tip geometry.	88

3-4	Measured HGA inductance versus bias current curves for the four different designs. Inset: Schematic shapes of four tested pedestals as trimmed by ion milling. The flare angle of approximately 35 degrees is the same for all designs. The lengths of the pole noses and pedestals are listed in Table 3.1.	92
3-5	Magnetization switching curves measured at different P_2 locations from trailing edge toward the top of the P_2 . Circle corresponds to the trailing edge (corresponding rise time is 0.65 ns), square is separated from the trailing edge by 0.5 mm (1.0 ns), diamond – by 1.7 mm (1.45 ns), triangle – by 2.3 mm (1.65 ns). Note that this Kerr image is inverted with respect to the one shown in the Fig. 3-1: the pole P_2 is on the top.	93
3-6	Temporal magnetization switching curves (between the two saturation states) scanned by TR-SKM at P_2 leading edge at 40 mA write current.	94
3-7	Temporal profiles of magnetization recorded at the edges of the recording poles P_1 (inverted, dashed) and P_2 (solid) right across the gap for the head mounted on the head gimbal assembly (a) and directly for a head slider (b). The lines with markers represent the difference between P_1 and P_2 pole responses. . .	97
3-8	(a) Temporal scans normalized to the saturation levels recorded at different positions at the head and the current onset measured by garnet optomagnetic sensor. Note, that the response of unsaturated shield material right below the P_1 pole (Fig. 3-2a) almost coincides with the true current profile. (b) Temporal scans normalized to the <i>plateau</i> levels for the garnet sensor (dashed) and corresponding shield response (solid) for different current levels. Within the noise, traces almost coincide.	98

3-9	(a) An unnormalized response of the shield to a typical bipolar pulse of different amplitudes. Numbers indicate the highest level at the positive plateau measured independently using an inductive probe. (b) Average top (diamonds) and bottom (triangles) plateau levels versus the current strength. Linear response makes the shield a built-in magneto-optic sensor for recording heads.	100
4-1	The NRL sample. (a) An AFM scan of the ferromagnetic element. The edge of the wire is seen as a white stripe, but an elongated grey element does not show significant roughness. (b) corresponding MFM scan of a sample in remanent state (zero bias field). The grayscale shows out-of-plane magnetization of the sample, but also non-magnetic features such as the edge of the wire. Closure domains are observed. The wire edge produce an artefact in the measurement. (c) Schematic cross-section of the crossed-wire element. (d) Measured static hysteresis loop for a similar element.	106
4-2	Typical temporal traces of the easy-axis (x) magnetization switching history for different Word field amplitudes in the "Swiss cross" geometry. The Kerr signal is normalized to the saturation levels (-1 for magnetization pointing to the left and +1 for M_x to the right).	107

4-3	A scanning optical micrograph of the “railway” crossed wire element, rendered in linear grayscale is proportional to the reflectivity of the sample. The top gold wire is thus brighter than the bottom wire coated by SiN dielectric. The fast-rising, 10 ns duration principal pulses propagate down the top wire. The ferromagnetic element is at the center of the wire intersection. An initial sample magnetization direction is shown as the dashed arrow.	109
4-4	(a): Kerr signal representing the x -component of the magnetization change for a single 10 ns pulse on WW1 arriving at $t = 0$ ns, for various pulse amplitudes. The values listed represent the magnitude of the applied magnetic pulse. Complete reversal is observed for fields of 250 Oe or greater and the initial state is preserved for fields of 160 Oe or lower. We attribute the intermediate values of plateau height to the statistical nature of the switching events. (b): the dependence of the final average level of magnetization change at the long time delay on the applied field strength.	110
4-5	(a): Schematic of the arrival and overlap times of two pulses. Inset: The inverse switching time $1/\tau_s$ as a function of overlap $t_{1,2}$. Open circles denote statistically incomplete reversal. (b): X -component of Kerr signal during the application of two pulses applied to WW1 and WW2 for varying amounts of overlap, $t_{1,2}$, between the pulses. The second pulse begins at $t=0$ ns for all traces. The switching time can be seen to decrease for greater overlap of the pulses.	113

4-6	(a) Time-amplitude scan of the easy-axis magnetization M_x of the sample. Linear grayscale represents the magnetization level, horizontal axis shows the time (principal pulse is present from zero to ten ns), and the vertical axis auxiliary pulse strength. (b) Line scans from panel (a) at several values of the auxiliary pulse strength.	116
4-7	Switching rate as a function of the applied auxiliary pulse strength.	118
4-8	(a) spatial scan of the easy-axis magnetization M_x recorded two nanoseconds after the principal pulse start (10 ns at the scans below). (b) M_x variations across the sample (spatio-temporal scan) induced by a principal pulse of 280 Oe (no auxiliary pulse). The pulse starts at $t = 8$ ns. (c) Complementary M_y scan. . .	120
4-9	(a) Simulated hysteresis loop for a 200×100 nm ellipse. (b) simulated magnetization configurations at the strange point at the rising (falling) edge of the hysteresis curve (± 360 Oe) and at the neighboring field values.	121
4-10	(a) The first layer of the lithography. A snake-like digit wire is deposited. (b) The final sample. The digit wire is buried underneath the planarising dielectric, then the mask is rotated 90° and the second (word) wire is deposited. After the secondary planarization by spin-on glass (SOG) and the deposition of the protective layer (SiO_2), arrays of permalloy elements are deposited atop the wire intersections. (c) AFM image of the $3 \times 1 \mu\text{m}$ ellipses and the roughness test (AFM) of the finished sample.	125
4-11	Schematic planar view (a) and a cross-section (b) of the crossed wires element. Two $3 \times 1 \mu\text{m}$ permalloy elliptical samples are placed at the intersection.	126

4-12	Time-amplitude scans for different values of the word field pulses: 19 Oe (a,b) and 34 Oe (e,f). The vertical axis corresponds to the digit pulse strength H_{hard} , horizontal axis to the time in nanoseconds. Grayscale represents the value of the Kerr signal. (c,d) The cuts of the TA scans (a,b) at $H_{hard} = -60$ and $+60$ Oe respectively. Solid line represents M_x , dashed line $-M_y$. (g,h) Analogous cuts of the TA scans (e,f).	129
4-13	TA scans for different values of the easy-axis pulse strengths. The grayscale represents the easy-axis Kerr signal, and it is normalized to the saturation levels for all plots.	130
4-14	Switching easy-axis magnetization diagram evolution during the pulse. Subplot titles indicate the time during the pulse when the signal was measured. The gray scale represents the value of the easy-axis magnetization (white – unswitched, black – switched). No data points are taken below 5.8 Oe of the easy-axis field (plain gray stripe in the middle of every diagram). Easy axis pulse durations are indicated in the subplot titles.	132
4-15	Cartoon schematic of different switching scenarios for opposite initial magnetizations of a sample in the “S” magnetization state to illustrate the possibility of antisymmetric diagrams during the switching process.	134

- 4-16 Switching diagrams for different easy-axis pulse durations. In all cases the digital pulse precedes the word pulse by one nanosecond and both pulses end at the same time. The gray scale represents the value of the easy-axis magnetization (white – unswitched, black – switched). No data points are taken below 5.8 Oe of the easy-axis field (plain gray stripe in the middle of every diagram). Easy axis pulse durations are indicated in the subplot titles. The last diagram also shows the theoretical Stoner-Wolfarth astroid. 135
- 4-17 Time-resolved history of switching of the two elliptical samples at the intersection of the crossed wires, by the combined action of word and digit magnetic field pulses in the half-select regime. The time is clocked from the beginning of the word pulse, the digit pulse arrives 1 ns before the word pulse. Nucleation starts in the middle of both samples and propagates towards the edges. 136

- 4-18 Simulated switching histories for $3 \times 1 \mu\text{m}$ ellipses for different word and digital magnetic pulse profiles. (a) Simple pulse profiles used in the simulations. Linear rise time / plateau duration / linear fall time are as follows: 60/400/400 ps for a fast digital pulse (solid line); 250/3750/1000 ps for a slow digital pulse (dash-dotted line); and 300/2700/1000 ps for word pulse. The word pulse lags one nanosecond behind the digital pulse. (b) Coherent rotation caused by fast digital pulse of 140 Oe of amplitude and formation of a vortex after the end of a pulse. The grayscale represents the magnetization parallel to the long axis of the ellipse in all plots below. The numbers at the top of the subplots indicate the time passed from the beginning of the digital pulse in nanoseconds. (c) The same as (b) for a stronger 300 Oe digital pulse. A band of switched material and two vortices are formed after the pulse. (d) Incomplete switching by a slow negative digital pulse of -60 Oe combined with a word pulse of 35 Oe in the half-select regime. In this simulation the crystalline anisotropy is tilted fifteen degrees with respect to the long axis of the ellipse. A single vortex at the center of the sample is eventually formed. (e) The same as (d) for a positive 60 Oe slow digital pulse and the same word pulse. Incomplete switching resulting in a double-vortex state. 139
- 4-19 The edge reluctance to switching in a dumbbell-shaped sample perturbed by a fast hard-axis field pulse (Fig.4-18a, solid line) of 250 Oe. The numbers indicate the time from the pulse beginning. 141

4-20	In-plane magnetization shots for thin-film elliptical samples with aspect ratio 2×1 of various thicknesses subjected to 300 Oe hard-axis field. The shots are taken before the pulse (≈ 500 ps); at quarter period of precession, at the first maximum of M_x , (≈ 680 ps), at $3/4$ period and at the first minimum of M_x . Linear greyscale spans from -1 to 1.	143
4-21	(Continued) In-plane magnetization shots for thin-film elliptical samples with aspect ratio 2×1 for smaller samples. Same field as in Fig. 4-20. Shots taken before the pulse, at quarter, half, three quarters and full period.	145
4-22	Coherent rotation of magnetization components by fast hard-axis magnetic field pulse of different amplitudes (a-c). The pulse profile is shown schematically at the inset of the Fig. 4-26. For all graphs, solid and dash-dotted lines represent easy-axis (X) and polar (Z) components of the Kerr signal respectively. . . .	146
4-23	The effect of the hard-axis pulse duration on the final state of the easy-axis magnetization. Pulse durations of ≈ 600 ps FWHM (solid) and 850 ps (dashed).	147
4-24	Simulated distribution of magnetization for precessional oscillations for a fast 140 Oe hard-axis field pulse (corresponding to the trace shown at Fig. 4-22 a). Movie shots are taken at indicated moments. Note, that the out-of-plane component of magnetization does not exhibit full swing from -1 to 1, but rather it is suppressed by shape anisotropy.	149

4-25	Comparison of experimental and simulated temporal traces of in- and out- of-plane magnetization components. (a) Experimental Kerr X signal normalized to the saturation levels (solid) vs corresponding simulated M_x component (dashed); (b) experimental Kerr Z signal (arbitrary units, solid) vs simulated M_z multiplied by fifteen times to fit the experimental data (dashed); (c) Kerr Z vs Kerr X signal – experiment; (d) Corresponding M_z vs M_x plot – simulation.	150
4-26	Half-select switching. (a) Slow incoherent switching by a strong (70 Oe) easy-axis (Word) magnetic field pulse. It is used to determine the saturation magnetization levels. (b) Very fast (180 ps 10-90%) half-select switching caused by 90 Oe fast hard-axis (Digital) pulse and 40 Oe Word pulse, properly timed with Digital pulse. (c) 40 Oe Word pulse is delayed 170 ps with respect to 90 Oe Digital pulse. Inset: Measured Digital (solid) and Word (dashed) pulse profiles (arbitrary units)	152
5-1	Plan view (top) and cross-section (bottom) transmission electron microscopy images of iron nanoclusters in SiO ₂ host. Fe ions are implanted to an areal dose of 1.5×10^{17} ions/cm ² at room temperature. This sample was not subsequently annealed. Iron nanoparticles are concentrated within 60 nm of the sample surface. The characteristic diameter of the clusters is approximately 10 nm.	157

5-2	Schematic layout of the experimental set up. (a) Plan view of the sample. An ion-implanted SiO ₂ is glued atop thin-film gold wires deposited on a sapphire plate. (b) Cross-section of the sample perpendicular to the write wires. The probe beam is focused, through the SiO ₂ plate, on the optically-active iron nanocluster layer. Both transient and bias (static) magnetic field lines are shown.	159
5-3	In-plane magnetization response measured atop the write wire. The transient in-plane pulsed field strength is approximately 440 Oe. The bias (DC) fields are negative 200 Oe (thin line with a marker) and zero (thick line). The pulse duration is 10 ns, starting at $t = 0$	162
5-4	(a) Typical out-of-plane signal without bias magnetic field (solid line) and in strong bias field (thin line and circles). (b) High temporal resolution scans across the rising edge measured for nano-implantation (NI) sample in presence of the bias field (dashed) without bias field (solid) and using Yttrium Iron Garnet (YIG) current sensor biased by approximately 2200 Oe DC field (dash-dotted).	164
5-5	The dependence of the out-of-plane Kerr signal on applied field pulse amplitude. (a) Successive traces recorded at the strongest available pulse of 210 Oe, and attenuations of 6 dB (220 Oe), 11 dB (125 Oe) and 13 dB (100 Oe). (b) Corresponding plateau heights averaged between 3 and 8 ns plotted versus the field strengths.	165

5-6	(a) Schematic layout of the patterned ion-implantation sample. Some islands of the implanted material partially overlap with underlying aluminum mirrors. (b) Intensity (brightness) spatial scan of the patterned sample. (c) Corresponding polar Kerr/Faraday optomagnetic image. The signal from the mirror has an opposite polarity to the signal of the bare implantation islands. The grayscale colorbars in the plots (b,c) correspond to the brightness and the magneto optic signal amplitude (arbitrary units) respectively.	167
5-7	Kerr versus Faraday magneto optical response of the implanted nanoparticles. Stronger Faraday signal (dashed) has an opposite polarity to Kerr signal (solid), and is inverted for direct comparison.	169
5-8	Comparison of different simulations: (i) a randomly scattered 10 nm cubic cells [a-c], cubic anisotropy is imposed; (ii) randomly scattered (in both radius and position) flat circle elements with no crystalline anisotropy [d-f] and (iii) more densely packed (filling factor 59%) circles with zero crystalline anisotropy [g-i]. The top row [a, d, g] represents the design masks (not to scale, refer to the text for exact parameters). The second row [b, e, h] shows corresponding histograms for the out-of-plane component of magnetization M_z distribution before (solid black line) and during (gray line) the duration of the magnetic field pulse for each design. The third row [c, f, i] maps the corresponding distribution for the in-plane component of magnetization M_x before and during the pulse.	171

5-9	(a) The in-plane response of average magnetization to the in-plane field pulse $H_x = 600$ Oe. (b) Out of plane response of magnetization to the combined in- and out-of plane field pulse $H_x = 200$ Oe, $H_z = 200$ Oe. The details of the pulse's temporal profiles are described in the text. Solid, dash-dotted and dashed lines represent the "random cubes" (i), "random disks" (ii) and "densely packed quasi-regular disks" (iii) models respectively.	174
5-10	Simulated out-of-plane magnetization M_z response averaged over entire array. Magnetic field pulse profile is shown schematically as a dotted line. Gray curve corresponds to the response to 200 Oe Z -axis pulse only, while the black trace represents M_z response to a slanted pulse: $H_z = H_x = 200$ Oe.	176
A-1	(a) Model square lattice of rectangular pillars similar to the structure formed by developing crossed trenches in the resist. (b) Plan view of the same structure. (c) Micropillar array as seen from 0° azimuth and 30° elevation. (d-f) analogous projections for a hexagonal lattice of cylindrical pillars. The view in the plot (f) is from 30° azimuth, 30° elevation. (g) Typical structure of hexagonal wires as would be deposited in hexagonal array. Two sets of wires (light and bold gray) intersect forming an array of elongated rhombic elements (black).	194
A-2	Thin wire formation by GLAD. Glancing angle deposition of the first layer in the case of wide trench (a) and narrow trench (b). Second deposited layer may (c) or may not (d) overlap with the first one. In the case of the overlapping layers the lift-off results on double thickness "wire" narrower than the trench itself (e) that can be converted to a real wire by ion milling (f).	196

A-3	(a) Plan view of the ring (donut) shaped trench in the resist. (b,c) different cross-sections of the trench and schematic view of the glancing angle deposition of a material in the trench. Molecular flux is does not reach the bottom of the trench in the middle of the donut (b), but does so closer to the edges (c). (d) 3-D view of the trench at 50° elevation angle. (e) A schematic representation of simultaneous GLAD on a rotating substrate by two independent sources.	198
A-4	(a) Two-source GLAD onto a pillar coats its walls and the shadowed area with metal or insulator; but the top of the pillar and the rest of the substrate are coated by both of them. (b) Rotating the substrate during the deposition results in spiral/helical wrapping of the pillar by metal and insulator sheets. Subsequent normal ion milling destroys the coating everywhere but at the pillar wrapping. The resulting “coil” cross-section is shown in the plot (c).	200
A-5	(Top) assembled vacuum-tight stepper motor housing in the deposition chamber. (Bottom) The substrate holder with tapered clamps that do not impede the glancing angle deposition. . . .	202
A-6	Crossed wire deposition by GLAD after lift-off. The central area is elevated as the thickness of deposited material doubles there. The burrs of Al/Al ₂ O ₃ are the result of the resist wall coating and incomplete lift-off.	203
A-7	Wide-trench deposition. (a) General case where one trench is wider than the other. Horizontal double-thickness wires are fully developed, while in the narrower vertical trench deposited layers do not overlap. (b) Enlarged narrow-trench area. (c) Thin wire formed in a 3- μ m wide trenches. (d) The same, plan view, enlarged.	206

A-8	(Top) A micropillar coated by Al/Al ₂ O ₃ composite forming a mushroom-like cap at the top of the pillar. (Bottom) Similar structure, plan view. The cap is removed during lift-off. The pillar shadow causes clover-like dip in the deposited material.	207
A-9	A complex structure created in a square well of the resist. Different levels of material elevation are the result of the shadow overlap.	209
B-1	Schematic field (thin dashed lines) generated by recording tip poles in the very beginning of the switching process (a) when the pole P ₁ is being switched, but P ₂ still hesitates; and further down the switching when the horseshoe magnet is nearly saturated (b). Thick dashed line represents the out-of-plane component of the field.	212
B-2	Spatio-temporal scans of thin film permalloy sample excited by a separated recording head placed directly underneath it. The entire fixture is subjected to in-plane magnetic field caused by a permanent magnet. The orientation of the magnet can be changed in plane, zero degrees corresponds to the field direction from P ₂ to P ₁ in the ABS plane of the recording head.	214
B-3	“Temporal profiles” cut from the spatiotemporal scans in the Fig. B-2 by spatial averaging across indicated ranges. All traces show a strong peak of ≈400 ps FWHM, corresponding to the fast out-of-plane response of the P ₁ pole of the recording head.	216
C-1	(a) A schematic representation of an ideal lossless transmission line as uniformly distributed inductance and parallel capacitance. (b) Model representation of a lossy line. (c) A typical coaxial line. (d) A coaxial line with close inner and outer radii can be represented as a collection of parallel strip-lines.	220

C-2	(a) A transmission line of impedance Z_0 terminated through a resistor of impedance Z . (b) Scattering from a resistor of impedance Z embedded between two sections of impedance Z_0 . (c) Schematic representation of a T-junction. (d) An illustration of a smooth “adiabatic” splitting of a strip-line.	226
C-3	An illustration of multiple reflections at two transmission line junctions.	228
C-4	Absolute values of transmission amplitudes through an impedance-mismatched insert of characteristic impedance Z as a function of the junction length, for different values of Z . The wave vector k corresponds to the bouncing wave inside the insert. All curves are periodic with a period of π	230

List of Symbols.

α	Damping parameter
γ_0, γ_{LLG}	Gyromagnetic ratio
δ	Kerr rotation angle
δ, Δ	Domain wall width
ε	Dielectric constant
ε_0	Electric constant
λ	Wavelength
$\vec{\mu}, \mu$	Magnetic moment
μ	Micro ($\times 10^{-6}$)
μ	Permeability
μ_0	Vacuum permeability
μ_B	Bohr magneton
μ_W	Domain wall mobility
τ	Time interval
ϕ, φ, θ	Angle, angular coordinate
χ	Magnetic susceptibility
ω	Angular frequency
Ω	Ohm
A	Ampere
A	Exchange constant
Au	Elemental gold
AFM	Atomic force microscopy
\vec{B}, B	Magnetic induction
c	Speed of light
CIP	Current-in-plane
CPP	Current perpendicular to plane

<i>Co</i>	Elemental cobalt
<i>demag</i>	Demagnetization
<i>DRAM</i>	Dynamic random access memory
<i>DW</i>	Digital wire
\vec{E}, E	Electric field
<i>E</i>	Energy
<i>emu</i>	Electromagnetic unit
<i>Fe</i>	Elemental iron
<i>FeRAM</i>	Ferroelectric RAM
<i>FWHM</i>	Full width half maximum
<i>g</i>	Landé factor
\mathbf{H}, H	Hamiltonian
\vec{H}, H	Magnetic field
<i>H_c</i>	Coercivity
<i>HGA</i>	Head gimbal assembly
<i>Hz</i>	Hertz
\vec{I}, I	Current
<i>IR</i>	Infrared
<i>J</i>	Exchange integral
\vec{k}, k	Wave vector
<i>K_u, K₂, K₄</i>	Anisotropy constant
<i>LLG</i>	Landau-Lifshitz-Gilbert
\vec{M}, M	Magnetization
<i>M_s</i>	Saturation magnetization
<i>MFM</i>	Magnetic force microscopy
<i>MOKE</i>	Magneto-optical Kerr effect

<i>MRAM</i>	Magnetic random access memory
<i>MTJ</i>	Magnetic tunnel junction
<i>NA</i>	Numerical aperture
$\overleftrightarrow{N}, N_x, N_y, N_z$	Demagnetization tensor and demag factors
<i>Ni</i>	Elemental nickel
<i>NSERC</i>	Natural Science and Engineering Research Council
<i>Oe</i>	Oersted (10^{-4} Tesla)
<i>PMMA</i>	Electron resist
<i>PMT</i>	Photomultiplier tube
<i>Py</i>	Permalloy
<i>RMS</i>	Root mean square
<i>RW</i>	Read wire
\vec{S}, S	Spin
<i>SEM</i>	Scanning electron microscopy
<i>SiO₂</i>	Silicon dioxide
<i>SKEM</i>	Scanning Kerr microscopy
<i>SOM</i>	Scanning optical microscopy
<i>SRAM</i>	Static random access memory
<i>t</i>	Time
<i>TEM</i>	Transmission electron microscopy
<i>Ti</i>	Elemental titanium
<i>TR – SKM</i>	Time-resolved scanning Kerr microscopy
<i>UV</i>	Ultra-violet
<i>v</i>	Velocity
<i>V</i>	Volts
<i>W</i>	Energy density
<i>WW</i>	Write wire, Word wire
<i>YIG</i>	Yttrium iron garnet
<i>x, y, z</i>	Cartesian coordinates

Chapter 1

Introduction.

This chapter is devoted to an introduction to the area of micromagnetism and the current status of state of the technology. It consists of three sections: current and prospective technological applications such as Magnetic Random Access Memories (MRAMs); theoretical introduction to the field; and a brief outlook of the following chapters. More details on the experimental system are presented in Chapter 2.

1.1 Motivation.

Rapid development of the computer hardware is evident in every aspect of our lives. Exponential growth of the density of the integrated elements is known as “Moore’s law”, and this empirical rule holds over decades, giving base for more and more potent computers and providing the ability to tackle sophisticated computational tasks. However, this miniaturization trend has its limit at the atomic scale, which is within reach over a couple of decades (a concept known as “hitting a wall”). Some say that the development rate is already decreasing.

On the other hand, in a race of the performance sophistication as well as user friendliness, application software also grows in size exponentially (Fig.

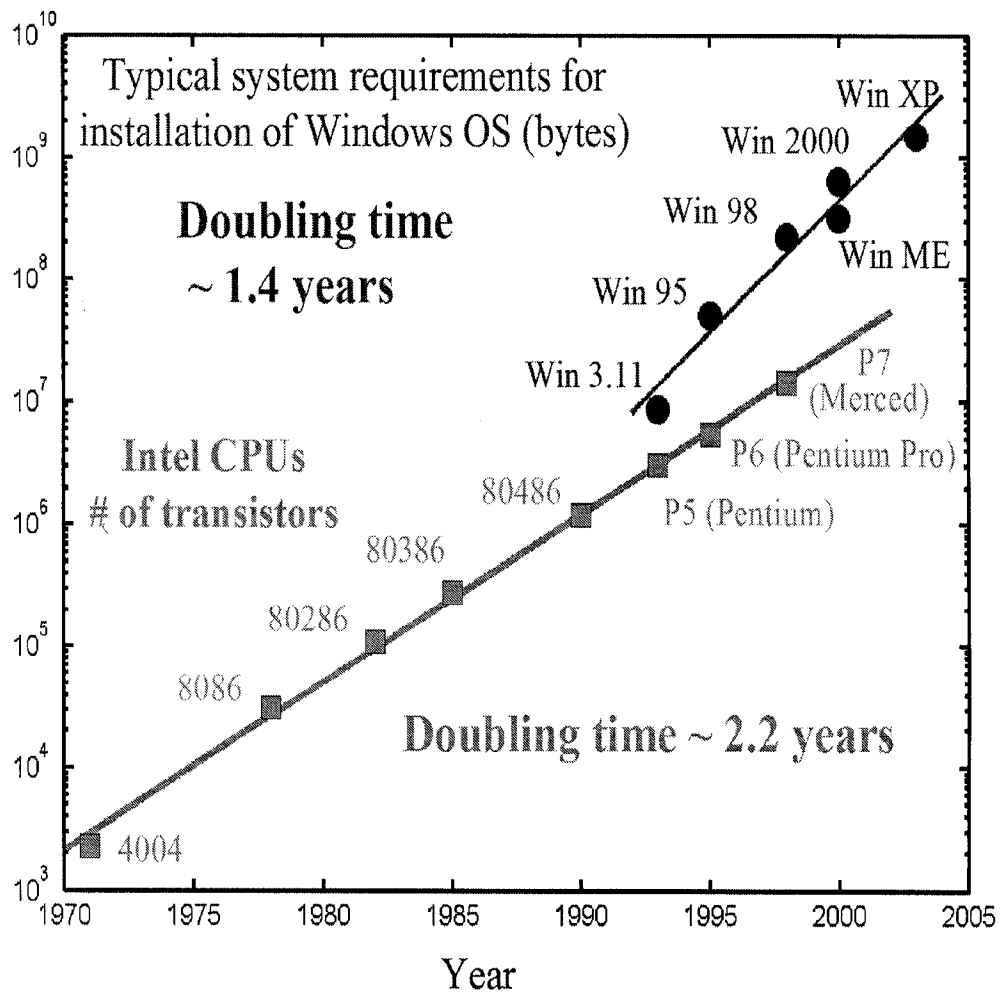


Figure 1-1: Comparison of the rates of development of hardware and the software demands. (gray) Number of transistors of the PC CPUs (Intel). (black) Typical memory requirements for installation of the Windows operation system.

1-1). The growth rate is higher than that of the hardware (in the example shown in Fig.1-1 the system demands doubling time is 1.4 years versus 2.2 years for the number of transistors in the CPU), and there is no wall to hit in sight.

The bottleneck will eventually be the rate of the data transfer between the storage and the processing units. Today, just like in the beginning of the computer era, reading data from and writing to the permanent storage unit (the hard disk) is in most cases performed sequentially, one bit at a time using magnetorecording heads and magnetic disk. The head moves across the disk mechanically, which limits the data access time, and it can only access the surface of the disk, eliminating the possibility of three-dimensional integrated storage architecture. Each time the computer is turned on or off, the operation system must be installed from the hard drive, as the volatile random access memory (RAM) cannot hold the data while the computer is turned off.

One way to circumvent this limitation is to create non-volatile random access memory (NRAM). The most part of this work is devoted to the specific NRAM design, a magnetic random access memory (MRAM). In addition to the advantage of non-volatility, MRAMs allow parallel access to the entire row of the memory elements in a square matrix; it has no moving parts and potentially allow multi-layer deposition and 3D integration. Price wise, MRAMs are still very far from the hard disk storage, but are expected to be close in both price and performance to the conventional RAM elements in the near future, while possessing the advantage of non-volatility. MRAMs are described in more details in section 1.2.1.

In addition to the MRAM project, I worked in collaboration with industrial companies on characterization of the conventional recording heads (section 1.2.2).

1.2 Magnetic recording.

1.2.1 MRAMs

The Magnetic Random Access Memory is a relatively recent kind of non-volatile memory that has certain advantages over conventional semiconductor RAM and storage disk media, and potentially can replace them both (although considering the production cost of modern hard drives, replacing a magnetic disk is a long shot). The operation of any MRAM is based on half-select switching, the regime where simultaneous action of two independent magnetic field pulses are necessary to switch the memory element magnetization (see section 1.3.6 for more details). The write assembly consists of two mutually isolated crossing arrays of parallel thin film wires with ferromagnetic elements sandwiched between them at the intersections (Fig. 1-2 *a*). These wires are inductively coupled to the ferromagnetic elements and are used to flip their magnetization back and forth. Wires generating the magnetic field along the easy axis of the elements are usually called Word or Write lines, and the ones inducing the field along the hard axis are the Digit, Digital or Bias lines.

For reading the elements' magnetoresistance up to two extra sets of wires are added: the reading "Bit" set; and a set of "Transistor" (or "Bit" again, in general, word "Bit" is reserved for reading process) lines that act like a valve opening or closing the sense current drain (see below). In some designs two sets of extra wires are used for reading, one of the Bit line sets can be integrated either with Word or with Digit lines. A single wire (whether Word, Digit or Bit) serves multiple elements, thus resolving the wiring problem.

The purpose of the writing is to "select" (meaning "flip"; the word "disturb" also means "flip" in MRAM literature) the particular element's magnetization while not disturbing the rest of them. To achieve this goal, two relatively weak current pulses are sent down the Word and Digit lines intersecting at the

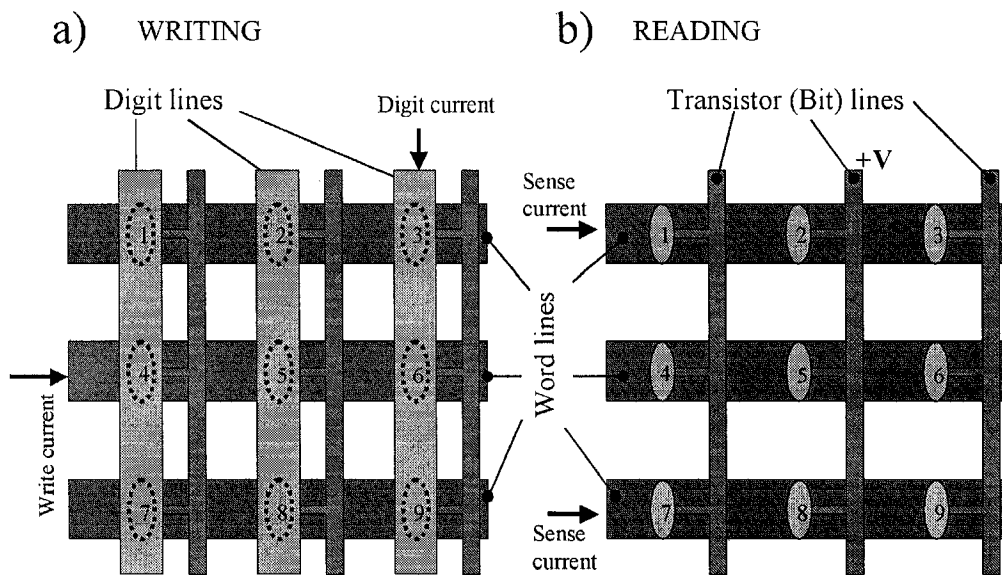


Figure 1-2: Schematic representation of a typical MRAM design. (a) Writing process. A current pulse propagating down the right Digit line half-selects the elements #3,6,9. Write current pulse flips the magnetization of the element #6 only. (b) Reading process, Digit lines are not shown. Transistors are open for the elements #2,5,8. Weak sense current pulses propagate down the top and bottom Word lines, and the magnetoresistance of the elements #2 and #8 is measured simultaneously.

desired element (Fig. 1-2 *a*, Fig. 1-3 *b* [1]). The pulses' amplitudes are chosen so that the induced fields lie in the "half-select" range of the diagram shown in the Figure 1-10 *b*. Each pulse is too weak to switch the magnetization of any element, but their combined action at the intersection is sufficient. In the figure 1-2 *a* the elements #3, and 9; 4 and 5 are stressed by Digit and Word pulses respectively, but not selected – they are "half-selected", hence the name of the process. The element #6 is switched (if its initial magnetization opposed the direction of Word field). Note, that all elements along a wire can be written simultaneously, as opposed to the recording head/disk combination that can only write one bit at a time.

The reading process is similar, it also uses crossed wires in order to address specific element, but in this case all currents lie well within the switching astroid, and do not disturb the element magnetization. In the particular case of 1T1MTJ (one transistor per magnetic tunnel junction) MRAM architecture [1] shown in figure 1-2 *b*, positive voltage is applied to the transistor line opening the drain (Fig. 1-3 *a*) for the elements #2,5,8. In this case the second Bit line is integrated with Word line and selective reading is controlled by transistor line voltage. Now, if weak sense currents are applied to the top and bottom Word wires, and the tunneling resistance to the drain is measured, the bits #2 and #8 are read. Again, this design allows one to read the entire row of the elements (along the Bit or Transistor line) at once (and again beats the one bit at a time performance of the recording disk).

There are two general designs of the thin film ferromagnetic elements used in MRAMs, differing by the direction of the sense current flow: Current-in-Plane of the film (CIP) and Current Perpendicular to the Plane (CPP). CIP employs low-resistivity non-magnetic / ferromagnetic layered structures. Most common designs are the Giant Magnetoresistance (GMR) [2],[3],[4],[5] multilayer sandwiches and two-layer spin valve operating on the same principle. Some of the ferromagnetic layers are harder to switch (Hard or Pinned

a) Read mode

b) Write mode

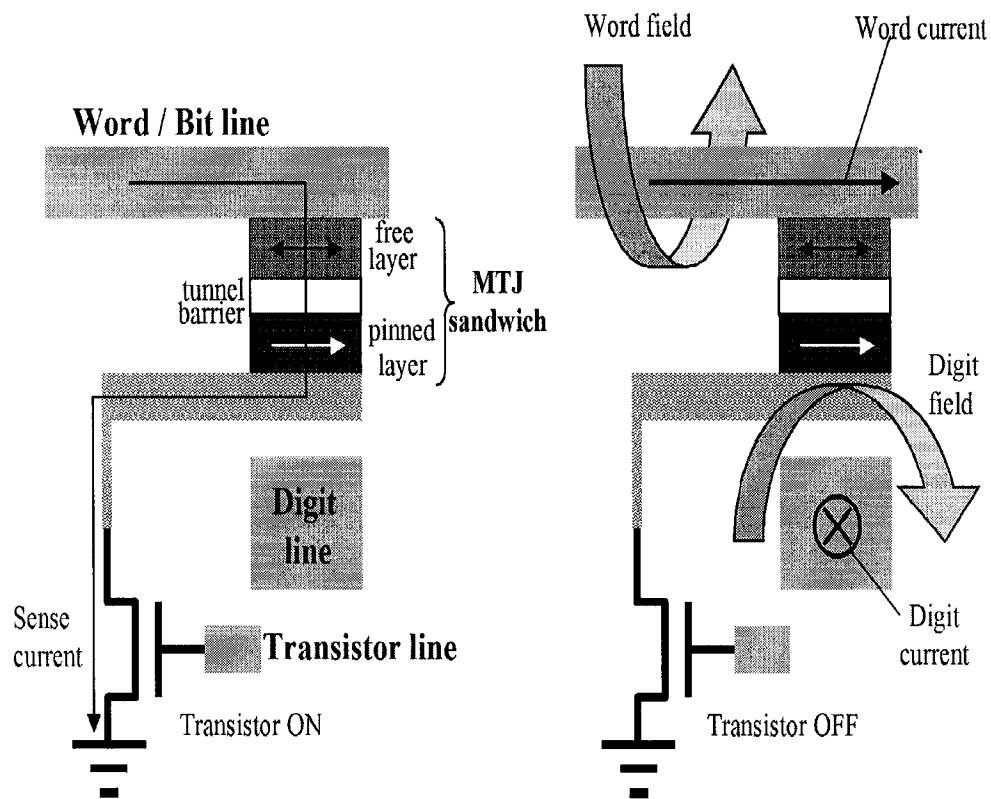


Figure 1-3: One transistor per magnetic tunnel junction (1T1MTJ) architecture of MRAM (after Tehrani et. al.) (a) Read mode. Only one transistor along the Bit line is open allowing the current drain. The tunneling resistance to the sense current depends on the orientation of the free layer magnetization. (b) Write process. No current drain is allowed, as the top wire serves dual purpose (both Bit and Word) in this design. Combined action of Digit and Word pulses ensures the free layer orientation parallel to the Word pulse field. (After Tehrani *et.al.*, used with permission).

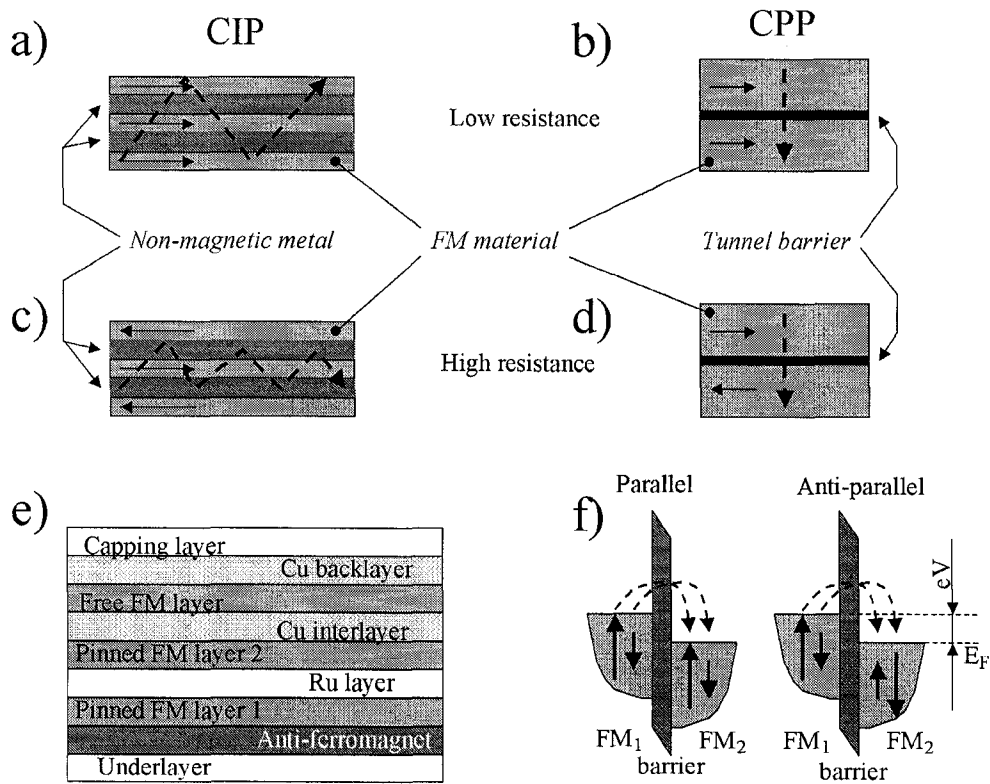


Figure 1-4: (a,c) Current-in-plane (CIP) geometry of magnetoresistive sensors. (b,d) Current perpendicular to the plane (CPP) geometry. In both cases parallel orientation of magnetization (a,b) in all layers results in lower resistance than antiparallel (c,d). (e) A spin valve (CIP) sandwich, similar to the ones actually used in contemporary designs. (f) Schematic energy diagram for the Magnetic Tunnel Junction (MTJ) CPP element (after Parkin et. al.).

layers) than the other (Free layers) (Fig. 1-4 *a, c*). Free layers are flipped by applied field, and the resistance of the layered structure in parallel orientation of the magnetization is lower than that of antiparallel orientation due to the increased probability of reflection of spin-polarized electrons at the ferromagnetic boundary with opposite magnetization. Although the discovery of GMR was quickly adopted by recording head industry, its range of 4-8% is not sufficient for MRAM applications. The resistance of the junctions is low and is further reduced as the elements are scaled down.

Most of the attention is recently turned to the CPP designs, and specifically to the Magnetic Tunnel Junction (MTJ) elements. The method is based on the difference in the tunneling probabilities between parallel and antiparallel aligned pinned and free ferromagnetic layers separated by a thin dielectric tunnel barrier (Fig. 1-4 *b, d*). Figure 1-4 *f* illustrates schematically the tunneling process between partially polarized parallel and antiparallel ferromagnetic layers. Magnetoresistance MR for MTJ elements is predicted to be

$$MR \equiv \frac{R_{AP} - R_P}{R_P} = \frac{2P_1P_2}{1 - P_1P_2} \quad (1.1)$$

$$P = \frac{N_{\uparrow} - N_{\downarrow}}{N_{\uparrow} + N_{\downarrow}} \quad (1.2)$$

where P_1, P_2 are spin polarizations of the ferromagnets, and $N_{\uparrow}, N_{\downarrow}$ are the concentrations of spin-up and spin-down electrons in each layer. Tunneling Magnetoresistance (TMR) values of 30-50% were widely reported recently [1],[6],[7]. Magnetic Tunneling Junctions are being pursued as the building block of commercial MRAM [9],[10]: they have high magnetoresistance and excellent scalability as the tunneling probability can be controlled and varied in a wide range, and the flow of current perpendicular to the plane allows fabrication of small area memory cells [8].

In reality, both CIP and CPP junctions include more than three layers, and designs are becoming more and more complex as engineers pursue higher performance [11]. A schematic representation of all layers of a real-life spin valve design is shown in the figure 1-4 *e*. Magnetic tunneling junctions are just as complex. In our experiments we did not test real GMR or MTJ sandwiched structures placed between crossed wires, but rather single layer patterned ferromagnetic elements placed on top of the crossed wire structures. Therefore, our results might differ from the transport measurements performed on multilayer elements [12],[13].

The possibility to read and write entire rows of elements at once opens tremendous opportunities for speedy access to information compared to disk media; while the element non-volatility is advantageous to the semiconductor RAM designs. MRAM can serve as a logical next step in the memory design, provided it can be made cheap enough. This is how (according to S. Tehrani [8]) the MRAMs are expected to compete with conventional RAM designs in the near future [Table 1.2]. This is just a snapshot of a fast changing landscape illustrating the current level of technology and motivating the research in this area. MRAM is expected to compete with DRAM in terms of speed, density and durability with an additional advantage of non-volatility.

Summarizing, MRAMs offer great advantages of non-volatility, easy addressability of the elements using crossed write/read wires and “half-select” current pulses, lack of moving parts and relatively fast switching time. On the longer term one might also expect integrated 3-dimensional MRAM architectures..

However, these promising advantages should be balanced against the principal difficulties, such as the need of high current write pulses which can cause excessive heat generation that in turn can compromise the spatial dimensions of the elements; and the fact that unavoidable lowering of the potential barrier between two magnetized states with downsizing of the elements can result in

Head Technology	MRAM			Flash	SRAM	DRAM	FeRAM
	600 nm	180 nm	90 nm	90 nm	90 nm	90 nm	90 nm
Density	256 Kb-1 Mb	1 Mb-32 Mb	4 Mb-256 Mb	4 Mb-64 Mb	4 Mb-64 Mb	16 Mb-256 Mb	4 Mb-64 Mb
Wafer size (mm)	150/200	200	200/300	200/300	200/300	200/300	200/300
Performance (MHz)	16	50-100	75-125	20-100 read	50-2000	20-100	15-50
Array Efficiency	40-60%	40-60%	40-60%	25-40%	50-80%	40%	40-60%
Voltage	3.3	3.3/1.8	2.5/1.2	2.5-1.2; 9-12 internal	2.5/1.2	2.5/1.2	2.5/1.2
Additional cost, to CMOS	NA	15-25%	15-25%	25%	0	15%	15-25%
Cell Size (μm^2)	7.2	0.7	1	0.15-0.25	1-1.3	0.25	0.4
Block Size ($\mu\text{m}^2/\text{Mb}$)	12	2-3	0.3-0.5	0.6-1	1.2-1.7	0.6	0.8
Endurance	$>10^{15}$	$>10^{15}$	$>10^{15}$	$>10^{15}$ read, $<10^6$ write	$>10^{15}$	$>10^{15}$	$<10^{13}$ write
Non-volatility	YES	YES	YES	YES	NO	NO	YES

Table 1.1: Comparison of MRAMs and other random access memories

thermal switching known as superparamagnetism.

1.2.2 Recording heads and media.

Throughout my project I've been involved in a collaborations with magnetic data storage corporations (Read-Rite, Maxtor/Quantum and Seagate). Within these partnerships I have tested and characterized numerous commercial and prototype designs of recording heads. Here we provide a brief introduction to the principles of operation of contemporary write-head designs. The active element of a typical recording head includes a writer charged by a spiral thin-film coil, and a magnetoresistive flux sensor. In our measurements we only tested the writer's performance.

The writer of any recording head (whether conventional longitudinal or prospective perpendicular) is a horse-shoe electromagnet [14]. Thin-film coils induce a magnetic flux passing between the North and South poles of the

magnet, which interacts with the recording layer of the hard disk directly underneath the flying recording head, locally changing the orientation of its magnetization.

In the case of the longitudinal heads (Fig. 1-5 *a*) the flux is closed inside the recording layer. In order to increase the recording density, the gap between the head poles (called in the industrial jargon P_1 and P_2) must be as small as possible. In order to increase the lateral recording density as well, one of the poles (P_2) is made much thinner than the other. The writer's geometry is discussed in more detail in chapter 3. Since each head serves a dual purpose of both writing and reading, and the reader element is shielded from strong write fields by at least two shield layers made of soft magnetic material. In the old days (three years ago) the P_2 pole width could still be as large as $2 \mu m$, and the gap between the poles as wide as $0.5 \mu m$ and the recording areal density of the order of 600 Mbit/inch^2 . Most of the tests reported below are conducted on the heads with P_2 width of $\approx 300 \text{ nm}$, and the gap of $\approx 100 \text{ nm}$. Now these values are approaching 100 nm and 50 nm respectively [15], corresponding to the recording densities approaching 100 Gbit/inch^2 .

By contrast, in perpendicular recording heads, flux lines penetrate the recording layer and close through the underlying soft magnetic material Fig. 1-5 *b*. In this case, there is no point keeping the gap small, and indeed the gap between the recording tip P_3 and P_1 in new designs is typically a few micrometers, but the dimensions of the tip itself in the ABS plane are typically smaller than $50 \times 50 \text{ nm}$. The recording layer is thicker than for longitudinal recording heads, and strong out-of plane anisotropy is induced via a special deposition process. The information is stored in the domains magnetized perpendicularly to the plane of the disk (hence the name). This geometry allows higher recording density while maintaining stability against thermal fluctuations due to the relatively high thickness – despite reduced lateral dimensions. One issue associated with perpendicular recording is the existence of the soft un-

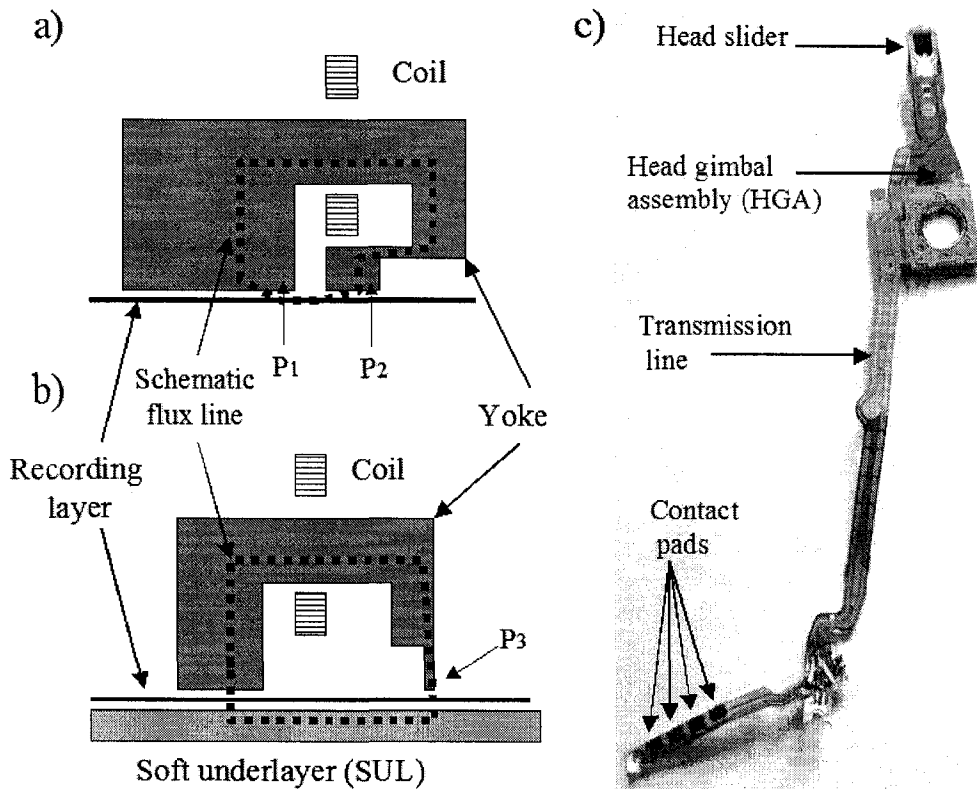


Figure 1-5: Schematic design of longitudinal (a) and perpendicular (b) recording heads. (c) A complete head gimbal assembly (HGA) of a recording head.

derlayer (SUL) which can in principle compromise the head performance. An important feature of the perpendicular recording heads is aforementioned high separation between the horseshoe poles. It is very tempting to design multi-layer, or better helical coils in order to squeeze the head dimensions, reduce the inductance and improve the rise time of the magnetic flux. We suggested a new type of lithography (described in Appendix A), which promises the deposition of micron-sized helical coils with arbitrary number of layers in 1-2 lithography steps.

The tests of the longitudinal recording heads were conducted on two levels: as Head Gimbal Assemblies (Fig. 1-5 c, the way the heads are mounted in

the computer hard drive) for characterization of the commercial heads; and detached from the assembly crystal sliders, for the prototype designs and to eliminate the influence of the long transmission of the suspension on the flux rise time.

1.3 Introduction to micromagnetics.

Hark to the locusts in their shrill armadas.

Locusts aren't locusts. Locusts are cicadas.

To seals in the circuses I travel on bee lines.

Seals aren't seals. Seals are sea lions.

I'm a buffalo hunter. Want to see my license?

Buffaloes aren't buffaloes. Buffaloes are bison.

I'm too old to be pedantically hocus-pocused.

I'll stand on the buffalo, the seal and the locust.

Ogden Nash.

The goal of this section is to familiarize the reader with commonly used concepts (and their actual meaning) and also to explain some of the technical jargon used throughout the text.

1.3.1 Weiss theory.

It is well-known that ferromagnetic materials such as iron at room temperature interact strongly with external applied magnetic fields. In particular, the field inside a bulk iron slab can be hundreds of times stronger than the external field due to the polarization (magnetization) of the material, and the specimen can retain some of its magnetization once the field is removed. A typical magnetization curve is shown schematically in Figure 1-6 *a*, (thick solid line). The average magnetic moment parallel to the direction of the external field inside a bulk specimen is plotted against the applied field strength. Starting from the negative plateau $-M_s$ at strong negative external field, the sample magnetization M follows the bottom part of the loop until it reaches the high saturation value of M_s . If the magnetic field is subsequently decreased, magnetization

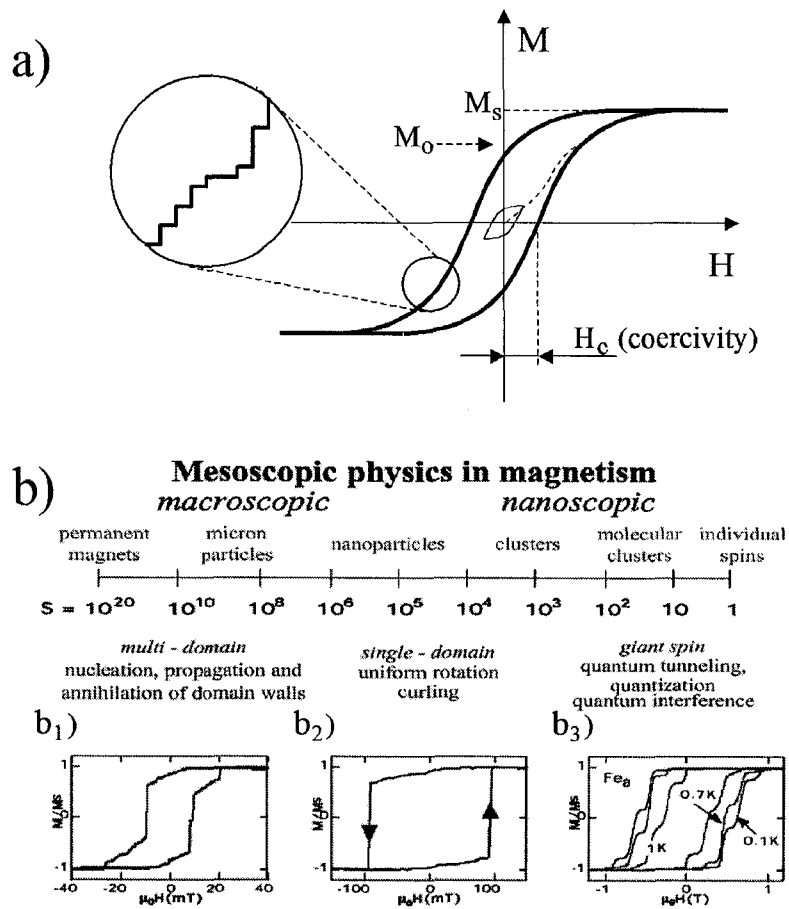


Figure 1-6: (a) Schematic hysteresis loop observed in bulk materials. Enlarged section shows roughness associated with switching of individual domains or domain wall depinning. (b) Different switching regimes observed in scaled down particles: (b₁) Few-domains sample; (b₂) Nearly-single-domain particle; (b₃) Molecular magnets. (after W. Wernsdorfer [14], used with permission).

follows the top part of the loop. This curve is known as a hysteresis loop, and in fact represents the limiting case of the magnetization reversal history, achieved only if the field cycles between sufficiently high positive and negative values.

The switching history can deviate significantly from this scenario depending on the initial state of the slab magnetization and the field strength. In particular, if the sample is initially subjected to fast-oscillating field, it can be demagnetized, so that its average magnetization M is close to zero. If it is subsequently placed in the slow increasing external field H , the magnetization follows the dashed curve until it reaches the saturation value M_s , and then follows the limiting trajectory. However, if the external field is not sufficiently strong, the magnetization does not plateau, and follows a small loop such as the thin line in Figure 1-6 *a*. Such curves not reaching saturation are called “minor loops”.

Several important quantities are associated with the limiting hysteresis loop. First, the aforementioned saturation magnetization M_s occurs when the magnetization plateaus at sufficiently strong field values. When the field is subsequently decreased to zero, the sample magnetization follows the loop curve and to the non-zero remanent magnetization state or “remanence” M_0 . In order to demagnetize the sample, an additional magnetization field in the opposite direction must be applied. The value of that field that zeroes the sample magnetization is known as the “coercive force” (although it is not a force, but a field) or “coercivity” H_c . Close examination of the edge of the diagram reveals its step-like nature (Fig. 1-6 *a*, inset), these Barkhausen steps [16] are usually irreproducible cycle to cycle.

In order to explain the remanence and the fact that relatively weak fields (of order a few Oe for “soft” magnets, compared to the huge internal field inside the magnetized sample of thousands of Oe) are sufficient to switch the sample magnetization, Weiss (1907) suggested the hypothesis of magnetic *do-*

mains, or regions of the material nearly uniformly magnetized, whose size and orientation depend on the local field. These domains are separated by so-called domain walls where magnetization changes direction smoothly. Under the influence of local magnetic fields these domain walls can move through the sample, varying the relative size of neighboring domains or eliminating some of them completely; or, entire domains can rotate from one orientation to another. Weiss' hypothesis has been experimentally confirmed in numerous experiments including direct observation of the domain structure using Bitter patterns [17],[18]; scanning Hall probe microscopy [19]; scanning electron microscopy with polarized electrons (SEMPA) [20]; Lorentz microscopy where the electron beam is deflected by internal magnetic field and the resulting phase contrast made visible by slight defocusing of the beam [21]-[23]; magnetic force microscopy [24],[25]; and magneto-optical Kerr effect microscopy [26], [27]. Detailed descriptions of different domain observation techniques (and pretty pictures!) can be found in an excellent book by Alex Hubert and Rude Schäfer [28].

This model also explains the step-like roughness of the hysteresis curve: each step is indicative of switching of an individual domain [16]. Saturated magnetization corresponds to nearly parallel orientation of all domains. Magnetization approaches the saturation level asymptotically, so it is not easy to define the switching field for a bulk sample. It is shown in the next sections that the multidomain structure helps to minimize certain energy terms, while domain walls result in an energy penalty. Naturally, one can hope that reducing the sample size would lead to transitions from multi-domain structures through few-domain and eventually to a uniform "single-domain" configuration of magnetization due to the unfavorable surface-to volume ratio of multi-domain configurations in small samples.

Different switching scenarios for scaled-down samples [29] are shown in the Figure 1-6 *b*. For few-micron samples ($10^{10} - 10^{13}$ spins) a few-domain

switching scenario takes place (Fig 1-6 b_1): the hysteresis loop is qualitative similar to the plot Figure 1-6 a , but encounters fewer steps. Also, the switching behavior is more reproducible cycle to cycle than in the multi-domain case, as there are not as many ways the domains can rearrange themselves during the switching. In micro- and nano-scale regimes (from tens of nanometers to a few micrometers, depending on the material anisotropy and sample shape, or $10^4 - 10^{10}$ spins) nearly single-domain behavior can be observed (Fig 1-6 b_2). The hysteresis loop is nearly square, the switching field is equal to the coercivity field if the sample is sufficiently small and has no metastable multi-domain or vortex states. Note, that in this regime the sample can not be demagnetized — the macrospin is bound to point in *some* direction, and there is no averaging over a number of domains that can lead to zero net magnetization. Also, there are no minor loops in this regime, the sample is either switched or not. This property makes the single-domain regime a particularly attractive candidate for a memory-cell element. As the sample is further scaled down to few-spin molecular magnets, (Fe_8 low-temperature hysteresis loops are shown in Fig 1-6 b_3) the loops becomes stepped again, but for a different reason: one observes quantum transition between different spin states. The last regime is shown for the sake of completeness, all of our measurements were performed at room temperature and on much bigger samples, exhibiting the few- and nearly single- domain switching scenarios.

The following sections (1.3.2-1.3.9) are devoted to the theory of the domain wall formation, wall width and the switching dynamics of a single-domain particle.

1.3.2 Different Hamiltonian terms.

Ferromagnetism is a quantum mechanical effect related to the interaction between magnetic moments of individual electrons. In principle, both orbital and

spin contribution should be considered in order to rigorously describe this effect, but in most commonly used ferromagnets the orbital contribution cancels due to the crystalline symmetry, and only spin-spin and spin-magnetic field interactions play a significant role. Despite its quantum nature, the behavior of ferromagnetic materials can be satisfactorily described in the semi-classical limit where individual spins are represented as classical vectors [30], and all Hamiltonian terms depend only on the mutual orientation of the interacting spins and the distance between them.

Exchange energy.

This term emerges from purely quantum mechanical calculations based on antisymmetrization of multi-electron wave-functions. The technical details of the original derivation can be found in references [30] and [31], and the final result is:

$$\mathcal{E}_{ex} = - \sum_{i \neq j} J_{i,j} \vec{S}_i \cdot \vec{S}_j \quad (1.3)$$

where $J_{i,j}$ are so-called exchange integrals, and the summation is carried out over all spins in the system. However, the value of the exchange integrals decays rapidly with the distance between the sites, and only the nearest-neighbor (and in some cases such as indirect exchange or double exchange, next-nearest-neighbor) terms play a significant role. Calculations of the exchange integrals in real materials do not yield sufficient accuracy, and quantum mechanical many-body problem are far too complex to tackle with any reasonable precision. As mentioned before, a semiclassical approximation is used, summation is carried over the nearest neighbors only, and moreover, the exchange term is assumed to have the same value for all nearest-neighbor sites. Altogether, it is a set of rather strong assumptions, but the behavior of ferromagnetic materials is described surprisingly well. The exchange term is transformed as follows:

$$-\sum_{i \neq j} J_{i,j} \vec{S}_i \cdot \vec{S}_j \approx -JS^2 \sum_{\substack{\text{nearest} \\ \text{neighbors}}} \cos \phi_{ij} \quad (1.4)$$

where ϕ_{ij} are the angles between neighboring spins' directions.

This is the most important energy term, responsible for the willingness of all spins to be aligned in the same direction if $J_{i,j} > 0$. However, it does not have any *preferential* direction, as long as all relevant spins are aligned with each other. Large-angle misalignment results in severe energy penalty, so in most cases angles ϕ_{ij} are small (although in some exotic cases of severely constrained structures, such as atom-thick terraces of a crystal, large-angle atom-to-atom variations are observed [32]). In the common small-angle case $\cos \phi \approx 1 - \frac{1}{2}\phi^2$. Considering the magnetization orientation ϕ as a continuous variable, the exchange energy can be transformed (to within a constant) as:

$$\mathcal{E}_{ex} \approx \frac{1}{2}C \int [(\vec{\nabla} m_x)^2 + (\vec{\nabla} m_y)^2 + (\vec{\nabla} m_z)^2] dV. \quad (1.5)$$

Here C is a constant (determined empirically) and $\vec{m} = \vec{M}/M_s$ is the normalized magnetization, a unit vector parallel to the magnetization direction. Curling of magnetization results in an energy penalty, but this effect is second order if the magnetization changes its direction smoothly enough. Some small-angle edge magnetization bending is predicted in simulations even for the smallest samples. In most cases, though this bending or curling plays no significant role and nanoclusters effectively behave as giant-spin particles known as macrospins or superspins.

Zeeman energy.

Here we discuss the interaction of a spin (or a macrospin) with local magnetic induction \vec{B} . Throughout this section we follow the derivation presented in reference [33]. Magnetic induction in classical electrodynamics [34] has the

form:

$$\vec{B} = \vec{H} + 4\pi\vec{M} \quad (1.6)$$

If the spin is subjected to the action of the magnetic field, the corresponding Hamiltonian term (Zeeman term) [35] reads:

$$\mathcal{E}_Z = -\vec{\mu} \cdot \vec{B} = -\frac{g\mu_B}{\hbar} \vec{S} \cdot \vec{B} \quad (1.7)$$

where $\vec{\mu}$ is the electron magnetic moment, g is the Landé factor, μ_B is the Bohr magneton (or the total magnetic moment, for a macrospin).

Quantum mechanics states [36] that the time evolution of the mean value of any observable (such as spin operator in our case) can be derived from the Schrödinger equation as follows:

$$i\hbar \frac{d}{dt} \langle \vec{S} \rangle = \langle [\vec{S}, \mathbf{H}] \rangle \quad (1.8)$$

where square brackets represent a commutator, and \mathbf{H} is the corresponding Hamiltonian (not to be confused with the magnetic field in the equation 1.6). Substituting the Zeeman Hamiltonian H_Z and applying commutation rules

$$[S_x, S_y] = i\hbar S_z; \quad [S_y, S_z] = i\hbar S_x; \quad [S_z, S_x] = i\hbar S_y \quad (1.9)$$

one obtains after some algebra the equation of motion for an isolated spin in a magnetic field:

$$\frac{d}{dt} \langle \vec{S} \rangle = \frac{g\mu_B}{\hbar} \left(\langle \vec{S} \rangle \times \vec{B} \right) \quad (1.10)$$

For average magnetization \vec{M} (average magnetic moment per unit volume) in external field \vec{H} the equations for magnetization and energy density (cf. 1.10) can be rewritten as:

$$\mathcal{E}_Z = -\vec{M} \cdot \vec{B} \quad (1.11)$$

$$\frac{d}{dt}\vec{M} = -\gamma_0[\vec{M} \times \vec{H}] \quad \text{where } \gamma_0 \approx 17.6 \times 10^7 \text{ MHz/Oe} \quad (1.12)$$

Equations (1.10),(1.12) clearly describe precessional motion of a spin (or magnetization) around the direction of the applied field, thus an analogy to the precession of a spinning top is widely used throughout the literature. However, the spin is not a top [37], as it does not nutate. As soon as the magnetic field is applied, the precession starts, and this fact is related to the quantum nature of the phenomenon.

Anisotropy energy.

The crystalline anisotropy can be included in the equation of motion by means of effective fields. Anisotropy fields are the result of the interaction of relativistic electron with the crystalline electric field (Van Vleck, 1937). Empirical constants are again used for micromagnetic calculations. The effective field can be found by taking the negative gradient of the energy expression with respect to the components of the magnetization (compare Eq. 1.11). For instance, in a crystal with strong tetragonal anisotropy, the effective contribution to the system energy density can be approximated as:

$$\mathcal{E}_A = K_2 \left(1 - \frac{M_z^2}{M_s^2} \right) = K_2 \left(\frac{M_x^2 + M_y^2}{M_s^2} \right) \quad (1.13)$$

where K_2 is a uniaxial anisotropy constant per atom. Taking a negative gradient of the first part of the equation (1.13) obtain:

$$H_z = \frac{\partial \mathcal{E}_A}{\partial M_z} = 2K_2 \frac{M_z}{M_s^2} \quad H_x = H_y = 0; \quad (1.14)$$

while from the second part of the equation (1.13) one obtains

$$H_x = -2K_2 \frac{M_x}{M_s^2} \quad H_y = 2K_2 \frac{M_y}{M_s^2} \quad H_z = 0. \quad (1.15)$$

These fictitious effective fields differ from regular magnetic fields as there is certain arbitrariness in their definition [38] (e.g. compare (1.14) and (1.15)).

Either way, the equations of motion are the same:

$$\frac{dM_x}{dt} = \gamma_0 H_{eff} M_y \quad \frac{dM_y}{dt} = -\gamma_0 H_{eff} M_x \quad \frac{dM_z}{dt} = 0. \quad (1.16)$$

where $H_{eff} = 2K_2 M_z / M_s^2$ and depends on the magnetization along z -axis. In the absence of any other external fields M_z does not change, the crystalline anisotropy acts an effective field applied in z -direction and the magnetization precesses around the crystalline anisotropy axis. The equilibrium state is along the anisotropy axis if K_2 is positive, and lies in the equatorial plane if it is negative.

This is the lowest-order uniaxial anisotropy term, more precise approximations include terms proportional to M_z^4, M_z^6 etc., and the minimum energy may lie in the cones of angles (not necessarily parallel or perpendicular to the anisotropy axis), depending on particular values of anisotropy constants.

Another common representation of uniaxial anisotropy is to characterize the energy as a function of the angle between the magnetization and the anisotropy axis. The forms

$$\mathcal{E}_A = K_u \sin^2 \theta \quad (1.17)$$

$$\mathcal{E}_A = K_1 \cos^2 \theta + K_2 \cos^4 \theta \quad (1.18)$$

are widely used in the literature.

Crystals with cubic symmetry such as iron do not possess uniaxial anisotropy, but rather cubic anisotropy. A commonly used form of the fourth-order cubic

anisotropy term reads as

$$\mathcal{E}_A = K_c (m_x^2 m_y^2 + m_y^2 m_z^2 + m_x^2 m_z^2) \quad (1.19)$$

This gives the same result as writing the cubic anisotropy term as

$$\mathcal{E}_A = -\frac{K_c}{2} (m_x^4 + m_y^4 + m_z^4) \quad (1.20)$$

which emphasizes the crystalline symmetry and clearly shows the directions of minimal energy. For some mysterious reason this form is not popular in the literature [38]. Cubic anisotropy can have higher order terms as well. Similarly to the uniaxial anisotropy energy, cubic anisotropy energy can be represented in terms of the direction cosines. In many cases cubic and uniaxial anisotropies coexist.

Demagnetization energy.

The last energy term originates by long-range magnetostatic interaction between the spins. It is this term which is responsible for the coercivity, shape anisotropy and energetically favorable division of a ferromagnetic slab into multiple domains. The last effect gives rise to the name of this particular interaction: large enough uniformly magnetized samples tend to reduce their average magnetization (“demagnetize”) by splitting into multiple domains, closed-flux domain sets or a vortex state in order to minimize the magnetostatic energy associated with stray magnetic fields.

The expression of the magnetostatic energy can be written in terms of the magnetic fields as

$$\mathcal{E}_D = -\frac{1}{2} \int_{all\ space} \vec{B} \cdot \vec{H} dV \quad (1.21)$$

where the integration is carried over the entire space, and \vec{B} is magnetic induc-

tion. This method helps to qualitatively explain the energy gain of splitting the material into domains (Fig. 1-7), but has limited use in practical calculations.

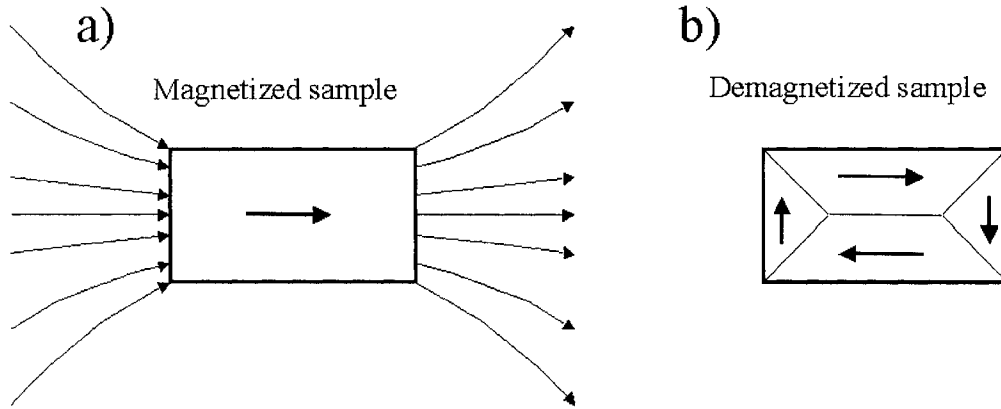


Figure 1-7: (a) Magnetized (single domain) slab. Magnetic field emerges from the specimen ends. (b) Demagnetized sample. Magnetic flux is enclosed. Bold arrows represent the domain magnetizations, thin arrows schematically show the fringing magnetic fields.

In the case of the single-domain “magnetized” structure (Fig. 1-7 a), strong fringing fields at the sample ends contribute to the magnetostatic energy, while in the case of closed domain structure the field outside the sample is weak.

Magnetization self-energy can also be estimated via summation of the individual contributions of magnetic moment energies in local magnetic field (1.11):

$$\mathcal{E}_D = -\frac{1}{2} \int_{\text{specimen}} \vec{M} \cdot \vec{B}_{\text{demag}} dV \quad (1.22)$$

here the factor 1/2 is introduced in order to avoid double summation. Magnetostatic Maxwell equations for \vec{B}_{demag} state (in the absence of currents):

$$\vec{\nabla} \cdot \vec{B}_{demag} = 0 \quad \vec{B}_{demag} = \vec{H}_{demag} + 4\pi \vec{M} \quad (1.23)$$

$$\vec{\nabla} \times \vec{H}_{demag} = 0 \implies \vec{H}_{demag} = -\vec{\nabla} U \quad (1.24)$$

The demagnetization field \vec{H}_{demag} can be represented as a gradient of some scalar potential U as its vorticity is equal to zero. Equations (1.23),(1.24) state:

$$\nabla^2 U = 4\pi \vec{\nabla} \cdot \vec{M} \quad (1.25)$$

with standard boundary conditions ([34]): the tangential component of \vec{H}_{demag} and normal component of \vec{B}_{demag} must be continuous at the interface between the ferromagnetic and vacuum:

$$U_{in} = U_{out} \quad \text{and} \quad \frac{\partial U_{in}}{\partial n} - \frac{\partial U_{out}}{\partial n} = 4\pi \vec{M} \cdot \vec{n} \quad (1.26)$$

The formal solution of the differential equation (1.25) with boundary conditions (1.26) can be written in the form [30]:

$$U(r) = - \int_{\text{volume}} \frac{\vec{\nabla}' \cdot \vec{M}(r')}{|\vec{r} - \vec{r}'|} dr' + \int_{\text{surface}} \frac{\vec{n} \cdot \vec{M}(r')}{|\vec{r} - \vec{r}'|} dr'. \quad (1.27)$$

Substituting this value of the scalar potential U subsequently into (1.24),(1.23) and (1.22) one finds the demagnetization energy and demagnetization fields. This method is used for analytical calculations of demagnetization energy in simple structures such as ellipsoids [17],[39],[40] and rectangular platelets [30].

For numerical simulations of dynamic problems, the most common method of the demagnetization field calculation is a direct summation of individual dipole fields over the sample. The local field at the site "i" can be represented as

$$\vec{H}_i = \sum_{j \neq i} \left[-\frac{\vec{\mu}_j}{r_{ij}^3} + \frac{3(\vec{\mu}_j \cdot \vec{r}_{ij}) \vec{r}_{ij}}{r_{ij}^5} \right] \quad (1.28)$$

This term accounts only for simple dipole-dipole interaction, its accuracy isn't sufficient in some numerical calculations as the model assumes a single dipole at the center of each cell [41],[42] and can be improved by volume averaging the numerical coefficients within each cell [43].

1.3.3 Landau-Lifshitz wall.

In this section and the following one we discuss the 180° domain wall, a transitional region between two oppositely magnetized domains (Fig. 1-8 *a*). As bending of magnetization results in an exchange energy penalty (Eq. 1.5), this transition cannot be sharp. Two scenarios for a smooth transition were suggested: (i) the magnetization rotates in the plane parallel to the plane of the domain wall (Bloch wall, Fig. 1-8 *b, c*); and (ii) the magnetization always remains in the plane perpendicular to the wall (Néel wall, Fig. 1-8 *d*).

Exchange, anisotropy and demagnetization contributions ought to be taken into account in calculation of the wall structure in both cases. However, in the special case of the Bloch wall in an infinite slab where demagnetization energy can be neglected: $\vec{\nabla} \cdot \vec{M} = 0$ everywhere so that the volume contribution to Eq. (1.27) vanishes, and the surface integral is neglected in the bulk. Historically this case represents the first successful attempt to calculate the wall structure, performed in 1936 by Landau and Lifshitz [44], hence it is best known as the Landau-Lifshitz wall. More general cases of Bloch and Néel walls are presented in the next section.

A schematic view of a typical 180° domain wall is shown in the Figure 1-8 *a*. Uniaxial anisotropy is along the \hat{z} direction. Magnetization is set by crystalline anisotropy in the opposite directions ($\pm \hat{z}$) outside of the domain wall, and adiabatically changes its orientation inside the wall, while always

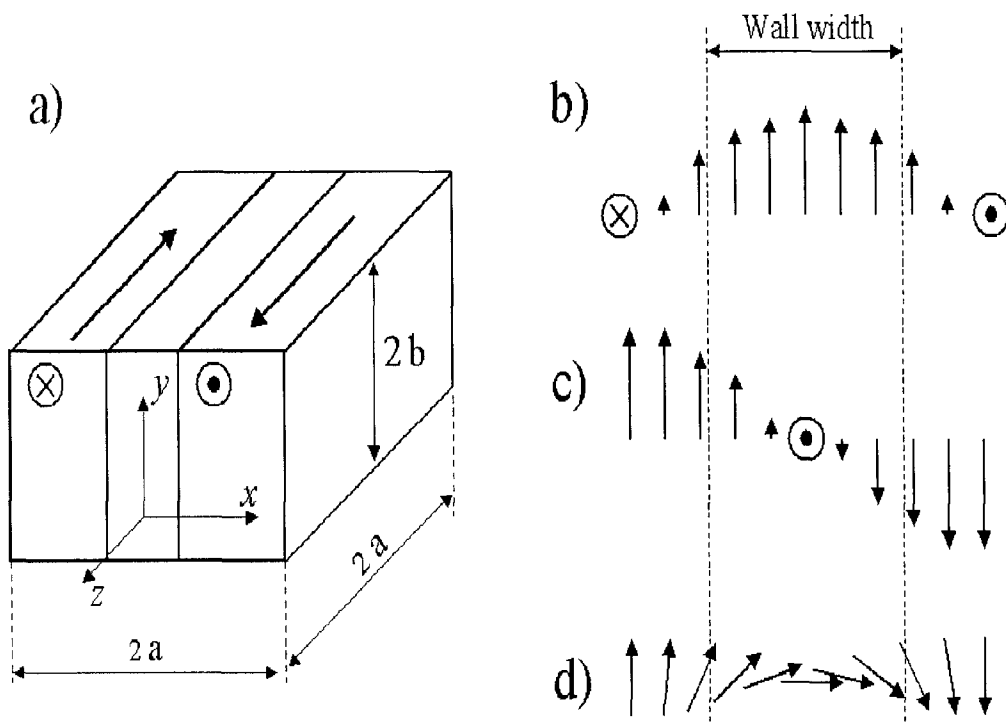


Figure 1-8: (a) A schematic representation of a 180° domain wall. (b,c) The structure of the Landau-Lifshitz or Bloch walls, cross-section and plan view respectively. (c) Néel wall, plan view.

staying parallel to the wall plane yz . The orientation of the magnetization vector depends only on the position along the \hat{x} axis.

Here we again consider normalized magnetization \vec{m} (all Hamiltonian terms are scaled accordingly). The volume energy density takes the form:

$$w = K_2 m_y^2 + \frac{1}{2} C \left[\left(\frac{dm_y}{dx} \right)^2 + \left(\frac{dm_z}{dx} \right)^2 \right]. \quad (1.29)$$

It is convenient to introduce the magnetization rotation angle θ so that $m_z = \cos \theta$; $m_y = \sin \theta$ to enforce the constraint $m_x^2 + m_y^2 = 1$. The energy per unit area in the yz -plane is

$$E = \int_{-\infty}^{\infty} \left[K_2 \sin^2 \theta + \frac{1}{2} C \left(\frac{d\theta}{dx} \right)^2 \right] dx \quad (1.30)$$

The Euler differential equation for minimizing this integral is

$$C \frac{d^2 \theta}{dx^2} - 2K_2 \sin \theta \cos \theta = 0 \quad (1.31)$$

with the boundary conditions

$$\left(\frac{d\theta}{dx} \right)_{x \rightarrow \pm \infty} = 0; \quad \theta(-\infty) = 0; \quad \theta(\infty) = \pi \quad (1.32)$$

ensuring the “wall-type” structure of the solution. Integrating Eq. 1.31 yields

$$\cos \theta = \tanh \frac{x}{\delta}; \quad \delta = \sqrt{\frac{C}{2K_2}}. \quad (1.33)$$

Substituting this expression into equation 1.30 and integrating, we obtain for the aerial wall energy

$$E = \sqrt{2K_2 C} \quad (1.34)$$

Consider two typical examples of commonly used materials. For “soft” (low anisotropy) permalloy ($\text{Ni}_{80}\text{Fe}_{20}$) $C \approx 1.05 \times 10^{-6}$ erg/cm, $K_2 \approx 10^3$

erg/cm³. Formula (1.33) yields $\delta \approx 230$ nm. One might expect near-single domain behavior when the sample size approaches a few hundreds of nanometers. However, at this scale magnetostatic interactions (demag fields) cannot be ignored. Even in thin films of unlimited lateral size, demagnetization effects lead to an order of magnitude reduction of the wall width. Another example is cobalt, $C \approx 3 \times 10^{-6}$ erg/cm, $K_2 \approx 4 \times 10^6$ erg/cm³; $\delta \approx 8$ nm. It appears, that cobalt structures would remain in multi-domain state down to very small lateral size. However, experimental evidence indicates that cobalt nanostructures turn into single-domain states more willingly than permalloy particles of similar shape. The reason for that is again magnetostatic interactions, neglected in the Landau and Lifshitz's derivation.

1.3.4 Bloch and Néel walls.

If the crystal is finite, the proposed wall structure has a non-zero normal component of the magnetization at the surface, and magnetostatic energy must be taken into account. This effect is especially important in thin films, where the magnetostatic contribution literally squeezes the magnetization into the plane of the film.

Here we will not follow all steps of the derivation [30], but rather describe the model used in the calculations, and list some important results. A special form of magnetization components is assumed:

$$m_x(x) = 0 \quad m_y(x) = \frac{q^2}{q^2 + x^2} \quad \text{Bloch wall} \quad (1.35)$$

$$m_x(x) = \frac{q^2}{q^2 + x^2} \quad m_y(x) = 0 \quad \text{Néel wall} \quad (1.36)$$

$$m_z(x) = \frac{x\sqrt{2q^2 + x^2}}{q^2 + x^2} \quad \text{both Bloch and Néel walls} \quad (1.37)$$

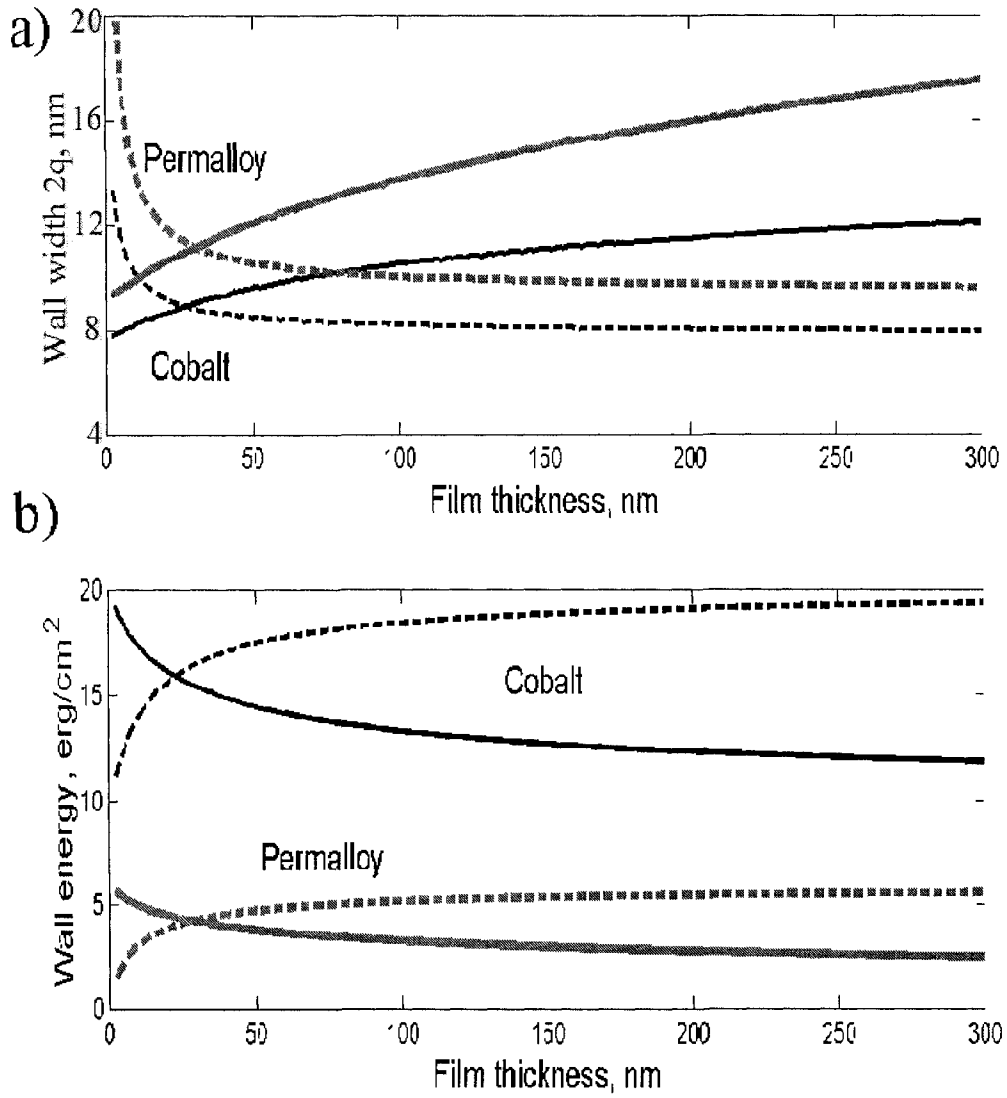


Figure 1-9: Comparison of Bloch (solid) and Neel (dashed) walls for permalloy (thick grey) and Cobalt (black). (a) Effective widths of the walls dependence on the film thickness. (b) Corresponding energy densities.

where q is an adjustable parameter (effectively, half-width of the Lorentzian at half-maximum level) used to minimize the total energy. The magnetostatic energy of a square platelet of the dimensions $2a \times 2a \times 2b$ (Fig. 1-8a) for the special case of magnetization independent of y (thin film) and of z (a wall along z -direction) magnetization can be found [30] as:

$$\frac{E_M}{2M_s^2} = \int_0^\infty \frac{1 - e^{-2bt}}{t} \int_{-a}^a \int_{-a}^a \cos[(x - x')t] [m_z(x)m_z(x') - m_x(x)m_x(x')] dx dx' dt + 2\pi b \int_{-a}^a [m_x(x)]^2 dx \quad (1.38)$$

where M_s is the saturation magnetization of the material. Exchange and anisotropy terms analogously to Equation 1.29 have the form

$$E_{ex} + E_A = \frac{1}{2}C \left[\left(\frac{dm_x}{dx} \right)^2 + \left(\frac{dm_y}{dx} \right)^2 + \left(\frac{dm_z}{dx} \right)^2 \right] + K_2 m_y^2 \quad (1.39)$$

Substituting the magnetization distributions 1.35,1.36 into 1.38 and 1.39 integrating from $-\infty$ to ∞ for the platelet width a obtain for the total wall energy per unit area of the wall

$$E_{Bloch} = \frac{\pi C}{q}(\sqrt{2} - 1) + \frac{\pi q}{2}K_2 + \frac{\pi^2 M_s^2 q^2}{b} \ln \left(1 + \frac{b}{q} \right) \quad (1.40)$$

$$E_{Néel} = \frac{\pi C}{q}(\sqrt{2} - 1) + \frac{\pi q}{2}K_2 + \pi^2 M_s^2 q \left[1 - \frac{q}{b} \ln \left(1 + \frac{b}{q} \right) \right] \quad (1.41)$$

Minimizing E_{Bloch} and $E_{Néel}$ with respect to q one obtains the equations for corresponding wall widths:

$$\frac{C}{q^2}(\sqrt{2} - 1) = \frac{K_2}{2} + \pi M_s^2 \left[\frac{2q}{b} \ln \left(1 + \frac{b}{q} \right) - \frac{q}{q+b} \right] \quad (\text{Bloch}) \quad (1.42)$$

$$\frac{C}{q^2}(\sqrt{2} - 1) = \frac{K_2}{2} + \pi M_s^2 \left[1 - \frac{2q}{b} \ln \left(1 + \frac{b}{q} \right) + \frac{q}{q+b} \right] \quad (\text{Néel}) \quad (1.43)$$

Numerical solution of the equations 1.40-1.43 for permalloy ($C = 1.05 \times 10^{-6}$ erg/cm, $K_2 = 10^3$ erg/cm³, $M_s = 800$ emu) and cobalt ($C = 3 \times 10^{-6}$ erg/cm, $K_2 = 4 \times 10^6$ erg/cm³, $M_s = 1414$ emu) are shown in the Figure 1-9. Surprisingly, the wall widths for these are not that different (Fig. 1-9 *a*), nowhere near the expectations based on Landau-Lifshitz theory (in particular, the Bloch wall width for permalloy is more than an order of magnitude narrower). This is a strong indication that demagnetization plays a crucial role in constrained structures. As for the wall energies, (Fig. 1-9 *b*), one can notice, that Néel wall becomes energetically favorable at wall thicknesses below approximately 30 nm for both materials. The transition between these two regimes is not sharp: around the transition to a complex three-dimensional wall appears. It is called the “cross-tie” wall and it demonstrates periodic behavior of all three components of magnetization along the wall [17],[45]. In most experiments we are far from this transitional regime and for film thicknesses below 15 nm the Néel wall is expected. Micromagnetic simulations confirm this scenario of domain wall formation. On the other hand, the 45-nm thick Fe₂₀Co₈₀ film used in our prototype railway-cross element (Section 4.1) could demonstrate this complex structure or exhibit Bloch wall behavior. However, Scott Zelakiewicz of the Naval Research Laboratory performed Magnetic Force Microscopy (MFM) measurements on analogous samples made of the same material, and found neither cross-tie walls nor high out-of-plane magnetization stripes indicative of the Bloch walls. We believe that this sample also exhibited Néel wall behavior.

Both the Bloch and Néel walls descriptions yield two equivalent structures — for clockwise and counter-clockwise rotation of the magnetization vector inside the wall. If two Néel walls collide, they can either annihilate if they have opposite vorticities, or form a 360° Arrott wall otherwise [46],[47]. We discuss the Arrott wall in the section 4.1.4.

1.3.5 Uniformly magnetized ellipsoid.

In general, the magnetization-induced field inside a uniformly magnetized body is non-uniform. There is, however, a very important exception: if and only if the specimen's boundary is a second-degree surface, the resulting field is uniform. In practice, this means an ellipsoidal structure, as the rest of the second-degree surfaces are not bounded. It is also approximately the cases with a reasonable degree of precision, for long cylinders and thin film planes as limiting cases. The general theorem states that for a uniformly magnetized ellipsoid the total field inside the sample is given by expression (in CGS units):

$$\vec{H}_{total} = \vec{H}_0 - \vec{H}_D = \vec{H}_0 - 4\pi \overleftrightarrow{N} \vec{M} \quad (1.44)$$

$$\overleftrightarrow{N} \equiv \begin{pmatrix} N_x & & \\ & N_y & \\ & & N_z \end{pmatrix} \quad (1.45)$$

$$Tr \overleftrightarrow{N} = 1 \quad (1.46)$$

where \vec{H}_0 is the external field and \overleftrightarrow{N} is a diagonal demagnetization tensor. In literature it is more often addressed by its components N_x, N_y, N_z known as demagnetizing factors. From symmetry and equation (1.46) one can immediately see that for spherical particles $N_x = N_y = N_z = 1/3$.

The values for the demag factors of uniformly magnetized ellipsoids can be

Table for N_x										
b/a	1	0.9	0.8	0.7	0.6	0.5	0.4	0.3	0.2	0.1
$c/a \downarrow$										
1	0.3333									
0.9	0.3191	0.3057								
0.8	0.3028	0.2904	0.2760							
0.7	0.2840	0.2726	0.2593	0.2441						
0.6	0.2621	0.2519	0.2400	0.2262	0.2100					
0.5	0.2364	0.2275	0.2171	0.2050	0.1907	0.1736				
0.4	0.2059	0.1985	0.1897	0.1795	0.1674	0.1529	0.1351			
0.3	0.1693	0.1635	0.1566	0.1486	0.1390	0.1274	0.1132	0.0954		
0.2	0.1248	0.1207	0.1160	0.1103	0.1036	0.0954	0.0853	0.0725	0.0558	
0.1	0.0696	0.0675	0.0651	0.0621	0.0586	0.0544	0.0490	0.0422	0.0331	0.0203
0.0	0	0	0	0	0	0	0	0	0	0

Table for N_y										
b/a	1	0.9	0.8	0.7	0.6	0.5	0.4	0.3	0.2	0.1
$c/a \downarrow$										
1	0.3333									
0.9	0.3191	0.3472								
0.8	0.3028	0.3302	0.3620							
0.7	0.2840	0.3106	0.3417	0.3779						
0.6	0.2621	0.2876	0.3175	0.3529	0.3950					
0.5	0.2364	0.2605	0.2888	0.3226	0.3633	0.4132				
0.4	0.2059	0.2279	0.2541	0.2856	0.3240	0.3717	0.4324			
0.3	0.1693	0.1884	0.2114	0.2394	0.2740	0.3180	0.3752	0.4523		
0.2	0.1248	0.1397	0.1579	0.1805	0.2090	0.2461	0.2959	0.3662	0.4721	
0.1	0.0696	0.0786	0.0896	0.1036	0.1218	0.1462	0.1805	0.2322	0.3183	0.4899
0.0	0	0	0	0	0	0	0	0	0	0

Table 1.2: Demagnetizing factors N_x and N_y for uniformly magnetized ellipsoids. Factor $N_z = 1 - N_x - N_y$

expressed exactly in terms of elliptical integrals [39],[40]. The most important point to stress in this section is that the demagnetization factors do not depend on the ellipsoid *size*, but only on the *ratio* of the ellipsoids half-axes a , b and c (conventionally, $a > b > c$). This makes ellipsoidal shapes very attractive for both theoretical speculations and for experiments. On the other hand, this example illustrates the long-range nature of magnetostatic interactions: one can not neglect the surface effects, no matter how far away the surface is [30]. Numerical values for some selected values of the axis ratios are listed in the Table 1.1. For the special case of a long cylinder ($a \gg b, c$), $N_x = 0$; $N_y = N_z = 1/2$. Analogously, for a plane ($a = b \gg c$), $N_x = N_y = 0$, $N_z = 1$.

In this work we used lithographically patterned thin-film elliptical samples. These are not true ellipsoids, as the film does not thin down towards the edges, but ellipsoid is often used as an approximation for this kind of structure. We partially agree with this approach: indeed if no magnetic field is applied, magnetization is nearly uniform in the equilibrium state according to micromagnetic simulations and direct observations by other groups [48]. When the sample starts to switch however, the edges lag behind the center of the sample, which switches first, as we both observed in experiment and modeled in micromagnetic simulation. We discuss this phenomenon the sections 4.2.3 - 4.2.5.

1.3.6 Stoner-Wohlfarth Astroid, half-select switching.

An ultimate goal of this work is to achieve a single-domain (or nearly single-domain) switching of a small thin-film ferromagnetic element. An analytical theory of single-domain particle switching by a quasi-static magnetic field was developed by Stoner and Wohlfarth [49]. The diagram called the “switching Astroid” has established the basis for development of the Magnetic Random Access Memory.

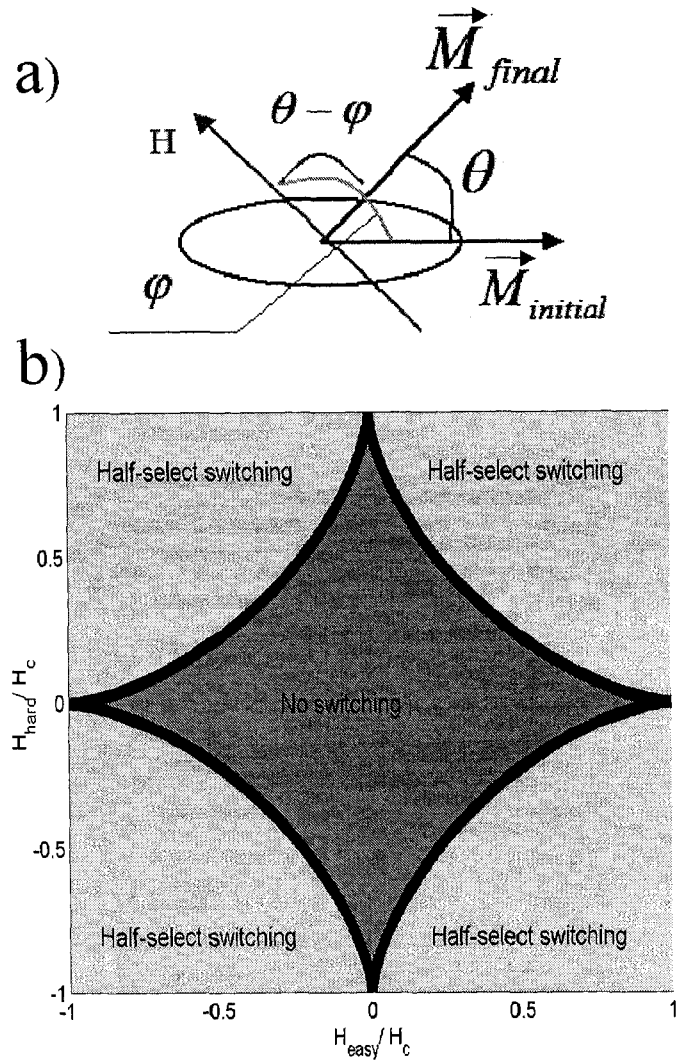


Figure 1-10: (a) Schematic illustration of the magnetization tilt under influence of the external magnetic field H . (b) The Astroid switching diagram, both hard- and easy-axis fields are normalized to the coercivity.

Consider an arbitrary sample small enough to behave as a single-domain particle with well-defined uniaxial anisotropy (whether crystalline or shape-induced magnetostatic, or a combination of both), such as the elliptical specimen shown in Figure. 1-10 *a*. The initial magnetization $\vec{M}_{initial}$ is parallel to the long axis. As magnetic field is applied at an angle φ to this direction ($\varphi > \pi/2$), the magnetization finds a new equilibrium position M_{final} at an angle θ to the initial state, minimizing Zeeman and anisotropy energies (exchange doesn't contribute as all spins are parallel; and magnetostatic interactions are included in the anisotropy term):

$$E = K_2 \sin^2 \theta - H\mu \cos(\theta - \varphi) \quad (1.47)$$

where K_2 is the uniaxial anisotropy constant, and μ is the total magnetic moment. The tilted state \vec{M}_{final} is found by minimizing this energy with respect to θ (Eq.1.48). Denote the states of $\theta < \pi/2$ as unswitched states: upon removal of the external field the magnetization relaxes to its original direction $\vec{M}_{initial}$. Switching is prevented by crystalline anisotropy. However, if the external field is strong enough, the equilibrium becomes unstable, and the magnetization slips into the “switched” state $\varphi < \theta < \pi$ when the second derivative of the expression 1.47 with respect to θ vanishes (1.49) :

$$\frac{\partial E}{\partial \theta} = 2K_2 \sin \theta \cos \theta + H\mu \sin(\theta - \varphi) = 0 \quad (1.48)$$

$$\frac{\partial^2 E}{\partial \theta^2} = 2K_2(\cos^2 \theta - \sin^2 \theta) + H\mu \cos(\theta - \varphi) = 0 \quad (1.49)$$

Upon removal of the external field the magnetization relaxes to the direction opposite to $\vec{M}_{initial}$. Substituting $H_x = H \cos \varphi$, $H_y = H \sin \varphi$ one obtains the relations for two components of the critical field:

$$H_x = -\frac{2K_2}{\mu} \cos^3 \theta, \quad H_y = \frac{2K_2}{\mu} \sin^3 \theta \quad (1.50)$$

$$H_x^{2/3} + H_y^{2/3} = H_c^{2/3} \quad H_c = \frac{2K_2}{\mu} \quad (1.51)$$

The switching diagram corresponding to equation 1.51 is shown in Figure 1-10 *b*. The dark area inside the four-pointed star (the astroid) corresponds to weak fields unable to switch the magnetization. The left part of the diagram corresponds to the initial magnetization pointing to the right, and vice versa. For fields outside the shaded grey area switching always occurs. In particular, an easy-axis field $H_x > H_c$ flips the magnetization with or without assistance of a hard-axis field. Conversely, a hard-axis external field $H_y > H_c$ magnetizes the sample along the hard axis, and any negative easy-axis field, however small, is sufficient to complete the switching process. The light grey area is the most important for MRAM applications. It is called the “half-select” switching region for the reasons explained in section 1.2.1. In this regime both easy- and hard- axis fields are required in order to complete the magnetization reversal.

This derivation of the diagram shape corresponds to the simplest case of the second-order uniaxial anisotropy. If higher-order terms and/or cubic anisotropy are taken into account, the diagram becomes more complex: it can have multiple self-intersections corresponding to metastable states [37].

Another complication arises once time-dependent fields are considered. Magnetization tends to precess around the effective field (Eq. 1.12), and a half-cycle of precession may lead to switching at a much lower field than required in the adiabatic approximation used by Stoner and Wohlfarth (so-called “ballistic switching”). If the magnetic field pulse is terminated at the proper moment, the magnetization remains in the switched state. For a field pulse of constant duration, the precessional frequency dependence on the field

strength may lead to a stripe-like switching diagram pattern: for field values corresponding to $1/2, 3/2, 5/2 \dots$ rotations during the pulse, the magnetization flips; whereas for $0, 1, 2 \dots$ rotations per pulse it ends up back in the initial state. Moreover, when the magnetization of thin film samples starts to tilt out of the film plane, induced demag fields influence the precession, which can further reduce the field required for switching.

Switching diagrams based on simulations predicting this scenario [50] are shown in Fig. 1-11 for an infinitely sharp Π -like pulse (left column) and for a smoother bell-like pulse (the pulse rise and fall times equal the pulse length measured at half-maximum level, the pulse profile is half-sine in shape) – right column. Each grey level panel represents the final state of magnetization of an elliptical sample characterized by three demagnetizing factors $N_x = 0.008$; $N_y = 0.012$; $N_z = 0.980$. Indeed, for slow rising field (Fig. 1-11, lower right panel) the triangular notch at the right hand side of the panel looks like half of the Stoner-Wohlfarth astroid. At shorter pulse durations, however, a complex stripe pattern is developed with pockets of switching between stripe-like areas of no switching at the diagram. We observed (Fig. 4-16) the existence of related pockets in our experiments.

1.3.7 Landau-Lifshitz-Gilbert (LLG) equation.

Local magnetization precesses under the influence of the magnetic field (external and induced by magnetization of the rest of the sample) according to equation 1.12. However, eventually the precession is damped and the magnetization settles down. A simple way to introduce the damping term is to include a “viscous friction” term into the effective magnetic field [33]:

$$\vec{H}_{eff} = \vec{H} - \frac{\alpha}{\gamma_0 M_s} \frac{d\vec{M}}{dt} \quad (1.52)$$

Inserting (1.52) into (1.12) yields:

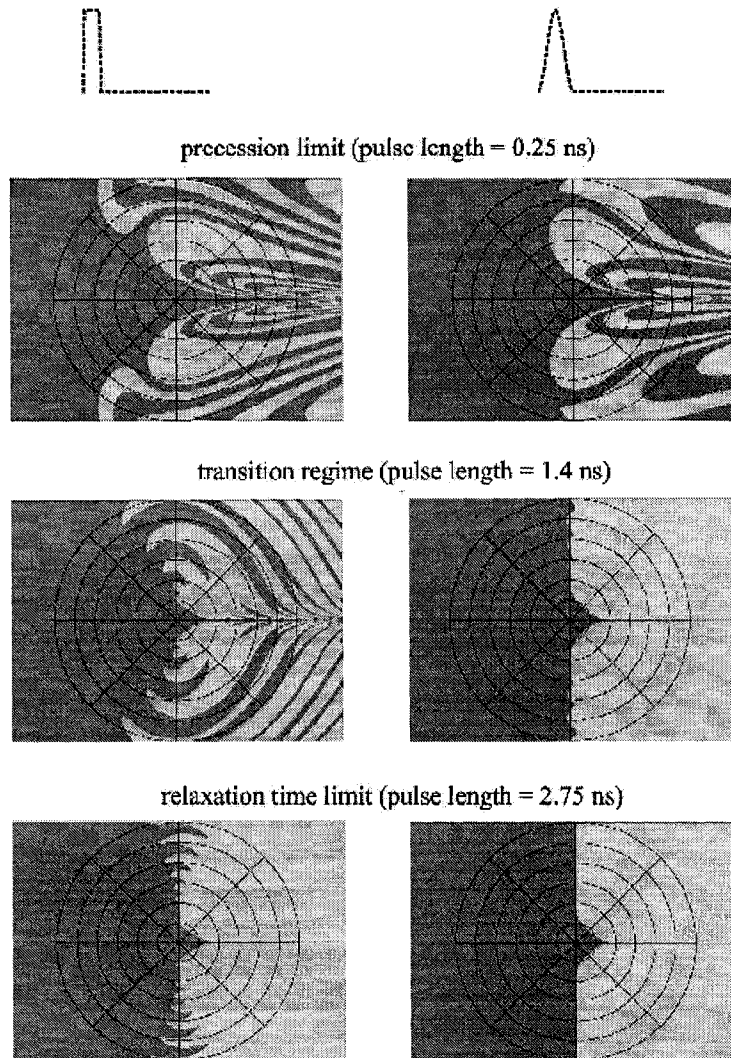


Figure 1-11: Switching diagrams for a single-domain elliptical samples perturbed by a finite duration sharp (left column) and half-sinusoidal (right column) pulses. In all cases the sample is initially magnetized to the left. Grayscale represents the final magnetization dark – unswitched, light – switched.

$$\frac{d\vec{M}}{dt} = -\gamma_0 [\vec{M} \times \vec{H}] + \frac{\alpha}{M_s} \left[\vec{M} \times \frac{d\vec{M}}{dt} \right] \quad (1.53)$$

Equation 1.53 is known as Landau-Lifshitz-Gilbert (LLG) equation. All simulations discussed below were performed on LLG Micromagnetic simulator [51]. It demonstrates very good agreement with experiment in many cases.

A side remark can be made in relation to the form of the friction term in equation 1.52. Just as the spin starts precession without transitional regime of decaying nutations, the friction engages at the very moment the field is turned on [37]. The nature of precessional motion is quantum mechanical and well-understood, while the friction term is introduced classically although the nature of the dissipation – spin-spin, spin-magnon scattering is quantum mechanical as well. It is possible that there is some delay (such as scattering time) between the beginning of the precession and engagement of the friction force, but such a delay has not been detected experimentally.

Equation 1.53 can be transformed as follows:

$$(1 + \alpha^2) \frac{d\vec{M}}{dt} = -\gamma_0 [\vec{M} \times \vec{H}] - \frac{\alpha\gamma_0}{M_s} (\vec{M} \times [\vec{M} \times \vec{H}]) \quad (1.54)$$

$$(1 + \alpha^2) \frac{d\vec{M}}{dt} = -\gamma_0 [\vec{M} \times \vec{H}] - \alpha\gamma_0 \left[M_s \vec{H} - \frac{(\vec{H} \cdot \vec{M})}{M_s} \vec{M} \right] \quad (1.55)$$

$$(1 + \alpha^2) \frac{d\vec{m}}{d\tau} = -[\vec{m} \times \vec{h}] - \alpha (\vec{m} \times [\vec{m} \times \vec{h}]) \quad (1.56)$$

The last equation is written in the dimensionless variables: $m = \vec{M}/M_s$; $\tau = \gamma_0 M_s t$; $h = \vec{H}/M_s$. All three forms are used in publications.

The LLG equation preserves the absolute value of the local magnetization (it is equal to the saturation magnetization M_s at every point). This is a very good approximation, based on the strength of the exchange interactions, aligning the spins of small groups of atoms parallel to each other. One can argue

that a single spin is parallel to itself by definition, but then again, a single spin is to be treated quantum mechanically, and all three direction cosines cannot be defined simultaneously. Other models, such as Bloch-Blombergen [52] equation include the possibility of non-constant value of the local magnetization, but are not as naturally suited to the ferromagnetic case.

For nearly-single-domain elements the LLG equation describes damped precessional motion. In the case of flipping the element magnetization from some initial state to the opposite direction (such as in two-level memory elements), reaching equilibrium in most cases requires time determined by the relaxation constant α , generally a small number ($\alpha \simeq 0.01$ for permalloy). With small damping, the element magnetization precesses about (or “rings”) the new equilibrium position for a long time. There is a much faster switching scenario: coherent rotation of the sample magnetization around the hard-axis field. If the magnetic field pulse is terminated at the proper moment (as briefly described in section 1.3.6), magnetization remains in its final state with no ringing and the switching time is defined by half period of precession and independent on the damping.

1.3.8 Domain wall motion.

Incoherent switching is more complicated, even if the element is nearly uniformly magnetized initially. It includes some or all of the following stages:

1. Nucleation. Magnetization starts curling at the edges forming areas (domains) of switched material and domain walls between them and the rest of the structure. Nucleation can start at multiple sites [53], as the initial magnetization loses stability under stress. Nucleation usually happens on sub-nanosecond temporal scales.
2. Domain walls start to move, increasing the size of the domains with favorable orientation (minimizing the Zeeman energy term) at the expense

of the rest. Some sites reverse by precession of magnetization on a local scale. Effectively the most significant net change of the magnetization occurs in this regime. The typical duration of this step is from half a nanosecond to a few nanoseconds for micrometer-sized particles.

3. The switching is almost complete, but some topological structures (such as vortices and antivortices) remain in the sample, and closure domains exist at the edges. Vortices and other features can be expelled at the surface of the sample, or form a metastable state. Closure domains slowly decrease in size. This longest step of the switching can last from a few nanoseconds to a few hundred nanoseconds. Worse, sometimes the metastable states persists, and the resulting magnetization pattern is irreproducible from one event to another.

Most of the “switching” takes place during the second phase of domain wall motion and incoherent rotation. Most reasonable definitions of the switching rise time (such as 10-90% of the saturation level) fall in this regime’s duration, although complete switching is only achieved by the end of the phase 3.

The speed of steady motion of a 180° wall under the influence of a constant magnetic field was derived in the pioneering work of Landau and Lifshitz [44]. It demonstrates the linear dependence of the wall speed on applied magnetic field:

$$v = \mu_w(H - H_0) \tag{1.57}$$

where μ_w is the wall mobility, and H_0 is some offset such as coercivity. In many calculations this offset is neglected [54]. In a one-dimensional model the propagation speed can be estimated as

$$v = \frac{\gamma_0 \Delta}{\alpha} H \tag{1.58}$$

where α is the dimensionless Landau-Lifshitz damping parameter, and Δ is the (Bloch) wall width. These derivations assume that the domain wall shape and effective width do not change as the domain wall propagates down the crystal. It is also customary to express the wall mobility and velocity in terms of the wall width itself [54],[55] rather than in terms of fundamental constants (such as exchange and anisotropy constants). As we saw before (section 1.3.4), demagnetization effects can lead to the resulting domain wall width different from the analytical Landau-Lifshitz result (Eq. 1.33) by an order of magnitude, while the domain wall width can in some cases be measured directly.

Taking into account a possible change of the domain wall width with time leads to significantly lower mobility [56]. The domain wall loses lateral stability at the Walker breakdown velocity

$$v_W = 2\pi\gamma_0\Delta M_s \quad (1.59)$$

which can be used as an upper boundary for domain wall speed. All of these formulas yield order of magnitude estimates. For instance, substituting for the permalloy wall width $\Delta \approx 12$ nm (Fig. 1-9 a) and $4\pi M_s \approx 1$ Tesla (in MKS units) one obtains $v_W \approx 1060$ m/s. On the other hand substituting the Landau-Lifshitz wall width $\Delta \approx 200$ nm would result in $v_W \approx 18$ km/s. In general, the domain wall propagation speed is in the ballpark of a few kilometers per second [53] (or, perhaps more relevant a few micrometers per nanosecond), which indeed explains the relevant temporal scale of the multi-domain particle switching. For quantitative estimations, it is recommended to stick to the LLG Simulator.

1.3.9 Kittel formula.

An important application of the Ferromagnetic Resonance solution of the equation 1.12 to the time-dependent problem of small vibrations was suggested by

Charles Kittel [57]. A simple relation known as the Kittel formula was derived analytically and showed excellent agreement with experiment in numerous microwave absorption measurements. In this problem, a general ellipsoidal particle characterized by its demagnetizing factors N_x, N_y, N_z is subjected to a static DC field H_z^0 in z -direction and to a weak harmonic radio frequency field in x -direction. Including the demagnetizing effects the field inside the specimen reads

$$H_x = H_x^0 - 4\pi N_x M_x; \quad H_y = -4\pi N_x M_x; \quad H_z = H_z^0 - 4\pi N_z M_z \quad (1.60)$$

and the equations of motion (1.12) take the form

$$\frac{dM_x}{dt} = \gamma_0 [H_z + 4\pi(N_y - N_z)M_z] M_y \quad (1.61)$$

$$\frac{dM_y}{dt} = \gamma_0 [M_z H_z - 4\pi(N_x - N_z)M_z M_z - M_x H_x] \quad (1.62)$$

$$\frac{dM_z}{dt} \simeq 0. \quad (1.63)$$

Substituting harmonic fields ($\propto \exp(i\omega t)$) after some manipulations the expression for the susceptibility $\chi_x = M_x/H_x$ is

$$\chi_x = \frac{\chi_0}{1 - (\omega/\omega_0)}, \quad (1.64)$$

$$\text{where } \chi_0 = \frac{M_z}{H_z + 4\pi(N_x - N_z)M_z}, \quad (1.65)$$

and the resonance frequency

$$\omega_0 = \gamma_0 \sqrt{[H_z + 4\pi(N_y - N_z)M_z] \times [H_z + 4\pi(N_x - N_z)M_z]} \quad (1.66)$$

For the very important case of the uniformly magnetized yz -plane ($N_y = N_z \equiv N_{\parallel} = 0$; $N_x = 1$) it gives

$$\omega_0 = \gamma_0 \sqrt{H_{\parallel} \times [H_{\parallel} + 4\pi M_{\parallel}]} \quad (1.67)$$

where M_{\parallel} is the in-plane magnetization parallel to the applied field. Relations 1.66 and 1.67 are the famous Kittel formulas. In strong ferromagnetics the term M_{\parallel} can be replaced by the saturation magnetization M_s . Equation 1.67 predicts zero resonance frequency in the case of zero bias field applied (it is not so for general ellipsoids, though). However, if there is a crystalline anisotropy, the sample can self-magnetize and some corrections to (1.66), (1.67) are to be made. In particular, in the case of the uniaxial anisotropy parallel to the bias field, (1.67) for an infinite plane takes the form

$$\omega_0 = \gamma_0 \sqrt{\left[H_{\parallel} + \frac{2K_2}{M_s} \right] \times \left[H_{\parallel} + 4\pi M_s + \frac{2K_2}{M_s} \right]} \quad (1.68)$$

where K_2 is the uniaxial anisotropy constant.

1.4 General idea of the project.

This work is application-oriented, and the experiments are focused on potential industrial use in the magnetic storage industry. Several independent projects discussed below are bound by the Time Resolved Scanning Kerr Microscopy (TR-SKM) method used for magnetic sample characterization. All the specimens were designed and results were analyzed with a perspective of industrial applications, such as optimization of the recording head performance; downsizing the element in order to obtain fast precessional single-domain half-select switching of a prototype MRAM element; application of the fast magneto-optic response of the ion-implantation sample as a remote ultra-fast current sensor; and invention of a new lithographic technique for complex multi-layer struc-

tures. This work is structured as follows:

Chapter 2 outlines the principles of the vectorially-resolved TR-SKM measurements, the details of the experimental layout, describes custom-made blue-light sensitive dual detectors, and illustrates special techniques used in the measurements and details of the sample fabrication.

Chapter 3 is devoted to the characterization of prototype magnetorecording heads. It describes the idea of direct technique of the flux risetime measurements using TR-SKM. Several heads are compared in order to derive the dependence of their performance on the geometric design parameters. This chapter is based on the paper [58].

Chapter 4 represents the main results of this work: observation of the half-select switching in crossed-wire geometry for MRAM elements. It combines two projects. First, we characterized a “Railway Cross” prototype element with both write wires lying at 45° to the easy magnetization axis of the ferromagnetic element (section 4.1). This sample was made by Scott Zelakiewicz of the Naval Research Laboratory (NRL). Half-select switching of a relatively large $7 \times 1 \mu\text{m}$ FeCo element was investigated as a function of the switching fields duration and overlap. This section is based on the reference [59]. Second, a traditional crossed-wire element with write wires parallel and perpendicular to easy-axis and much smaller element was analyzed in attempt to find single-domain switching behavior and coherent precessional switching (section 4.2). This section is based on our recently submitted paper [60]. These TR-SKM measurements are backed by micromagnetic simulations [51].

In Chapter 5 we discuss fast magnetization response of a thin layer of magnetic nanoclusters embedded into the silicon dioxide matrix. An application of this and analogous materials as magneto-optic current sensors is proposed. This section is based on the recently submitted paper [61] and the Report of Invention [62].

Appendix A presents a new method for microfabrication of crossed wires

and spiral or helical structures. This method was not used in the fabrication of the crossed-wire structures used for the Kerr microscopy measurements, and thus is not presented in the main body of the thesis. On the other hand, we believe that it is one of the most important results of this work from the technological perspective. A report of invention is in preparation.

In Appendix B we discuss qualitatively a response of an unpatterned permalloy film to the fast out-of-plane field kick generated by a recording head. Observed fast magnetization change simulates the performance of the soft underlayer used in the recording media for perpendicular recording heads.

Finally, in Appendix C we discuss the general principles of transmission line design important for obtaining fast risetimes of the write currents and consequently the magnetic field pulses used throughout this work. The issues of pulse reflection and signal mixing are emphasized.

Chapter 2

Experimental.

In this Chapter we describe specific details of the experimental layout and principles of Time Resolved Scanning Kerr Microscopy (TR-SKM) system assembled at the University of Alberta. This system is an improvement based upon an older measurement set-up built in the Ultrafast Magnetization Laboratory by Wayne Hiebert, Mark Freeman and Roger Hunt. In the following sections I focus on general principles of operation and on specific devices designed to improve the existing system performance and versatility. More details on the TR-SKM apparatus can be found in Wayne Hiebert's Ph. D. Thesis [63].

2.1 Vectorially resolved Kerr measurements.

A polarized beam reflected from a magnetized sample may experience a small change of polarization direction known as a Kerr shift. Other magneto-optic effects may include magnetic circular dichroism (inducing ellipticity in an initially linearly polarized beam), magnetic linear birefringence, and non-linear magneto-optic effects. The Kerr effect and Faraday effect (polarization shift of a transmitted beam) are examples of magnetic circular birefringence. In fact, Kerr and Faraday effects are so closely related, that the Kerr shift is some-

times described as a Faraday rotation of the reflected beam polarization. A review of the origins and a qualitative explanation of these effects can be found in references [28],[64]. A theoretical explanation of magneto-optical effects is beyond the scope of this work.

Experimentally it is observed that the Kerr shift δ is roughly proportional to the scalar product of the incoming beam wave vector \vec{k} and the sample magnetization \vec{M} (Fig. 2-1 a). Consider two beams A and B hitting a magnetized surface from opposite directions (differing in the sign of the wave vector component parallel to the plane, k_x) as shown in the Figure 2-1 b). The sum and the difference of their polarization shifts are proportional to the out-of-plane and in-plane components of the sample magnetization respectively:

$$\begin{aligned}\delta_{A'} &= C \vec{k}_{A'} \cdot \vec{M} = C \begin{pmatrix} k_x \\ 0 \\ k_z \end{pmatrix} \cdot \begin{pmatrix} M_x \\ M_y \\ M_z \end{pmatrix} = C(k_x M_x + k_z M_z) \quad (2.1) \\ \delta_{B'} &= C \vec{k}_{B'} \cdot \vec{M} = C \begin{pmatrix} -k_x \\ 0 \\ k_z \end{pmatrix} \cdot \begin{pmatrix} M_x \\ M_y \\ M_z \end{pmatrix} = C(-k_x M_x + k_z M_z) \quad (2.2) \\ \delta_{A'} - \delta_{B'} &= 2Ck_x M_x; \quad \delta_{A'} + \delta_{B'} = 2Ck_z M_z \quad (2.3)\end{aligned}$$

where C is a proportionality coefficient.

Kerr shifts are quite small, ranging from tens of microradians to milliradian for materials such as permalloy and nickel. A crossed-polarizer analysis would yield a signal proportional to $1 - \cos^2 \delta \approx \delta^2/2 \simeq 10^{-8}$. In order to enhance the signal and bring it to the first order of smallness in δ , the beam is split in two by a Glan-Thomson prism rotated by 45° (Fig. 2-1 c), and analyzed by two detectors denoted by A and B in the figure. The difference of the detector readings is proportional to δ , rather than to δ^2 :

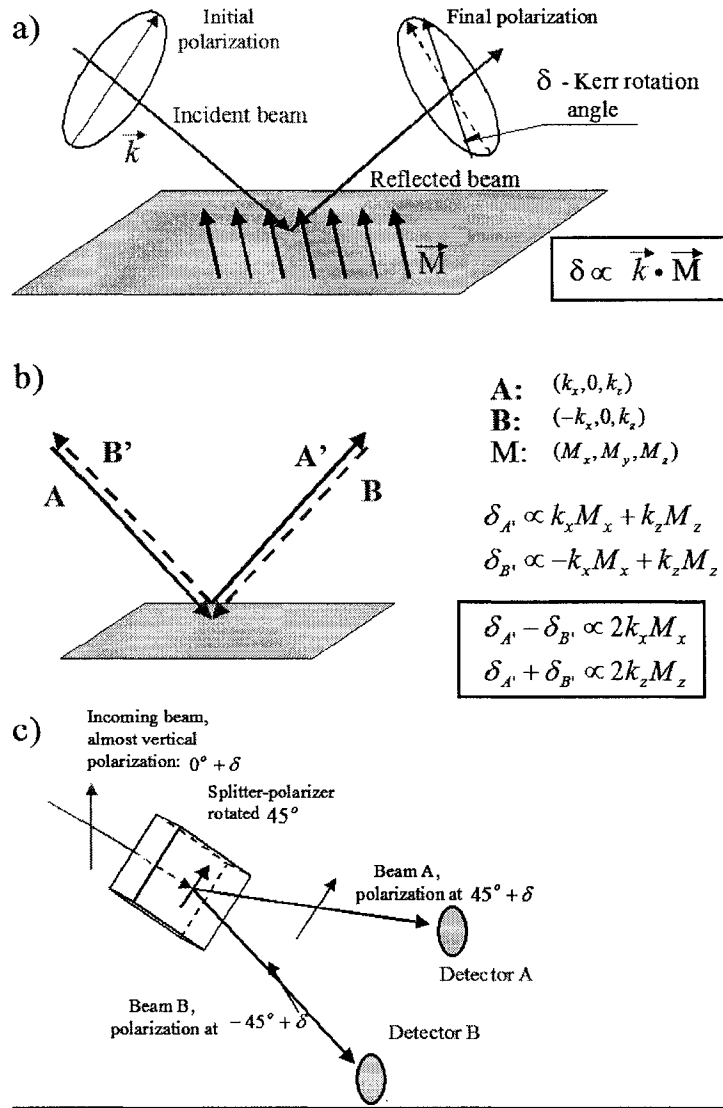


Figure 2-1: (a) General case of Kerr rotation. A polarized beam reflected from a magnetized sample experiences a small polarization shift δ . (b) Specific case of two symmetrical (mirrored) beams incident to the sample. (c) Bridge balancing set-up for detection of small polarization shifts.

$$A \propto \cos^2(45^\circ + \delta) \approx \frac{1}{2} - \delta; \quad B \propto \cos^2(-45^\circ + \delta) \approx \frac{1}{2} + \delta; \quad B - A \propto 2\delta. \quad (2.4)$$

In order to better isolate the signal from background noise a lock-in technique is used. We discuss this technique in more detail in section 2.3.

Measuring the polar component of magnetization relies on the out-of-plane component of the beam wave vector k_z so normal reflection of a plane or focused beam will do (Fig. 2-2 *a*). An elegant way of delivering light at glancing angles for in-plane magnetization measurements while maintaining high spatial resolution was suggested by Wayne Hiebert [63]. The beam of finite width is focused at the sample with an infinity-corrected high-NA objective, and then four sectors of the reflected beam are analyzed by a quadrant detector (Fig. 2-2 *c*). The linear combination of the detector readings $A + C - B - D$ is proportional to the in-plane magnetization M_x (compare to Fig. 2-1 *b* and formulae 2.3). Analogously, $A + B - C - D \propto M_y$; and $A + B + C + D \propto M_z$. Note that the angles are integrated within the solid angle of the aperture opening, so the proportionality coefficients are different for in-plane and polar Kerr signals and unique for each objective. High numerical aperture (NA) objectives are favorable as they both enhance the in-plane signal by applying a higher portion of glancing-angle beams and improve the spatial resolution. Two pairs of quadrant detectors in combination with a Glan-Thomson prism are used to double the signal (Fig. 2-1 *c*, Eq. 2.4) and reduce common-mode laser noise. The reflected beam must be properly centered at the quadrant detector (“balanced”) and each sector should have the same sensitivity in order to end up with clean in-plane signals. Otherwise the in-plane signal is mixed with the polar component. It isn’t a problem with matched silicon detectors, but balancing other types of detectors such as photomultiplier tubes (PMTs)

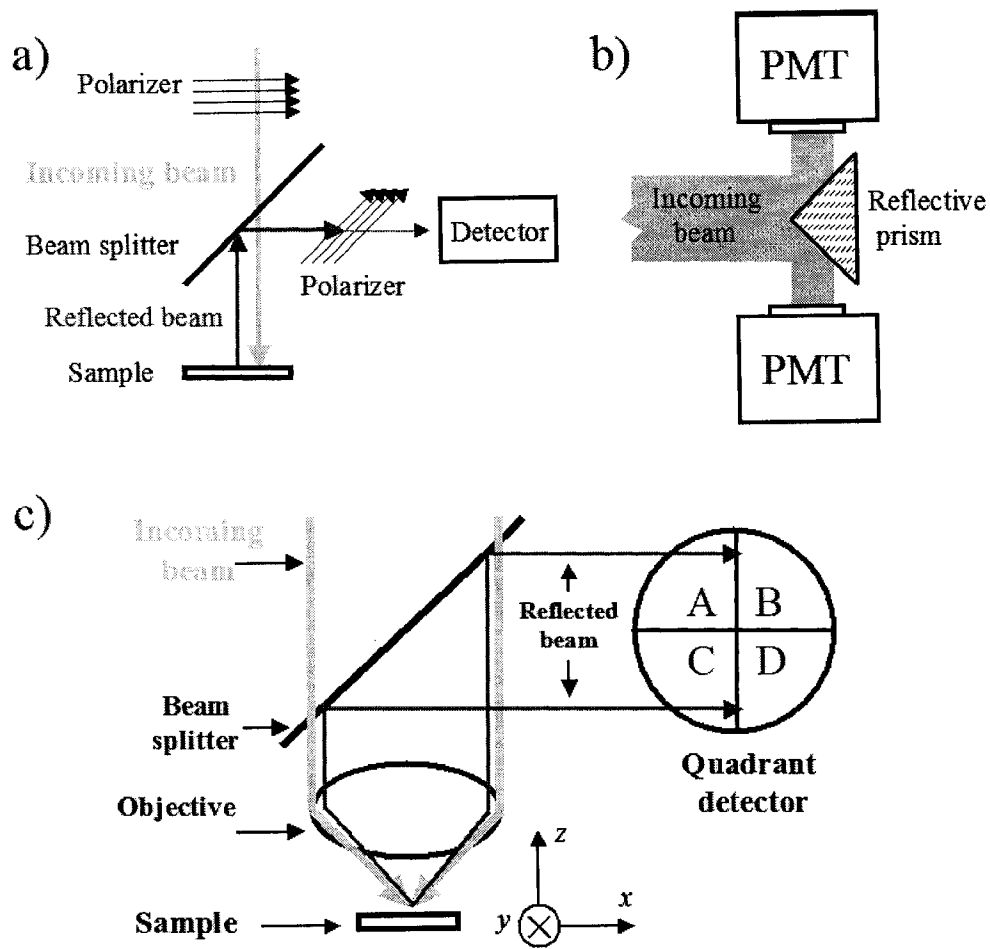


Figure 2-2: (a) Normal set-up for measuring out-of plane (polar) Kerr shift. (b) Dual detector analyzing both polar and one of the in-plane components of magnetization. (c) Quadrant detector set-up for simultaneous mapping of all three magnetization components.

might become a challenge. The last type of detector used in this project is a dual PMT detector (Fig. 2-2 b). The beam is split in two halves by a metallized reflective prism and analyzed by a pair of photomultiplier tubes, as opposed to four sectors of quadrant detector. This dual detector can measure one in-plane and the polar components of magnetization, but not read all three components at once. The advantage of this scheme is that the detectors can be arbitrarily large, and different types of detectors can be employed for different wavelengths. The detectors do not have to come packaged as a split quadrant structure. We used PMT detectors in combination with blue (400 nm) light for doubling the spatial resolution. Such a detector can be physically rotated by 90° in order to measure the other in-plane magnetization component. Moreover, a *pair* of dual detectors combined with lock-in amplifiers can measure both in-plane components of magnetization at once, at the expense of signal-to-noise ratio: the signal is two times lower in this case, and there is no common-mode subtraction. We discuss the construction of the dual detector in section 2.4.

The spatial resolution of the method is defined by a focused laser spot size and is in turn a function of the beam wavelength and the numerical aperture of the objective. A problem with detector balancing and strong artifacts in the in-plane signal might appear when the reflectivity of the sample changes significantly within the focused laser spot, e.g. when the beam is focused at the edge of the sample.

Testing our quadrant detectors we measured the magnetization profile of a relatively large $10 \times 4 \mu\text{m}$ elliptical permalloy element biased with a permanent magnet. The sample magnetization was flipped by appropriate current pulse propagating down the write wires and returns to its initial state by the end of the pulse. The beam is focused in the center of the sample where magnetization is supposed to be nearly uniform, parallel to the long axis of the ellipse and the applied field. Corresponding signals of the quadrant detectors are shown

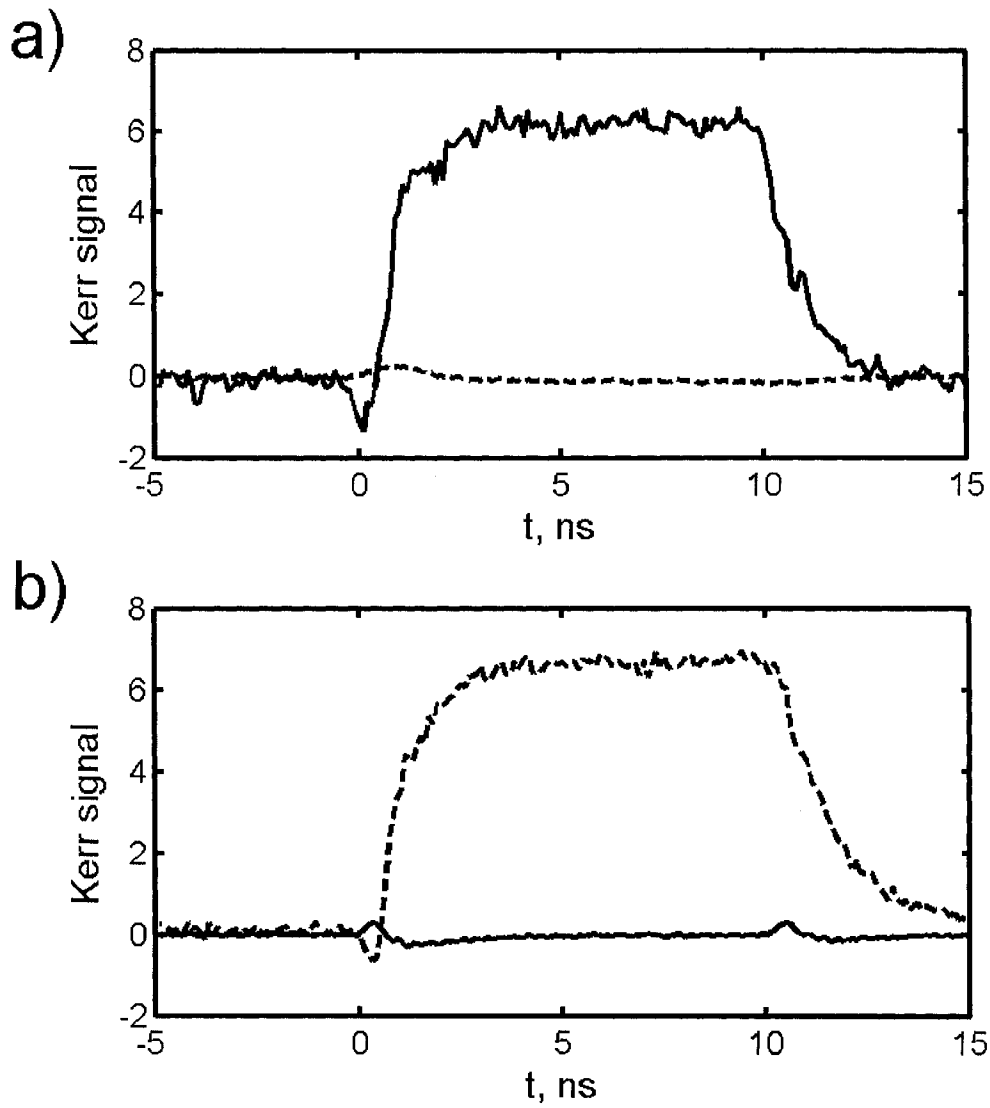


Figure 2-3: (a) Quadrant detectors' in-plane magnetization measurements (arbitrary units) of a horizontal sample. Solid line corresponds to M_x channel, dashed – to M_y . (b) Analogous measurement on the same sample rotated 90°. The channel readings are interchanged.

in the Figure 2-3 *a*. Solid line corresponds to the output $A + C - B - D$, dashed one – to $A + B - C - D$. As expected, the channel corresponding to the first magnetization yields a nearly rectangular signal, while the other one results in almost no signal. Then the entire assembly (including biasing magnet and write wires) was rotated by 90° (so that the sample is oriented along y -axis now) and the measurement repeated (Fig. 2-3 *b*). Clearly, the channel outputs are interchanged, now the x -channel produces very low signal and the y -channel response is similar to the x -signal in the original sample orientation. One can conclude that two in-plane components of magnetization can be measured independently in quadrant set-up.

2.2 System layout.

In section 2.1 we described the principles of vectorially-resolved Kerr measurements, with an arbitrary light source, for instance, a continuous-wave (CW) laser. Using a pulsed laser brings an additional degree of freedom: time. If the magnetization has been flipped by a magnetic field pulse created by a short current pulse propagating down the wire adjacent to the sample (called the “write wire” or WW below), probing magnetization with an ultra-short laser pulse of known delay with respect to the field pulse results in a magnetization measurement at a given moment of time at a certain spatial position. Flipping the magnetization back and forth periodically and varying the delay between the laser and current pulses one can track the magnetization change history in a stroboscopic technique. Mounting the objective (or the sample) on a flexure translation stage, allows probing of the magnetization change across the sample thus forming a scanning optical microscope [27],[65],[66].

A conceptual layout of the measurement set up is shown in Figure 2-4 *a*. The pulsed laser beam is split in two parts in order to both probe the magnetization of the sample and to trigger the current pulse generators. Relative

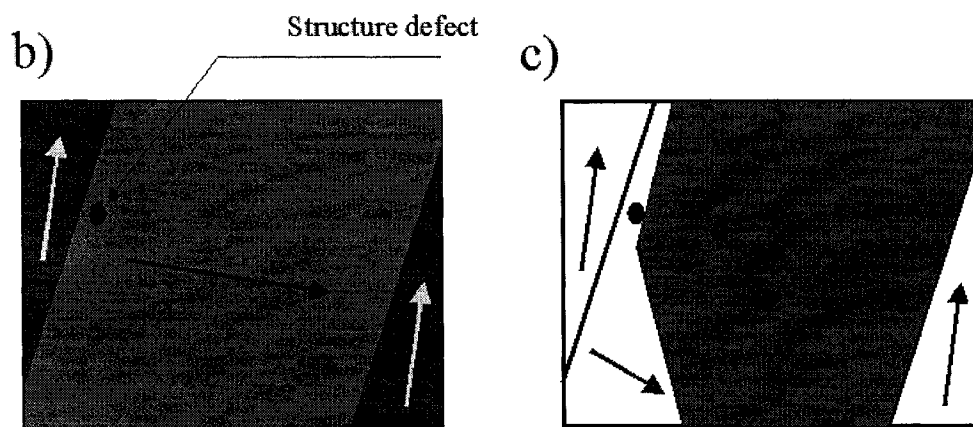
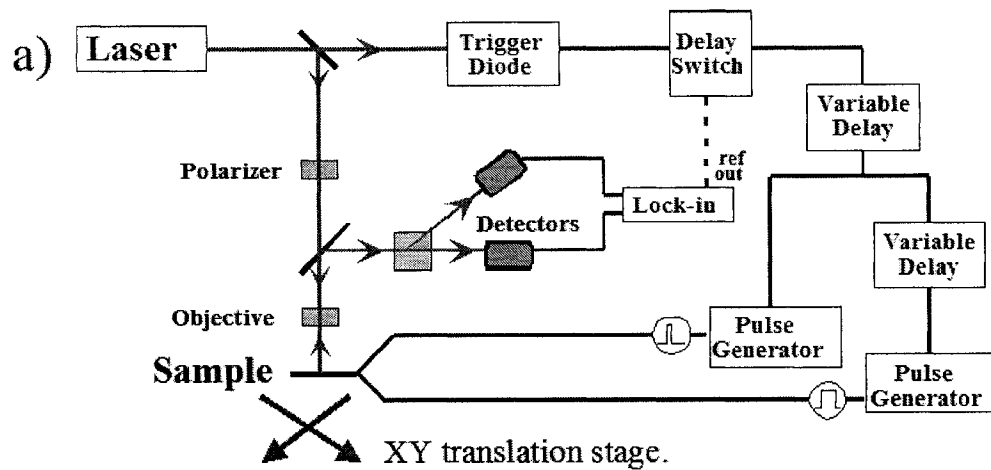


Figure 2-4: (a) A schematic layout of the stroboscopic measurements set up. (b) An example of an idealized domain structure of a rectangular sample. The central (gray) domain can be flipped back and force under influence of an appropriate magnetic field pulse. (c) Magnetization change in the case (b) as it would be seen by our system.

delays between the pulses are controlled by two delay generators. The lock-in amplifier reference drives a modulation of the delay, yielding an AC signal (see Section 2.3), and the lock-in measures the detector readings. Note that the magnetization itself is not measured in the system, but the change of magnetization with respect to the initial level (averaged over many cycles, typically 1000 to 100,000) and averaged spatially across the focused laser spot. This is a certain limitation of the stroboscopic technique, as it relies on (i) perfect repeatability of the magnetization history cycle to cycle and (ii) it assumes that the initial state is known. To illustrate this limitation, consider an idealized example of a square sample with a defect, nearly uniformly magnetized at its center and having closure domains at the edges (Fig. 2-4 *b*). Once one attempts to switch the sample magnetization, the central domain does flip back and forth through motion of the right hand side domain wall (Fig. 2-4 *c*), while the other domain wall is pinned by a defect. Both closure domains retain their initial state and thus would be invisible to the stroboscopic measurement. In this example an odd hexagonal shape rather than true domain structure would be seen in the stroboscopic method. The interpretation of the data presents some challenge, and we use two methods to assist with correct interpretation of the data: (i) biasing the sample with a strong DC field from a permanent magnet; and (ii) running micromagnetic simulations on Mike Scheinfein's Micromagnetic LLG Simulator [51]. In turn, our measurements are testing the ability of the simulations to correctly predict the evolution of magnetization.

In order to return the magnetization to its initial state a strong negative current pulse can be applied to the same write wire (a reset pulse), rather than biasing the sample by a DC magnetic field. However, this method does not take care of the closure domains. On the other hand, these measurements are the most important for the industry, as neither logic nor memory elements are going to be biased by external field in computers (naturally, if the DC field is strong enough to return the magnetization to its initial state, it is also

good enough to erase the memory). Therefore, a large part of this work is devoted to investigation of remanent magnetization states using reset pulses rather than DC bias.

To put the numbers in perspective, the spatial resolution of this method is limited by the size of the diffraction spot, that is by the wavelength of the beam used and the numerical aperture of the objective. Most of the measurements are done using 0.75 NA Nikon objective either with near infrared light (740-800 nm) or with frequency-doubled UV light (400 nm). The spatial resolution according to the Rayleigh criterion is approximately 800 nm or 400 nm respectively. Temporal resolution is often limited by our delay generator's jitter of approximately 200 ps. One way to circumvent this limitation is using a jitter-free optical delay line, where the delay between the pulses is determined by the optical path of the pump laser pulse, controlled by the position of a retroreflector sliding along a rail. In this case, only the pulser jitter itself (2 ps, according to the manufacturer's specification) is a factor. The optical pulse width of 100-150 femtoseconds is negligible. The current pulse rise times are approximately 50 ps, 250 ps and 300 ps for different pulse generators. We can measure the response faster than 50 ps with an optical delay line set up, but in most cases it is overkill as the magnetization response is generally slower than the field pulse rise time (but can also be faster, since the response is non-linear and magnetization change can saturate before the current reaches the peak amplitude).

The arrangement of the optical table is shown in Figure 2-5. Pulsed 800-nm beam of the Coherent Mira laser has a repetition rate of 76 MHz, too high for the triggering of the pulsers (designed for a maximum repetition rate of 1 MHz). An acousto-optic pulse picker reduces the pulse rate approximately 100 times, to about 760 kHz. Then the beam can be sent directly to the microscope if the flipper mirror $M2$ is up, or to the frequency-doubler, if $M2$ is down. In the former case, the beam hits 30/70% beam splitter $BS1$ that

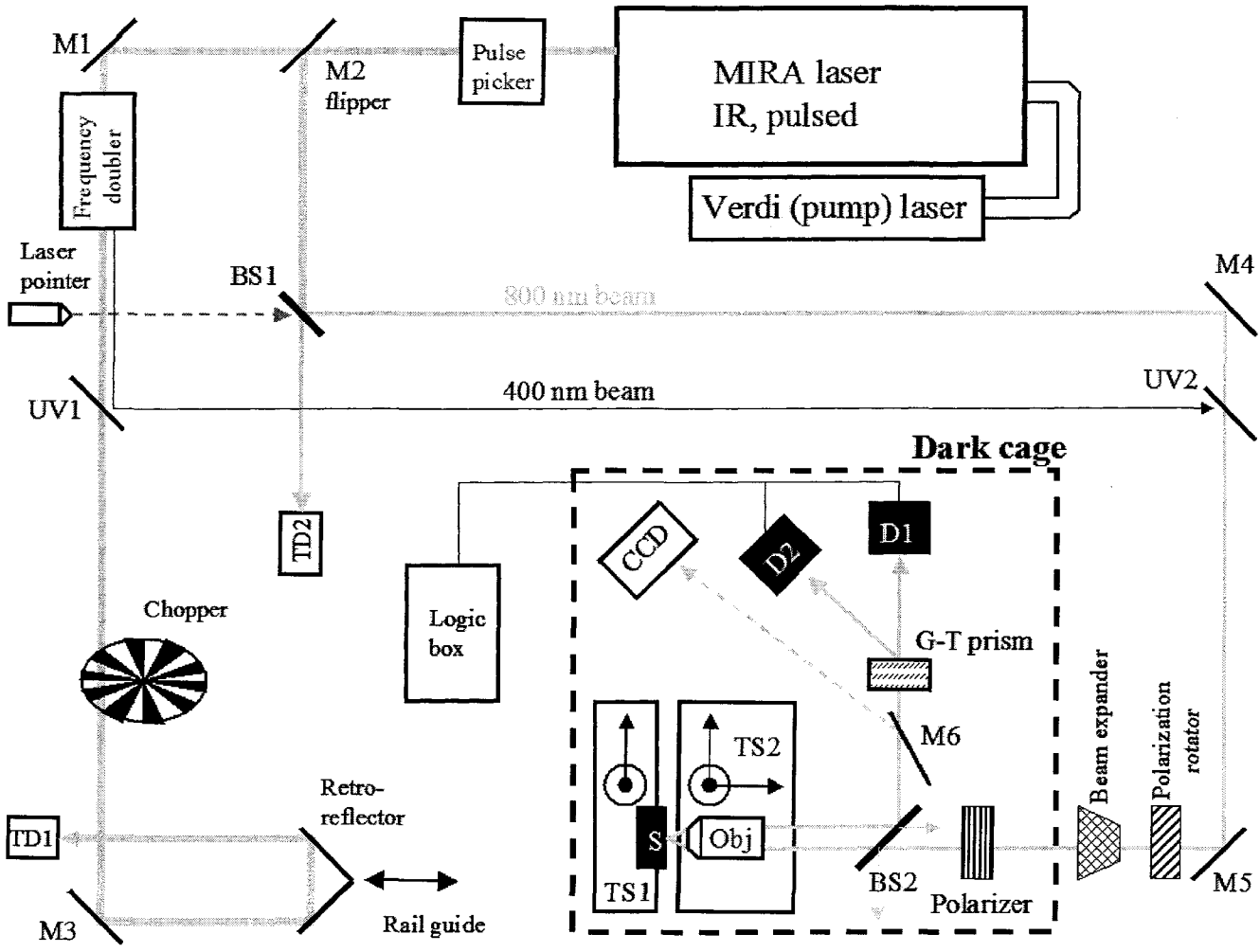


Figure 2-5: System layout. Details in the text.

directs $\approx 30\%$ of the light to the triggering diode $TD2$ and then it is directed to the microscope by the mirrors $M4$ and $M5$. A bright red laser pointer is used as an alignment laser for coarse positioning of the almost invisible IR light at the detector faces, as the visible alignment beam follows the same optical path as the main beam after $M4$.

If the flipper $M2$ is down, the beam passes through the frequency-doubler. The output of the doubler contains both IR (800 nm) and UV (400 nm) components, where the latter is much weaker than the former (only 2-3% of the energy is converted to the blue light). In order to purify the blue light it is sent through two dichroic mirrors (UV1 and UV2), reflective for UV light but transparent to the IR, and joins the same path as the IR beam in the first case after the mirror $M5$. The infra-red component passed through the mirror $UV1$ is used for triggering of the pulsers either directly when the trigger diode $TD1$ is placed in the beam path, or through the optical delay line consisting of the mirror $M3$, and a retroreflector sliding along the delay rail. The position of the retroreflector is remotely controlled by a computer. The triggering is modulated by a spinning chopper wheel, which also triggers the lock-in amplifier. The same system with slight modifications allows use of the optical delay line with IR (800 nm) light.

The paths of blue and IR light merge at the mirror $M5$ and then pass through the combination of polarization rotator and fixed polarizer that allows variation of the intensity of the light (a few samples were destroyed by a too strong focused beam), and a beam expander that increases the diameter of the beam reaching the objective in order to overfill its aperture. The beam is focused at the sample S through the objective Obj and the reflected beam is directed by 30/70% beam splitter $BS2$ to the detectors $D1$ and $D2$ through a Glan-Thomson prism. Detector readings are processed by the "logic box" that produces required output combination (such as $A + C - B - D$ for different sectors) before being amplified and analyzed by a Lock-in amplifier).

Removable mirror $M6$ directs the beam to the CCD camera in order to image and easily find the sample.

Both the sample holder and the objective are mounted on the flexure stages TS and $TS2$ respectively. The stage $TS1$ manually controllable by micrometer screws serves for positioning the focused laser spot properly at the desired point of the sample, while the other stage $TS2$ has both manual and remote fine position control and serves to raster scan the sample yielding the spatial distribution of both sample reflectivity and all components of magnetization. As for the detectors $D1$ and $D2$ they are also mounted on micrometer-screws controllable translation stages (although less complex than the flexure stages) in order to place the beam exactly at the middle of the quadrant and balance the detectors.

A photograph of the actual sample holder and the objective assembly are shown in the Figure 2-6. An enlarged picture of the removable sample holder block is also shown in the Fig. 2-13. The arc guides the permanent magnet cart around the sample, so that a DC bias field can be applied at any angle in the plane of the sample (total angle span is more than 180 degrees and the magnet itself can be flipped). The DC bias magnetic field strength is determined by sample-to-magnet distance and can range from 30 to 400 Oe. It is also important to note, that the sample holder is made from non-magnetic materials such as brass and aluminum, otherwise the DC bias magnet could produce unwanted forces causing the sample drift from the desired position as the magnetic field is changed in strength or direction.

In conclusion, the TR-SKM is a very versatile method, capable of examining the influence of different factors on magnetization evolution. Parameters one can vary include:

- Spatial coordinates (2).
- Delay between optical and current pulses.

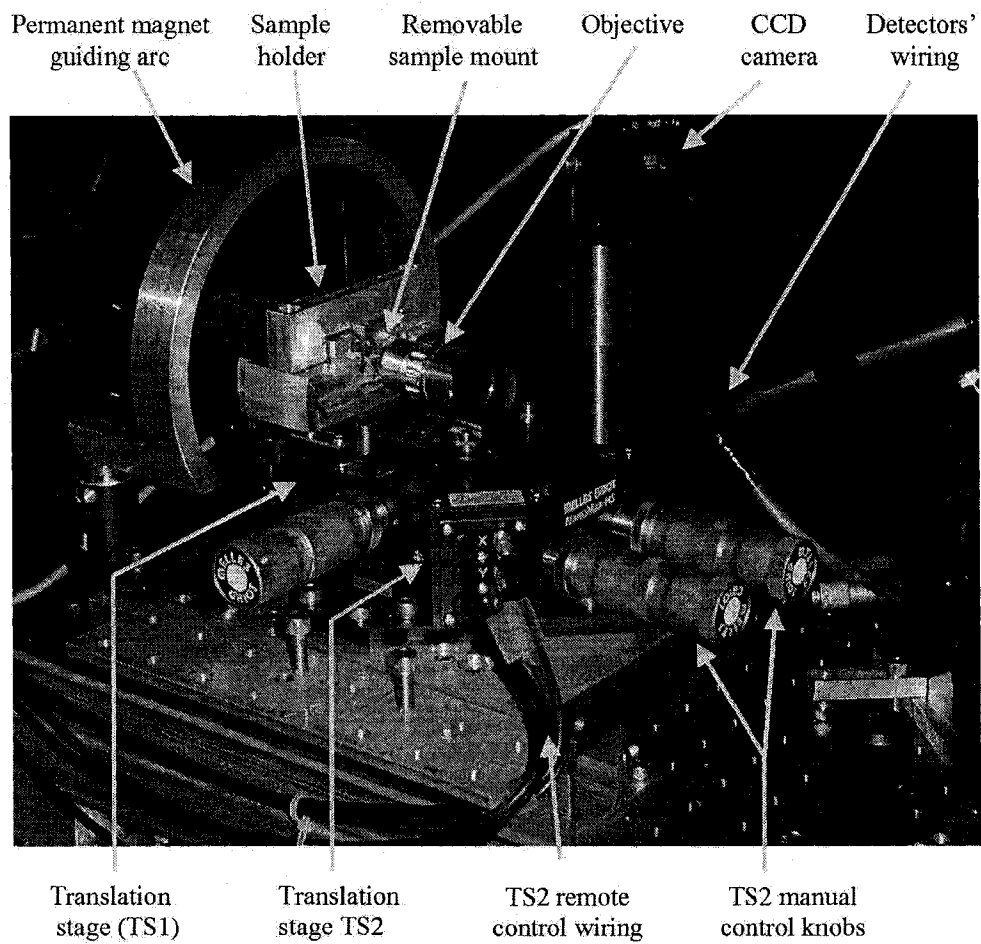


Figure 2-6: A photograph of the actual sample holder and the objective assembly. Details in the text.

- Pulses' amplitude (2).
- Pulses' duration (1-2).
- Delay between the pulses.

Parameters that can be measured are:

- Magnetization components (3)
- Reflectivity (brightness) of the sample.

Overall, 11+ dimensional parameter space. In order to collect useful data quickly, the cuts of this parameter space are to be done. Typical cuts used throughout this work are:

1. Temporal scans. The beam is focused at the same point, and magnetization history (two or three components) is recorded as a function of the delay between optical and current pulses.
2. Spatial scans. The delay is fixed, and the probing spot scans across the sample measuring its magnetization and brightness.
3. Movies: collections of spatial scans at progressively higher delays.
4. Spatiotemporal (XT) scans: one of the objective displacement coordinates is frozen, two or three components of magnetization are measured along the other axis at fixed delay. Then this measurement is repeated at progressively higher delay values.
5. Time-amplitude (TA) scans: both spatial coordinates are frozen, a collection of temporal scans at progressively increasing pulse amplitudes is recorded.

Other types of measurements certainly can be constructed. The disadvantage of the method is that it is a "stroboscopic" technique yielding averaged signal over many cycles.

2.3 Time resolved measurements, triggering sequence.

In this section we describe special modulation techniques used in our measurements. The typical repetition rate of the pulsed beam is 760 kHz, but the roll-off frequency of the detector pre-amplifiers is much lower at ~ 3 kHz. Typical modulation frequencies used range from 1.3 to 1.7 kHz to avoid electronic roll-off. The details of two types of lock-in detection are best explained in the context of a simple example.

Consider a soft permalloy structure deposited atop a write wire (WW), biased by a DC magnetic field. In the absence of current through the wire, the magnetization aligns with the bias field, call it the “low” magnetization state. The current pulse sent through the WW inductively coupled to the sample, creates its own magnetic field that overrides the bias field and switches the sample magnetization to the opposite direction (the “high” state). For few-micrometer sized thin film samples this switching process typically takes 2-3 ns, and then the sample magnetization stays in the “high” state as long as the pulse is on. At the end of the pulse the magnetization returns to the “low” state, again typically in a few nanoseconds. An example of such a process was shown in the Figure 2-3. Now consider a fixed delay such that the optical pulse is timed exactly with the middle of the positive plateau, and is supposed to measure the “high” state of the magnetization.

The first modulation technique uses a mechanical chopper (Fig. 2-7 *a*). The trigger beam is periodically blocked by a spinning chopper wheel, and the chopper circuitry controls the lock-in amplifier by sending it the frequency it should lock to. When the chopper wheel lets the trigger beam through, the trigger diode triggers the pulser which flips the magnetization and the detector “sees” the high magnetization state. On the other hand, when the

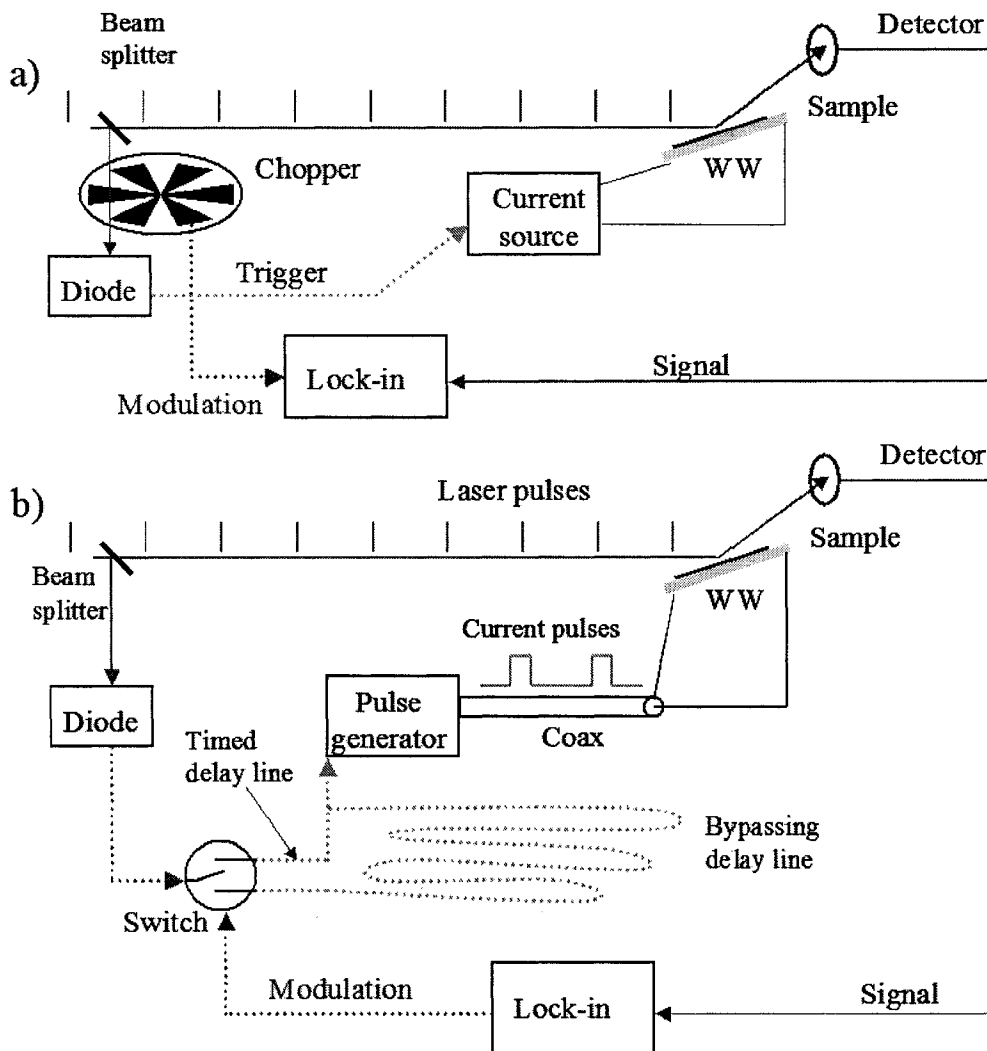


Figure 2-7: (a) Chopper modulation. The chopper wheel periodically blocks the beam triggering the pulse generator. The chopper circuitry sends the modulation frequency to the lock-in amplifier. (b) The lock-in sets the modulation frequency, flipping the switch between two positions and modulating the delay between optical and current pulses.

trigger beam is blocked the pulser does not fire, and the sample magnetization stays in the “low” state (Fig. 2-8 *a, b, e*). The advantage of this technique is simplicity, and that it is also easily used in conjunction with optical delay. The main disadvantage of this method is an additional jitter induced by a repetition rate dependence of the propagation delay through the avalanche transistor pulsers.

The other technique is based on redirecting the electronic trigger pulse through an additional delay coil adding some 400 ns of extra delay to the current pulse timing. Now the lock-in amplifier internal reference is the master, and the switch directing the trigger pulses is a slave. When the current pulses are properly timed with optical ones, “high” state is measured, and when they are deliberately delayed, the laser pulses hit the sample in the “low” magnetization state (Fig. 2-8 *c, d, e*). Since the current pulses are not turned off, the average heat generation in the transistor junction is constant, and no additional jitter is introduced in this configuration. All measurements reported below are done in this triggering configuration with the exception of the ones where the optical delay line was used.

2.4 Dual detector.

This section describes specific technical details of the dual PMT detector I designed to measure the in-plane component of magnetization using blue light. I would like to thank Gilber Lachat and Paul Zimmermann for crafting this tool in metal and Greg Popowich for sharing his experience in electronics design. The corresponding logic box circuitry design is based on his pre-amplifiers for the quadrant detectors.

The advantage of PMT detectors is their relative sensitivity to blue light, and high gain eliminating the need for pre-amplifiers. The disadvantage is higher variability compared to the silicon detectors. For instance, tube to

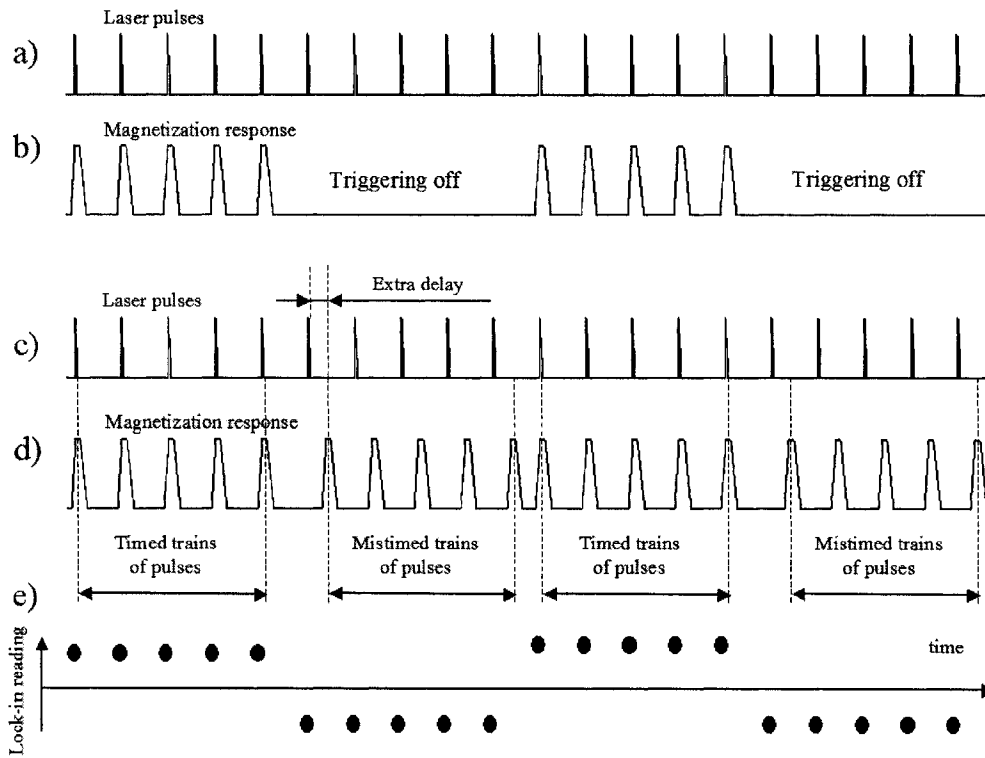


Figure 2-8: (a,b) Chopper modulation. (a) Schematic sequence of the optical pulses. (b) A sequence of the current pulses modulated by a chopper. (c,d) Delay modulation. (c) The same sequence of optical pulses as in case (a). (d) Sequence of the current pulses modulated by delay triggering (e) Corresponding Kerr signal for both modulation techniques. Whether the current pulses are turned off or mistimed, the probing laser pulses hit the sample alternately in the “high” and “low” magnetization states.

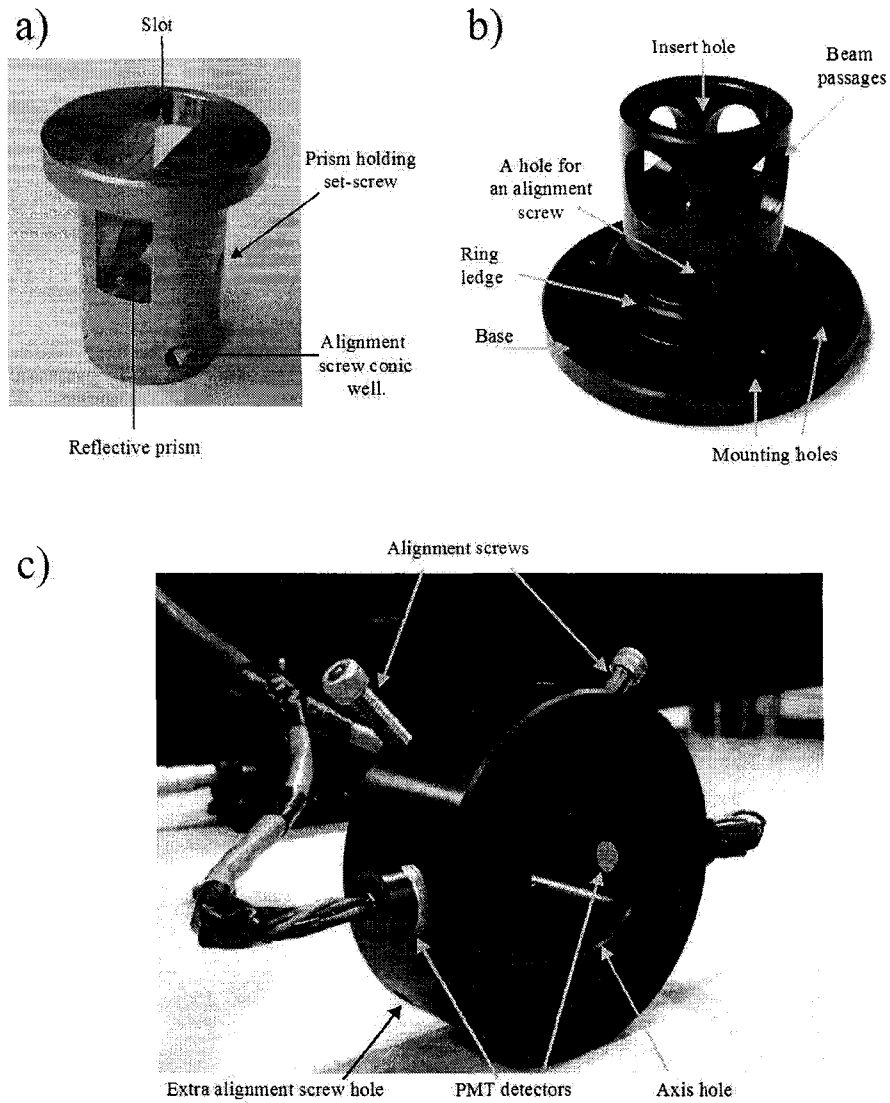


Figure 2-9: (a) The Insert part with a reflective metalized prism mounted at the bottom of the slot. (b) The Axis, holding both the inner Insert part and outer Ring part. (c) The Ring with PMT detectors and alignment screws.

tube variations in sensitivity are as high as 10%, and the detector balance might change when different a bias voltage is applied. In this experiment four Hamamatsu R7400U series photomultiplier tubes were used to build two dual detectors, and the detector holder is designed to handle this particular class of PMTs. However, other detectors can be used in the same assembly with only minor modifications.

The holder consists of three main concentric parts (Fig. 2-9): an Insert, containing a metalized glass prism that splits the beam in two (compare to Fig. 2-2 *b*); a hollow Axis holding the Insert and the outer Ring part with two PMT detectors. The entire assembly is shown in Figure 2-10. Both the Ring and the Insert can be indexed in 90° steps with respect to the Axis by means of the conic-point alignment screws and corresponding wells. After measuring one of the in-plane magnetization components the Ring and the Insert of both detectors can be rotated 90° to measure the other in-plane component. Or, if the signal-to-noise ratio allows both in-plane components can be probed simultaneously (each with one pair). Rotating the Axis by 180° interchanges the beams reaching each detector of the pair, used for gain equalizing of the detector pair. Each Axis is attached to a micrometer-screw controlled XY translation stage, so that the prism can be shifted allowing equal portions of the light to reach both detectors of the pair (or deliberately delivering all the light to one of them).

The “logic box” for this detectors must be able to compensate the PMT’s differing sensitivities by means of a variable gain, and also produce the outputs proportional to the magnetization components of interest. A block scheme of the logic box is shown in Figure 2-11 *a*. The variable amplifiers have linear gain in the interval $\{0,2\}$ controlled by a wire-wound resistor pot. We denote the pairs of PMTs belonging to different dual detectors as *A* and *B*; *C* and *D* respectively. Once the detectors are balanced and all switches connected, the output “Out1” is proportional to the polar component of magnetization

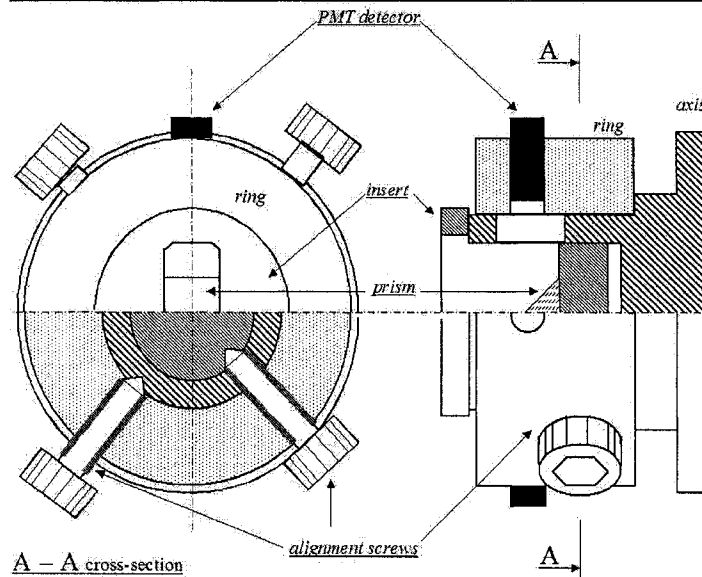


Figure 2-10: (Top) A photograph of an assembled detector. Inset: enlarged central area. Reflections of halves of the PMT faces in the prism can be seen. Likewise, a beam emitted from the direction the observer sees the prism would be split in two and reach the corresponding PMTs. The entire assembly is mounted on a translation stage, whose micrometer screws can be seen in the background. (Bottom) Plan view, side view and cross-sections of the detector assembly.

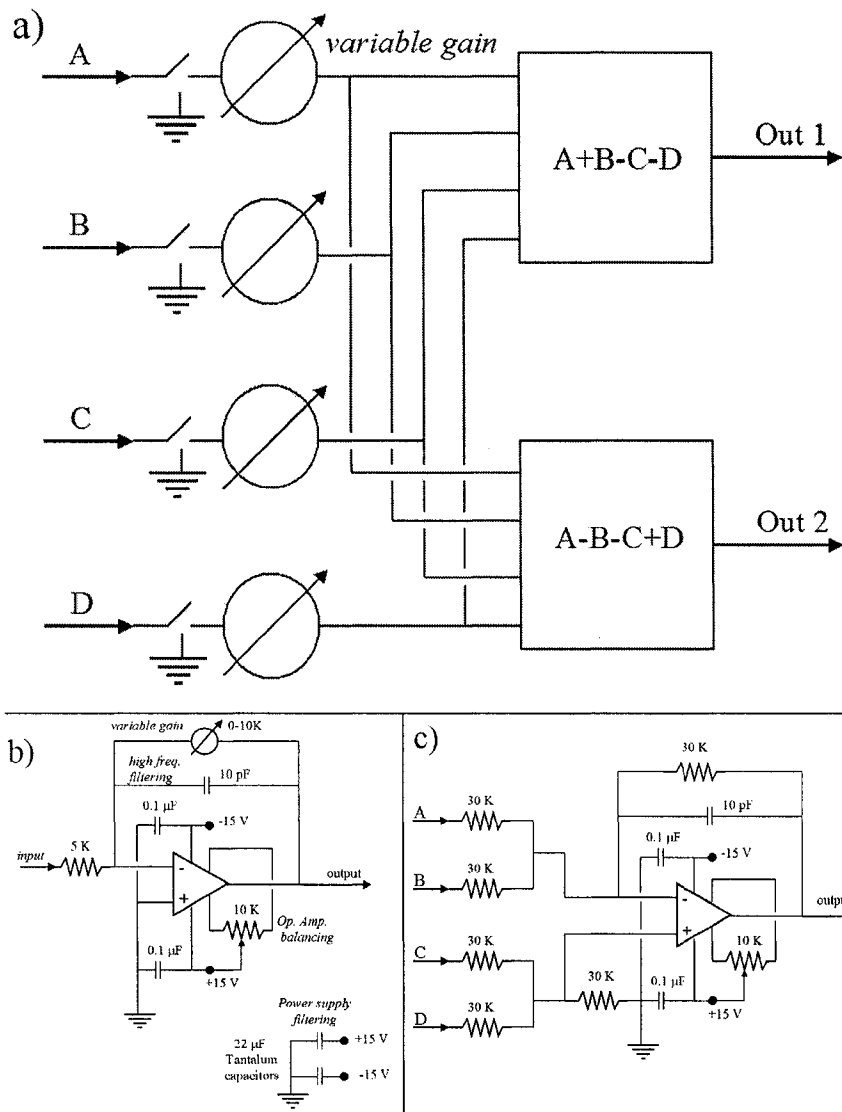


Figure 2-11: (a) Schematic representation of the logic box design. The gain of each channel can be adjusted for proper balance with variable gain amplifiers, then two summers produce the outputs proportional to the polar and in-plane components of magnetization. (b) The circuitry of each amplifier. (c) The circuitry of the first summer (the second summer is the same up to the input channel permutation).

and the output “Out2” –to the in-plane component. The amplifiers and summing circuits are shown in the Figure 2-11 *b, c*. Both are designs, are slightly modified from those of Greg Popowich.

Here is an easy procedure for balancing the detectors:

1. Ground all the switches. Bring the gain of the amplifier of the channel *A* to the middle of the range (unity gain).
2. Connect switch *A*. Shift the translation stage to maximize Out1 (achieved when all the light of a corresponding beam falls on the detector *A*). Ground detector *A*.
3. Connect switch *C*. Direct all the light of the corresponding beam to it by shifting the other translation stage in order to minimize the reading of Out1.
4. Connect switch *A*. Bring Out1 to zero by changing the gain of the detector *C*. Ground switches *A, C*.
5. Repeat steps 3,4 with detector *D* Instead of *C*.
6. Analogously, balance the gain of the detectors *B* and *C* by zeroing Out1 when both beams are directed to the corresponding detectors. Now the sensitivities of all channels are equal.
7. Ground *C, D*; connect *A, B*. Bring the prism of the first detector to the middle by shifting it so that Out2 is zero.
8. Ground *A, B*; connect *C, D*. Bring the prism of the second detector to the middle by shifting it so that Out2 is zero.
9. Connect all channels and start your measurement.

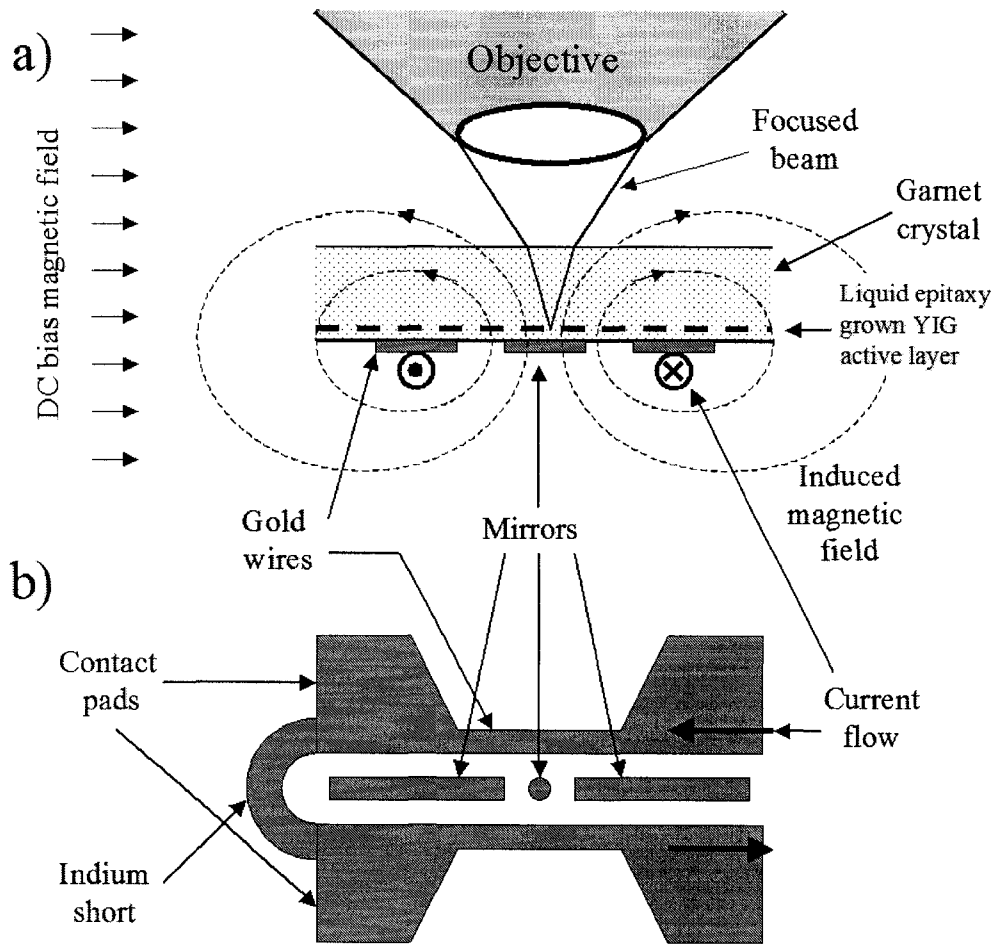


Figure 2-12: (a) Idealized cross-section of the garnet sensor. The beam is focused at the mirror adjacent to the active YIG layer between the WW creating an out-of plane magnetic field. The YIG layer magnetization is initially set by an in-plane bias field of a permanent magnet. (b) Schematic plan view of the sensor (rotated 90°).

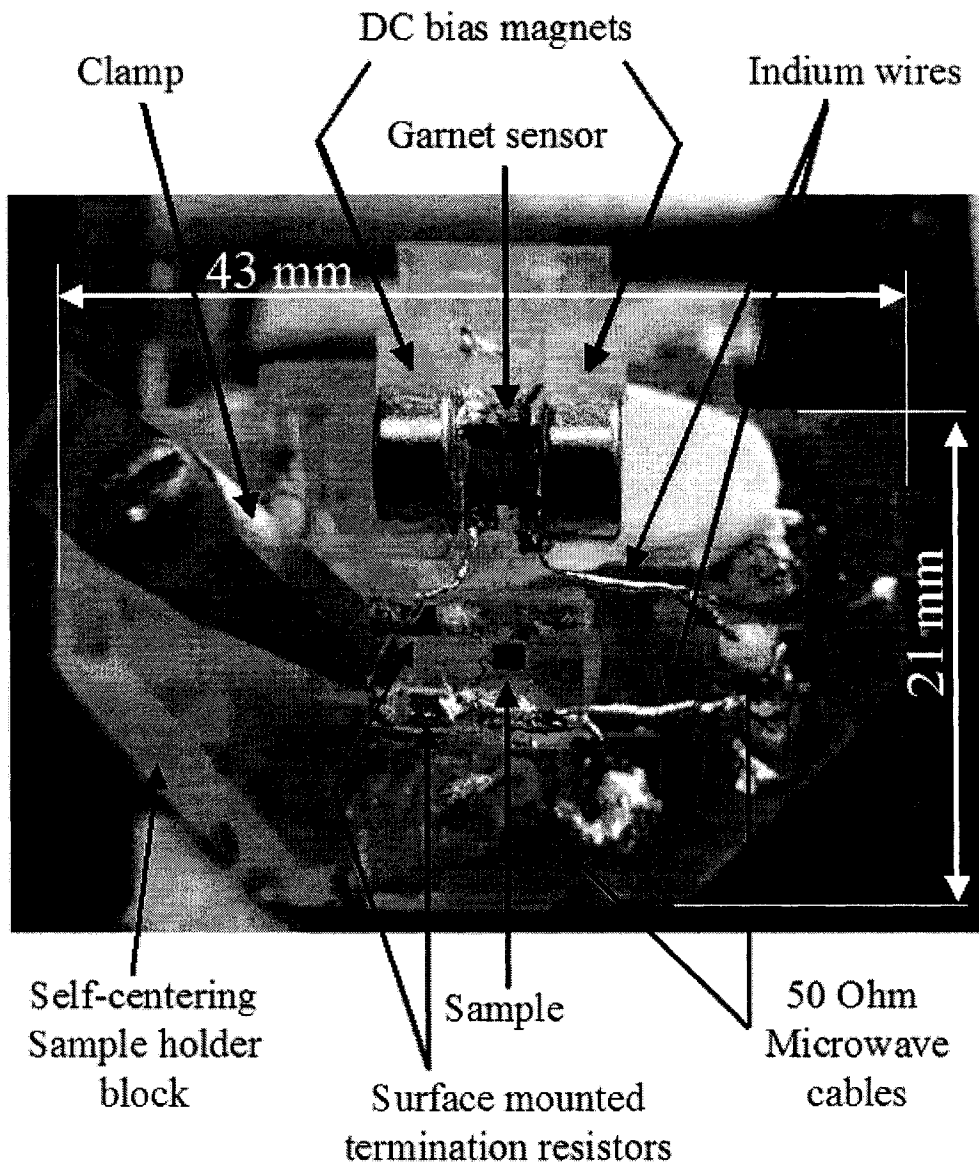


Figure 2-13: Typical garnet sensor assembly. In this case the garnet sensor is mounted in series with a recording head slider and terminated to 50 Ohms by surface-mounted resistors.

2.5 Garnet current sensor.

This method of direct measurement of the current profile based on strong Faraday effect [68], [69] observed in yttrium iron garnet (YIG) gives a unique opportunity to reference the sample magnetization change to the absolute temporal current onset. The idea of the sensor is shown in Figure 2-12. Initially the active layer magnetization is parallel to the direction of the in-plane DC magnetic field created by permanent magnets. When a current pulse is applied to the write wires adjacent to the active layer it creates a relatively weak out-of-plane field affecting the magnetization of YIG. The latter can be measured using the TR-SKM method. The thin mirror deposited on the back side of the garnet crystal increases the amount of light collected by the objective thus increasing the magneto optic signal. The bandwidth of such sensors is limited by the frequency of the FMR oscillations.

Some examples of the current profile measurements with garnet sensors are shown in Figures. 3-8 and 5-4 *b*. The ripples in the trace shown in Figure 5-4 *b* have a period of approximately 160 ps, or frequency of ≈ 6 GHz, fast enough for most pulse characterization measurements, occurring on characteristic temporal scale of nanoseconds. Substituting this value of the FMR and frequency to the Kittel formula (and the saturation magnetization of the garnet of $4\pi M_s = 160$ Oe [63]) obtain the estimated value of the bias DC field of ≈ 2200 Oe. The write wire width used in this design is $10 \mu m$, inter-wire spacing is $30 \mu m$. For typical current values of 50 mA used in the recording head testing the out-of-plane component of the pulsed field at the center of the spacing between the wires is just 9 Oe, indeed much smaller than the bias field, yielding perfectly linear response in this current range as confirmed by numerous measurements.

In the Chapter 5 we discuss an alternative magneto optic sensor that uses ion-implanted ferromagnetic nanoclusters in a silicon dioxide matrix as the

active layer. This promising material exhibits even faster linear magnetic response (10-90% rise time is estimated as at most 50 ps) *without* any bias field.

The garnet crystal is not transparent to blue light, so these measurements are limited to the IR set-up, and we could not measure the current onset of the blue light directly (it has different optical path in the system layout, see Fig. 2-5). A typical layout for current onset measurements is shown in Figure 2-13. A recording head slider is connected in series with the garnet sensor by indium wires and terminated to 50 Ohm with surface-mounted resistors. The length of the indium wire connecting the sensor and the slider is less than 5 mm, so the absolute delay between magneto-optic response of the sensor and true current pulse through the slider coils does not exceed 25 ps (roughly estimating the wave propagation speed as $2/3 c$).

2.6 Lithography and tricks.

This section is devoted to technical details of the lithographic multilayer patterning. All microstructures tested in this work were produced by lithographic techniques – either by photo lithography or using the e-beam system. The general line of processing is rather straightforward following common micro-fabrication recipes and established techniques of either subtractive (etching, ion milling) or additive (lift-off) patterning. Things become much more complicated when multi-layer processing is involved especially if the next layer of lithography intersects several structures deposited in previous steps and thus belonging to different layers. Step coverage becomes an issue and one can no longer treat the substrate as a nice plane surface. This is the problem we had to face trying to deposit crossed wires for the prototype MRAM element.

Additive and subtractive techniques result in different step profile, (Fig. 2-14 *a – h*). In the subtractive methods the edge profile results in a sharp

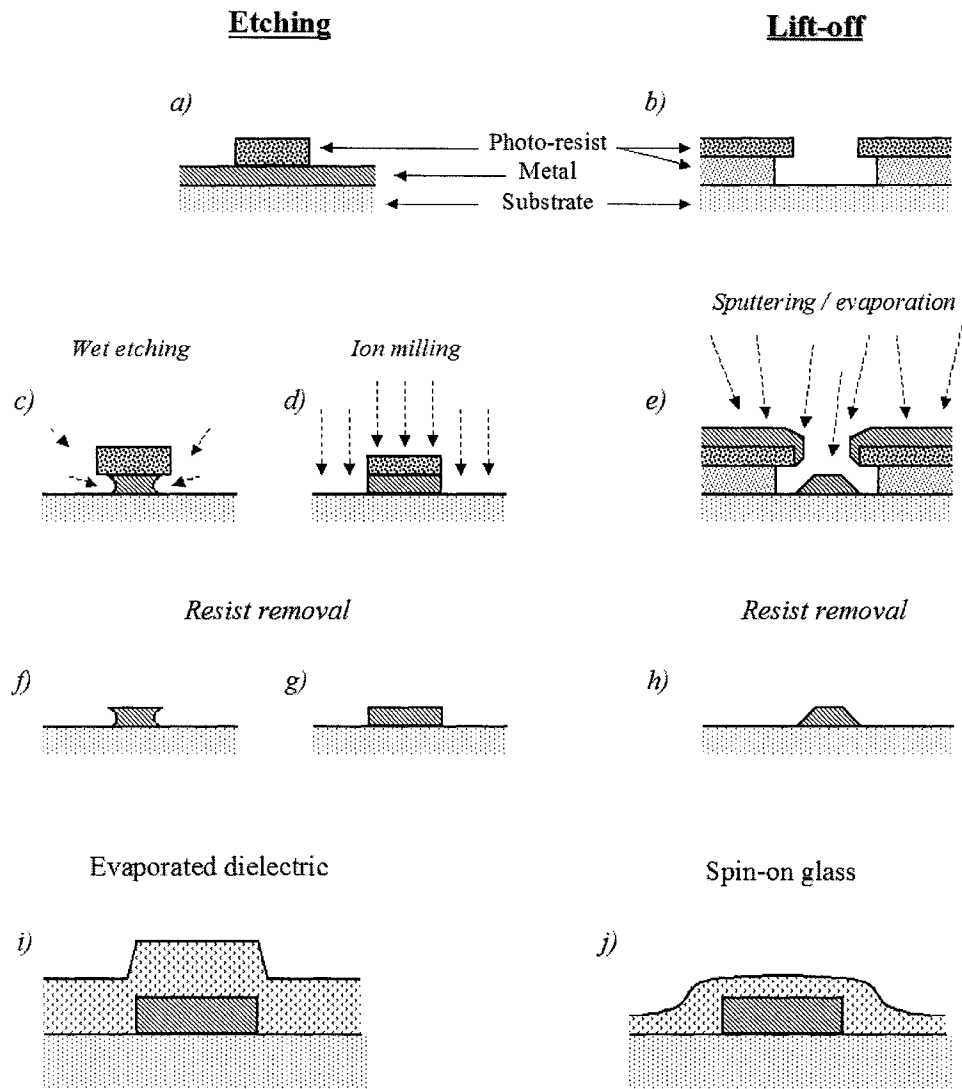


Figure 2-14: (a-h) A comparison of the etching and lift off techniques. Etching and ion milling result in a sharp step at the edge of the deposited structure (f,g) while a lifted-off structure may be thinner at the edges than in the middle (h). An example of sharp step coverage (i) by directional deposition and smooth step coating by spin-on glass (j).

step not suitable for a smooth deposition of the next layer (Fig. 2-14 *f, g*). Idealized lift-off is a little better in this respect, as the material is accumulated at the resist edge the effective width of the patterned trench reduces, resulting in a structure that is thinner at the edges than at the middle (Fig. 2-14 *h*), although in some cases it can do exactly the opposite by leaving burrs. Still, directional deposition of the second layer of a different material (such as silicon dioxide dielectric atop the write wire) results in a reduced thickness weak link at the edges (Fig. 2-14 *i*). Combined with the thermal stress caused by different thermal expansion coefficients of the dielectric and a metal this structure is bound to fail. In our attempts of silicon dioxide deposition the dielectric stuck to the surface everywhere but on the wire. Other samples built in the Naval Research Laboratory (NRL) by Scott Zelakiewics with silicon nitride insulator held for about two months and then the dielectric peeled at the wire intersection in all samples but one (our measurements reported below were conducted on that lucky sample). Even diffusive high-pressure sputtering coating failed to isolate crossed wires, likely because of pinholes.

The solution that worked for us was using spin-on-glass (SOG) dielectric rather than a vapor deposited thin film. These silicon-organic compounds are dissolved in organic solvent and are applied to the surface in liquid form (we used the Filmtronics planarizing dielectric #300F). Centrifugal spinning of the substrate results in thin film coating by SOG, and the viscous flow of the material results in increased planarization of the surface (Fig. 2-14 *j*). Applying several coats of SOG one obtains after appropriate baking a glass-like continuous coating of the surface. The residual organic content may be susceptible to organic solvents such as acetone (several samples were spoiled in acetone before this was figured out) so we chose to protect the SOG with evaporated silicon dioxide. This coating also improves the surface smoothness. Planarization of the top surface improves the subsequent coating of the surface by PMMA resist resulting in the high-quality e-beam lithography (performed

by Miroslav Belov).

In order to reach buried electrodes one could etch both SOG and silicon dioxide with hydrofluoric acid-based etchants, but here a brute-force method was used: scratching the contact pad with a hot soldering iron tip under a pool of molten indium. This shortcut approach worked extremely well, resulting in perfect electric contacts.

Chapter 3

Characterization of commercial and prototype recording heads.

3.1 Recording head imaging.

The idea of TR-SKM imaging of the recording heads was first suggested in reference [27], and later developed in other projects ([58],[70],[71]). In all cases, the sample is interrogated by the probe beam focused on the slider ABS interface, probing the local surface magnetization directly at different delay times as described in the Introduction. The head is driven by a bipolar current waveform, in practice sometimes created by unipolar short positive pulses superimposed on a negative DC bias current. The polarity pole tip magnetization changes in response to the pulse application (Fig. 3-1), and returns to an in-plane magnetized state when the pulse is gone. In the absence of a bias field, the net magnetization out-of-plane of the poles stays at zero level, with no flux channeled from the multiple domains in the bulk of the soft yoke material. This is of course a desirable regime, as the head should write nothing, unless it is driven.

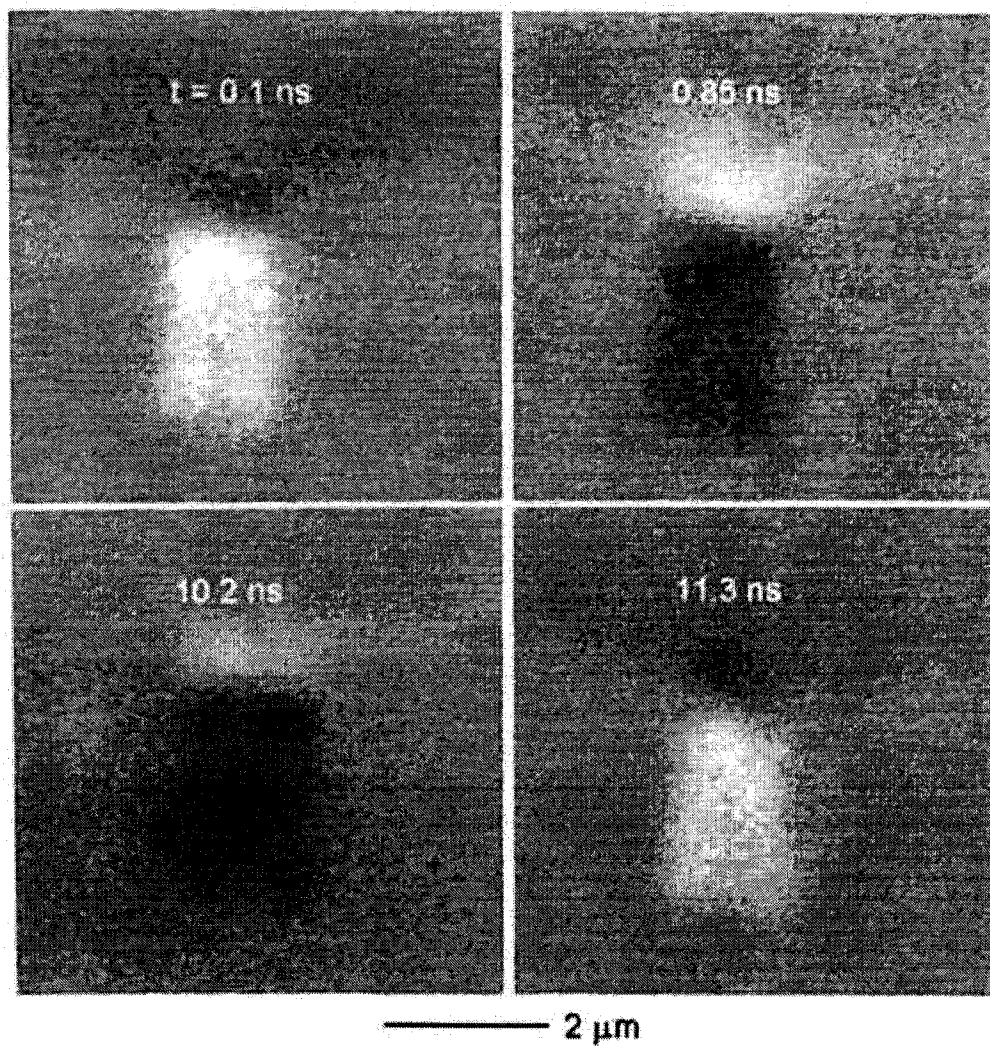


Figure 3-1: Time-resolved polar Kerr images, rendered on a linear grayscale. Times are relative to the onset of a bipolar switching pulse of 10 ns duration. Each scan area is $6 \times 6 \mu\text{m}$.

3.2 The effect of pole-tip geometry on the flux rise time of write heads.

3.2.1 Motivation.

With the increases of linear density and disk spinning speed, very high data rates are now an essential feature of magnetic recording technology. One limiting factor governing the achievable data rate is the finite flux rise time of the write transducer. The overall field rise time of a thin film write head is determined by (i) the finite rise time of the coil current as caused by the pre-amplifier performance, the interconnect dispersion, and the overall head inductance. (ii) The propagation of the flux in the write head as delayed by eddy current damping and gyromagnetic relaxation. The total write field rise time can roughly be expressed as:

$$\tau = \sqrt{\tau_h^2 + \alpha\tau_c^2} \quad (3.1)$$

where τ_h is the head's intrinsic flux rise time for an infinitely fast rising coil current, τ_c is the current rise time, and the (write current dependent) coefficient α lies in the interval $\{0,1\}$.

Reducing the current rise time requires the use of a pre-amplifier with fast current response. In addition, the overall head impedance needs to be reduced, especially at high frequency. Even for an ideal abrupt write current transition ($\tau_c = 0$), however, the overall flux rise time would still be finite owing to the head flux rise time (τ_h). Numerous measures have already been implemented to decrease the intrinsic flux rise time of write heads. These include reducing the yoke length by tightening the turn pitch [72],[73]; employing multilevel coils [74]; and using high resistivity or laminated pole materials to control eddy current effects [66]. Below, we present a systematic exploration of the

effect of pole tip geometry on a writer's flux rise time.

3.2.2 Experimental set-up.

The Device Family.

Recording heads with different front-end geometries (nose length, pedestal length and shape, see Fig.3-3) were fabricated together on the same wafer. Apart from the front-end pole tips, all other design features such as yoke length and width, coil turn/pitch, and pole materials were kept the same. Scanning electron microscope (SEM) images of the air-bearing surface (ABS) and the cross-section of one of these heads are shown in Fig. 3-2 *a, b*. The writer has 10-turn single layer coil. The 'throat height' (the depth of write gap, or the length of the minimal separation range between the poles) is defined by the pedestal length because the flat region of the P_2 pole is longer than the pedestal (Fig. 3-2 *b*). Fig. 3-2 *c* shows a polar Kerr image of the ABS at a fixed time delay of 3 ns, corresponding to the nearly steady state of the magnetized head. One can see that the pole tips are clearly outlined in the magneto-optical signal (compare to Fig. 3-2 *a*).

Fig. 3-3 shows a schematic three-dimensional drawing of the front-end pole tip configuration. In this study, the P_2 thickness, gap width, flare and angle are the same for all designs.

Different nose and pedestal lengths are obtained by ion mill pole trimming. As shown in Fig. 3-3, after the pole trimming process, designs with different nose length and pedestal length also end up with different pedestal shape. The track width (determined by the pole/nose width) is the same for all designs. Schematic shapes of the pedestal discussed in this paper are shown as the inset of Fig. 3-4, while their values are listed in the Table 3-1. The head inductances as a function of bias current, measured at the head gimbal assembly (HGA) level with a 1 MHz excitation (measurements are performed in the Read-Rite

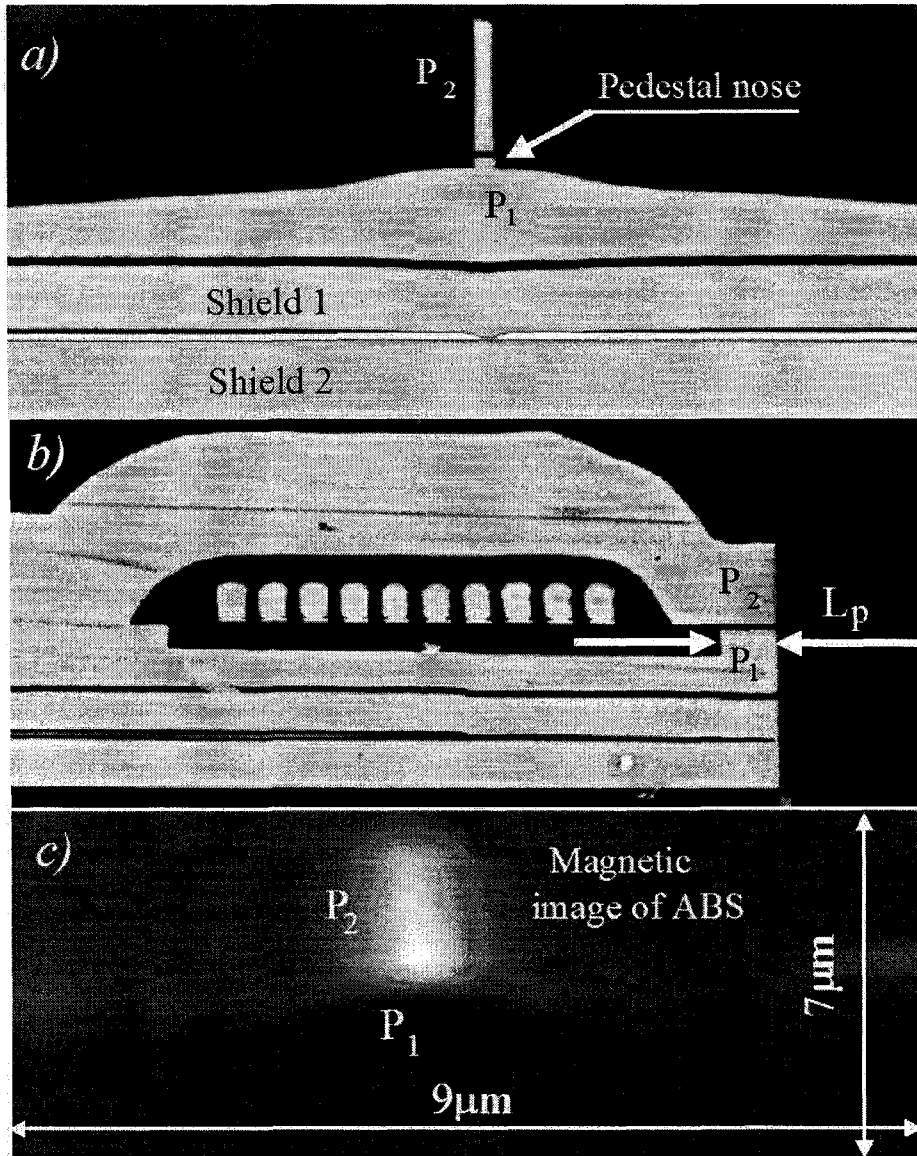


Figure 3-2: (a) SEM image of the slider air bearing surface (ABS). (b) SEM image of the same head cross section. The length L_p of the pedestal determines the throat height. (c) A typical Kerr imaging from ABS spatial scan. Both P_1 and P_2 poles demonstrate the highest magnetization (and hence the highest flux density) at the edges right across the write gap. Note that the horizontal scale of frame (c) has been stretched relative to the vertical (as indicated), for presentation purposes

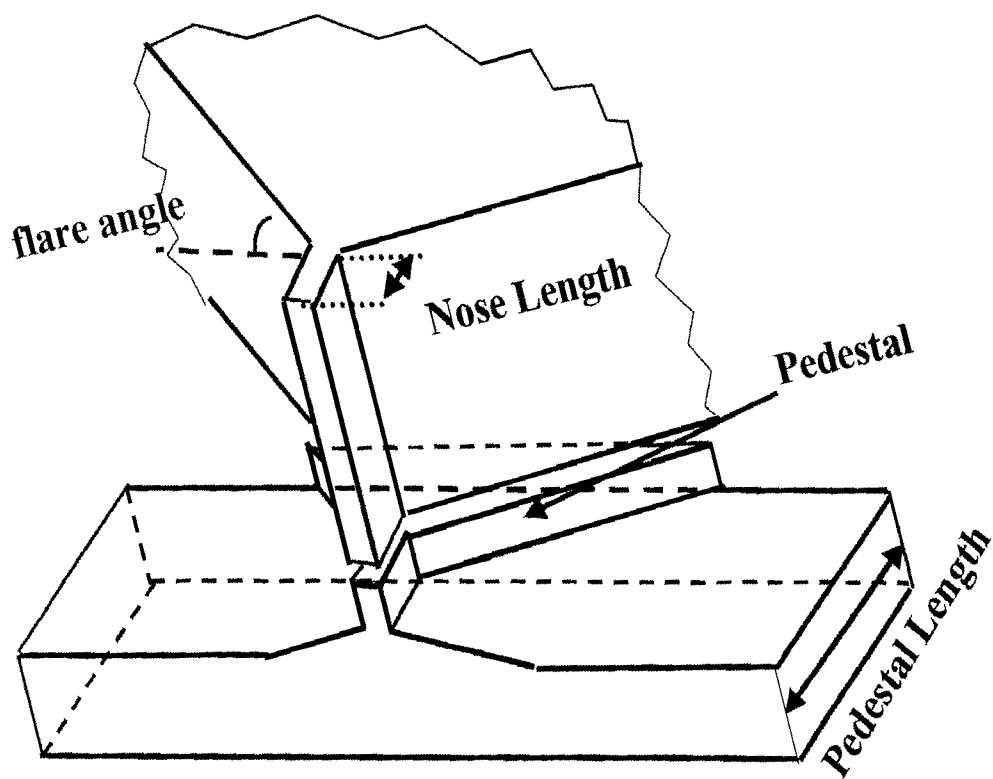


Figure 3-3: Schematic plot of the front end pole tip geometry.

Design	Nose/pedestal length, μm	Pedestal Area, μm^2	Inductance at zero current, nH	Flux rise time, ns
A	0.6 / 2.0	3.40	65.68	0.65
B	0.6 / 3.5	13.06	72.82	1.05
C	1.2 / 2.0	1.51	62.98	0.95
D	1.2 / 3.5	8.6	67.51	1.30

Table 3.1: Comparison of the geometrical parameters, inductance, and the resulting flux rise time for different designs.

Corp. by Heng Gong), are plotted in Fig. 3-4. Each curve is the average of the values measured from 5 HGAs of each design. Since all the heads were built on the same suspension with the same interconnects, and have exactly the same structures except the nose and pedestal, the inductance variation comes from the nose and pedestal differences. Since more than half of the overall inductance at HGA level (section 1.2) in this case is actually attributable to the interconnects on the head suspension, one concludes that the relative inductance variations at slider level are even more significant. The inductance variation among different designs is highest at low current, apparently owing to the pedestal area differences. At high current the overall inductance becomes very similar for all designs, once the front ends of the pole tips are nearly saturated. The measured inductance values at zero current and the corresponding pedestal areas are listed in Table 3-1. The inductance increase was observed with pedestal area or volume. The inductance results serve as a complementary characterization of the differences between device geometries, but cannot be extrapolated into rise time information in the orders-of-magnitude higher frequency regime of interest for high data rate switching.

Time Resolved Kerr Microscopy set up.

The polar magnetization rise time was measured by time-resolved scanning Kerr microscopy (TR-SKM). Simulations show that the flux and polar magnetization rise times are very similar [66], thus allowing the estimation of the flux

saturation rate by measuring the tip magnetization switching speed. The pole tip magnetization change is directly measured in the time domain, by stroboscopic magneto-optic inspection of the slider's air bearing surface (ABS) [27]. The temporal profile of the local magnetization is traced by varying the delay between the laser probing pulse and the write current pulse. In this experiment we used a mode-locked Ti-sapphire laser, with probe beam frequency-doubled to the blue (400 nm wavelength) in order to improve the spatial resolution. The Ti-sapphire beam is acousto-optically pulse-picked to reduce the repetition rate to 690 kHz before frequency doubling. The focal spot size is approximately 400 nm. With the microscope objective mounted on a piezo-driven positioning stage, local magnetization changes may be accurately mapped. The spatial resolution of the TR-SKM used for this study is determined by the laser spot size of approximately 400 nm. The overall system rise time is 200 ps, dominated by jitter in the electronic delay module.

Two independent rectangular pulses of opposite polarity are superimposed to create a bipolar excitation. A similar current profile is shown in the Fig. 3-9 *a*. The resulting excitation waveform has a short voltage rise time of 60 ps (10-90% negative to positive at the second pulse edge, as measured with a 10 GHz bandwidth oscilloscope). The flux rise time is measured at this transition.

In order to reduce the overall inductance and better evaluate the write head's intrinsic flux rise time, the sliders were detached from the head gimbal assemblies (HGAs) and the write interconnects were cut to approximately 5 mm. The sliders were then mounted on a special fixture at the end 50-ohm coaxial cable and terminated to 50 ohm using surface mount resistors. The impedance match was characterized by measuring the amplitude of the reflected pulse using a 2 GHz bandwidth single turn inductive probe. The reflected pulse amplitude was less than 5% of the incident level.

Flux Rise Time Measurements.

We characterize the flux rise time using the 10-90% criterion. The convolution of the slider response with the jitter smearing function introduces a small systematic error to the measurements. The actual response time can be estimated as

$$\tau = \sqrt{\tau_{measured}^2 - \tau_{jitter}^2} \quad (3.2)$$

which even for the fastest rise times observed (650 ps) results in only a 25 ps correction. The reproducibility of the measurements is characterized by a 2% standard deviation within a set of multiple examinations of the same device. The variance is influenced by the positioning uncertainty associated with returning to the same spatial position on the ABS for a repeat measurement.

3.2.3 Results.

Spatial Dependence of the Flux Rise time.

In magnetic recording, the trailing pole P_2 , as the region of highest flux concentration, plays a significant role in the writing process. In order to study the spatial dependence of the flux rise time, the laser beam of average power of 25 μW was focused at various locations across the ABS of head "A", and temporal scans acquired. The flux rise time varies significantly across the pole tip. Fig. 3-5 shows the temporal magnetization switching curves at different locations of the pole P_2 , starting from the edge of the write gap and moving further away from the gap.

The local magnetization switching speed decreases when moving away from the trailing edge. The rise time of this device changes from 0.65 ns to 1.65 ns with translation across the pole. It is important to note that the overall temporal response is not fully described by these rise times alone, there are

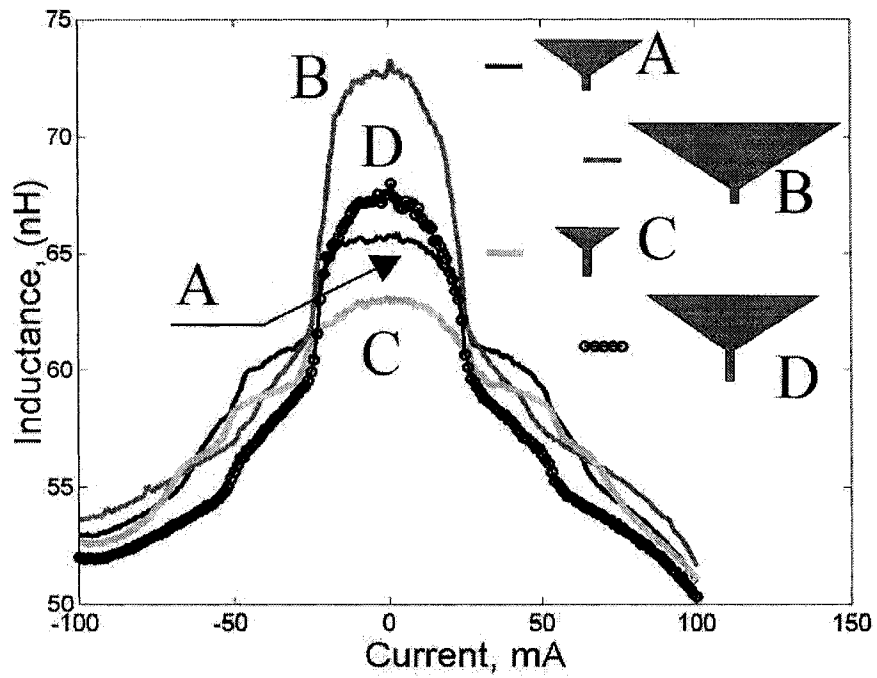


Figure 3-4: Measured HGA inductance versus bias current curves for the four different designs. Inset: Schematic shapes of four tested pedestals as trimmed by ion milling. The flare angle of approximately 35 degrees is the same for all designs. The lengths of the pole noses and pedestals are listed in Table 3.1.

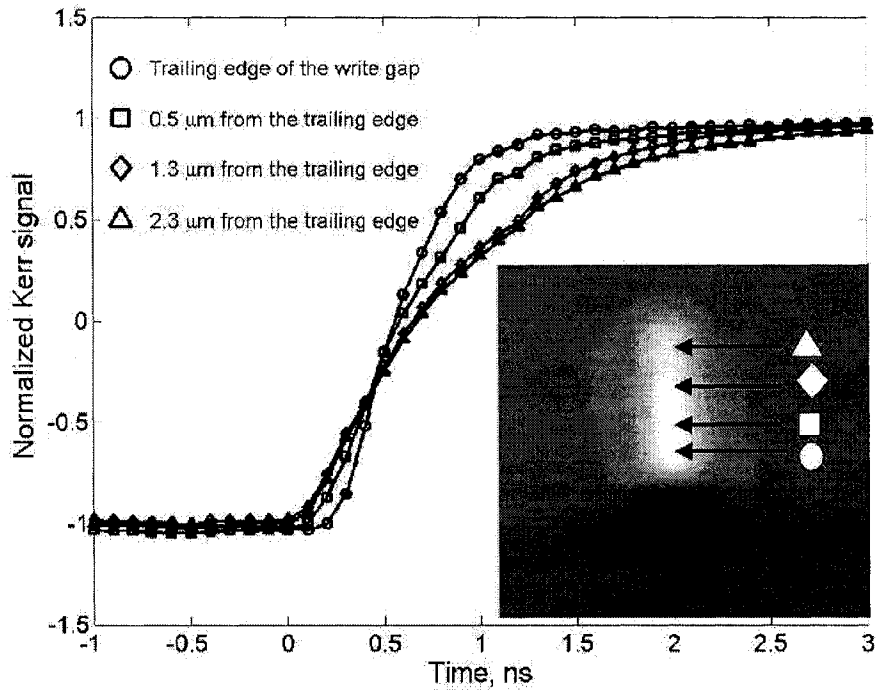


Figure 3-5: Magnetization switching curves measured at different P_2 locations from trailing edge toward the top of the P_2 . Circle corresponds to the trailing edge (corresponding rise time is 0.65 ns), square is separated from the trailing edge by 0.5 μm (1.0 ns), diamond – by 1.7 μm (1.45 ns), triangle – by 2.3 μm (1.65 ns). Note that this Kerr image is inverted with respect to the one shown in the Fig. 3-1: the pole P_2 is on the top.

also very apparent position-dependent delays of the onset of response. Most interestingly, the fast transition at the leading edge of P_2 (the closest to the gap) starts only when the rest of the pole has undergone a significant part of the transition, but then it saturates faster. This edge may be driven strongly by partially switched pole, and is quickly saturated. Most heads we tested exhibit this P_2 leading edge lag, varying between 50 ps and 200 ps which may itself eventually limit the maximum data rate.

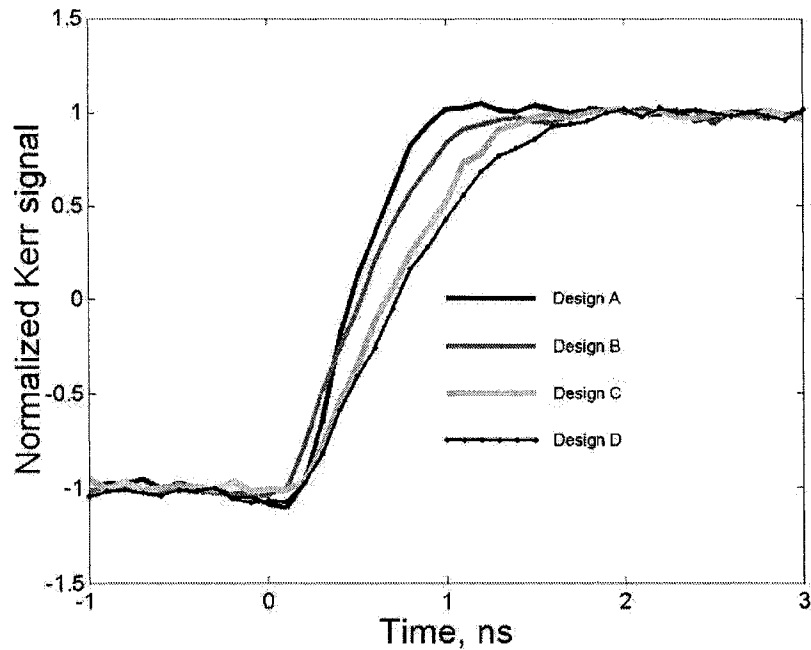


Figure 3-6: Temporal magnetization switching curves (between the two saturation states) scanned by TR-SKM at P_2 leading edge at 40 mA write current.

Effect of Front-end Pole-tip Geometry.

To compare different designs, the flux rise time measured at the leading edge of P_2 pole (next to the gap, (Fig. 3-5, inset) is examined. The recording heads with different nose length and pedestal length were fabricated on the same wafer by using different masks. Besides the nose length and pedestal length, after the pole tip trimming process, the pedestal shape, area and volume also differ from design to design.

The effect of both nose length and pedestal volume on rise time is shown in Fig. 3-6, which illustrates the temporal profiles at the trailing edge of the pole P_2 measured at 40 mA drive current. Rise times vary significantly from design to design, from approximately 650 ps for the design with the shortest nose and smallest pedestal, to 1.3 ns for the longest nose and pedestal. No-

tably, although at fixed pedestal length the designs with shorter nose have larger overall inductance (since the nose is a part of the pedestal shortening the nose results in greater pedestal area, compare the designs A and C, B and D), the measured flux rise times are faster for the shorter nose (the results are summarized in the last column of Table 3-1). Comparing designs B and C, one finds similar rise times indicative of a crossover point where nose length and pedestal volume effects largely offset each other. The latter may be attributed to both higher inductance of the heads with larger pedestal and to the reduction of the magnetic reluctance at the front end for larger pedestal area under the write gap, which results in having more flux in that region. At high frequency, this effect incurs more eddy current damping, retarding the flux propagation. This result is consistent with a theoretical prediction based on eddy current analysis [75].

The results indicate that the narrow nose region is part of the critical path limiting the flux rise time at the trailing edge of the gap (the leading edge of the P_2 pole). Attention has also been focused on this region by Taratorin et al. [15], who have demonstrated a 1.6 GHz data rate using an ultra-short nose prototype head.

Summarizing, it was found that the designs with shorter nose length and pedestal length switch faster and that shortening the nose is more effective in reducing rise time than shortening the pedestal. We also observed the dependence of the flux rise time on the position along the pole and the switching lag of the leading edge of P_2 with respect to the rest of the pole. The latter factors may in turn influence the data rate, at the next level beyond the raw flux rise time itself.

Considering the lag of P_2 response with respect to P_1 , we compared the performance of a recording head on HGA mount with an analogous head slider (Fig. 3-7). An effective lag time in both cases was approximately 200 ps. This effect appears to be an intrinsic property of the head slider, as there is no

qualitative difference between the traces recorded at HGA level and at slider level (Fig. 3-7 *a* and *b*). During the lag period the magnetic field emerging from the pole P_1 has a strong out-of-plane component. The duration of this out-of-plane “kick” can be roughly estimated as a width of the peak obtained by subtraction of P_1 and P_2 traces, 400-450 ps in both cases.

3.3 Current onset.

In the previous section we found that the response of the P_2 pole of a longitudinal recording head lags behind the response of P_1 . This feature appears to be generic to the recording head as it was observed in numerous characterization experiments both on HGA level and on separate sliders. The next question is: “How much does it (and the response of P_1) lag behind the current onset?” In order to characterize the current onset we mounted the head slider in series with a magneto-optic garnet current sensor (Fig. 2-13) connected to the sample via short (≈ 1.3 cm) indium wires. As the sensor and the head are connected in series, the same current propagates through both objects. Of course, there are some reflections introduced by the impedance-mismatched connecting wire, but the reflection amplitude is significant only for fractional wavelength ($\lambda/8$) comparable with the wire length, which in our case corresponds to the characteristic time of $\simeq 500$ ps, still within the risetime of interest here.

The results are shown in Figure 3-8 *a*. The dotted line represents the garnet response which in this particular case starts ≈ 200 ps in advance of the P_1 switching (dashed) and ≈ 500 ps before P_2 . The P_2 trace reaches 90% saturation in 650 ps, so the **total** switching time of 1150-1200 ps is much longer than previously estimated in rise time measurements. This time may compromise the performance of the recording heads.

In one set of measurements we accidentally misplaced the beam position so that it was focused below the second pole P_1 , at the first shield level (Fig.

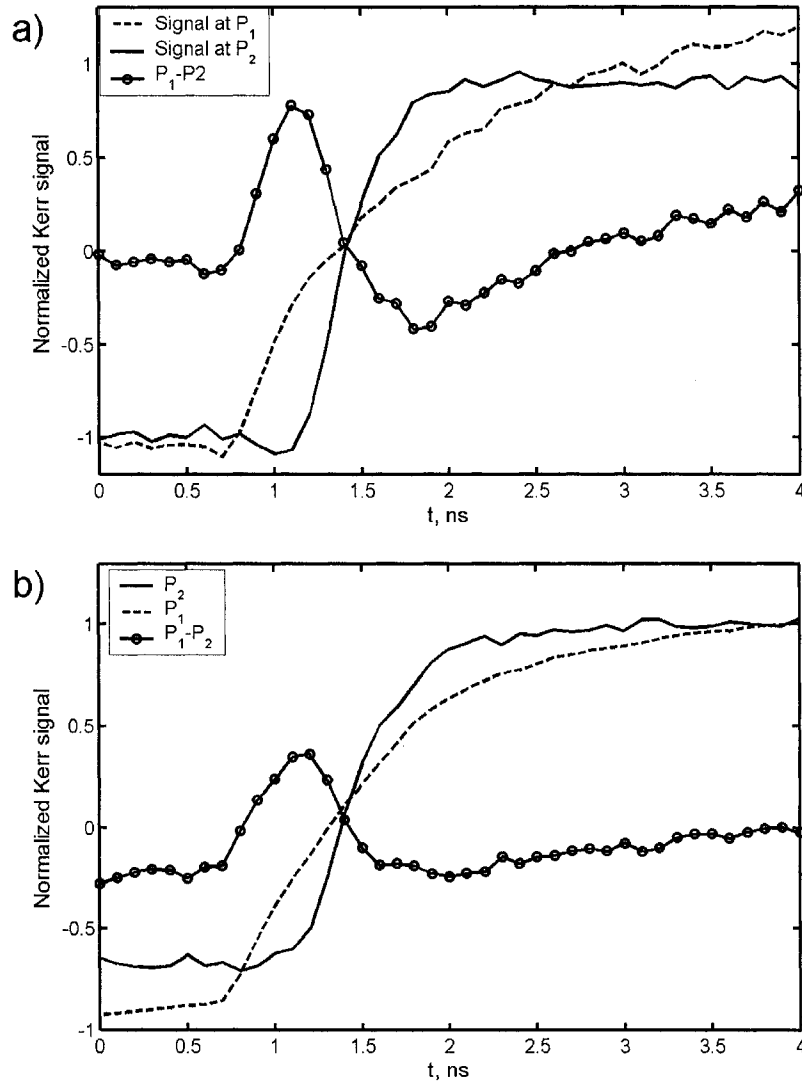


Figure 3-7: Temporal profiles of magnetization recorded at the edges of the recording poles P_1 (inverted, dashed) and P_2 (solid) right across the gap for the head mounted on the head gimbal assembly (a) and directly for a head slider (b). The lines with markers represent the difference between P_1 and P_2 pole responses.

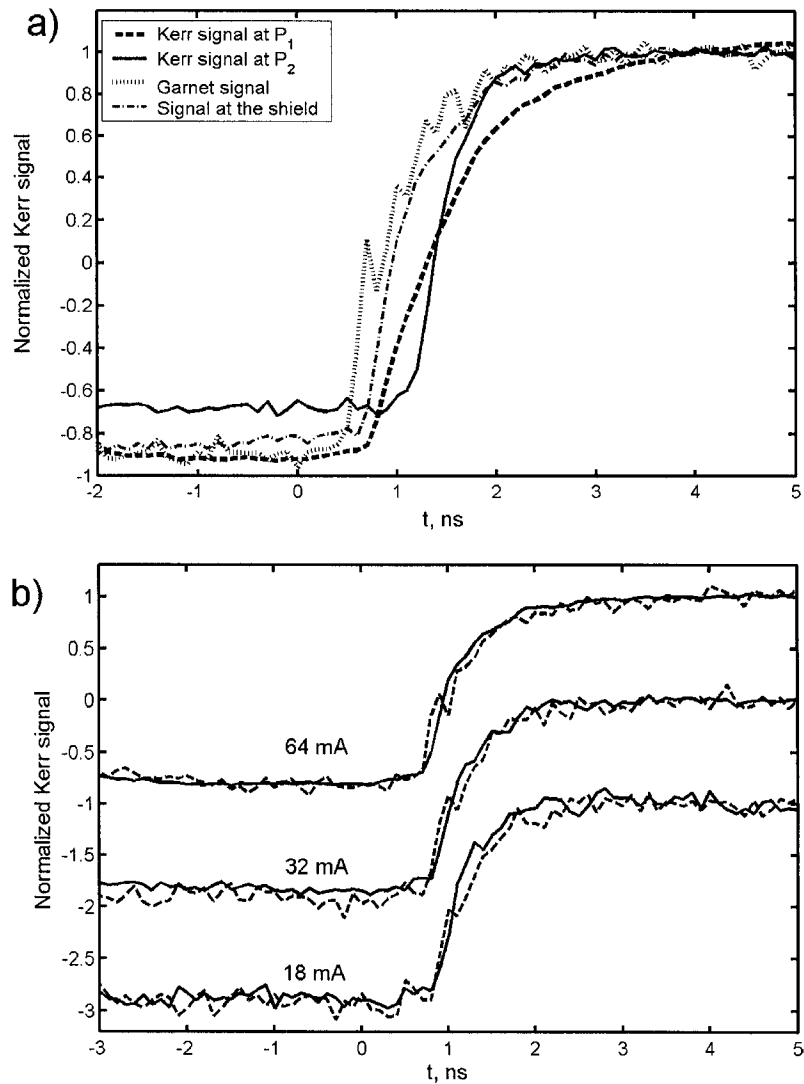


Figure 3-8: (a) Temporal scans normalized to the saturation levels recorded at different positions at the head and the current onset measured by garnet optomagnetic sensor. Note, that the response of unsaturated shield material right below the P_1 pole (Fig. 3-2a) almost coincides with the true current profile. (b) Temporal scans normalized to the *plateau* levels for the garnet sensor (dashed) and corresponding shield response (solid) for different current levels. Within the noise, traces almost coincide.

3-8 *a*, dash-dotted). That was a lucky mistake, as the signal from this unsaturated bulk shield area proved very interesting: it was not lagging behind the current onset but rather almost retraced it (within noise and a normalization factor). These measurements were repeated the next day at different current attenuation levels (Fig. 3-8 *b*). At each value of attenuation (0, 6 and 11 dB) the laser was successively focused at the shield and then at the garnet sensor. All traces in Figure 3-8 *b* are normalized to the plateau level: the purpose of this experiment was to verify the proper timing of the shield response with respect to the current onset. It appears that the corresponding shield and garnet traces coincide within the accuracy of experiment even better than in shown in the Figure 3-8 *a*. Probably, the reason for this is deliberate positioning of the beam on the shield [76].

Unnormalized temporal traces at different attenuations for the same shield spot are shown in the Fig. 3-9 *a*. Successive attenuation levels result in proportionally reduced traces of similar shape. In order to demonstrate the linearity of the signal level with respect to the current strength we plotted the top and the bottom plateau levels versus coil current directly measured by inductive probe (Fig. 3-9 *b*). The plateau levels are averaged between $[-2, 0]$ and $[3, 5]$ ns respectively, and the negative plateau levels are inverted for direct comparison. One can see linear (although not proportional as the y -intercept is non-zero) dependence of the magneto-optic signal of the first shield on coil current in wide range of current levels.

It appears that the first shield layer of longitudinal recording heads can serve as a built-in current sensor, conveniently placed for comparison of the pole tip response to the true current onset.

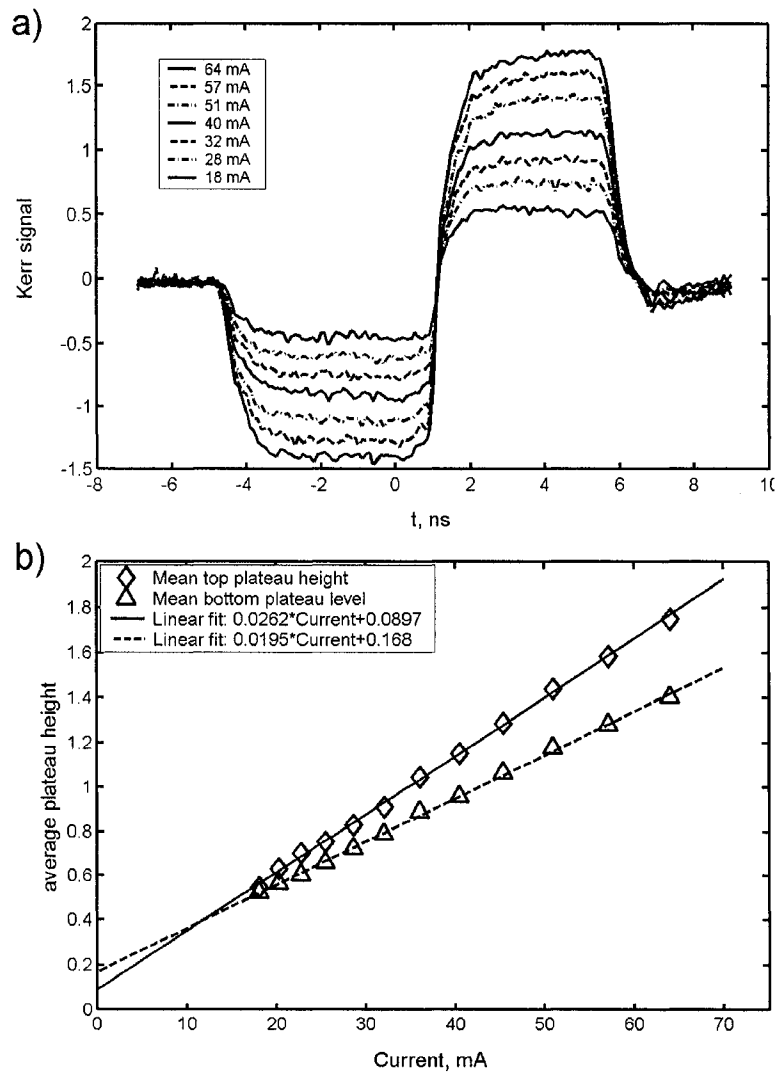


Figure 3-9: (a) An unnormalized response of the shield to a typical bipolar pulse of different amplitudes. Numbers indicate the highest level at the positive plateau measured independently using an inductive probe. (b) Average top (diamonds) and bottom (triangles) plateau levels versus the current strength. Linear response makes the shield a built-in magneto-optic sensor for recording heads.

3.4 Chapter summary.

We characterized numerous recording heads using TR-SKM techniques and found that the pole tip geometry strongly influence the saturation time of the pole tip. Shortening the write “nose” of the tip helps to cut the saturation time almost by a factor of two. Reducing the pedestal area helps improves the head performance as well, but to lesser effect. Switching of the thin pole (P_2) often lags behind P_1 100-200 ps, it appears to be a generic feature of new recording heads observed on both HGA and slider levels. The saturation risetime of the pole P_2 is shorter than that of P_1 at the edge of the gap, but increases (in some cases as much as by a factor of two) along the pole further away from the gap.

Both P_1 and P_2 response lag 100-200 ps behind the current onset. This effect, rather than the pole saturation rise time may ultimately limit the head performance. This lag is probably associated with the domain wall propagation within the yoke and can be reduced by shortening yoke dimensions [15]. In contrast, the response of the shield layer is timed with current onset and nearly linear with the coil current strength. Thus each recording head has a built-in magneto-optic current sensor, a helpful feature for future TR-SKM head characterization experiments as it allows one to directly measure true current onset.

Chapter 4

Magnetization reversal with vector control of in-plane switching field.

This chapter is based on two separate projects [59], [60] both devoted to half-select switching of a micrometer-sized ferromagnetic element between remanent states in zero external bias field. This is of course the regime utilized by real MRAMs. However, the nature of these experiments makes them a challenge for a stroboscopic TR-SKM technique, because only the averaged change of magnetization between two states, not the absolute magnetization itself, is measured. A bias field to nearly saturate one of the states would make the measurements easier to interpret.

Both projects involve the crossed-wire element – a building block of many MRAM architectures. However, in contrast with transport MRAM measurements or their operational regime, the ferromagnetic element is not placed between the write wires but on top of them. Since magnetization is probed optically there is no need for read wires. Another difference with transport measurements is that the elements are just single-layer patterned thin film

islands and not complex multilayer (GMR or MTJ) sandwiches. An easy axis of all elements is ensured by a pronounced shape anisotropy.

Magneto-optic probing reveals spatial structure of the magnetization states during the switching and helps one to judge whether the element behaves as a single domain or not. In addition, Landau-Lifshitz-Gilbert based micromagnetic simulations [51] were performed in order to model observed switching dynamics. However, the LLG Simulator was used with caution, and we tried not to use any fitting parameters. I would like to quote Michael Scheinfein, the creator of the Simulator: “The Simulator is useless without experiments”. Although the code worked well, and showed a lot of magnetization structure details actually observed in experiment, no conclusions are drawn based on simulations alone. On the other hand, the simulations helped to explain the experimental results and design prospective experiments for further development of the TR-SKM technique. Running stroboscopically averaged experiments without simulations is about as much fun as walking blindfolded.

4.1 Railway-cross element.

4.1.1 Swiss-cross and railway-cross samples.

This project was conducted in close collaboration with the Naval Research Laboratory (NRL of Washington DC). Elongated samples of relatively thick 45 nm $Fe_{0.1}Co_{0.9}$ were prepared and preliminarily tested at NRL by Scott Zelakiewicz. Two kinds of crossed-wire elements were fabricated: a conventional “Swiss-cross” element with the long axis of the ferromagnetic element parallel to the digit or bit wire; and a “Railway-cross” element with orthogonal write wires (WW) at $\pm 45^\circ$ to the long axis of the thin film element. The idea of the railway-cross alignment was to increase the density of the memory cells by aligning the longer axis of the sample with the diagonal of the crossed wires.

An obvious disadvantage of this set-up is, of course the fact that the element magnetization can be disturbed by either WW, unlike the case of the Swiss cross alignment where the digit pulse cannot flip the magnetization, however strong it is. In both set-ups we tried to achieve a reliable half-select switching and study the effects of the pulses' strength and overlap on the switching process. In particular, the minimum amount of overlap between the pulses and the dependence of the switching rate on the pulse strength are important from an engineering perspective as they eventually determine the operational rate of MRAM cells. Mark Johnson also suggested that we add the third dimension – switching time to the critical Astroid-like switching diagram, at that time investigated only in the quasi-static regime. Another point of interest is the range of pulse amplitudes over which half-select switching takes place.

AFM and MFM images of a photolithographically patterned ferromagnetic element is shown in the Fig.4-1 *a, b*. The element is a 45 nm thick $\text{Fe}_{0.1}\text{Co}_{0.9}$ film, with width $1\mu\text{m}$ and length $7\mu\text{m}$, patterned by optical lithography and lift-off. The $\text{Fe}_{0.1}\text{Co}_{0.9}$ was deposited in the presence of a field $H_x \sim 200$ Oe at the substrate in order to ensure the crystalline anisotropy along the sample axis, and the 7:1 aspect ratio provides sufficient shape anisotropy to ensure an easy magnetization axis along \hat{x} . This $7 \times 1 \mu\text{m}$ element has relatively smooth edges and it is nearly uniformly magnetized (Fig.4-1 *b*) in the central region, although slight stripe-like variations of the out-of plane magnetization reveal themselves even at the center; and clearly shows closure domains at the ends. Fig.4-1 *c* shows a schematic cross-section of the sample. For the Swiss-cross sample the top 220-nm thick gold WW is perpendicular to the long axis of the sample, and thus we traditionally call it Word wire, and the bottom 150 nm-thick wire is a Digital one. For the railway-cross sample we address the top and bottom WWs as “Principal” and “Auxiliary” correspondingly.

Quasi-static Hall effect measurements on a similar element[77] showed a relatively square hysteresis loop with 80% remanence, a coercivity of 90 Oe

and a saturation field of 150 Oe (Fig.4-1 *d*). They also demonstrated the lack of minor loops below a threshold of 90 Oe. However, a metastable “step” at the falling edge of the hysteresis curve (at approximately minus 70 Oe) indicates complexity of the switching history during the field sweep. A possible reason for this metastable state will be discussed below.

In our time-resolved measurements inductive switching of the element is accomplished with current pulses applied to write wires. The field strengths were calculated for each write wire from the current pulse amplitudes. First, consider the Swiss-cross element.

In a typical experiment, the initial magnetization state of the element is along the negative x direction. We position the focused laser spot near the center of the element where the easy axis magnetization component is much stronger than the hard axis one due to the shape anisotropy of the sample. A switching current pulse of variable amplitude with rise time of 50 ps and duration of 10 ns is applied to the Word wire to create a magnetic field in positive x direction, while longitudinal Kerr data are recorded. The reset pulse (amplitude 300 Oe, duration 150 ns) is applied to word wire more than 350 ns after the end of the switching pulses, resetting the magnetization states to the initial value along $-\hat{x}$. The actual repetition rate was set at 691 kHz, so there are about 850 ns before the next switching pulse arrives, allowing the magnetization to completely stabilize. The principal and the (slow rising) reset pulses propagating down the same wire and are coupled via a bias tee mixer.

Typical temporal magnetization traces for different amplitudes of the word pulse are shown in the Fig. 4-2. Magnetization is switched completely by a strong 215 Oe pulse and remains in the switched state when the pulse is ended. However, weaker pulse amplitudes (135 to 190 Oe) fail to achieve reliable switching. By the end of these pulses the easy-axis magnetization M_x has plateaued at a lower level, between the saturated “switched” and

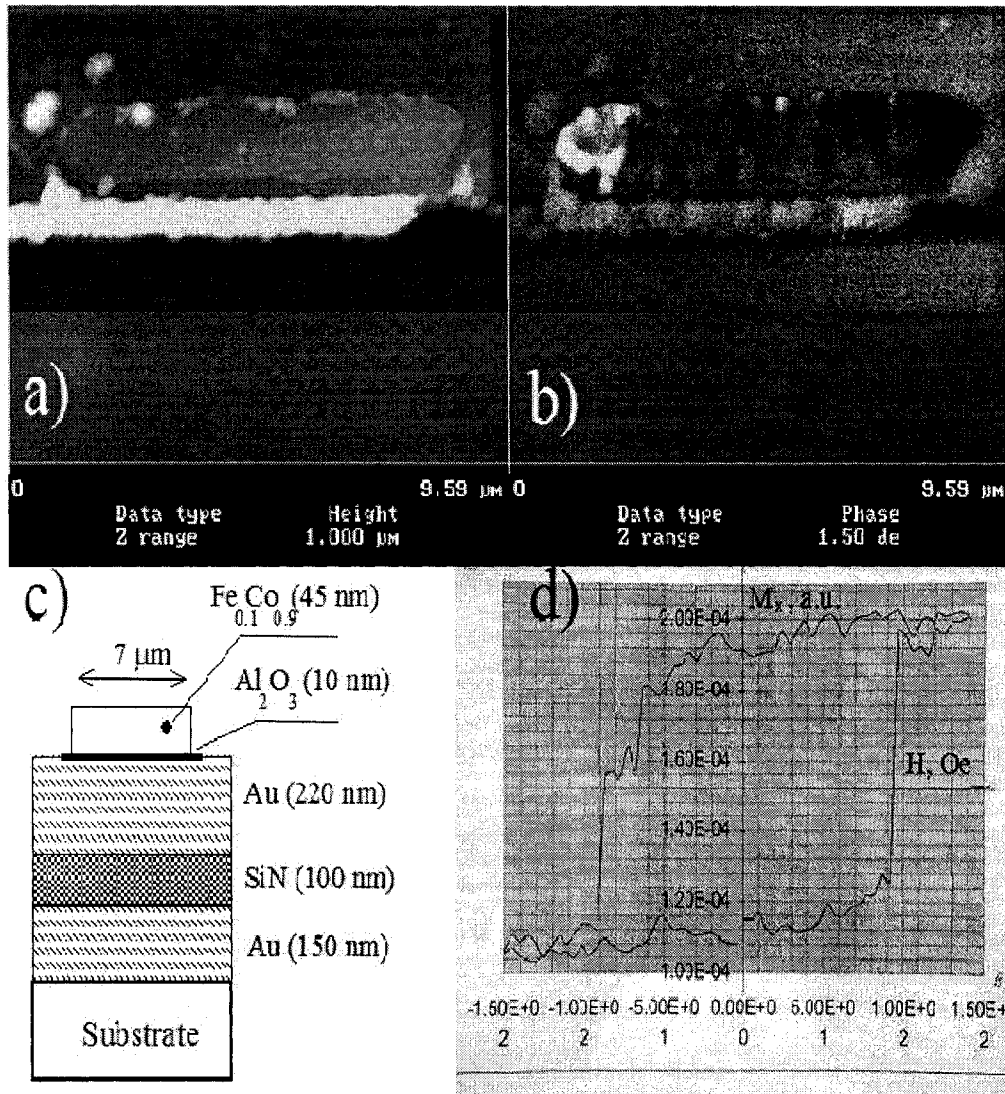


Figure 4-1: The NRL sample. (a) An AFM scan of the ferromagnetic element. The edge of the wire is seen as a white stripe, but an elongated grey element does not show significant roughness. (b) corresponding MFM scan of a sample in remanent state (zero bias field). The grayscale shows out-of-plane magnetization of the sample, but also non-magnetic features such as the edge of the wire. Closure domains are observed. The wire edge produce an artefact in the measurement. (c) Schematic cross-section of the crossed-wire element. (d) Measured static hysteresis loop for a similar element.

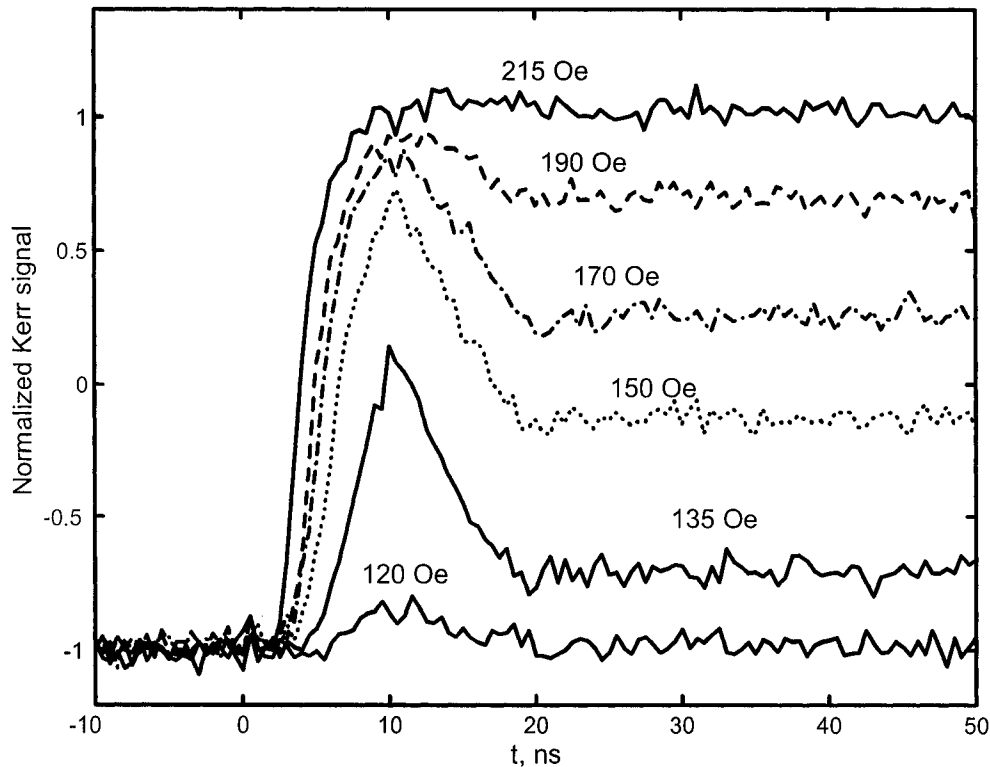


Figure 4-2: Typical temporal traces of the easy-axis (x) magnetization switching history for different Word field amplitudes in the "Swiss cross" geometry. The Kerr signal is normalized to the saturation levels (-1 for magnetization pointing to the left and +1 for M_x to the right).

"unswitched" states.

We attribute this incomplete switching to the stroboscopic nature of our experiment. That is, the final plateau does not represent the final state of the magnetization, but rather shows the percentage of the events ended up in the switched state. Below we address this regime as "Statistically Incomplete switching" or SIC. It is clear, however, that this sample is not a good candidate for the half-select switching experiment, as it demonstrates unreliable switching even in the case of a single word pulse. The "railway cross" sample demonstrated more reliable switching with a narrower range of the statistically

incomplete switching than the Swiss cross one, so the rest of the measurements on the NRL samples was conducted in that geometry.

4.1.2 Railway cross element: the effects of pulse amplitudes.

An optical scanning micrograph of the element on the “railway” crossed wires is shown in Fig.4-3. In this configuration a single current pulse has magnetic field components along the easy (\hat{x}) and hard (\hat{y}) magnetization axes. Again, we position the spot near the center of the element where the easy axis magnetization component is much stronger than the hard axis one due to the shape anisotropy of the sample. Switching current pulses I_1 and I_2 , with rise times of 50 ps and 150 ps and durations of 10 ns and 70 ns respectively, are applied, individually or simultaneously, while Kerr data are recorded. A single reversal pulse that propagates down either write wire has an associated magnetic field with equal components in the x - and y - directions, with a positive x -component (i.e. opposite the initial orientation \vec{M}_i). The same reset pulse as previously (300 Oe, duration 150 ns) is applied to WW1 in order to restore the magnetization along $-\hat{x}$.

For integrated digital applications, half-select processes are required where a single pulse of normalized amplitude in WW1 does not switch the magnetization state of the element but simultaneous pulses in WW1 and WW2 reverse the magnetization state. The easy axis magnetization response to single pulses of variable amplitude is shown with the data of Fig.4-4 *a*. The experiment directly measures the change in magnetization, and the raw data have been offset and normalized to saturation levels.

A single 280 Oe pulse saturates the magnetization change upon reversal, and a pulse with amplitude decreased by $\sim 10\%$ also causes complete reversal. Theoretically, the x -component should not reach saturation during the pulse

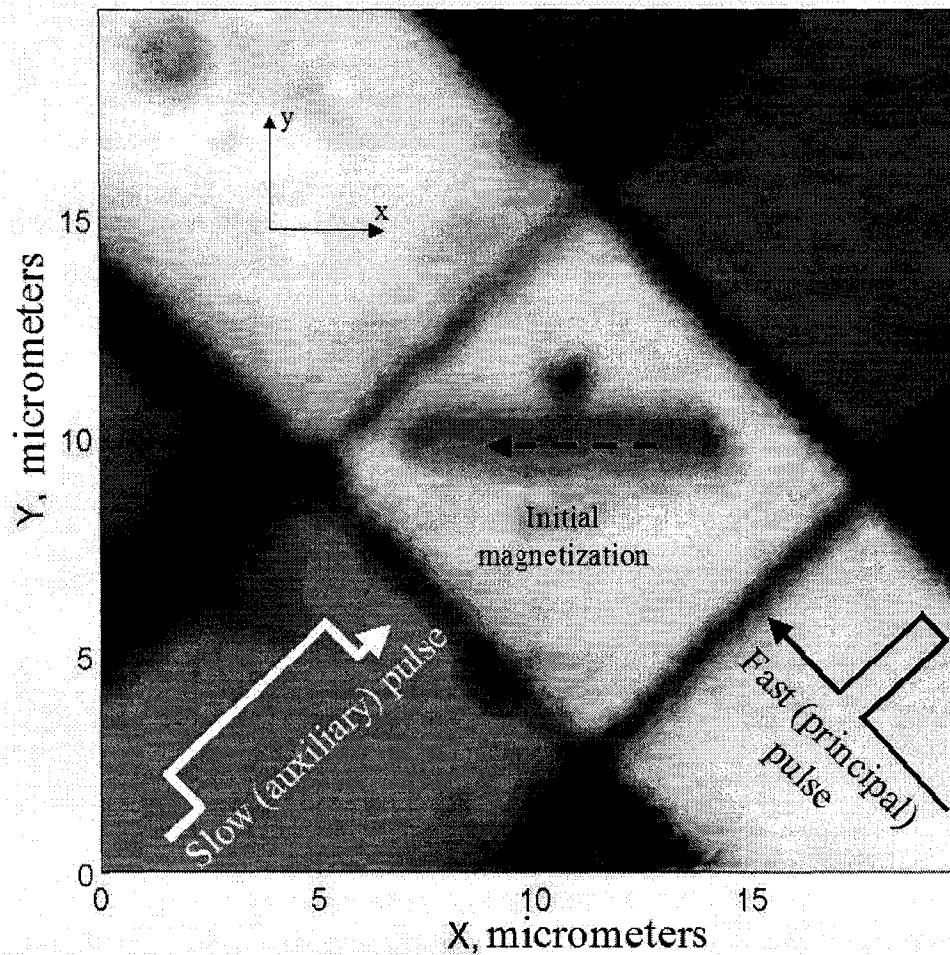


Figure 4-3: A scanning optical micrograph of the “railway” crossed wire element, rendered in linear grayscale is proportional to the reflectivity of the sample. The top gold wire is thus brighter than the bottom wire coated by SiN dielectric. The fast-rising, 10 ns duration principal pulses propagate down the top wire. The ferromagnetic element is at the center of the wire intersection. An initial sample magnetization direction is shown as the dashed arrow.

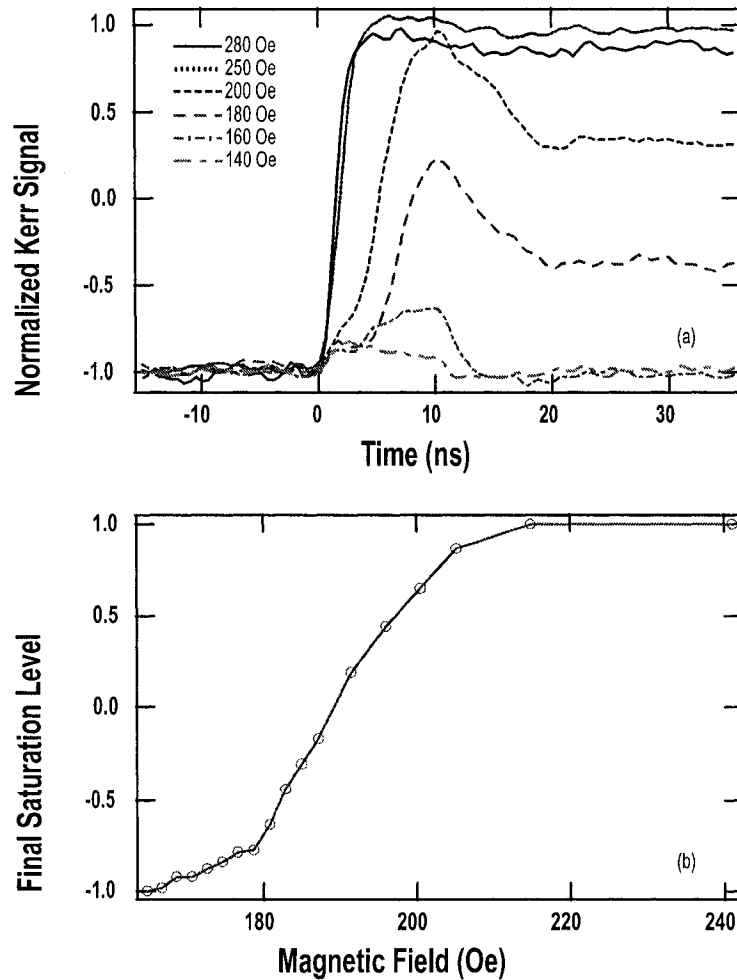


Figure 4-4: (a): Kerr signal representing the x -component of the magnetization change for a single 10 ns pulse on WW1 arriving at $t = 0$ ns, for various pulse amplitudes. The values listed represent the magnitude of the applied magnetic pulse. Complete reversal is observed for fields of 250 Oe or greater and the initial state is preserved for fields of 160 Oe or lower. We attribute the intermediate values of plateau height to the statistical nature of the switching events. (b): the dependence of the final average level of magnetization change at the long time delay on the applied field strength.

application since magnetization is slanted by the external field applied at 45° to the easy axis. The switching time τ_s , which we define as the interval from the arrival of the pulse to the instant where the x -component of the magnetization change reaches 90% of its total change, is approximately 3 ns. It varies slightly (± 0.5 ns) as a function of position on the sample. We have chosen the 90% threshold since the x -component indeed did not reach saturation during the pulse in part of our experiments (depending on the location at the sample).

The spatial scans of the sample exhibit multi-domain magnetization structure. The spatial resolution of the experiment does not allow us to determine conclusively the exact switching scenario [63] since the y -component of magnetization appears to be averaged over a few stripe domains. The x -component is relatively immune to this kind of averaging in structures of high aspect ratio, as in the present case.

As the pulse amplitude is decreased to 200 Oe, large magnetization changes arise during the duration of the pulse but we believe that the switching phenomena represented by the data ($t > 20$ ns) occur statistically, with randomness introduced through thermal fluctuations. That is, the intermediate values of average magnetization observed at long times represent the saturation change of magnetization scaled by the probability of switching (SIC). After the application of pulses with amplitude 160 Oe and 140 Oe the initial state \vec{M}_i is unchanged, and we identify 140 Oe as an appropriate half-select pulse amplitude.

As mentioned above, no minor loops were observed in quasi-static measurements performed on analogous structures. We do not believe that there exist several discrete saturation levels, although one could argue that multi-domain structure could result in a few different but deterministically arrived at final magnetization states due to domain rearrangement. In order to test this possibility we repeated the measurements at smaller field increments. This test was performed several months after the initial measurements. It was discov-

ered that although all of the qualitative features (general shape, half-select, incomplete switching etc.) of the earlier results were reproduced, the sample had “aged” in some way giving rise to quantitative differences. In particular, a narrowing of the range of field over which the transition from “no switching” to “complete switching” occurred. However the key finding was that the saturation levels filled a continuum of states between the two extremes. Figure 4-4 *b* represents the percentage of switching as a function of applied field strength.

4.1.3 Railway cross: the effect of pulse overlap.

Next, we study the dynamics of magnetization reversal in response to the application of two half-select amplitude pulses with variable relative arrival time and, therefore, variable overlap time $t_{1,2}$. The goal here is to estimate a minimum required overlap sufficient for a reliable half-select switching. A schematic of the arrival of two 140 Oe pulses is given in Fig. 4-5 *a*. A 10 ns pulse applied to WW1 arrives first at various times starting at $t = -10$ ns. The 70 ns pulse applied on WW2 always arrives at $t = 0$ ns. By changing the arrival time of the first pulse, the pulse overlap time, $t_{1,2}$, can be varied. For example, when the first pulse begins at $t = -10$ ns, the falling edge of this pulse (at $t = 0$ ns) coincides with the rising edge of the second pulse and there is no pulse overlap, $t_{1,2} = 0$. When the first pulse begins at $t = -6$ ns, however, both pulses are present from $t = 0$ ns to $t = 4$ ns, an overlap of $t_{1,2} = 4$ ns. Due to the write wire geometry the y -component of the applied fields when both pulses are present is zero whereas the x -component is equivalent to the case of a single 280 Oe pulse.

The dynamic magnetization response to two pulses of variable overlap is shown with the data of Fig. 4-5 *b*. Switching is very strongly dependent on the amount of overlap $t_{1,2}$. Although reversal does not occur for $t_{1,2} = 0$ ns (no overlap), surprisingly a small amount of statistically incomplete switching

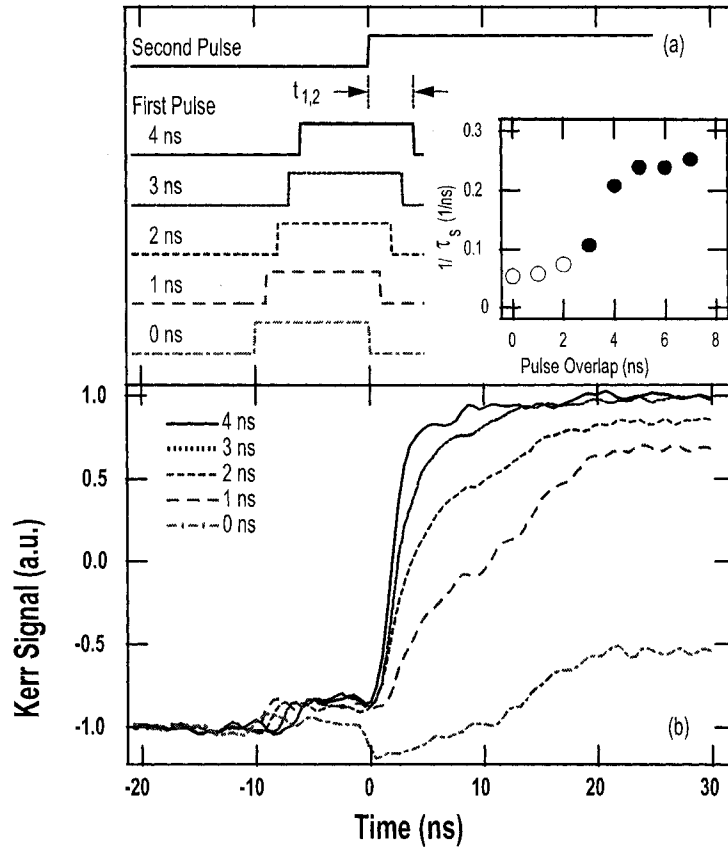


Figure 4-5: (a): Schematic of the arrival and overlap times of two pulses. Inset: The inverse switching time $1/\tau_s$ as a function of overlap $t_{1,2}$. Open circles denote statistically incomplete reversal. (b): X -component of Kerr signal during the application of two pulses applied to WW1 and WW2 for varying amounts of overlap, $t_{1,2}$, between the pulses. The second pulse begins at $t=0$ ns for all traces. The switching time can be seen to decrease for greater overlap of the pulses.

occurs during the duration of the second, long pulse. No such switching is seen in response to single long pulses of this amplitude. As the overlap time $t_{1,2}$ is increased, switching occurs during a larger fraction of events. At $t_{1,2} = 3$ ns the probability of switching is unity and the switching time is 10.7 ns. Further increasing the overlap time results in the same certainty of switching and the switching time decreases to approximately 4.8 ns for $t_{1,2} \geq 5$ ns. The inset to Fig. 4-5 *a* plots the inverse switching time as a function of overlap time. Data for $t_{1,2} = 3$ or 4 ns, along with the data of Fig. 4-4, demonstrate half-select events: a single 10 ns pulse of amplitude 140 Oe fails to disturb the magnetization state, but two 140 Oe amplitude pulses with sufficient overlap successfully switch the state.

Summarizing the data of Fig. 4-5, the characteristic switching time for large pulse overlaps, τ_c , is approximately 4.8 ns. As the overlap decreases to 4 ns and below, both pulses are simultaneously present for only a fraction of τ_c and completion of the reversal process is probabilistic. In the case of $t_{1,2} = 3$ ns, the process has sufficiently progressed so that the single remaining pulse can complete the reversal, albeit on a much longer time scale. For overlaps of 2 ns and lower, less than half of τ_c , the element frequently remains unswitched as seen in the reduced average magnetization at long times. These results suggest that optimal switching rates can be achieved only for pulse overlaps of $t_{1,2} \gtrsim \tau_c$.

Although the field components along the easy-axis (\hat{x}) are the same in cases of a single 280 Oe pulse and of two 140 Oe pulses, the responses of the ferromagnetic element varies greatly. The switching time for a single pulse is roughly half the minimum time obtained for two pulses. The significant difference of these two methods is that the single pulse has a finite y -component of field. This additional field in the hard-axis direction breaks the symmetry of the anti-parallel reversal condition and, in a single dipole approximation, lowers the energy barrier between states. The reduced switching time for a

single pulse is in qualitative agreement with calculations [78] where a small bias field applied along the hard axis cause large changes in the switching time.

In the case of single pulse excitations with attenuated pulse amplitudes, and for double pulse excitations with reduced temporal pulse overlap, the statistics of switching manifests itself in these stroboscopic measurements. This regime of statistically incomplete switching will be the subject of further investigation, but clearly should be avoided for practical device applications. Studies of a similar nature to those described here can also explore the trade-off between device switching speed and power. The present experiments focus on the dynamics of nanosecond scale magnetization reversal for low power pulse amplitudes near the threshold for switching, hence the relatively long switching times. Magnetization reversal times, however, are known to decrease as write pulse amplitudes are increased beyond the minimal values required for saturation [79]. Additionally, pulse shaping and the design of appropriate pulse sequences to tailor the in-plane angle of the switching field as a function of time during the reversal is a clear direction for further optimization of switching dynamics.

4.1.4 Spatial variations of magnetization during the switching. Arrott's wall.

In the previous section we discussed effects of pulse overlap on the switching process. Consider now the effect of the auxiliary pulse strength on the switching time in the half-select regime. We fix the principal pulse amplitude to the half-select level of 140 Oe, and vary the auxiliary pulse strength, to determine both the minimal required assistance for the complete switching and the rise time variations as a function of the second pulse strength (Fig.4-6).

Figure 4-6 *a* shows the time vs amplitude scan for M_x . Magnetization was

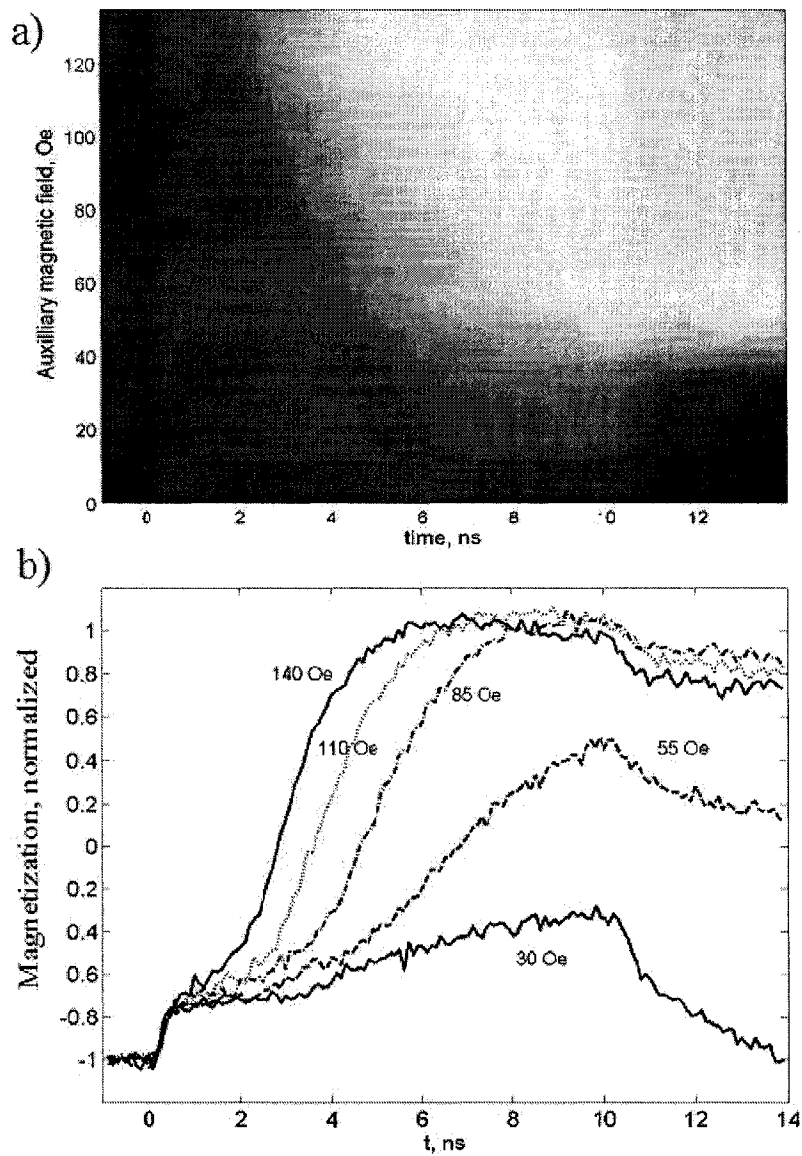


Figure 4-6: (a) Time-amplitude scan of the easy-axis magnetization M_x of the sample. Linear grayscale represents the magnetization level, horizontal axis shows the time (principal pulse is present from zero to ten ns), and the vertical axis auxiliary pulse strength. (b) Line scans from panel (a) at several values of the auxiliary pulse strength.

probed at a point near but not at the center of the sample. A collection of a number of temporal magnetization scans at this position, some of which are shown as line scans in Fig. 4-6 *b*, is represented by a linear grayscale in Fig. 4-6 *a*. The total temporal scan range is fifteen nanoseconds, entirely enclosed within the envelope of the auxiliary pulse (70 ns). The principal pulse is present for 10 ns, and it reveals itself as a light stripe seen at all auxiliary pulse values.

First, one sees that even a relatively weak 65 Oe auxiliary pulse is sufficient to completely reverse the magnetization in the half-select regime. Weaker auxiliary field values in the range of 35 to 60 Oe again lead to incomplete switching that represents the statistical nature of the switching events. Below 30 Oe the sample remains in the unswitched state. Second, the switching time decreases with increasing auxiliary pulse strength, but the changing shape of the temporal profiles (Fig.4-6 *b*) is indicative that the sample switches incoherently. Consider the traces corresponding to the complete switching regime (85, 110 and 140 Oe). At first the magnetization is just slightly perturbed by principal pulse, and stays at this state for some time until, apparently, a domain wall crosses the point where the magnetization is probed. This hesitation period is inversely proportional to the domain wall motion speed, which in turn is proportional to the field strength. Indeed, the “critical switching curve” in Fig 4-6 *a* has plausibly hyperbolic shape. The switching rate as a function of the applied field strength is plotted in the Fig 4-7. The graph is nearly linear, with a slope of $\approx 1.8 * 10^{-3} (ns * Oe)^{-1}$. Assuming that the propagation starts from the closure domains sample and that the probing spot is situated at $3 \mu m$ from the nearest end, the domain wall propagation speed can be estimated as $5 m/(s * Oe)$. This rough estimate is influenced by uncertainty in the closure domains’ size and consequently the initial position of the wall. At 140 Oe the top propagation speed of 700 m/s is comparable with the estimated Walker velocity of ≈ 700 m/s for 8-nm Néel wall (cf. Fig.1-9, equation 1.59).

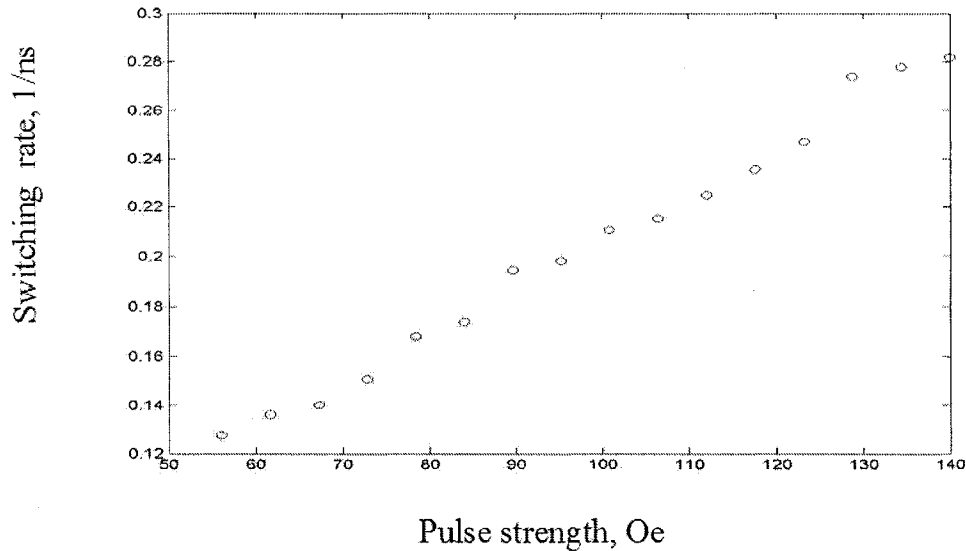


Figure 4-7: Switching rate as a function of the applied auxiliary pulse strength.

Direct evidence of the reversal via domain wall propagation is shown in Fig. 4-8. Figure 4-8 *a* shows a spatial scan of the sample perturbed by a strong principal pulse (280 Oe) only. The map of the easy-axis magnetization is recorded two nanoseconds beyond the pulse onset. The Kerr signal at the center of the sample is lower than at the neighboring regions. However, if an analogous spatial scan is recorded at 6 ns after the pulse leading edge, the sample looks almost uniformly magnetized. We attribute this anomaly to a domain wall that is formed repeatedly (shot-to shot) at the center of the sample and persists for a long time (2-3 ns) until it eventually loses stability and breaks. In order to demonstrate the domain wall formation we recorded spatio-temporal scans that track the history of the sample magnetization at different points across the long axis of the sample. Considering the spatial resolution of our method (≈ 800 nm at 740 nm infrared light) these spatio-temporal scans contain almost as much information as a corresponding movie.

Figure 4-8 *b* represents M_x history in grayscale and shows clearly several stripes that we believe correspond to the domain walls. It is important to note, that these stripes are horizontal, and not tilted. Tilted stripes would correspond to moving wall. However, here we deal with a special kind of the domain walls between already switched parts of the sample, that stay at the same position until their eventual disappearance (according to our simulations, a stressed wall eventually loses stability to a number of vortices and anti-vortices). Figure 4-8 *c* shows the corresponding M_y component. Only the central (the strongest) wall is visible at this scan.

The existence of such walls was predicted by A. S. Arrott [46][47]. A normal Neel wall between switched and unswitched parts of the sample implies a gradual 180° change of the magnetization direction in the plane of the sample. There are two possibilities: a clockwise or counter-clockwise change. In either case, when the wall moves towards the unswitched area, more of the material gets aligned along the applied field, and there is an obvious gain in Zeeman energy. If the nucleation starts at the sample ends, the left wall moves to the right, and, vice versa, the right wall moves to the left. If both Neel walls have opposite vorticities, they just annihilate at the center of the sample or wherever they meet. However, if they have the same vorticity, a metastable 360° (Arrott's) wall is formed. This wall has no preferential direction of motion and it acts much like a loaded spring. Upon release of the stress (removal of the applied field) Arrott's wall breaks into two 180° Neel walls that move from the center towards the edges of the sample and restore the initial magnetization.

Simulated formation of the Arrotts wall is shown in Fig. 4-9. Figure 4-9 *a* demonstrates a simulated hysteresis loop for a small 8 nm - thick 200×100 nm permalloy elliptical sample. The hysteresis curve is nearly rectangular, but there are two points sitting directly at the rising and falling edges of the loop at ± 360 Oe. Figure 4-9 *b* proves that it is not a coincidence: magnetization configurations at these points as well as the neighboring field values is plot-

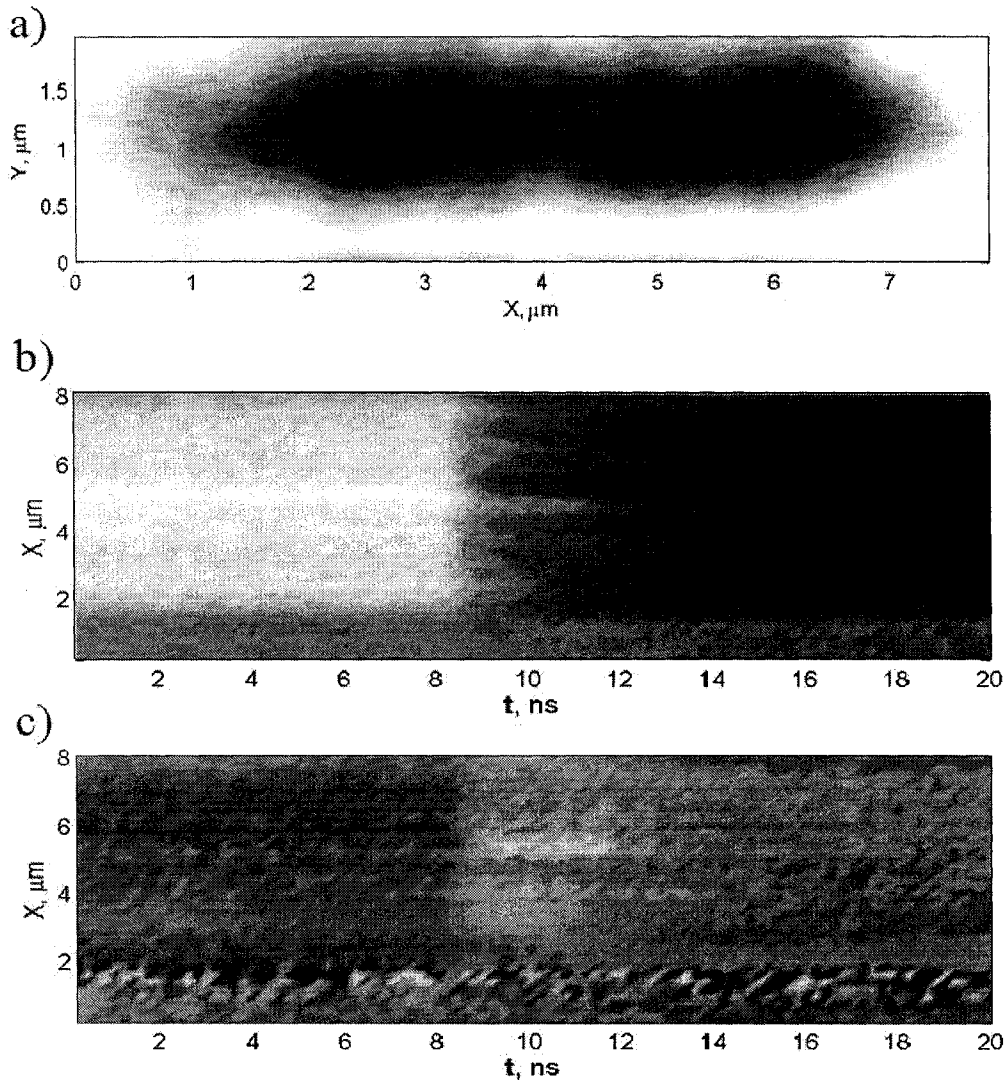


Figure 4-8: (a) spatial scan of the easy-axis magnetization M_x recorded two nanoseconds after the principal pulse start (10 ns at the scans below). (b) M_x variations across the sample (spatio-temporal scan) induced by a principal pulse of 280 Oe (no auxiliary pulse). The pulse starts at $t = 8$ ns. (c) Complementary M_y scan.

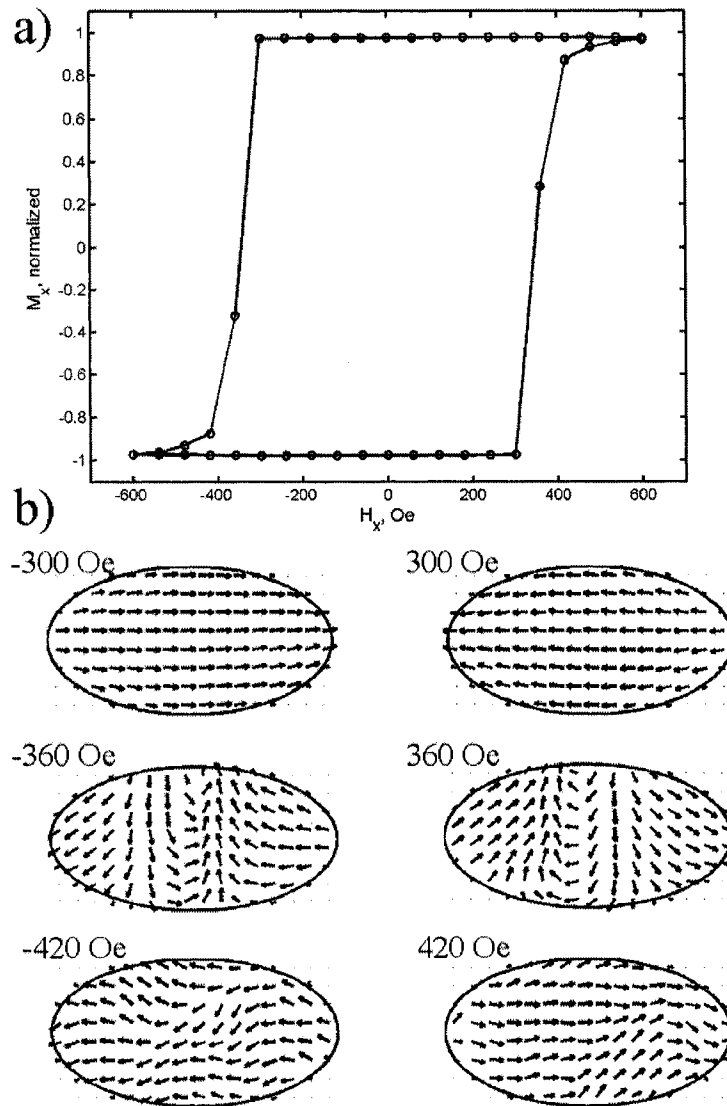


Figure 4-9: (a) Simulated hysteresis loop for a 200×100 nm ellipse. (b) simulated magnetization configurations at the strange point at the rising (falling) edge of the hysteresis curve (± 360 Oe) and at the neighboring field values.

ted. At ± 360 Oe the Arrott's wall is formed. Magnetization configurations at ± 420 Oe are not as uniform as at ± 300 Oe, but this must be just a calculation artifact of not letting the simulation enough time to relax – small angle oscillations persist for a long time. The 360° wall is predicted to form from initial C-state of initial magnetization, therefore trapezoidal shape distortion was imposed in original calculations [47]. However, this distortion is not required: under application of the external fields the symmetry of a uniformly magnetized specimen spontaneously breaks forming a low-energy C-state (as there is less gradient penalty in the energy). Mechanical analogy: a metal rod under compression loses stability to a bow-like C-state rather than to the S-like shape.

Certainly, the history of the magnetization change in a large $7 \times 1 \mu\text{m}$ and thick (45 nm) element is more complex than in a small 200×100 nm ellipse. The point is, whatever complex domain pattern emerges during the switching, all neighboring same-vorticity Neel walls quickly collapse, while opposite-vorticity walls form Arrott's walls which have no preferential direction of motion and stays (probably pinned by the defects) long enough to be observed in the experiment. The possibility of Arrott's walls formation should be taken into account in the design of the MRAM elements.

4.2 Multi-junction crossed (“snake”) wire structures

In this section we consider conventional (Swiss-cross-wire) elements made entirely at the University of Alberta. In the previous sections we found that a $7 \times 1 \mu\text{m}$ element explores a multi-domain switching scenario. The goal here is to try to observe single- (or at least few-) domain behavior during switching, as one would naively hope to find in smaller samples. Unfortunately, recent

simulations [80] show nonuniformities (vortices) down to the 10 nm scale. Our e-beam Lithography system resolution was limited to structures larger than 50 nm, and at this spatial scale (say, for 50×100 nm ellipse) a vortex state is definitely metastable as indicated by micromagnetic simulations. Still, exploring smaller samples is of scientific and technological importance. Few domain structures and less complicated magnetization patterns are expected, and the opportunity for convergence with micromagnetic simulation is greater (small structures also require less time for simulation). Finally, small the elements are the key to higher recording density.

4.2.1 Snake sample preparation.

In order to fabricate small elements, e-beam lithography and lift-off with a two-layer PMMA resist was used, in contrast to the photolithographically patterned samples in the previous section. The e-beam lithography was performed by Miroslav Belov. Crossed write wires are deposited using conventional photolithography and etching. Two principal steps of the wire deposition are shown in Fig. 4-10 *a, b*. First, a snake-like DW is deposited (Fig.4-10 *a*), then two layers of a planarizing dielectric (spin-on-glass, or SOG) completely bury the DW while planarizing the surface before the second metal layer deposition, and then the second layer (WW) is deposited. Both gold write wires are 200 nm thick, the width of the DW is approximately $6 \mu\text{m}$, and the width of the WW is $3.5 \mu\text{m}$. Different arrays of 15-nm thick nearly elliptical permalloy ($\text{Ni}_{80}\text{Fe}_{20}$) elements are deposited atop each intersection of the wires. The ferromagnetic elements are isolated from the wire by three layers of spin-on glass (which ensure uniform coating of the structure by the resist). A layer of silicon dioxide protects the SOG from the aggressive PMMA resist remover at the last step of the lithography, and improves the surface quality. The plan view of the finished sample is shown in Fig.4-10 *b*, and the AFM scans of the

$3 \times 1 \mu\text{m}$ elements and the AFM roughness analysis are presented in Fig. 4-10 c. RMS roughness of ≈ 1.6 nm is a good result considering the number of layers involved. A schematic cross-section of the intersection corresponding to the array of the same $3 \times 1 \mu\text{m}$ ellipses is shown in Fig.4-11

The experimental results reported below correspond to the $3 \times 1 \mu\text{m}$ elliptical samples. Smaller elements exhibited high coercivity and could not be properly characterized with the transient field available. A suggestion for future experiments is to reduce the film thickness to 8 nm or less.

The probe beam used in these experiment (mode-locked Ti-sapphire) is frequency-doubled from 800 nm in order to increase the spatial resolution of the system, to resolve sub-micrometer detail of the relatively small samples. Dual Photomultiplier Tube (PMT) detectors sensitive to 400 nm - wavelength blue light were used. This set-up probes the polar Kerr signal and one of the in-plane components. The other in-plane component of magnetization can be recorded separately once each detector is rotated by ninety degrees.

Electrical contacts to the write wires buried underneath the SOG dielectric were made by a brute-force technique: scratching the contact pads with a soldering iron under a tiny pool of molten indium. Subsequently, short indium wires were pressed to the residual indium pads. All samples are terminated to the characteristic 50Ω impedance of the current pulse electronics, with surface-mount resistors in order to ensure reflectionless absorption of the fast-rising current pulses. To obtain a nearly flat-topped current pulse profile we combined the word and reset pulses with a resistive coupler rather than with a bias tee which has insufficient bandwidth in one arm, ending up with nearly-trapezoidal pulses at the cost of 50% of the amplitude. Word and digit pulse amplitudes and durations can be varied independently.

In the next two sections we discuss a time-resolved imaging study of half-select switching between remanent states using the crossed-wires geometry in half-select and precessional regimes respectively.

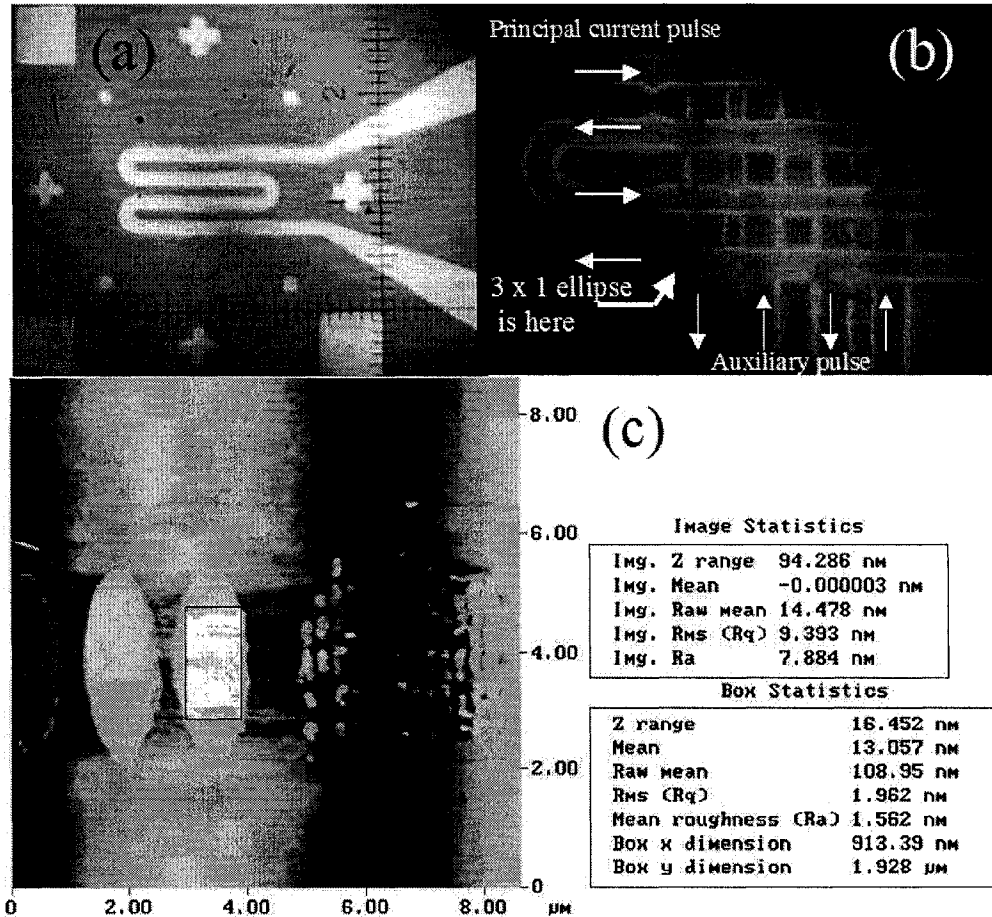


Figure 4-10: (a) The first layer of the lithography. A snake-like digit wire is deposited. (b) The final sample. The digit wire is buried underneath the planarising dielectric, then the mask is rotated 90° and the second (word) wire is deposited. After the secondary planarization by spin-on glass (SOG) and the deposition of the protective layer (SiO₂), arrays of permalloy elements are deposited atop the wire intersections. (c) AFM image of the 3x1 μm ellipses and the roughness test (AFM) of the finished sample.

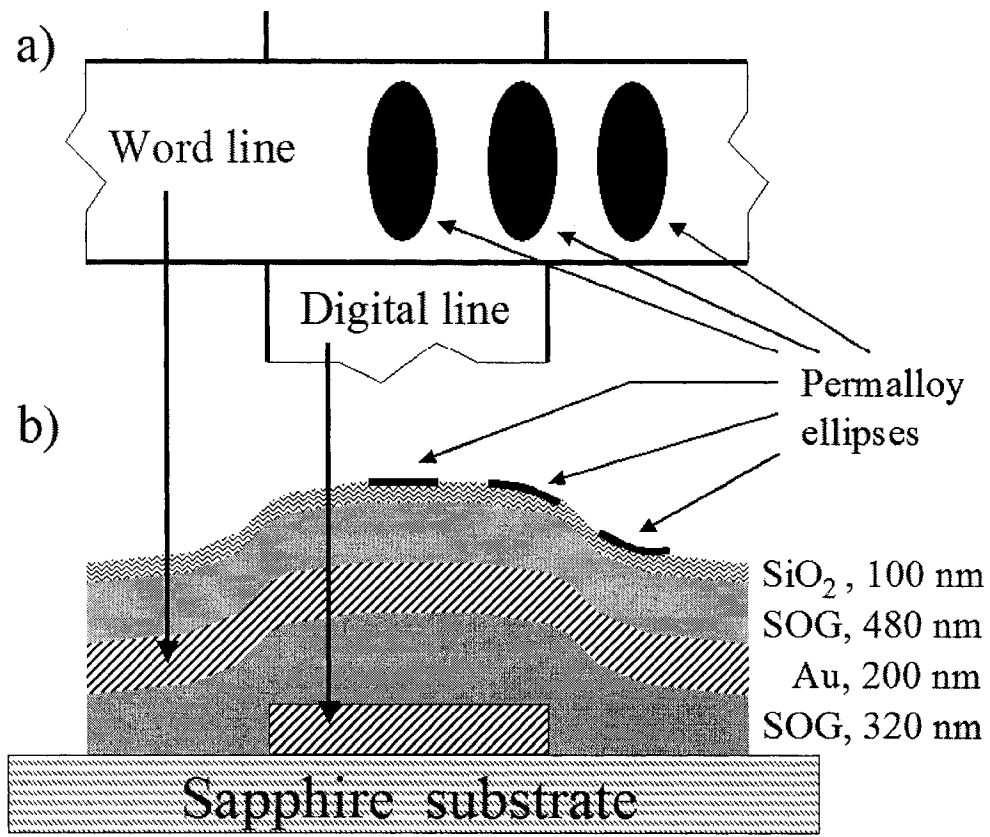


Figure 4-11: Schematic planar view (a) and a cross-section (b) of the crossed wires element. Two $3 \times 1 \mu\text{m}$ permalloy elliptical samples are placed at the intersection.

4.2.2 Antisymmetric switching.

In order to study pulse duration effects on switching diagrams we send nearly-trapezoidal short pulses down both write wires. The word pulse rise time is approximately 300 ps, digit pulse rise time 250 ps; with fall times 1 ns and 700 ps respectively. The duration of the plateau phase of the word pulse can be varied from approximately 250 ps, in which case the full width half maximum (FWHM) of the pulse is approximately 900 ps, to 10 ns. In our previous experiments we found that half-select switching was more reliable when the word pulse turned on during the digit pulse [59]. Other observations [53] and simulations [46] also indicate that the switching is faster when the hard-axis pulse precedes the easy-axis one. In order to achieve fast and reliable switching the pulse timing here is chosen such that the digit pulse arrives one nanosecond before the word pulse, with both pulses ending simultaneously. The word pulse duration is controlled in 250 ps steps by attaching different length charge lines to the back of the pulser. The duration of the digit pulse can be varied in 1 ns steps. The word pulse attenuation can be varied in the range from 0 to 22 dB in discrete steps of 1 dB, producing magnetic field pulses ranging from 5.8 to 73 Oe. The digit pulser is able to produce both positive and negative voltage pulses from -5 to 5 V in 100 mV steps, covering the range of the pulse strengths from -60 to 60 Oe. A reset pulse of fixed -14 V amplitude and duration of 10 ns produces a strong field pulse of -250 Oe sufficient to restore the initial magnetization state.

In order to explore the time-resolved switching diagram we measure Time-Amplitude (TA) scans similar to Fig. 4-6 *a*, for different values of the word pulse attenuation. Again, the laser spot is focused near the center of the element positioned closest to the center of the wire intersection. TA diagrams for two particular word field values, 19 Oe and 34 Oe, are illustrated in Fig. 4-12. Both easy- and hard-axis longitudinal Kerr signals are represented by

linear grayscale in the corresponding subplots, when black represents the initial (unswitched) state, and white is fully switched. The black stripe in the middle of the scans (a,e) for the Kerr X signal shows non-switching by the word pulse unassisted by digit pulse, while the gray area around it corresponds to a half-select switching regime. As expected, (b,e), the “non-switching” band is narrower for the stronger word pulse. Also, as expected, the Kerr Y signals have opposite polarities for opposite directions of the applied hard-axis field.

A surprising result, however, is contained in the easy-axis magnetization behavior. Depending on the sign of H_y , M_x plateaus at different levels during the pulse. In order to demonstrate this strange feature more clearly, the cuts of the TA scans at ± 60 Oe are shown in the Figure (4-12 c, d, g, h). M_x plateaus during the word pulse below its final level achieved at 30 ns for negative values of H_y ; and *above* the final level for positive ones. One hypothesis to explain this behavior will be presented below.

More TA scans are shown in Fig. 4-13. All scans demonstrate the same qualitative behavior as in figure 4-12: an asymmetric plateauing of the M_x component at the pulse duration, and widening of the unswitched stripe with decreasing of H_x amplitude. The final state of M_x is nearly saturated for the strongest easy-axis field value of 38 Oe.

The fact that M_x plateaus below the final level makes it difficult to reasonably define the switching time. To construct switching diagrams we decided to measure the level of the plateau at 70% of the easy-axis pulse duration, consistently for different values of the pulse duration. The other most important value is the final level of magnetization long after the pulse is gone. This is recorded at 20 ns after the word pulse leading edge. In order to change the polarity of the applied pulse we detached and switched the indium wires at the contact pads, thus flipping the direction of current and consequently the direction of the magnetic field. The digit wires were not flipped. The resulting evolution of the diagram of the plateau level during the pulse is demonstrated

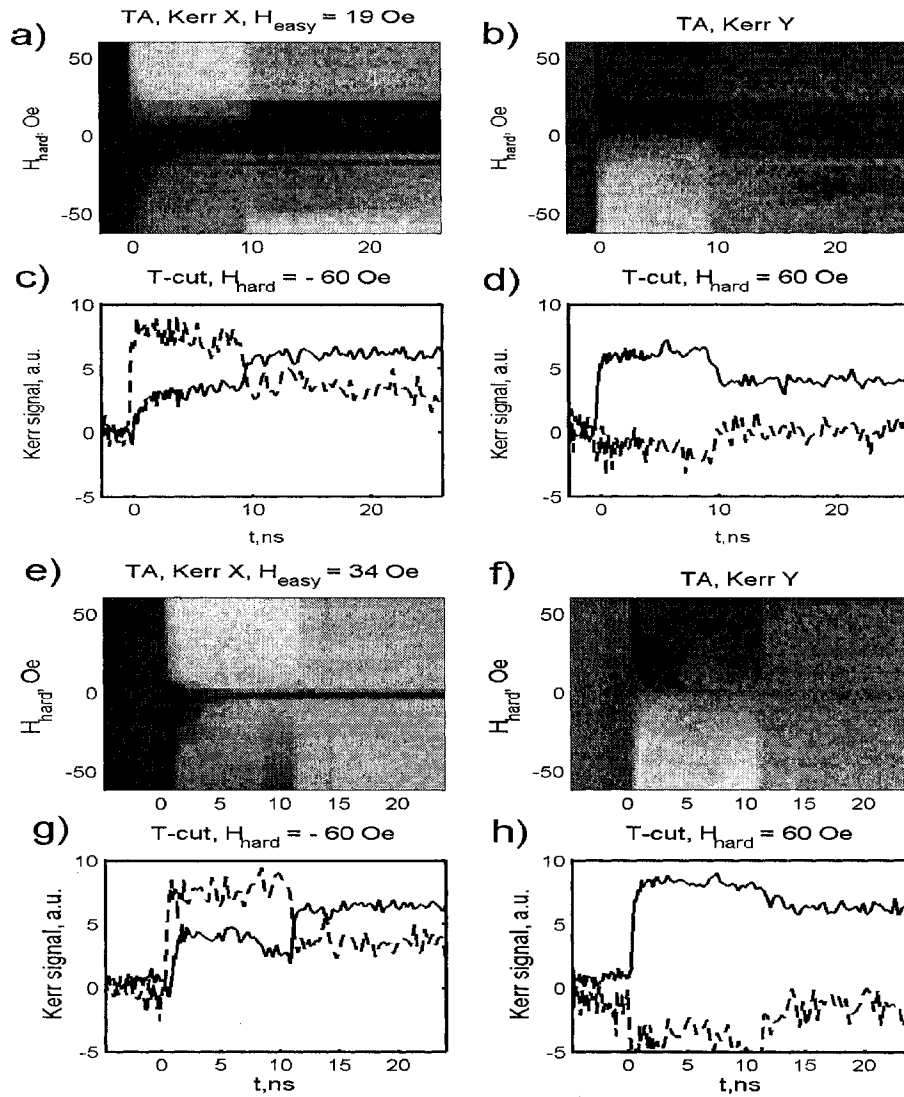


Figure 4-12: Time-amplitude scans for different values of the word field pulses: 19 Oe (a,b) and 34 Oe (e,f). The vertical axis corresponds to the digit pulse strength H_{hard} , horizontal axis to the time in nanoseconds. Grayscale represents the value of the Kerr signal. (c,d) The cuts of the TA scans (a,b) at $H_{hard} = -60$ and $+60$ Oe respectively. Solid line represents M_x , dashed line – M_y . (g,h) Analogous cuts of the TA scans (e,f).

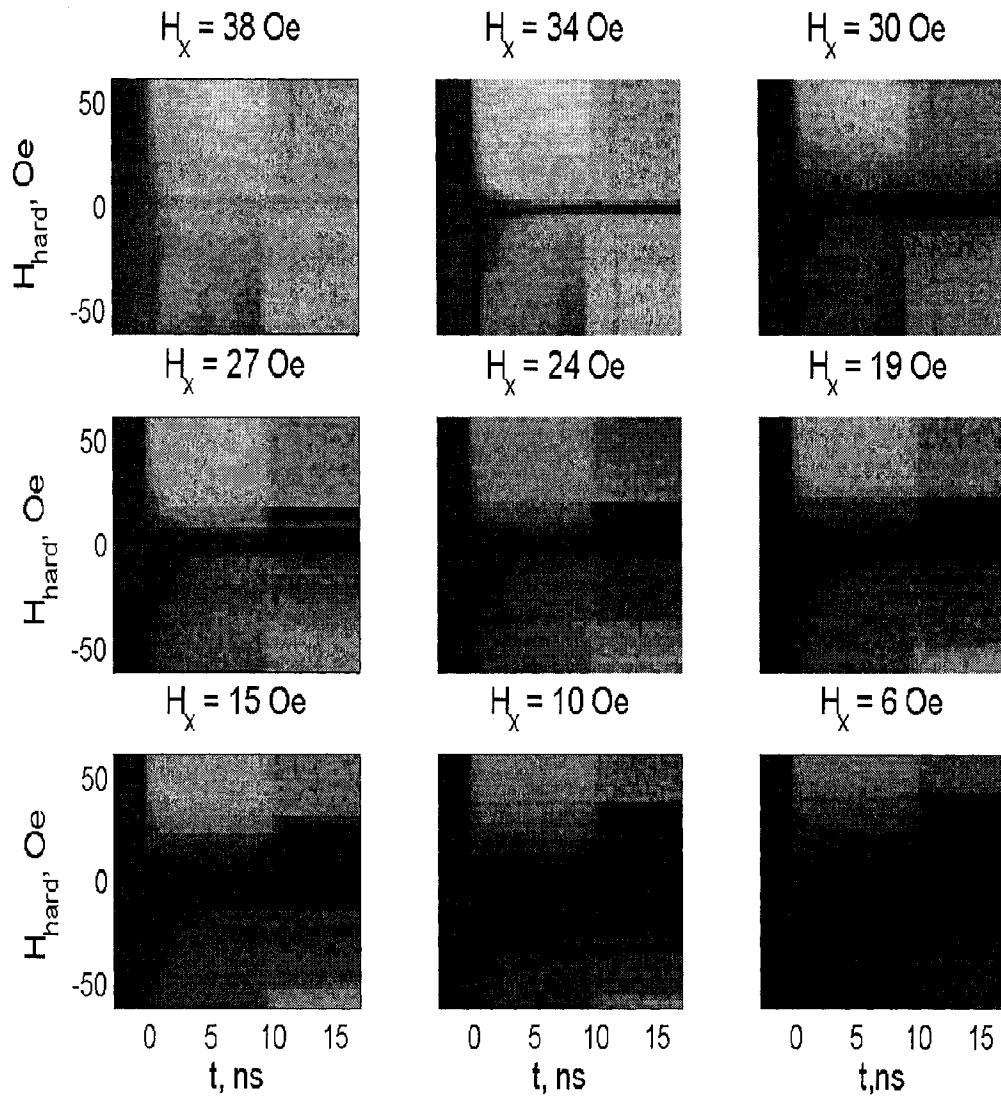


Figure 4-13: TA scans for different values of the easy-axis pulse strengths. The grayscale represents the easy-axis Kerr signal, and it is normalized to the saturation levels for all plots.

in Fig. 4-14. Not only is the signal asymmetric with respect to the direction of H_y , but it is also antisymmetric with respect to the direction of H_x .

The origin of this antisymmetry remains mysterious at this point, but we discuss it in terms of an hypothesis that the uniaxial anisotropy induced during the deposition of the film does not coincide with the long axis of the sample. If the anisotropy axis is tilted, resulting in an S-state of magnetization (Fig. 4-15), one can see that a positive hard-axis field enhances the reversal of the sample magnetization, while negative H_y suppresses it, when the sample is initially magnetized to the right. For a left-magnetized sample the opposite scenario takes place. (Fig. 4-15 also reflects schematically the higher reluctance of the sample edge magnetization to switching, a subject we discuss in the next section.) In micromagnetic simulations we have incorporated a uniaxial crystalline anisotropy axis of permalloy tilted 15° with respect to the long axis of the ellipse and observed different switching scenarios for negative and positive H_y pulse application. However, these simulations are not in quantitative agreement with the experiment. It remains to be seen whether such antisymmetric switching will be a feature often observed in experiment.

Note that in Fig. 4-14 the switching diagram shrinks in the easy-axis direction at longer times. The longer the pulse duration, the narrower and more symmetric the diagrams become as the switching field has more time to flip the magnetization.

The final-state “astroid” diagrams [49] measured 20 ns after the beginning of the easy-axis pulse for different pulse durations are shown in Figure 4-16. Several features must be noted. First, even the shortest pulse (≈ 900 ps FWHM) is sufficient for complete and reliable half-select switching. Second, switching astroids shrink in the easy-axis direction as the pulse duration increases, as longer pulses are better able to switch the magnetization. This reflects the well-known decrease of dynamic coercivity with increasing pulse duration [81]. Beyond the easy-axis pulse duration of 5 ns, the diagram stays

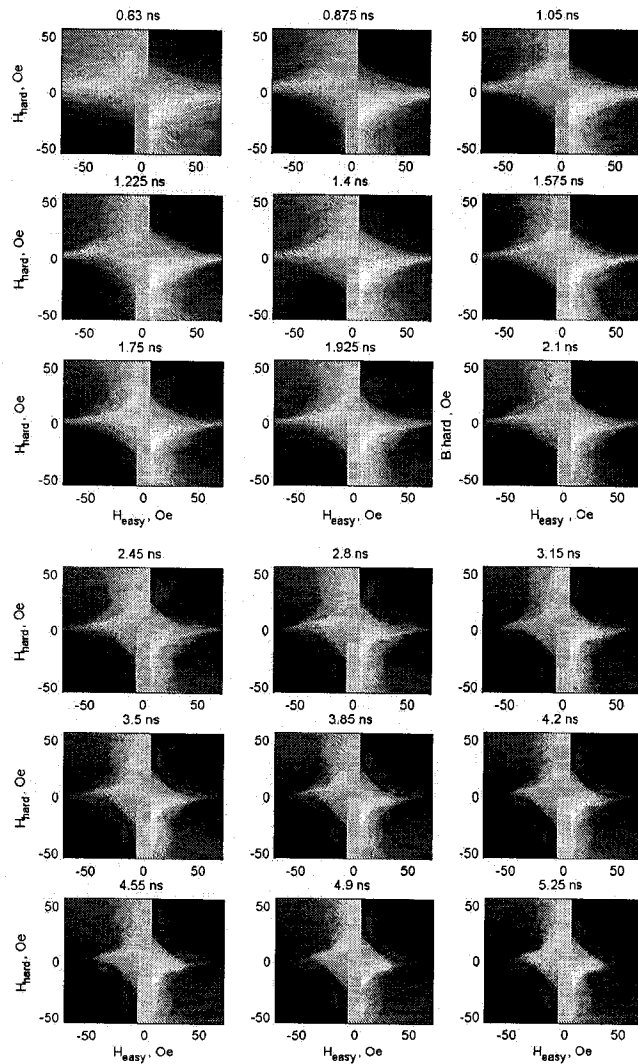


Figure 4-14: Switching easy-axis magnetization diagram evolution during the pulse. Subplot titles indicate the time during the pulse when the signal was measured. The gray scale represents the value of the easy-axis magnetization (white – unswitched, black – switched). No data points are taken below 5.8 Oe of the easy-axis field (plain gray stripe in the middle of every diagram). Easy axis pulse durations are indicated in the subplot titles.

virtually unchanged for longer pulses. Third, for weak easy-axis fields an “incomplete” switching is observed (gray area at the plots). A likely reason is vortex state formation at the center of the sample. This regime should be avoided in technological applications. Stronger easy-axis fields are able to expel the vortex (or prevent its nucleation) and end up in a completely switched state. Finally, in some cases of longer pulses of 5 ns in duration and above “pockets” of switching appear (local spots of switching in the diagram, surrounded by unswitched regions). This might be an indication of the complex structure predicted in the simulations [50]. The astroid-like diagrams look almost symmetric, but a little antisymmetry is still present in the fine details of these maps of the final magnetization state.

4.2.3 Sample edge reluctance to switching.

In this section we consider aspects of the spatial variation of the magnetization during a switching process.

The spatially resolved history of half-select switching by a 5 ns 40 Oe word, 30 Oe digital pulse pair is shown in the figure 4-17. Two ellipses placed at the wire intersection switch simultaneously. The switching starts in the center of each ellipse and then the switched area expand over the sample, while the edges are reluctant to switch. The reluctance of the sample edge to switching has been observed previously [48] and is also manifested in micromagnetic calculations [51]. This switching scenario is similar to previously observed switching in presence of static magnetic field [53]. One can notice here that the elongated switched central area itself is tilted with respect to the long axis of the ellipses (see, in particular, Fig 4-17, 0.2ns). We will see the same phenomenon in the simulations about to be discussed. Two independent elements exhibit very similar switching histories, achieving almost complete switching in just 0.6 ns after the arrival of the word pulse.

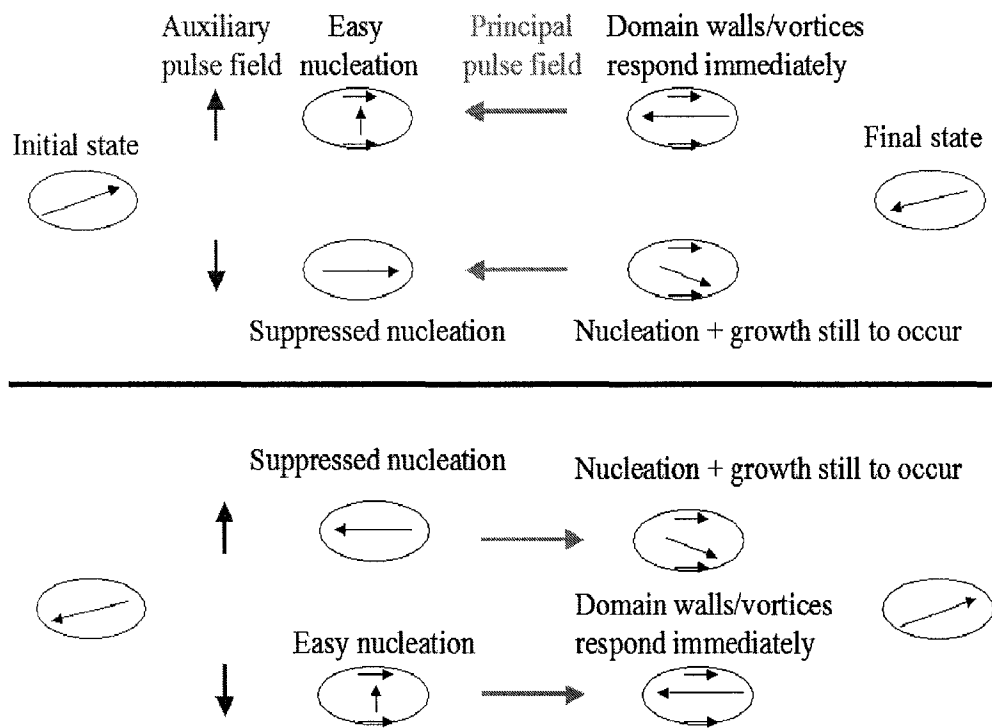


Figure 4-15: Cartoon schematic of different switching scenarios for opposite initial magnetizations of a sample in the “S” magnetization state to illustrate the possibility of antisymmetric diagrams during the switching process.

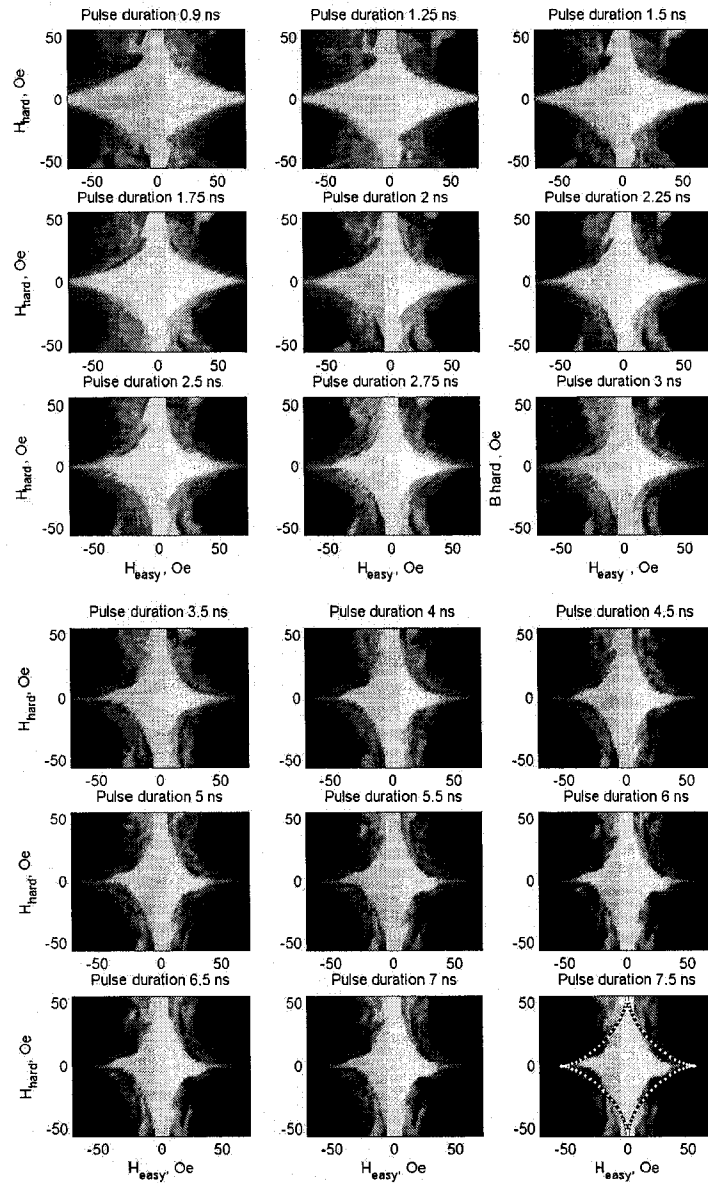


Figure 4-16: Switching diagrams for different easy-axis pulse durations. In all cases the digital pulse precedes the word pulse by one nanosecond and both pulses end at the same time. The gray scale represents the value of the easy-axis magnetization (white – unswitched, black – switched). No data points are taken below 5.8 Oe of the easy-axis field (plain gray stripe in the middle of every diagram). Easy axis pulse durations are indicated in the subplot titles. The last diagram also shows the theoretical Stoner-Wolfarth astroid.

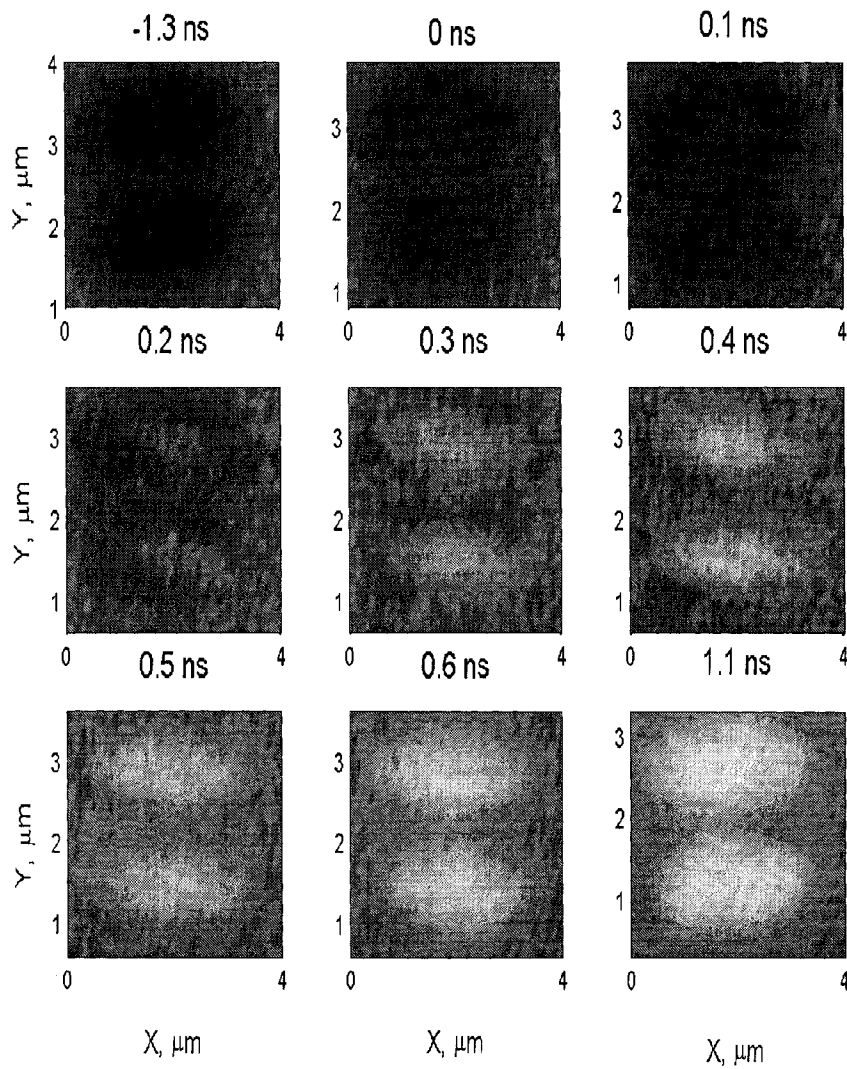


Figure 4-17: Time-resolved history of switching of the two elliptical samples at the intersection of the crossed wires, by the combined action of word and digit magnetic field pulses in the half-select regime. The time is clocked from the beginning of the word pulse, the digit pulse arrives 1 ns before the word pulse. Nucleation starts in the middle of both samples and propagates towards the edges.

4.2.4 Edge reluctance (simulations).

The aforementioned switching is induced by relatively slow rising digit and word pulses (250 and 300 ps rise time respectively). However, Hiebert [48] has observed the same effect in coherent precessional motion regime (in much bigger, $20 \times 10 \mu m$ elliptical samples). Since the ultimate goal of this work is to investigate the precessional switching, we ought to know what one can expect in the coherent regime as well. Both coherent and incoherent switching were modeled using the micromagnetic Simulator. An easy way to induce precessional motion is an application of fast-rising hard-axis field [48],[12],[13],[82],[83]. The theory states that the hard-axis field induces an initial tilt of the magnetization out of XY-plane, which in turn generates a strong out-of-plane demagnetization field, that eventually causes an in-plane coherent precession. For the precessional motion simulations we used the magnetic constants of the thin film permalloy: $M_s=800 \text{ emu/cm}^3$, $K_u2 = 1000 \text{ erg/cm}^3$, $A=1.05 \mu\text{erg/cm}$, uniaxial anisotropy aligned with the long axis of the ellipse. For the half-select switching simulations we assumed that the uniaxial anisotropy axis of the permalloy film does not coincide with the long axis of the ellipse, but is tilted 15° with respect to it in attempt to simulate the antisymmetry of the switching diagrams.

Several switching scenarios are illustrated in Fig.4-18. Simplified magnetic field pulse shapes (Fig. 4-18 *a*) were used in these simulations to model the magnetic response to fast- and slow- rise time currents produced by pulse generators. The evolution of the easy-axis magnetization component during and after the field pulses is shown in the Fig. 4-18 *b – d*. Figure 4-18 *b* corresponds to the simulated precessional switching caused by a short, fast-rising digital pulse (Fig 4-18 *a*, solid line) of 140 Oe of magnitude. Notably, two oscillations of magnetization occur during the field pulse, however, the sample edges demonstrate reluctance to the switching. The central magnetization

of the sample is reversed at the end of the pulse (0.65 ns), but the strip of switched material narrows after the pulse (1.2 ns), and breaks (1.5 ns). One of the ends of this broken band eventually disappears and the other forms a vortex near the edge of the sample. The details of this band breaking process vary from one run to the next even when started from the same initial state in these final temperature simulations. In some runs the broken band forms two vortices at the opposite ends. This irreproducible shot-to-shot behavior cannot be observed by the existing stroboscopic TR-SKM technique.

A stronger 300 Oe fast pulse (Fig. 4-18 *c*) causes three precessional rotations of the magnetization of the central part of the sample during the pulse. At the end of the pulse (0.85 ns) a wider band of the switched material is formed. After the pulse this band initially narrows (1.5 ns) and then starts to widen again forming two vortices that propagate slowly towards the ends of the sample. Here the magnetization ends up in a mostly-switched double-vortex state. The key reason for switching is the correct phase of the oscillation at the end of the pulse. Analogous simulations conducted for 250 Oe and 350 Oe pulse amplitude wind up in an unswitched state (similar to Fig. 4-18 *b*). It is also important to note that although the 300 Oe pulse drives the sample into almost coherent precession during the first half period of rotation (Fig. 4-18 *c*, 0.15 ns), the edges of the sample still remain unperturbed.

Figure 4-18 *d* and *e* show the magnetization change under influence of simultaneously acting easy- and hard- axis field (dashed and dash-dotted lines respectively in the Fig. 4-18 *a*). Pulse rise times are 300 and 250 ps respectively, the digital pulse starting one nanosecond prior to the word pulse and both pulses are terminated simultaneously. Figure 4-18 *d* shows the effect of positive 35 Oe word pulse and negative 60 Oe digital pulse (corresponding to the lower part of the astroid). A stripe of the switched material moves to one side of the ellipse effectively reversing the edge magnetization and quickly forming a single vortex that later propagates towards the center of the sam-

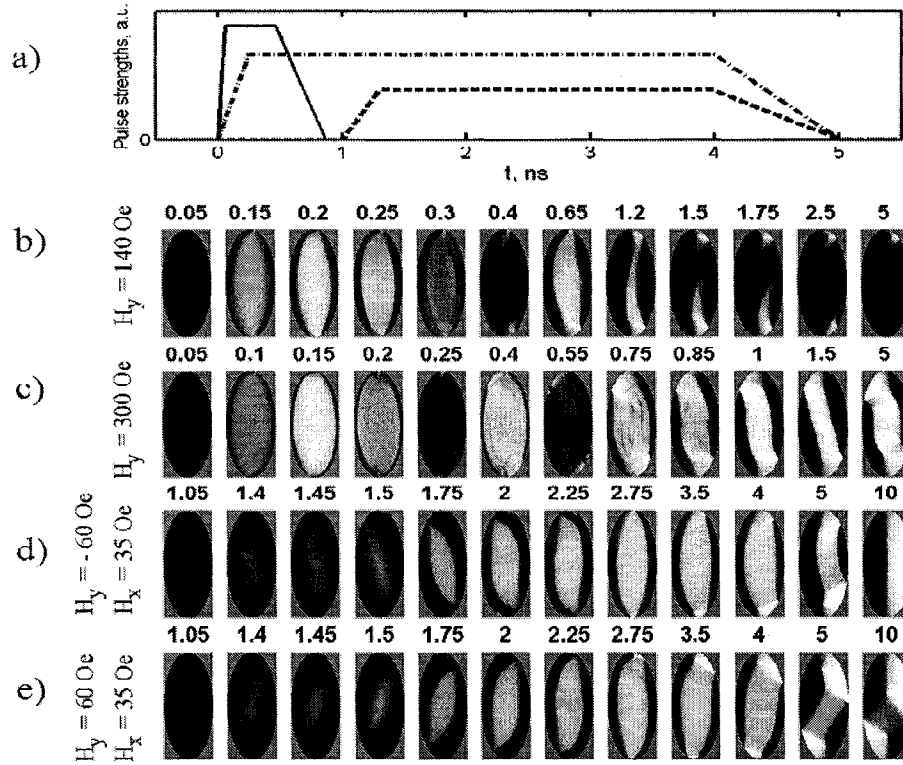


Figure 4-18: Simulated switching histories for $3 \times 1 \mu m$ ellipses for different word and digital magnetic pulse profiles. (a) Simple pulse profiles used in the simulations. Linear rise time / plateau duration / linear fall time are as follows: 60/400/400 ps for a fast digital pulse (solid line); 250/3750/1000 ps for a slow digital pulse (dash-dotted line); and 300/2700/1000 ps for word pulse. The word pulse lags one nanosecond behind the digital pulse. (b) Coherent rotation caused by fast digital pulse of 140 Oe of amplitude and formation of a vortex after the end of a pulse. The grayscale represents the magnetization parallel to the long axis of the ellipse in all plots below. The numbers at the top of the subplots indicate the time passed from the beginning of the digital pulse in nanoseconds. (c) The same as (b) for a stronger 300 Oe digital pulse. A band of switched material and two vortices are formed after the pulse. (d) Incomplete switching by a slow negative digital pulse of -60 Oe combined with a word pulse of 35 Oe in the half-select regime. In this simulation the crystalline anisotropy is tilted fifteen degrees with respect to the long axis of the ellipse. A single vortex at the center of the sample is eventually formed. (e) The same as (d) for a positive 60 Oe slow digital pulse and the same word pulse. Incomplete switching resulting in a double-vortex state.

ple. On the other hand, a positive digital pulse combined with the same word pulse (the top part of the astroid, Fig.4-18 e) causes formation of double-vortex state with a diamond-shaped region magnetized along the short axis of the ellipse. In both cases the net easy-axis magnetization of the sample is nearly zero (corresponding to the gray areas of the astroids in the figure 4-16). Again, in both cases edge reluctance (observed experimentally, 4-17) appears during the pulse. The edge reluctance in the simulation appears to be stronger than observed in the experiment, as these particular field values correspond to complete switching regime (black area of the astroids shown in the Fig.4-16). This effect might be a consequence of the lift-off lithographic process. Thin film samples patterned by lift-off are thinner at the edges than in the middle, which can reduce the edge reluctance. All simulations are performed for uniform thickness of the sample.

The edge roughness seems not to be a factor, as refining the discretization in our simulations had little effect on the switching scenarios. We also tried to make the central area of the sample narrower (a $3 \times 1 \mu m$ dumbbell-shaped specimen, Fig. 4-19) in order to ease the edge switching. When perturbed by a fast-rising 250 Oe hard-axis field pulse, it demonstrated similar reluctance to the switching, and similar general scenario of the magnetization evolution to the elliptical samples (precessional oscillations during the pulse, switched band formation after the end of the pulse, band breaking, formation of a vortex). The edge reluctance appears to be a generic property of small thin-film elements, and deserves serious attention in designing new MRAM elements, although it is likely to be less pronounced for smaller elements.

In order to characterize the effect of the sample size on the precessional switching scenario, we ran several simulations on elliptical samples with the same 2×1 aspect ratio of two longer axes and proportionally scaled down size. The material of choice is again permalloy, the easy axis of the crystalline anisotropy is chosen along the long axis of the ellipse. The sample initially

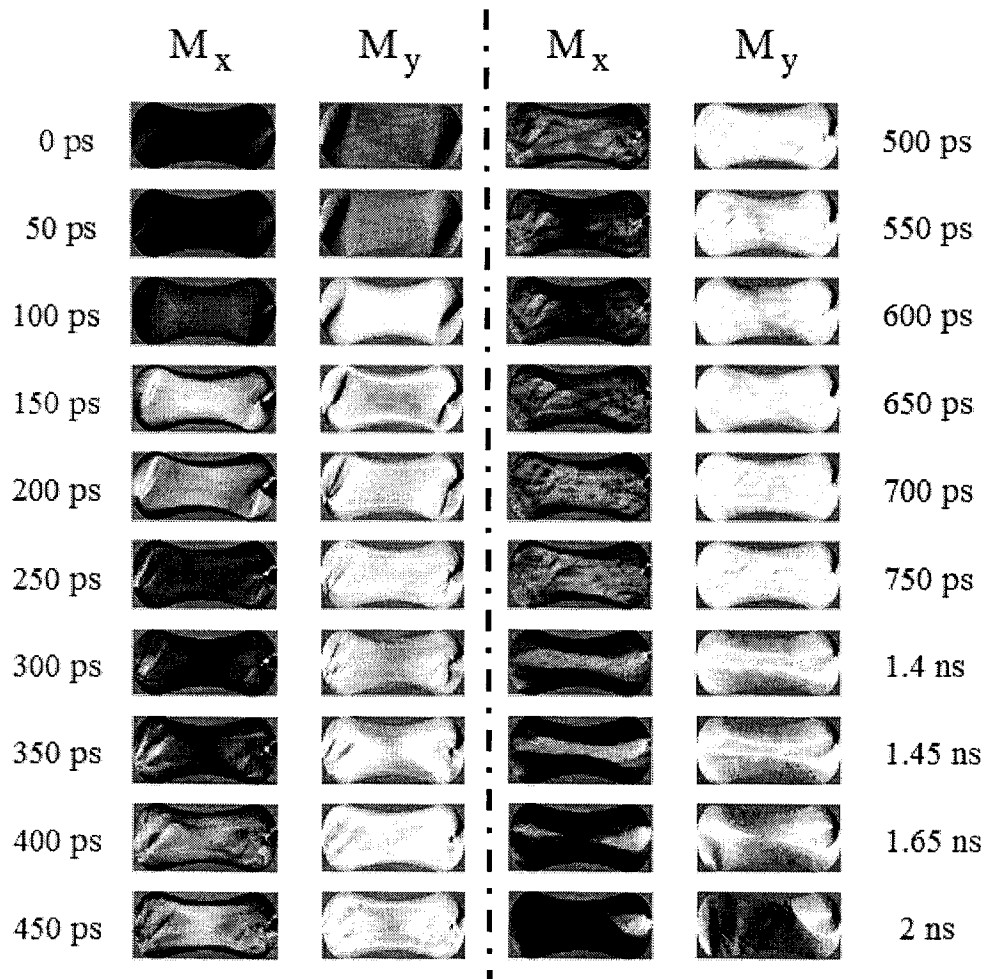


Figure 4-19: The edge reluctance to switching in a dumbbell-shaped sample perturbed by a fast hard-axis field pulse (Fig.4-18a, solid line) of 250 Oe. The numbers indicate the time from the pulse beginning.

uniformly magnetized along the easy axis stays unperturbed for 500 ps in order to find the equilibrium state, and then is subjected to the hard-axis fields to model a precessional switching. The field H_y linearly rises from zero to 300 Oe in 60 nanoseconds, and then stays at that level. Simulation results are shown in figures 4-20 and 4-21. Precessional motion of the sample magnetization results in oscillations of both M_x and M_y components. Five temporal shots are shown for each sample size: before the switching effectively begins; at quarter period of the first oscillation; at half period (the first maximum of M_x); at three quarters of a period; and at the completion of the first oscillation.

Several switching regimes are observed. First (Fig. 4-20), the edge reluctance is prominent in bigger samples ($2048 \times 1024 \times 16 \text{ nm}$ and $2048 \times 1024 \times 8 \text{ nm}$). The switching scenarios of scaled down samples $1024 \times 512 \times 8 \text{ nm}$ and $1024 \times 512 \times 4 \text{ nm}$ are very similar to $2048 \times 1024 \times 16 \text{ nm}$ and $2048 \times 1024 \times 8 \text{ nm}$ samples respectively. This is to be expected, as the demagnetizing factors of ellipsoids depend only on the ratio of the ellipsoid's axes but not on the size. Scaling fails however, with the next factor of two reduction of size: $512 \times 256 \times 4 \text{ nm}$ and $512 \times 256 \times 2 \text{ nm}$ start the precession almost coherently, yet the phase difference between the edges and the center of the sample accumulates over time and appears quite pronounced at 3/4 of a period. The size of the sample is closer to the width of a Néel wall, and the wall energy is closer to the rest of the energy terms. A thicker $512 \times 256 \times 8 \text{ nm}$ sample does demonstrate the reluctant edges behavior, as the energy density of a Néel wall decreases with the film thickness (cf. Fig. 1-9).

With further reduction of size (Fig. 4-21) magnetization changes become more coherent, and the sample's coercivity or stiffness reaches its maximum value as seen on the example of a $256 \times 128 \times 8 \text{ nm}$ structure: the easy-axis magnetization M_x does not change sign, but rings around its original direction with some phase variations across the sample. The thinner $256 \times 128 \times 4 \text{ nm}$ structure reaches a higher value of M_x during the pulse and the thinner yet

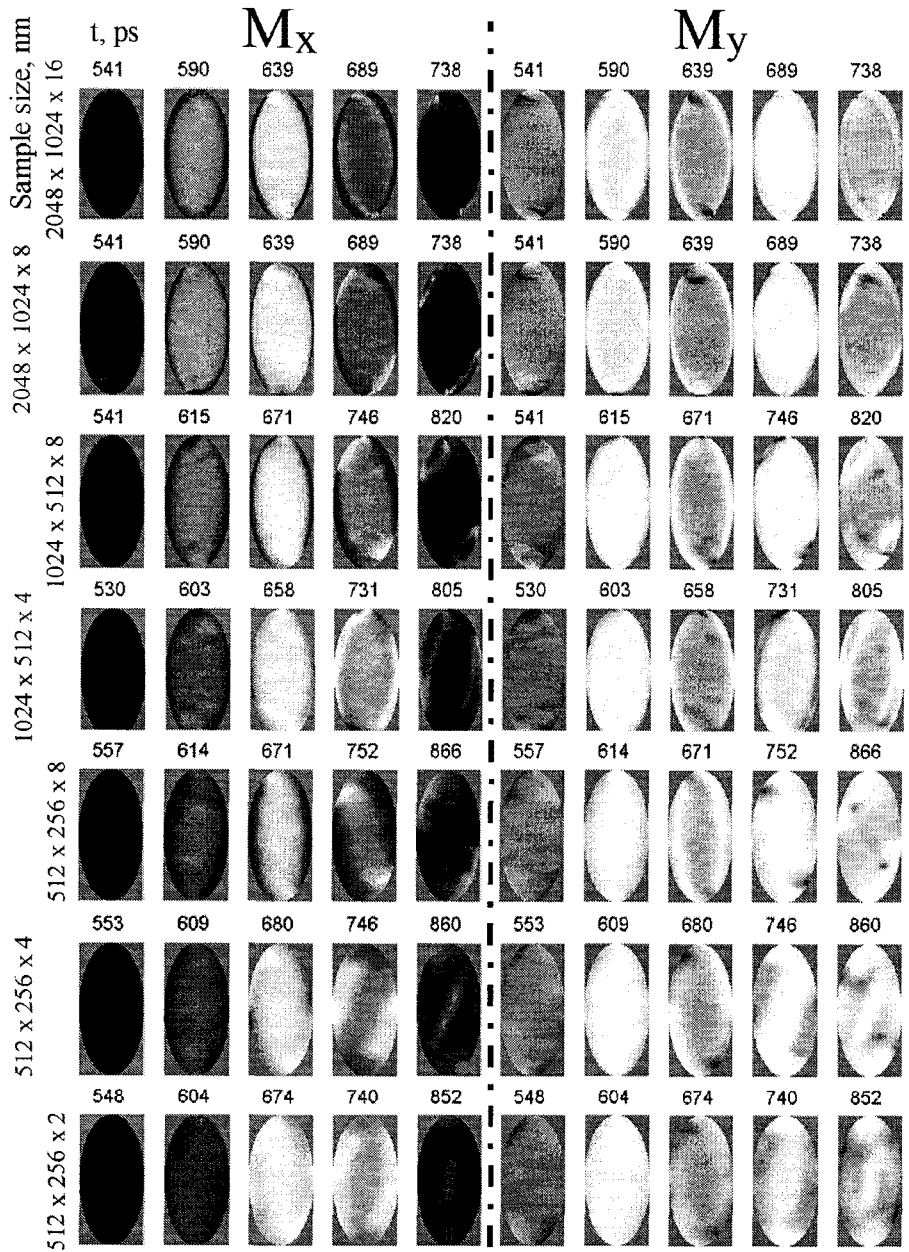


Figure 4-20: In-plane magnetization shots for thin-film elliptical samples with aspect ratio 2×1 of various thicknesses subjected to 300 Oe hard-axis field. The shots are taken before the pulse (≈ 500 ps); at quarter period of precession, at the first maximum of M_x , ≈ 680 ps), at $3/4$ period and at the first minimum of M_x . Linear greyscale spans from -1 to 1.

$256 \times 128 \times 2$ nm sample completes a precession period as switching becomes thermally assisted at 300 K and effective magnetic stiffness of the sample decreases. Some bending of magnetization across the sample is evident.

The very smallest sample we attempted to investigate was a 128×64 nm ellipse. At 4 nm thickness the sample stiffness is significant, the magnetization completes half of the precessional period as a single-domain particle, and then rings around the switched magnetization direction. Thinner structures $256 \times 128 \times 2$ nm and $256 \times 128 \times 1$ nm exhibit a clean single-domain precession.

4.2.5 Precessional switching.

In this section we discuss an experimental observation of precessional switching of the same 3×1 μm elliptical element.

In this experiment we use two pulse sources: a 10 V pulse of 50 ps rise time propagating down the DW for precessional rotation experiment; and an attenuated 50 V pulse with 250 ps rise time (in combination with the fast one) for half-select switching (see schematic pulse profiles in the inset of Fig. 4-26). The temporal resolution of the system is limited to 200 ps by electronic delay generator jitter. We also used an optical delay line, for which the jitter constraint is that of the pulser itself, approximately 2 ps) for the half-select switching experiment. A limited scan range of 3.5 ns is the only disadvantage of the latter method.

Precessional motion of the magnetization caused by Digital Pulses of different amplitudes is shown in Fig.4-22. Easy-axis (Kerr X) magnetization signal is normalized to the saturation levels, measured separately by applying a strong easy-axis pulse (Fig. 4-26 a). The out-of plane (Kerr Z) signal is not normalized. All traces demonstrate clear oscillatory character and $\pi/2$ phase shift of Kerr Z signal with respect to Kerr X. At the strongest pulse amplitude of 140 Oe (Fig. 4-22 a), the magnetization completes two oscillations before

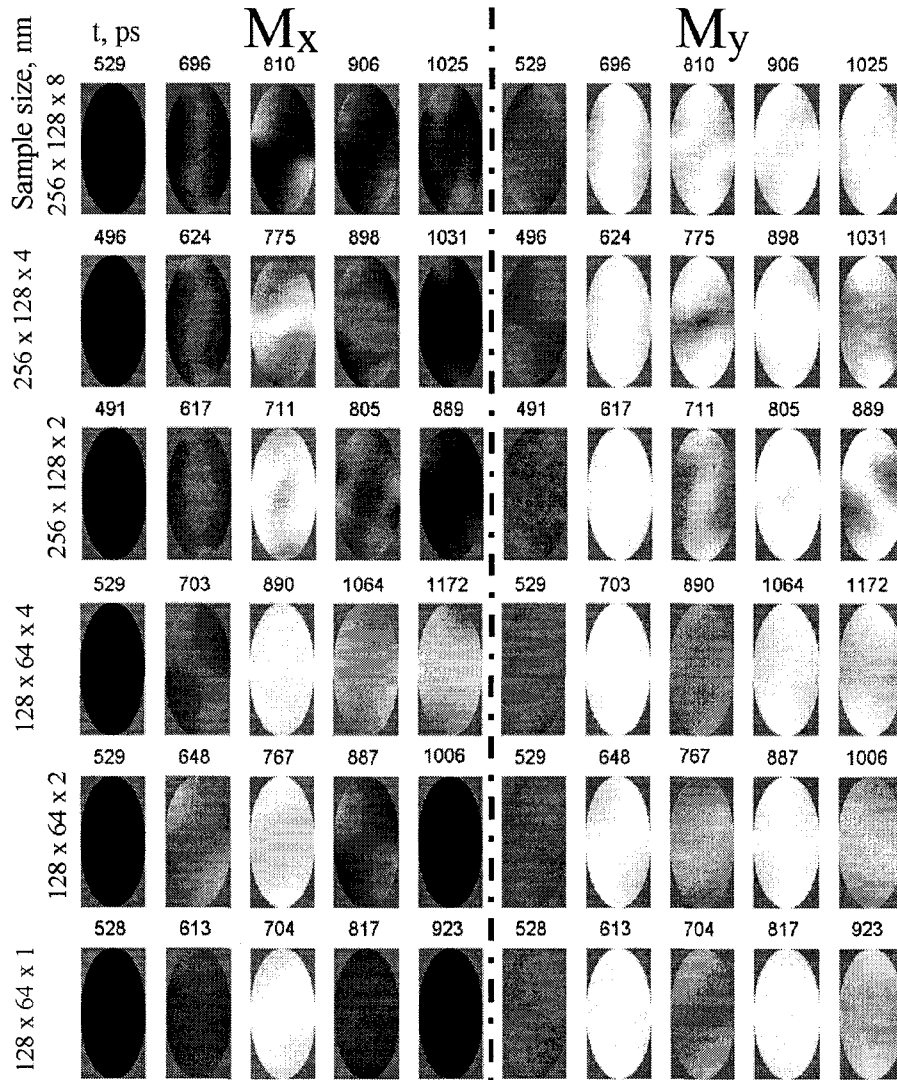


Figure 4-21: (Continued) In-plane magnetization shots for thin-film elliptical samples with aspect ratio 2×1 for smaller samples. Same field as in Fig. 4-20. Shots taken before the pulse, at quarter, half, three quarters and full period.

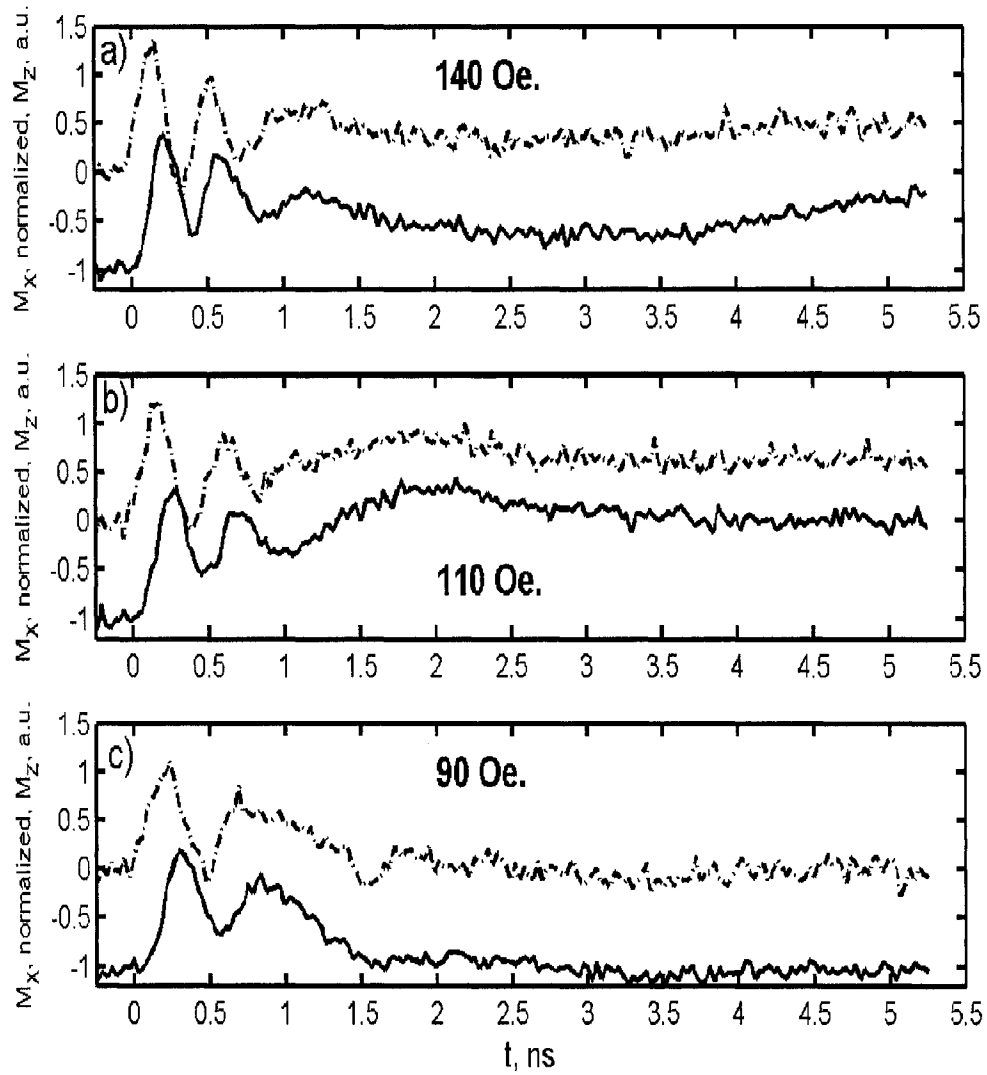


Figure 4-22: Coherent rotation of magnetization components by fast hard-axis magnetic field pulse of different amplitudes (a-c). The pulse profile is shown schematically at the inset of the Fig. 4-26. For all graphs, solid and dash-dotted lines represent easy-axis (X) and polar (Z) components of the Kerr signal respectively.

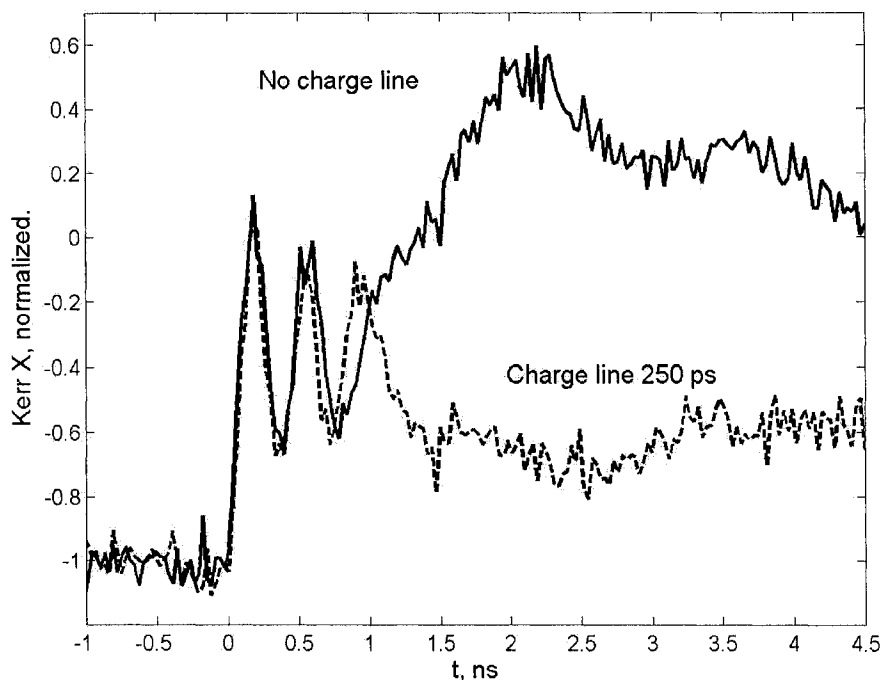


Figure 4-23: The effect of the hard-axis pulse duration on the final state of the easy-axis magnetization. Pulse durations of ≈ 600 ps FWHM (solid) and 850 ps (dashed).

the pulse ends. Following the end of the pulse, M_x decreases towards the initial (unswitched) state, and then *increases* almost to the zero net magnetization level over three nanoseconds. For the weaker 110 Oe pulse (Fig. 4-22 b) M_x does not complete two oscillations and stays at higher magnetized state after the pulse terminates. Over a longer time scale, the net magnetization runs through a maximum and then *decreases* – again, to nearly zero level. Interestingly the final state of M_x evolution caused by 125 Oe pulse (not shown) is also close to this magic 50% (zero) level). For weaker yet 90 Oe pulse (Fig. 4-22 c), the magnetization relaxes to its initial state after the pulse; this is a suitable candidate amplitude for half-select switching.

If the pulse is terminated in the right phase of the oscillation, the sample magnetization has better chance to remain in switched state (Fig. 4-23). Easy-axis magnetization traces driven by hard-axis pulses of the same amplitude of 110 Oe that differ only in duration by 250 ps virtually coincide during the pulse duration but end up in very different states when upon the pulses' termination. Later, though, the gap between magnetization levels start to close, presumably due to the vortex formation.

Simulated evolutions of all three components of magnetization for a 140 Oe pulse are shown in Fig. 4-24 (it is the same simulation shown in Fig 4-18 *b*). The easy-axis magnetization (top row of ellipses) behavior is discussed in the previous section. Only the central part of the sample switches easily (Fig. 4-24, 200 ps and 650 ps), while the sample edges are reluctant to reverse. This explains the fact that M_x does not reach the positive saturation level (Fig. 4-22).

The behavior of the hard-axis and out-of-plane magnetization components is also very interesting. Note that M_y doesn't turn negative until the vortex is formed. The magnetization here does not precess in the XY plane around a strong induced demagnetization field. Rather, it exhibits an oblate (flattened by demagnetization) XZ rotation around the applied field.

Comparison of our experimental results with simulation is shown at Fig. 4-25. The experimental Kerr X signal for 140 Oe pulse is normalized to saturation levels as at Fig. 4-22 *a*, no other fitting parameters are used for comparison of Kerr X and simulated M_x (all magnetic constants used for the simulation are those of the thin film permalloy). The simulated M_z was multiplied by fifteen in order to fit unnormalized Kerr Z signal. Figures Fig. 4-25 *b* and *c* show the XZ precession of magnetization, experimental Kerr Z signal vs Kerr X and simulated M_z vs M_x respectively.

Finally, we consider the half-select regime where the fast digital pulse is assisted by a slow word pulse (Fig. 4-26, inset) in order to accomplish switching.

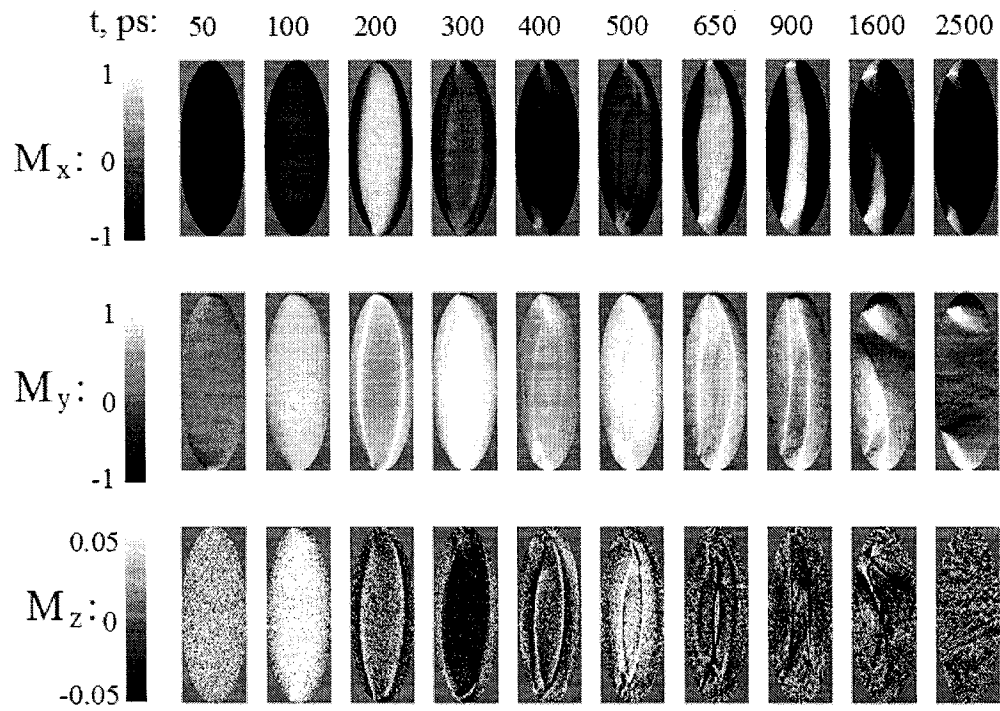


Figure 4-24: Simulated distribution of magnetization for precessional oscillations for a fast 140 Oe hard-axis field pulse (corresponding to the trace shown at Fig. 4-22 *a*). Movie shots are taken at indicated moments. Note, that the out-of-plane component of magnetization does not exhibit full swing from -1 to 1, but rather it is suppressed by shape anisotropy.

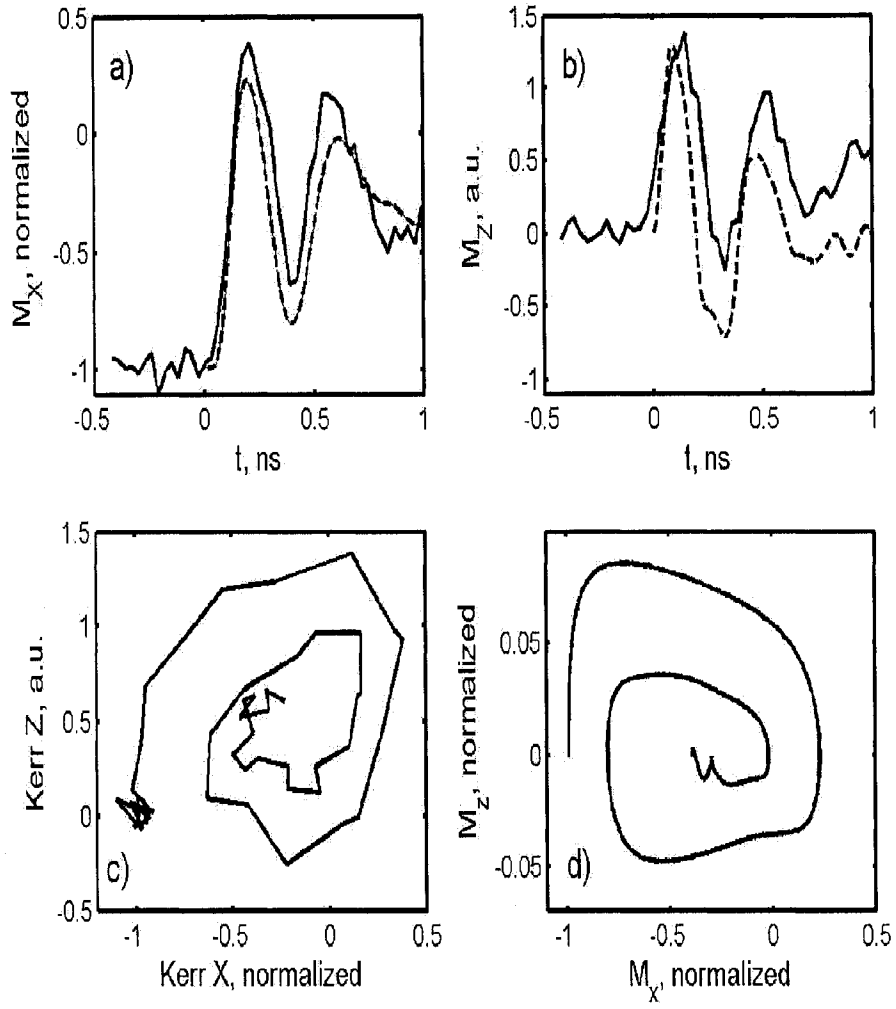


Figure 4-25: Comparison of experimental and simulated temporal traces of in- and out- of-plane magnetization components. (a) Experimental Kerr X signal normalized to the saturation levels (solid) vs corresponding simulated M_x component (dashed); (b) experimental Kerr Z signal (arbitrary units, solid) vs simulated M_z multiplied by fifteen times to fit the experimental data (dashed); (c) Kerr Z vs Kerr X signal – experiment; (d) Corresponding M_z vs M_x plot – simulation.

The top (dash-dotted) graph of Fig. 4-26 shows an incoherent switching of the easy-axis magnetization by a strong easy-axis field, to determine the saturation levels. The two bottom plots correspond to the half-select regime. As we saw before, the 90 Oe digital pulse leaves the magnetization in its initial state. The Word pulse of 40 Oe does not switch the sample magnetization either (Fig. 4-16, 0.9 ns). However, the combined action of the two results in complete ultra-fast switching (180 ps 10-90%). Evidently, the word pulse is able to prevent vortex formation. Moreover, if the pulses are properly timed (Fig. 4-26, middle graph), ringing [84] is suppressed (and virtually non-existent after 0.5 ns after the fast pulse leading edge). If the word pulse is deliberately delayed by 170 ps (roughly half of the oscillation period at Fig. 4-22 *c*), ringing becomes pronounced, although half-select switching still takes place.

In conclusion, we observed a new regime of precessional rotation of magnetization (XZ precession), and confirmed it through micromagnetic simulations. We also observed a reluctance of the sample edges to switching, leading to formation of a vortex state. However, a relatively weak easy-axis pulsed field effectively prevents formation of the vortex and assures complete ultra-fast (180 ps) half-select switching of the sample between remanent magnetization states. Proper timing of digital and word pulses eliminates ringing

4.3 Chapter summary.

In this chapter we conducted a detailed time-resolved study of the switching of micron-sized thin film ferromagnetic elements between remanent states in crossed wire geometry. A new type of cross-wire element (angled crossed wire) is suggested and characterized. This element demonstrated more reliable half-select switching than conventional cross element.

The effects of the pulses' strength and duration in half-select regime are

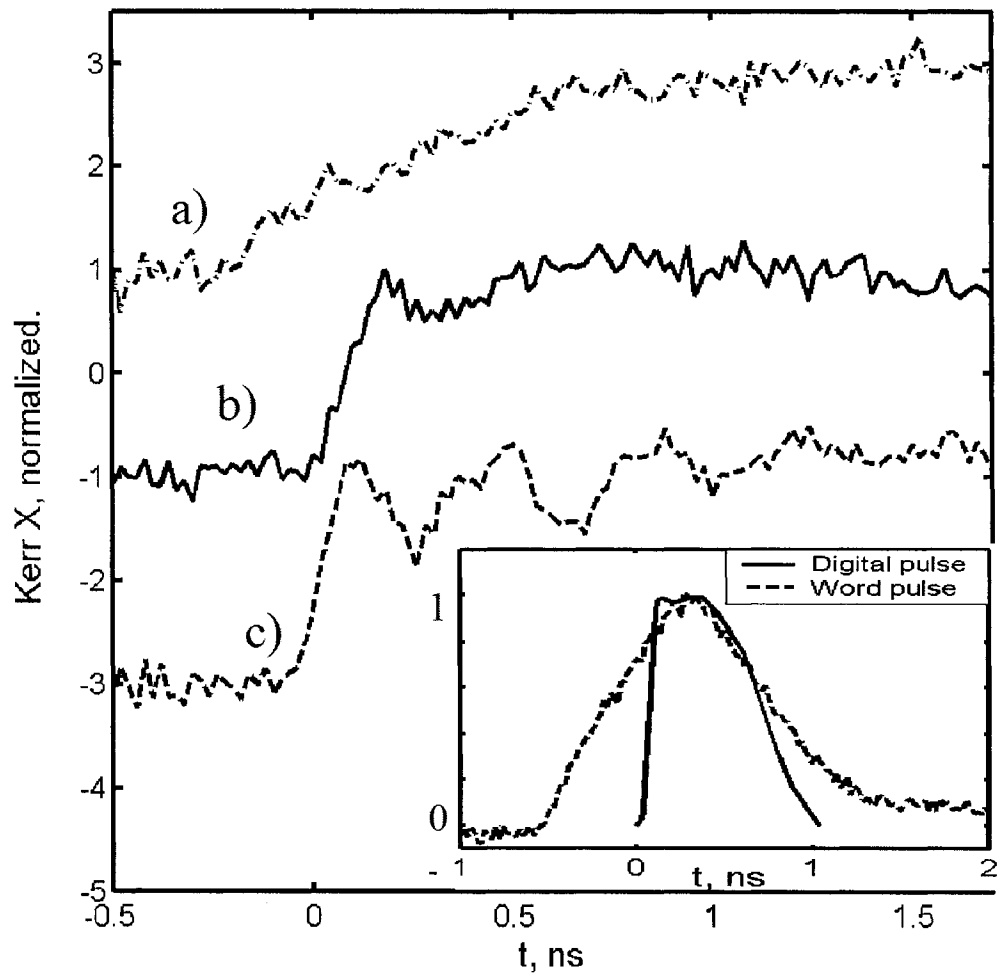


Figure 4-26: Half-select switching. (a) Slow incoherent switching by a strong (70 Oe) easy-axis (Word) magnetic field pulse. It is used to determine the saturation magnetization levels. (b) Very fast (180 ps 10-90%) half-select switching caused by 90 Oe fast hard-axis (Digital) pulse and 40 Oe Word pulse, properly timed with Digital pulse. (c) 40 Oe Word pulse is delayed 170 ps with respect to 90 Oe Digital pulse. Inset: Measured Digital (solid) and Word (dashed) pulse profiles (arbitrary units)

characterized. Insufficient strength and/or duration of the switching pulses results in statistically incomplete switching when the magnetization of the element is flipped only in a fraction of the events. Pulse overlap of 3 ns is required for a reliable half-select switching of a larger ($7 \times 1 \mu m$) FeCo element exhibiting a complex multi-domain switching scenario while smaller $3 \times 1 \mu m$ permalloy sample requires no more than 900 ps of the pulse overlap. Both values lie well within nowadays prototype MRAM operational switching time range of 10 to 20 ns.

The effect of the pulse duration on astroid switching diagrams is characterized for the $3 \times 1 \mu m$, and it was found that even the shortest pulse (≈ 900 ps FWHM) is sufficient for complete and reliable half-select switching. Switching astroids' shape varies with applied pulses duration: namely, the diagram shrinks in the easy-axis direction as the pulse duration increases. Beyond the easy-axis pulse duration of 5 ns, the diagram stays virtually unchanged for longer pulses. In some cases of longer pulses of 5 ns in duration and above "pockets" of switching appear (local spots of switching in the diagram, surrounded by unswitched regions). This might be an indication of the complex structure predicted in the simulations [50].

We observed the reluctance of sample edges to switching in the experiment, and confirmed by micromagnetic simulations for a variety of the sample shapes, sizes and switching regimes. It appears to be a generic feature of the fast switching scenarios, including precessional switching induced by a fast-rising hard-axis magnetic field. At the end of the pulse, simulations predict formation of the vortex magnetization state; and the experimentally observed tendency of the easy-axis magnetization to acquire zero net value was interpreted as an indication to existence of such a vortex. If hard-axis field is combined with sufficiently strong easy-axis field, the latter is able to effectively eliminate the vortex and end up in a completely switched state both in precessional and nucleation regimes.

Half-select switching in precessional regime is observed for the first time yielding the fastest half-select switching time of 180 ps reported to date [48],[59],[85]. With proper timing of the pulses the ringing is effectively suppressed.

Chapter 5

Magnetic implant sample.

This project was conducted in close collaboration with Al Meldrum's group, in particular with Kristen Buchanan, who performed the TEM characterization (Fig. 5-1) and the entire assembly of the nanocomposite sample and lithographically patterned wires on a separate substrate for Kerr measurements (Fig.5-2). I performed all time-resolved Kerr measurements and micromagnetic simulations reported below. This chapter is based on our recently submitted paper[61]and Report of Invention[62]. The sample was implanted by C. W. White at Oak Ridge National Laboratory.

5.1 Motivation.

For the most part, this work is devoted to well-defined lithographically patterned structures and their application to magnetic recording. However, there is another approach to novel recording media based on self-organized arrays (regular or random) of magnetic nanoclusters. Small enough nanoparticles act as single domains thus creating an opportunity for ultra-high recording density – and an opportunity for us to test magnetooptically single domain or superparamagnetic particles (although in this case not individually, but in the

form of random arrays).

Such nanoparticle arrays can be prepared using different techniques, such as chemical synthesis ([86],[87]), co-sputtering ([88],[89],[90]), Pulsed Laser Deposition ([91],[92]), sol-gel techniques ([93]) and ion-implantation ([95],[96]-[99]). Of those, ion-implantation formed clusters are of particular interest here. First, the magnetic nanoparticles are buried below the surface and thus protected. The depth of the active layer and its thickness can be controlled by the energy spectrum of accelerated ions. Multiple layers can be formed if necessary. The cluster density (or the amount of desired material in a certain layer) is easily controlled by the implantation rate and time. Finally, the average size of the particles in the nanocomposite may be controlled by the temperature and the duration of the annealing process.

In addition, as long as the nanocluster density is kept below the percolation density [93],[94], the material is relatively transparent and the interaction of highly susceptible ferromagnetic clusters with light might exhibit strong Faraday rotation, as well as an easily measurable Kerr shift for the reflected beam. “Giant” (compared to non-ferromagnetic materials) Faraday and Kerr polarization shifts were observed previously ([93],[87],[100],[101]) but no time-resolved experiments have been reported to date.

The ion implantation method is based on bombarding a host (target) material with ions of a desired substance (typically accelerated to 50-200 keV). Since the ions have a strongly energy-dependent interaction with the crystalline lattice, the concentration of the implanted ions does not decay exponentially into the depth of the host material, but rather a relatively narrow layer is formed at an energy-dependent penetration depth. Subsequently the implanted ions aggregate into nanoclusters via solid state diffusion. This aggregation and growth of the particles can be assisted by thermal annealing. We analyzed a nanocluster sample prepared at room temperature without subsequent annealing. Iron ions accelerated to 80 keV were implanted into the amorphous

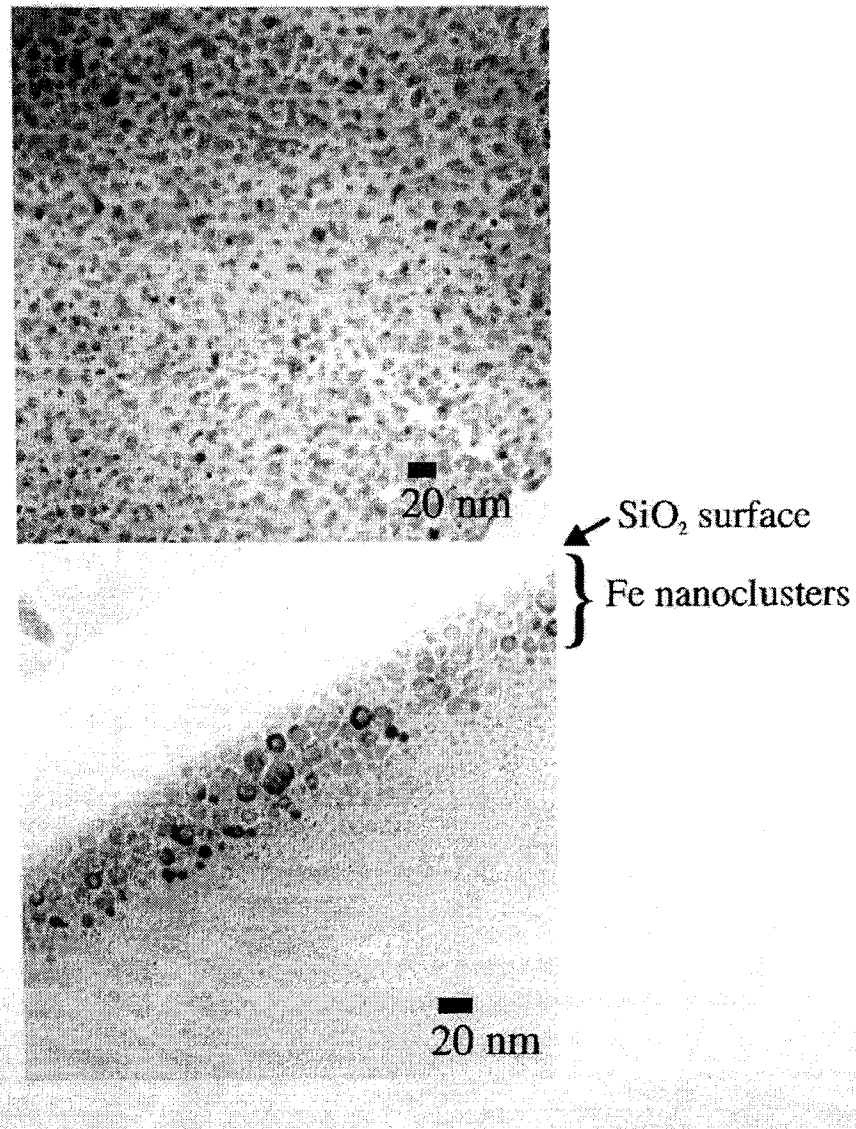


Figure 5-1: Plan view (top) and cross-section (bottom) transmission electron microscopy images of iron nanoclusters in SiO₂ host. Fe ions are implanted to an areal dose of 1.5×10^{17} ions/cm² at room temperature. This sample was not subsequently annealed. Iron nanoparticles are concentrated within 60 nm of the sample surface. The characteristic diameter of the clusters is approximately 10 nm.

SiO₂ host material to an integrated dose of 1.5×10^{17} ions/cm² (Fig. 5-1).

5.2 Experiment.

5.2.1 Kerr measurement set-up.

In order to quantitatively characterize the magnetic response of the sample we used the time resolved scanning Kerr microscopy technique [27], but instead of focusing directly at the sample face the beam has to travel through the silicon dioxide plate before being reflected by the optically active layer. It is important to note that the magnetization change rather than magnetization itself is measured so that the initial magnetization patterns (however complex) are undetected. In this chapter, of course, the actual nanoparticle size is also far beyond the spatial resolution of our system.

The probing beam (pulsed Ti-sapphire mode-locked beam of 800 nm wavelength) is focused through the silicon dioxide plate at the layer of the implanted nanoparticles. We estimate the focused laser spot size as $\approx 1.6 \mu m$. The plate itself is glued to a secondary sapphire substrate with lithographically developed 300-nm thick U-shaped gold write wire (WW) of width $10 \mu m$ with a $10 \mu m$ gap. The plan view and cross-section of the sample perpendicular to the write wires is shown schematically in the Fig. 5-2. The spacing between the plate and the substrate is several micrometers as diffraction fringes are observed. We used a value of $10 \mu m$ in our estimation of the field strength. According to the K. Buchanan's ellipsometry measurements [102], an initial mount of poorer quality exhibited $\approx 40 \mu m$ spacing, also in the ballpark of the wire width and the gap.

The particle magnetization is modulated by the magnetic field created by current pulses propagating down the WW. The pulsed field has a dominant in-plane component B_{\parallel} over the wire and out-of-plane component B_{\perp} between

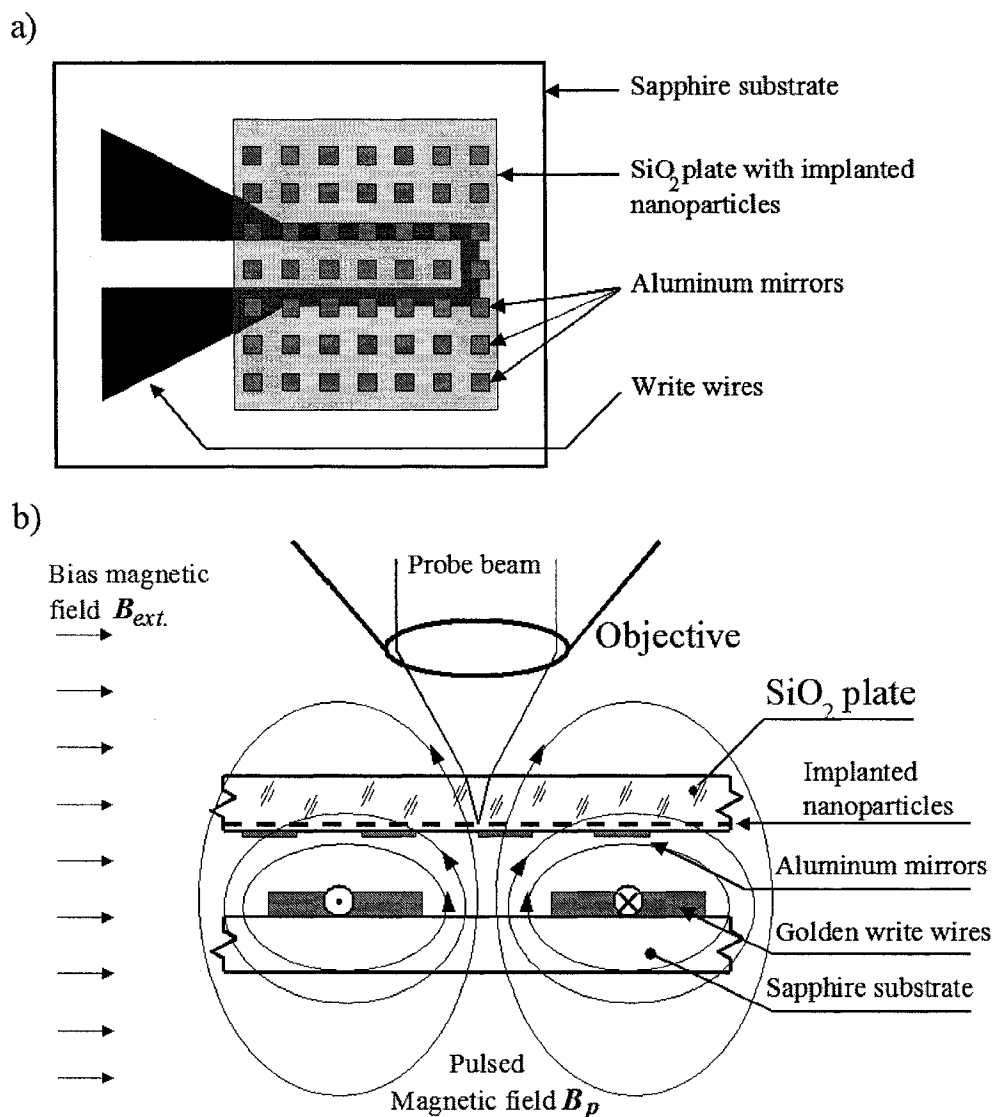


Figure 5-2: Schematic layout of the experimental set up. (a) Plan view of the sample. An ion-implanted SiO₂ is glued atop thin-film gold wires deposited on a sapphire plate. (b) Cross-section of the sample perpendicular to the write wires. The probe beam is focused, through the SiO₂ plate, on the optically-active iron nanocluster layer. Both transient and bias (static) magnetic field lines are shown.

the wires. These fields can be estimated as:

$$B_{\perp} = \frac{\mu_0 I}{2\pi b} \ln \frac{(a+b)^2 + h^2}{a^2 + h^2} = \frac{\mu_0 I}{2\pi b} \ln \frac{(1+b/a)^2 + (h/a)^2}{1 + (h/a)^2} \quad (5.1)$$

$$B_{\parallel} = \frac{\mu_0 I}{\pi b} \arctan \frac{b}{2h} \quad (5.2)$$

where b is the wire width ($10 \mu m$); h is the spacing between the plane of WW and the plane of the sample ($10 \mu m$); a is half-distance between the write wires ($5 \mu m$); and I is the current propagating down the write wire. Formulae (5.2),(5.1) correspond to B_{\parallel} immediately above the center of a single write wire and B_{\perp} in the middle between two wires, respectively. Note, that both B_{\parallel} and B_{\perp} decay $\propto 1/h$ far from the WW. Hence a flipped sample with the optically active layer at the bottom must be used to ensure that it lies as close to the write wires as possible, in the region of the strongest transient magnetic field. A constant in-plane bias magnetic field ranging from 0 to 400 Oe (exceeding the in-plane coercivity measured magnetooptically) can be applied to control the static magnetization.

In order to enhance the magneto-optical signal, $10 \times 10 \mu m$ square aluminum mirrors were placed lithographically at the nanoparticle layer side of the sample. With the probe reflected from a mirror, both Kerr and Faraday effects contribute to the response. The beam can be focused at the active layer, atop or between the mirrors, directly above the write wires or between them. In another sample the active layer itself was patterned using shadow masks, forming $5 \times 5 \mu m$ islands of implanted nanoclusters [103]. Focusing the beam at a mirror bypassing an island one can gauge the background signal of the host material itself.

In this experiment we used two pulse sources: a 50 V pulser with 250 ps rise time in combination with programmable electronic line with characteristic jitter of 220 ps; and a faster 10 V pulser of 50 ps rise time in combination with

an optical delay line. The first set-up provides a stronger signal and great scan range of more than 120 ns, at the expense of temporal resolution; while the second set-up is limited to short 4 ns scans but puts a closer bound on the response time of the sample itself. The write wires are terminated to 50Ω , so the maximum currents in these configurations are $\approx 1 A$ and $\approx 200 mA$.

5.2.2 In-plane magneto-optical response.

The response to an in-plane magnetic field pulse is shown in Fig. 5-3. The longitudinal Kerr signal is measured directly on top of the gold write wire for the unpatterned implantation sample. We estimate the pulsed field strength as ≈ 190 Oe according to the formula (5.2) for a 1 Ampere current pulse. DC bias field of negative 200 Oe is present in one case (thin line) or removed completely (thick line). The bias field has little effect on the in-plane response. The pulse duration is 10 ns, during which the Kerr signal rises almost linearly in both cases and clearly is still far from saturation by the end of the pulse (the maximum duty cycle of the pulser does not allow pulse durations longer than 16 ns). The pulse termination is followed by a slow decay of the sample magnetization over the scan range of 90 ns. We repeated the same experiment with other orientations of in-plane bias field (e.g. 200 Oe bias field at 90° to the pulsed field direction and parallel to the pulsed field), and repeated these measurements on the patterned implantation sample. The result was always the same: the in-plane Kerr signal is nearly independent on the bias field, has nearly linear rise during the pulse and slow decay after the pulse end. In section 5.3 we discuss a possible origin of these switching scenarios. No spatial magnetization structure (e.g. multiple domains) was observed in either case.

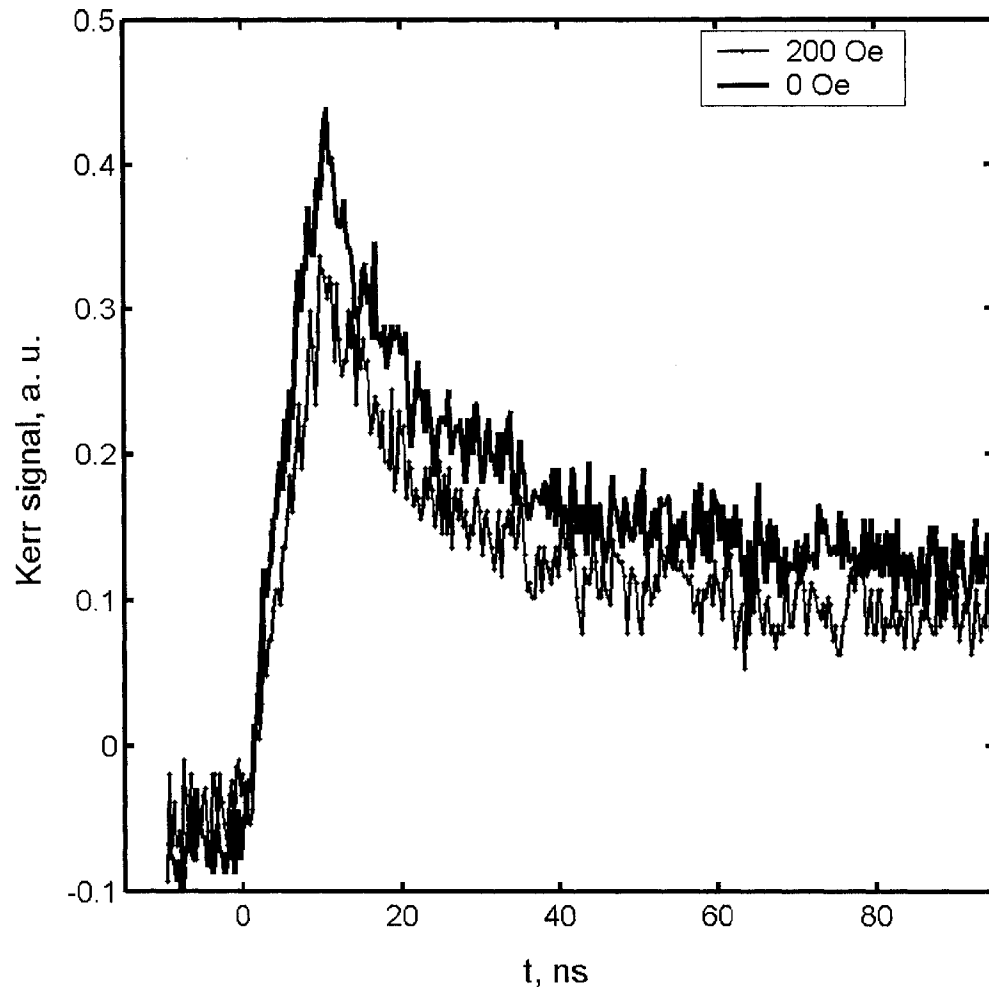


Figure 5-3: In-plane magnetization response measured atop the write wire. The transient in-plane pulsed field strength is approximately 440 Oe. The bias (DC) fields are negative 200 Oe (thin line with a marker) and zero (thick line). The pulse duration is 10 ns, starting at $t = 0$.

5.2.3 Out-of-plane signal.

The response to pulsed field applied perpendicular to the sample plane is completely different. Polar Kerr signal response to a 210 Oe 10 ns long out-of-plane pulse (between the WW, see formula 5.1 for 1 Amp current) is shown in Fig. 5-4 *a*. The signal follows the pulse profile regardless of applied bias magnetic field. In fact, the rise time of the polar Kerr signal measured with the 50 ps risetime Picosecond Pulse Labs Model 4050 pulser and optical delay line is limited by the system resolution. The traces shown in Fig. 5-4 *b*, recorded in strong bias field (dashed line) and without any bias field (solid) are again very close. The shoulder on the rising edge of each trace is an indication of pulse reflection at the impedance mismatch between the sample Write Wires and the incoming 50-Ohm coaxial cable. We have also compared these traces with the earlier recorded signal of a garnet current sensor (Fig. 5-4 *b*, dash-dotted). The garnet current sensor assembly is very similar to the one shown in Fig. 5-2, only the ion-implantation sample is replaced with yttrium iron garnet (YIG) crystal, and the write wires are patterned on the back side of the same crystal like the mirrors. The YIG sample is biased by 0.15 Tesla permanent magnets, and the temporal resolution of the sensor is determined by the FMR resonance frequency.

The fast polar Kerr response is also linear with pulse strength over a range of amplitudes (Fig. 5-5 *a*). Temporal profiles were recorded at current attenuation levels of 0, 6, 11 and 13 dB. The signal level plotted versus applied transient field strength in Figure 5-5 *b*, is linear across the range (averaged between 3 and 8 ns). Independent static measurements of Faraday rotation performed by Kristen Buchanan on a similar sample continue to show linear out-of-plane response over a wider range of fields of ± 6000 Oe [61].

The combination of strong signal at room temperature, ultra-fast rise time, linearity of response and absence of need for static field bias makes

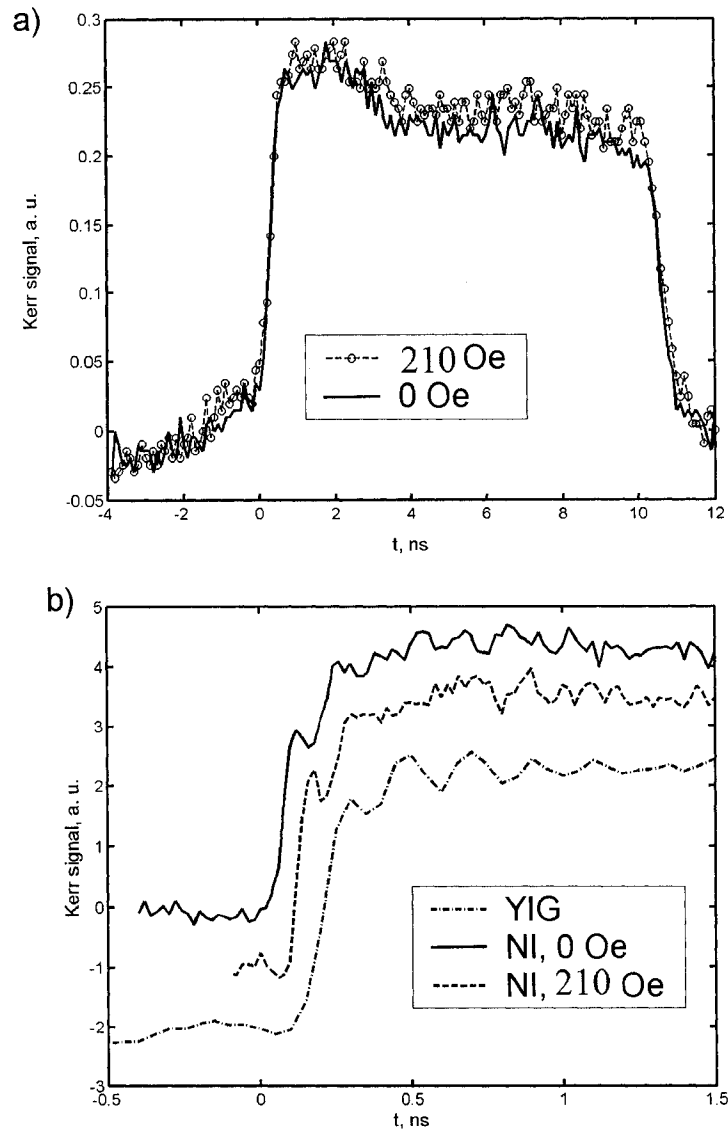


Figure 5-4: (a) Typical out-of-plane signal without bias magnetic field (solid line) and in strong bias field (thin line and circles). (b) High temporal resolution scans across the rising edge measured for nano-implantation (NI) sample in presence of the bias field (dashed) without bias field (solid) and using Yttrium Iron Garnet (YIG) current sensor biased by approximately 2200 Oe DC field (dash-dotted).

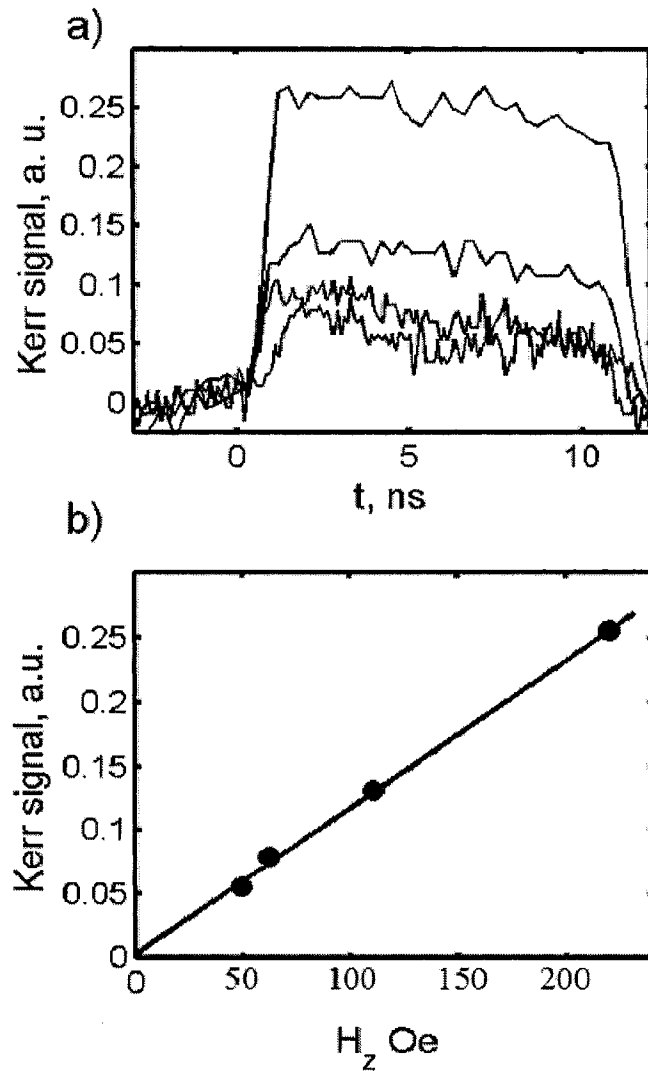


Figure 5-5: The dependence of the out-of-plane Kerr signal on applied field pulse amplitude. (a) Successive traces recorded at the strongest available pulse of 210 Oe, and attenuations of 6 dB (220 Oe), 11 dB (125 Oe) and 13 dB (100 Oe). (b) Corresponding plateau heights averaged between 3 and 8 ns plotted versus the field strengths.

this nanocomposite material an ideal candidate for an active element of new magneto-optic current sensor [62].

5.2.4 Kerr and Faraday effects.

In the semi-transparent sample with a mirror coating, the magneto-optic response is a combination of Kerr and Faraday effects for reflected and transmitted light respectively. In order to demonstrate the effect of Faraday rotation as opposed to Kerr polarization shift, we examined a patterned nanocomposite sample with mirrors at the back side (Fig. 5-6 *a, b*) in zero bias magnetic field. The nanocomposite layer is only 28% reflective, so the resulting Kerr signal is relatively weak. Forty-four percent of the light makes it through the sample, while the remaining 28% of the light is absorbed. Focusing at the nanocomposite island atop the mirror one can expect a greater polarization shift as the beam travels through the active layer twice. Figure 5-6 *c* indeed shows much higher signal at the mirror, and it has *opposite* polarity to the Kerr signal of the bare nanocomposite islands. It is to be expected, however, as the Faraday effect is non-reciprocal. The total signal from the mirror has a dominant Faraday component which overrides weaker Kerr rotation and is therefore negative. On the other hand, Kerr signal itself from a finite thickness bare nanocomposite may be weakened by Faraday effect as the light makes it way to and from the particles it is being reflected from. We would therefore address the signal as “magneto-optic response” without specifying its particular origin as Kerr and Faraday effects are so closely interconnected.

A time-resolved “movie” of the out-of plane magnetic signal for the field of view was recorded, but no internal spatial structure was recorded within the implanted regions. A typical Kerr image is shown in Fig. 5-6 *c*.

In order to compare the “mostly-Kerr” effect from the second square (5-6 *c*, top right) with “mostly-Faraday” signal reflected from the mirror (5-6 *c*, top

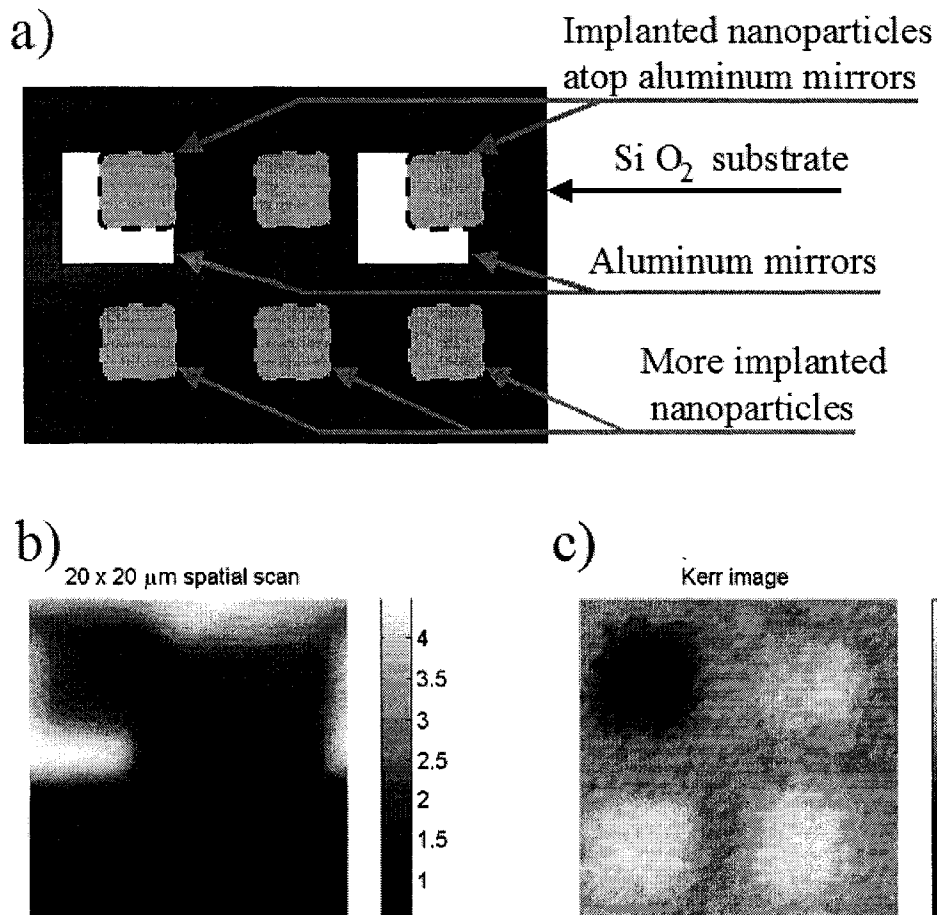


Figure 5-6: (a) Schematic layout of the patterned ion-implantation sample. Some islands of the implanted material partially overlap with underlying aluminum mirrors. (b) Intensity (brightness) spatial scan of the patterned sample. (c) Corresponding polar Kerr/Faraday optomagnetic image. The signal from the mirror has an opposite polarity to the signal of the bare implantation islands. The grayscale colorbars in the plots (b,c) correspond to the brightness and the magneto-optic signal amplitude (arbitrary units) respectively.

left) we repeated two temporal scans at the center of each square, over a 3 ns range and using a high lock-in integration time in order to reduce the noise. Both traces exhibit a similar shape, with a flat plateau following a fairly sharp onset as seen in Fig. 5-7. The risetime from the beginning of the pulse to the first notch at the rising edge (which we believe is a real feature of the pulse profile caused by reflection in the connecting wires) is approximately 80 ps; the time required to reach 90% of the plateau level is ≈ 150 ps.

As for the magnitude of the magneto-optic response, it appears to be very strong. No magneto-optic response was detected between the islands of implanted nanoclusters. Considering the relative thinness of the implanted layer (≈ 120 nm double pass) compared to the characteristic scale of field decay inside the host material (tens of micrometers) and at least 10:1 signal-to-noise ratio of the Faraday measurements, one can conclude that the Verdet constant (Faraday rotation angle per unit length per unit magnetic field) of the nanocluster material is at least three orders of magnitude greater than that of silicon dioxide. Independent direct Faraday rotation measurements (not time-resolved) performed by K. Buchanan [61] resulted in a value of Verdet constant of $7.2^\circ/(cm Oe)$. This value is on par with the best magneto-optic materials, such as YIG indicator ($30^\circ/(cm Oe)$), $Ce_xY_{3-x}Fe_5O_{12}$ ($14.1^\circ/(cm Oe)$), EuS doped TiO_2 ($0.15^\circ/(cm Oe)$); and four orders of magnitude higher than the Verdet constant for typical materials such as SiO_2 ($2.77 \cdot 10^{-4}^\circ/(cm Oe)$) or Flint Glass ($5.28 \cdot 10^{-4}^\circ/(cm Oe)$) [104]-[107].

5.3 Simulations.

In order to elucidate the unusual magneto-optic properties of the nanocomposite material, a finite element model was simulated. Since the nanoparticles are localized within a thin (60 nm) layer, the dipolar interaction between individual clusters imposes an in-plane anisotropy. Therefore, the magnetizations of

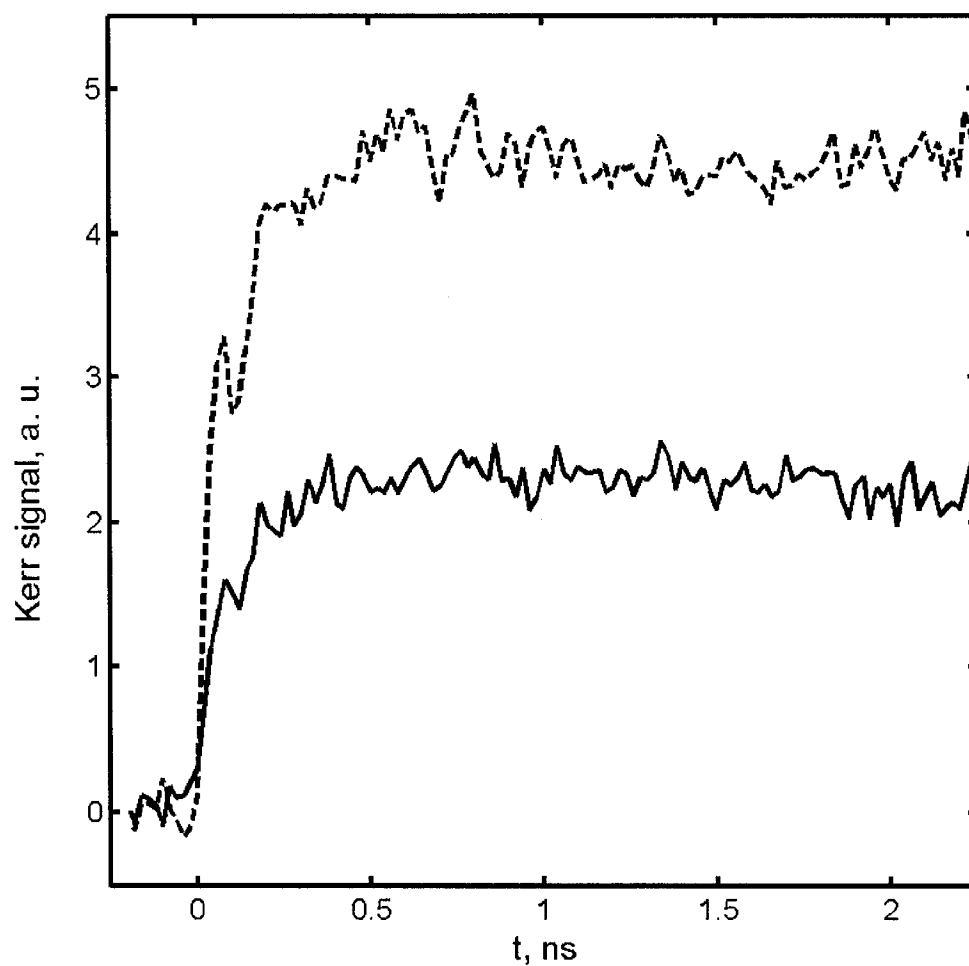


Figure 5-7: Kerr versus Faraday magneto-optical response of the implanted nanoparticles. Stronger Faraday signal (dashed) has an opposite polarity to Kerr signal (solid), and is inverted for direct comparison.

individual particles lie mostly in the plane of the layer (XY , parallel to the surface), and the in-plane orientation of any cluster is determined by a local field created by its nearest neighbors. These local fields can be strong compared to the external applied field, thus insensitivity to the bias field observed in the experiment. If external in-plane field is applied to such sample, some particles, randomly distributed across the specimen are more likely to hop into new equilibrium state, and they undergo large-angle magnetization change. Subsequently, switched particles rearrange the pattern of local magnetic fields and make their neighbors to switch as well, but there is no easy switching mechanism such as domain wall motion, thus in-plane switching is very slow. This leads to a strong rate dependence of the coercivity, which is in fact very low (~ 20 Oe) [61] in quasistatic measurements. On the other hand, in the reaction to out-of plane field H_z , almost all in-plane magnetized particles experience a coherent small-angle tilt, resulting in fast, linear response.

In order to explore these assumptions we conducted Landau-Lifshitz-Gilbert based simulations. The real structure of the specimen is shown in the Fig. 5-1 *a, b*. The nanoclusters are nearly spherical iron particles of 5-15 nm in diameter, and not touching each other (this is related to the growth process, two particles in contact would aggregate into a single bigger cluster), and thus exchange-decoupled. Iron itself has cubic crystalline anisotropy, and we assume that the anisotropy axes of different particles are oriented randomly. We ran several different models reflecting the underlying physics but still executing in reasonable time on a dual 2.4 GHz Xeon processor machine.

1. (i) The simplest model is randomly scattered $10 \times 10 \times 10$ nm cubic cells scattered on a 10×10 nm grid (Fig. 5-8 *a*). All magnetic constants correspond to those of bulk iron, and the cubic anisotropy axes are parallel to the principal axes of the cubes. No minimal separation is imposed, and individual cells are allowed to touch, and thus be exchange-coupled.

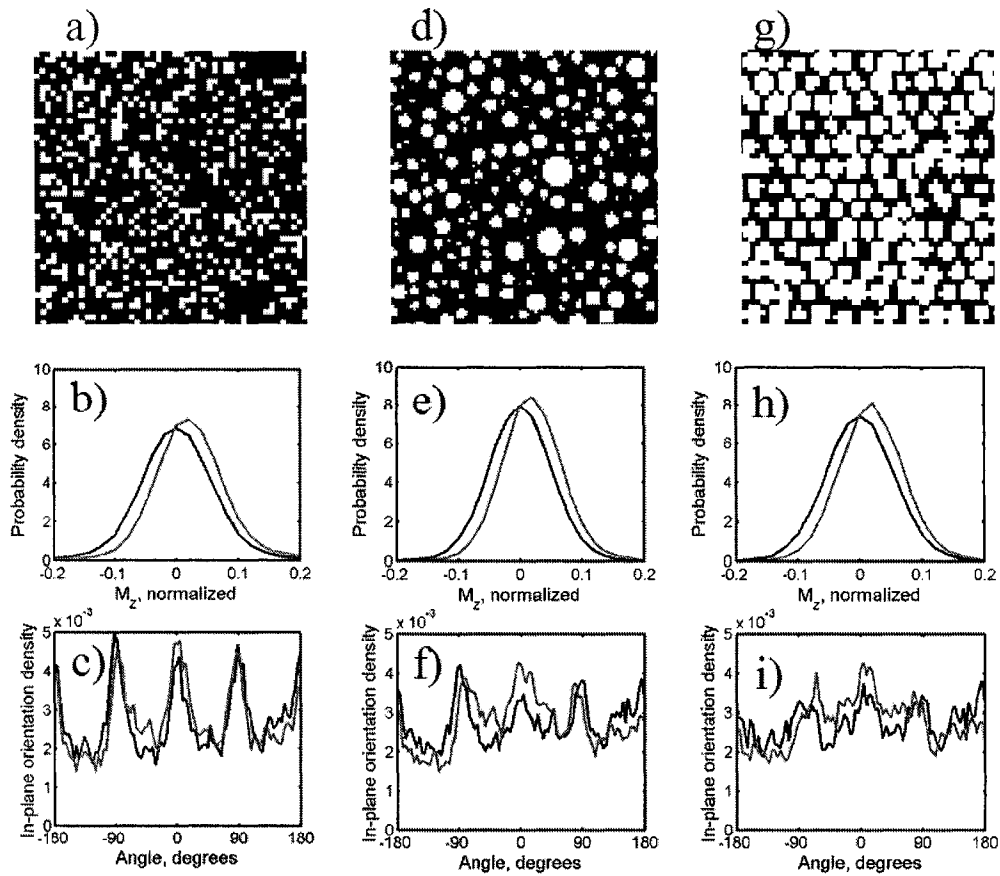


Figure 5-8: Comparison of different simulations: (i) a randomly scattered 10 nm cubic cells [a-c], cubic anisotropy is imposed; (ii) randomly scattered (in both radius and position) flat circle elements with no crystalline anisotropy [d-f] and (iii) more densely packed (filling factor 59%) circles with zero crystalline anisotropy [g-i]. The top row [a, d, g] represents the design masks (not to scale, refer to the text for exact parameters). The second row [b, e, h] shows corresponding histograms for the out-of-plane component of magnetization M_z distribution before (solid black line) and during (gray line) the duration of the magnetic field pulse for each design. The third row [c, f, i] maps the corresponding distribution for the in-plane component of magnetization M_x before and during the pulse.

However the filling factor of 25% is low, so there are some individual cells and those only coupled via diagonal. The result is a distribution of particle sizes, shapes and separations not very representative of the actual sample, and also with an anisotropy axis orientation not characteristic of the real specimen.

2. (ii) Randomly distributed non-touching “disks” constructed of 5×5 nm cells on 5×5 nm grid, with 10 nm layer thickness – Fig. 5-8 *d*). The disk diameters are randomly distributed with root mean square diameter of the particles 15 nm and the width of the diameter variation 15 nm. The minimal separation between the particles is set to 5 nm. In order to remove anisotropy axis alignment the crystalline anisotropy is set to zero. Filling factor is again 25%. This model has lower anisotropy than model (i), although the grid is still rectangular, and residual shape anisotropy persists especially in smaller elements.
3. (iii) Quasi-regular hexagonal array of the disks (Fig. 5-8 *g*). Disk centers are allowed to shift from the hexagonal lattice randomly within 2.5 nm. The disk RMS diameter is 20 nm, radii variation width is 1.5 nm (although actual size of the elements variations are higher because of the finite grid size). Disks are allowed to touch one another to achieve high filling factor of 59%. Zero crystalline anisotropy is imposed, same grid as (2). This model is designed to study the effects of packing density and array regularity.

All simulations are run on a 200×200 cell grid, at finite temperature (300 K). Each simulated sample was allowed to relax to its equilibrium state from a “random initial state” (randomly distributed magnetization orientation for every grid cell), and then subjected to a fast magnetic field pulse lying in XZ plane. The magnetization direction distributions before and during the

pulse (at 2.5 ns time from the beginning of the pulse) are shown in Fig. 5-8. In this particular case we used a pulse at 45° to the plane of the sample ($H_x = H_z = 200$ Oe, $H_y = 0$) to capture both in- and out-of-plane behavior simultaneously. The temporal profile of the pulse is shown schematically in the Fig. 5-10 (dash-dotted line). This pulse profile simulates the Picosecond Pulse Lab generator output. The fast edge rises from zero to the saturation level in 60 picoseconds, stays flat for five nanoseconds (we used a shorter 3 nanosecond plateau duration for the model (ii)), and then drops to zero in 940 picoseconds.

As expected, magnetization lies in XY plane for all models. The histograms of the out-of plane magnetization M_z (Fig. 5-8 *b, e, h* for the models (i), (ii), and (iii) respectively) are narrow with full width half maximum of about 0.1, centered at zero. During the pulse, the entire distributions shift slightly in the direction of the applied field (gray lines). The histograms for the in-plane orientation of magnetization are very different (Fig. 5-8 *c, f, i*, black lines). Here we plot the probability density of magnetization to have a certain angle in the XY plane. All histograms are wide and relatively flat, although the distribution for the model (i) shows pronounced peaks at -90, 0, 90 and 180 degrees (Fig. 5-8 *c*) – a consequence of the crystalline anisotropy. The models (ii) and (iii) demonstrate flatter histograms with lower peaks (which we attribute to the anisotropy caused by the square grid). During the pulse the low-angle parts of the histograms rise (gray lines), and large angle move down, manifestations of the large-angle in-plane rotations.

The dynamic response to a strong in-plane field pulse ($H_x = 600$ Oe, $H_y = H_z = 0$, the temporal profile is the same as before) for all three models is shown in Fig. 5-9 *a*. While it does not show quantitative agreement with experimental data (Fig. 5-3), some qualitative characteristics are quite similar. The in-plane magnetization response is slower than the out-of plane case (Fig. 5-3) and it doesn't fall back to zero when the field pulse ends – for all three

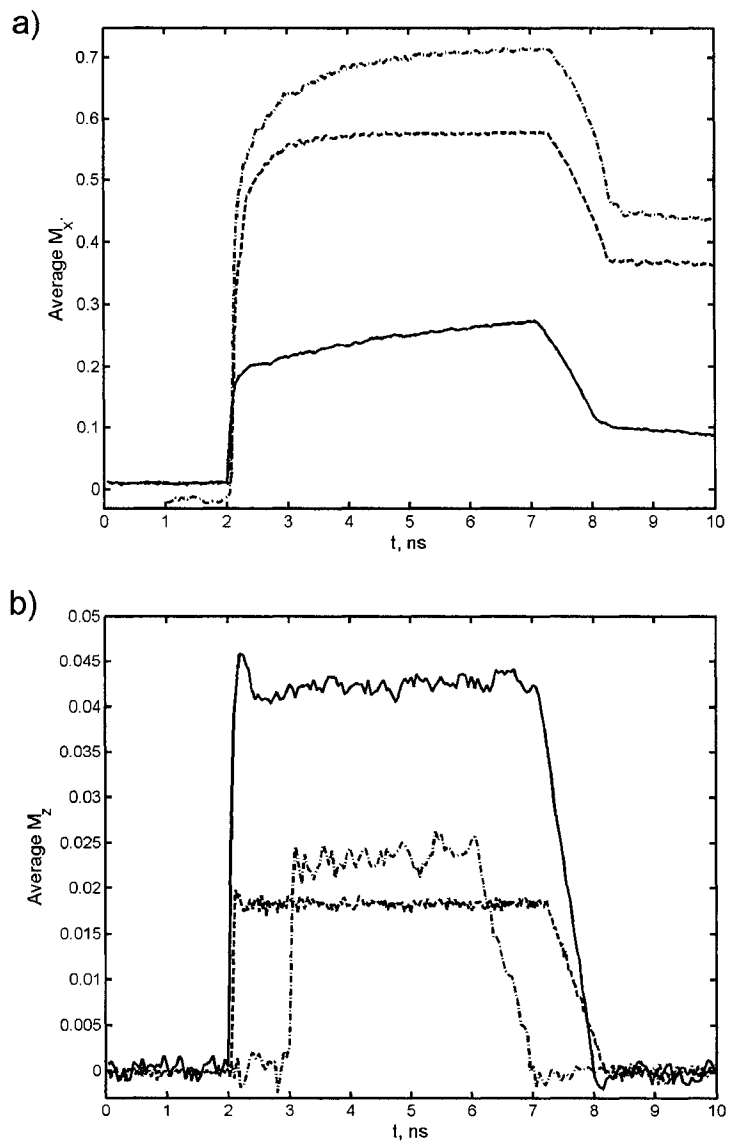


Figure 5-9: (a) The in-plane response of average magnetization to the in-plane field pulse $H_x = 600$ Oe. (b) Out of plane response of magnetization to the combined in- and out-of plane field pulse $H_x = 200$ Oe, $H_z = 200$ Oe. The details of the pulse's temporal profiles are described in the text. Solid, dash-dotted and dashed lines represent the “random cubes” (i), “random disks” (ii) and “densely packed quasi-regular disks” (iii) models respectively.

models. The trace for the model (i) (solid line) is lower than the others, and it does not saturate during the pulse, unlike the traces (ii) and (iii) (dash-dotted and dashed respectively). This should be an effect of the crystalline anisotropy.

The out-of plane response of the experiment is reproduced much better. The temporal traces of simulated M_z component for the same 45° pulses as for the histogram tests are shown in Fig. 5-9 *b*. The response follows the trapezoidal pulse profile for all models (note, that the pulse for the model (ii) is shorter, 3 ns plateau duration rather than 5 ns for the others), At first, the result for the model (i) (solid line), looks confusing: despite the crystalline anisotropy, the out-of plane response is the strongest of all models. Evidently the dipole interactions between cells in the models with larger particle size and/or higher density induce a stronger in-plane anisotropy, which exceeds in effect the crystalline one. In particular, the model (ii) (dash-dotted line) has the same filling factor as model (i), but the average particle size is larger within the disks. Note that there is virtually no ringing and all traces are nearly trapezoidal. This should be a consequence of the fact that each cluster is subjected to a different local field and thus has its own FMR resonance frequency [57], so the oscillations are out of phase and effectively average out across the array.

Finally, we investigate the effect of in-plane field on the out-of-plane response for the model (i). For comparison with the 45° pulse (Fig. 5-10, solid line), another trace for out-of plane pulse only ($H_z = 200$ Oe, $H_y = H_x = 0$) is shown at the same plot in gray. Both traces almost coincide, and nicely retrace the ideal field pulse profile (dash-dotted). The results for the other two models are very similar. This allows us to conclude that the fast out-of plane response is governed by collective small-angle (and thus linear in field strength) tilt of mostly in-plane magnetized particles. It is virtually decoupled from the slow, large angle in-plane switching of individual particles, consistent

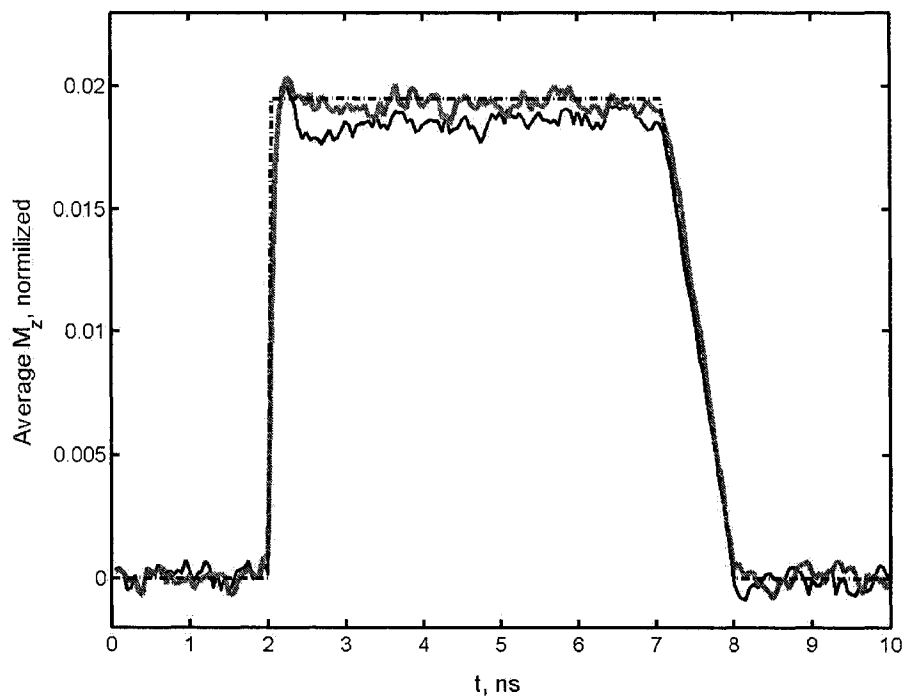


Figure 5-10: Simulated out-of-plane magnetization M_z response averaged over entire array. Magnetic field pulse profile is shown schematically as a dotted line. Gray curve corresponds to the response to 200 Oe Z -axis pulse only, while the black trace represents M_z response to a slanted pulse: $H_z = H_x = 200$ Oe.

with experimental results (Fig. 5-4 *a*).

The fast and linear out-of-plane response seems to be independent of the particular properties of the material used, of filling factor, regularity of arrays or presence of in-plane magnetic field (DC or pulsed). We predict similar fast and linear magnetization response in other “Exchange-Decoupled Nanoparticle Arrays” (EDNA).

5.4 Chapter summary.

The investigated nanocomposite material produced via ion-implantation process showed strong magneto-optic response (Verdet constant of 7.2 deg/(Oe cm), four orders of magnitude higher than the host material) and on par with the best magneto-optic materials known to date.

Out-of plane response is extremely fast (rise time faster than 150 ps), linear in wide range of field strength and independent of in-plane field (DC or pulsed). Time-resolved measurements are conducted up to 210 Oe, non-resolved – up to 6000 Oe. The effect stays linear in these ranges. Micromagnetic simulations demonstrated a very similar behavior of fast linear magnetic response regardless of filling factor; randomness or regularity of the particle centre distribution; of the size and shape of the particles, presence of crystalline anisotropy and presence of in-plane magnetic field in agreement with experimental observations. This effect seems to be a consequence of strong dipole interactions between the particles only, and almost does not depend on particular structure of the particles or the arrays themselves. We predict similar magneto-optic response in other exchange-decoupled nanoparticle arrays.

Fast and linear magneto-optic response and the fact that the nanocomposite does not need bias field to perform make this material (and others similar to it) good candidates for an active element of the magneto-optic current sensor. The Report of Invention was submitted [62].

Chapter 6

Conclusions.

In the previous chapters we discussed applications of the TR-SKM method to the characterization of the recording heads (Chapter 3), prototype MRAM elements (Chapter 4) and hybrid magnetic/non-magnetic nanocluster composite material (Chapter 5). The method proved very versatile, providing detailed spatially- and temporally- resolved data agreeing quantitatively with micro-magnetic (LLG-based) simulations.

New results presented in this work include the dependence of the recording head performance on the shape of the recording tip, as well as variation of the flux risetime along the pole and lag of the flux risetime at the poles with respect to the current pulse onset and to each other. We believe that both factors should be taken into account in designing high-performance writers.

Experiments on the prototype crossed-wires structures yielded several important details of the switching process in the half-select regime. Switching appears to be more reliable, when a non-zero hard-axis field component precedes the easy-axis switching field pulse, in agreement with predicted behavior [37]. The measured transition between “non-switching” and “switching” regimes is not sharp, but rather results in a surprisingly wide range (comparable with the half-select switching field itself) of incomplete switching events

which are either occurring statistically (in a larger structure with stronger uniaxial anisotropy), or through formation of a metastable vortex state in a thinner and softer sample. However, a strong enough easy-axis field is able to eliminate the vortex and yield half-select switching for pulse durations as short as 900 ps FWHM.

Precessional behavior of magnetization under the influence of fast-rising hard-axis pulses is observed, and complete precessional half-select switching is reported for the first time. This switching scenario is free of ringing if easy- and hard- axis pulses are properly timed, and yields the fastest switching time (180 ps 10-90%) reported to date [59],[85],[108]. We observed reluctance of the sample edges to switching in the half-select regime, and elucidated it through micromagnetic simulations of both incoherent and precessional switching scenarios even for the smallest samples. To reduce the edge reluctance one should reduce the sample thickness and lateral size.

The performance of the recording heads would benefit from reducing their lateral size (and in particular the yoke length) [15],[74]; and implementation of the MRAMs may be assisted by reducing of production costs in the complex lithography involved. In Appendix A we address both issues by suggesting a new lithographic process, promising formation of spiral, helical and crossed-wire structures in fewer steps. This method was not used for magneto-optic experiments, so it is presented as an appendix rather than in the main body of the thesis devoted to the TR-SKM measurements. However, with regard to applications we consider it one of the most important results of this work.

Finally, the TR-SKM method proved useful for examination of a nanocomposite material fabricated by ion-implantation of iron in a silicon dioxide matrix. The material yields strong magneto-optic signal, and its response is fast (at most 150 ps risetime) and linear with the pulse field strength in zero bias magnetic field. This makes the ion-implantation nanocomposite material an ideal candidate for the ultrafast magneto-optic current sensor.

Bibliography

- [1] Saeid Tehrani, short course on micromagnetics given at the American Physical Society meeting in March 2002.
- [2] H. Sato, P. A. Schroeder, J. Slaughter, W. P. Pratt Jr., and W. Abdul-Razzaq, “Galvanometric properties of Ag/M ($M=Fe, Ni, Co$) layered metallic films”, “*Superlattices and Microstructures*”, vol. **4**, 45-50 (1988).
- [3] E. Velu et. al. Phys. Rev. B, Vol. **37**, 668 (1988).
- [4] G. Binasch, P. Grunberg, F. Saurenbach, and W. Zinn, “Enhanced magnetoresistance in layered magnetic structures with antiferromagnetic interlayer exchange” Phys. Rev. B, **39**, 4828-4830 (1989).
- [5] Stuart Parkin et. al. “Magnetically Engineered Spintronic Sensors and Memory”, Proc. IEEE, Vol. **91**, NO 5, 661 (2003).
- [6] S. S. Parkin, R. E. Fontana, and A. C. Marley, J. Appl. Phys **81**, 5521 (1997).
- [7] W. J. Gallagher et. al. “Microstructured magnetic tunnel junctions” J. Appl. Phys. **81** 3741-3746 (1997).
- [8] Saeid Tehrani et. al. “Magnetoresistive Random Access Memory Using Magnetic Tunnel Junctions”, Proc. IEEE, Vol. **91**, NO 5, 703 (2003).

- [9] J. J. Sousa et. al. Appl. Phys. Lett. **73**, 3288-3290 (1998).
- [10] S. Tehrani et. al. “*Recent developments in magnetic tunnel junction MRAM*”, IEEE Trans. Mag. **36**, 2752-2757 (2000).
- [11] H. Kanai et. al. Fujitsu Sci. Tech. J. **37** 174 (2001).
- [12] H. W. Schumacher et. al., IEEE Trans. Mag. **38**, (5), Sept. (2002)
- [13] H. W. Schumacher, C. Chappert, R. C. Sousa, P. P. Freitas, and J. Militat; Phys. Rev. Lett. **90**, 17204 (2003).
- [14] M. T. Kief, Seagate Corp. “*Applied Magnetism and the Information Storage Industry*”, presentation at the MMM/Intermag Conference (unpublished), (2002).
- [15] A. Taratorin, S Yuan, V. Nikitin, “*High data rate recording*”, J. Appl. Phys., Vol. **93**, issue 10, pp. 6444-6446, 2003.
- [16] S. Shtrikman and D. Treves, chapter “*Micromagnetics*”, “Magnetism”, edited by G. T. Rado and H. Suhl, (Academic Press, New York), Vol. 3, . 394-414 (1963).
- [17] D. J. Craik and R. S. Tebble, “*Magnetic Domains*”, Repts Prog. Phys., **24**, 116-66 (1961).
- [18] R. Carey and E. D. Isaak, “*Magnetic domains and techniques for their observation*”, Academic Press, New York (1966).
- [19] K. Onishi, H. Tonomura and Y. Sakurai, J. Appl. Phys. **50**, 7624-6 (1979).
- [20] M. R. Scheinfein et. al. “*Scanning electron microscopy with polarization analysis (SEMPA)*”, Rev. Sci. Instrum. **61**, 2501-26 (1990).

- [21] R. E. Dunin-Borkowski et. al., “*Switching asymmetries in closely coupled magnetic nanostructure arrays*”, Appl. Phys. Lett. **75** (17), 2641 (1999).
- [22] J. N. Chapman and M. R. Scheinfein, “*Transmission electron microscopies of magnetic microstructures*”, Journal of Magnetism and Magnetic Materials **200**, 729-740 (1999).
- [23] R. E. Dunin-Borkowski, M. R. McCartney, B Kardynal and David J. Smith, “*Magnetic interactions within patterned cobalt nanostructures using off-axis electron holography*” J. Appl. Phys. **84** (1) 374-377 (1998).
- [24] C. Schönenberger and S. F. Alvarado, “*Understanding magnetic force microscopy*”, Z. Phys. B, **80**, 373-83 (1990).
- [25] A. Kubetzka, M. Bode, O. Pietzsch, and R. Wiesendanger, “*Spin-Polarized Scanning Tunneling Microscopy with Antiferromagnetic Probe Tips*”, Phys. Rev. Lett. **88**, 057201 (2002).
- [26] T. J. Silva, S. Schultz and D. Weller, “*Scanning near-field optical microscope for imaging of magnetic domains in optically opaque materials*”, Appl. Phys. Lett., **65**, 658-60 (1994).
- [27] M.R. Freeman and J. F. Smyth , J. Appl. Phys. **79**, 5898 (1996).
- [28] A. Hubert, R. Schäfer, “*Magnetic Domains: The Analysis of Magnetic Microstructures*”, Springer, 1998.
- [29] W. Wernsdorfer, “*Classical and quantum magnetization reversal studied in nanometer-sized particles and clusters*” to be published in Advances in Chemical Physics. A Wiley-Interscience Publication, NY.
- [30] A. Aharoni, “*Introduction to the Theory of Ferromagnetism*”, Clarendon Press, Oxford (1996).

- [31] W. Heisenberg, *Z. Physik* **49**, 619 (1928).
- [32] M. Pratzner, H. J. Elmers, M. Bode, O. Pietzsch, A. Kubetzka, and R. Wiesendanger, “*Atomic-Scale Magnetic Domain Walls in Quasi One-Dimensional Fe Nanostripes*”, *Phys. Rev. Lett.* **87**, 127201 (2001).
- [33] Jacques Miltat, Gonçalo Albuquerque, André Thiaville, “*An Introduction to Micromagnetics in the Dynamic Regime*”, Vol. 83, Burkard Hillebrands, Kamel Ounadjela (editors) Springer-Verlag, Heidelberg (2002).
- [34] J. D. Jackson, “*Classical electrodynamics*”, John Wiley & Sons, NY, 1975.
- [35] L. D. Landau, E. M. Lifshitz, “*Quantum Mechanics, Non-relativistic theory*”, 3 edition, Butterworth-Heinemann (1981).
- [36] C. Cohen-Tannoudji, B. Diu, F. Laloë, “*Quantum Mechanics*”, Wiley, New York (1987).
- [37] A. S. Arrott, “*Ultrathin Magnetic Structures*”, Vol. **IV** (chapter, “*Introduction to micromagnetics*”), B. Heinrich and JAC Bland (editors), Springer-Verlag 2004.
- [38] We would like to thank Prof. A. S. Arrott for stressing this point.
- [39] J. A. Osborn, “*Demagnetizing factors for the general ellipsoid*”, *Phys. Rev.* **67**, 351-357, (1945).
- [40] D. C. Cronmeyer, “*Demagnetization factors for general ellipsoids*”, *J. Appl. Phys.*, **70**, 2911-2914, (1991).
- [41] G. Ballentine, *Ph. D. Thesis*, University of Alberta (2002).

- [42] R. D. McMichael, M. J. Donahue and D. G. Porter, “*Switching dynamics and critical behavior in standard problem no. 4*”, J. Appl. Phys., **89**, 7603 (2001).
- [43] H. Fukushima, Y. H. Makatami and N. Hayashi, “*Volume average demagnetizing tensor of rectangular prisms*”, IEEE. Trans. Mag. **34** (1), 193 (1998).
- [44] L. D. Landau and E. Lifshitz, “*On the theory of the dispersion of magnetic permeability in ferromagnetic bodies*”, Phys. Z. Sowjetunion **8**, 153-169 (1935).
- [45] S. Middlehoek, “*Domain walls in thin Ni-Fe films*”, J. Appl. Phys. **34**, 1054-9, (1963).
- [46] M. R. Scheinfein, A. S. Arrott, Journal of Applied Physics, **93**, (10), 2003; A. S. Arrott, private communication.
- [47] METALLKUNDE – International Journal of Materials Research and Advanced Techniques, edited by Deutsche Gesellschaft für Materialkunde e. V.; Z. Metallkd. **93** (10) pp. 963-967 (2002).
- [48] W. K. Hiebert et. al., J. Appl. Phys. **93**, 6906 (2003).
- [49] E. C. Stoner and E. P. Wohlfarth, IEEE Trans. Mag. **27**, 3475-3518 (1991) (reprinted).
- [50] Bauer. et. al., Phys. Rev. B **61**, (5), Feb. 2000.
- [51] M. R. Scheinfein, LLG micromagnetic SimulatorTM.
- [52] F. Bloch, Phys. Rev. **70**, 460 (1946).
- [53] B.C. Choi, G.E. Ballentine, M. Belov, W.K. Hiebert, and M.R. Freeman, Phys. Rev. Lett. **86**, 728 (2001).

- [54] Vladimir. L. Sobolev, Huei Li Huang, and Shoan Chung Chen, “*Generalized equations for domain wall dynamics*”, J. Appl. Phys., **75** (10) 5797-5799 (1994).
- [55] N. L. Schryer and L. R. Walker, “*The motion of 180° domain walls in uniform dc magnetic field*”, J. Appl. Phys., **45** (12) 5406-5421 (1974).
- [56] A. P. Malozemoff and J. C. Slonczewski, “*Magnetic domain walls in bubble materials*” Academic Press, New York, (1979).
- [57] Charles Kittel, Physical Review **73** (2) 155 (1948).
- [58] A. Krichevsky, H. Gong, D. J. Seagle, M. Lederman and M. R. Freeman, IEEE Trans. Mag. **40**, (1), pp. 157-160 Jan. 2004.
- [59] S. Zelakiewicz, A. Krichevsky, Mark Johnson and M. R. Freeman, J. Appl. Phys. **91**, Vol. 10, pp. 7331-7333, May 2002.
- [60] A. Krichevsky and M. R. Freeman, accepted for publication in J. Appl. Phys. June 2004.
- [61] K. S. Buchanan, A. Krichevsky, M. R. Freeman, and A. Meldrum, submitted to Phys. Rev. B, Dec. 2003.
- [62] K. S. Buchanan, A. Krichevsky, M. R. Freeman and Al Meldrum, ILO Report of Invention, submitted Oct. 2003.
- [63] W. K. Hiebert, *Ph. D. Thesis*, University of Alberta (2001).
- [64] M. Mansuripur, “*The Physical Principles of Magneto-optical Recording*”, Cambridge University Press, Cambridge, 1995.
- [65] M. R. Freeman and W.K. Hiebert, “*Spin dynamics in confined magnetic structures*” (chapter, “Stroboscopic microscopy of magnetic dynamics”) Springer-Verlag, B. Hillebrands and K. Ounadjela, editors (2001).

- [66] Z. Shi, W. K. Hiebert and M. R. Freeman, “*Ultrafast Laser Diagnostics and Modeling for High-Speed Recording Heads*”, IEEE Trans. Mag., Vol. **35**, 632-636, 1999.
- [67] A. Y. Elizzabbi, M. R. Freeman, “*Ultrafast magneto-optic sampling of picosecond current pulses*”, Appl. Phys. Lett. **68**, 3546-3548 (1996).
- [68] M. R. Freeman, United States Patent and Trademark Office, “*Method for measuring current distribution in an integrated circuit by detecting magneto-optic polarization rotation in an adjacent magneto-optic film*”. Patent No. 5,663,652 (1997).
- [69] M. R. Freeman, United States Patent and Trademark Office, “*Fiber optic probe with a magneto-optic film on an end surface for detecting a current in an integrated circuit*”. Patent No. 5,451,863 (1995).
- [70] M. R. Freeman, G. M. Steeves, G. E. Ballentine, and A. Krichevsky, J. Appl. Phys. **91** (10), 15 May 2002.
- [71] M. R. Freeman, R. W. Hunt, and G. M. Steeves, Appl. Phys. Lett. **77**, number 5, 31 July 2000.
- [72] K. B. Klaassen, R. C. Hirko, and J. T. Contreras, “*High Speed Magnetic Recording*”, IEEE Trans. Mag, Vol **34**, pp. 1822-1827, 1998.
- [73] P. Arnett, R. Olson, D. Cheng, K. Klaassen, J. van Peppen, “*High Data Rate Recording at Over 60 Mbytes Per Second*”, IEEE Trans. Mag., Vol. **35**, pp. 2523- 2528, 1999.
- [74] S. W. Yuan *et al.*, “*Advanced Write Heads for High Density and High Data Rate Recording*”, IEEE Trans. Mag., Vol. **38**, pp. 1873 –1878, 2002.

- [75] R. Wood, M. Williams, J. Hong, “*Considerations for high data rate recording with thin-film heads*”, IEEE Trans. Mag., Vol. **26**, issue 6, 2954-2959, 1990.
- [76] M. Mallery, private communication.
- [77] M. Johnson *et al.*, Solid-State Electron. **44**, 1099 (2000).
- [78] R. L. Stamps and B. Hillebrands, Appl. Phys. Lett. **75**, 1143 (1999).
- [79] C. D. Olson and A. V. Pohm, J. Appl. Phys. **29**, 274 (1958); D. O. Smith in “*Magnetism*”, edited by G. T. Rado and H. Suhl, (Academic Press, New York, 1963), Vol. 3, p. 505.
- [80] J.-G. Zhu and Y. Zheng, IEEE Trans. Mag. 1998.
- [81] S. Schultz *et al.* “*The Magnetization Reversal Mode for Individual Single Domain Particles*”, J. Appl. Phys. **75**, 7989 (1994).
- [82] S. Kaka and S. E. Russek, Appl. Phys. Lett. **80**, 2958 (2002).
- [83] Th. Gerrits *et al.*, Nature **418**, 509 (2002).
- [84] H. W. Schumacher, C. Chappert, P. Grozat, R. C. Sousa, P. P. Freitas, M. Bauer; Appl. Phys. Lett. **80**, 3781 (2002).
- [85] Thomas Gerrits, private communication.
- [86] S. Sun, C. Murray, D. Weller, L. Folks, and A. Moser, Science **287**, p. 1989 (2000).
- [87] Q. Chen, A. J. Rondinone, B. C. Chakoumakos, and Z. J. Zhang, Journal of Magnetism and Magnetic Materials, **194**, 1, (1999).
- [88] S. Z. Jiang *et al.*, J. Appl. Phys., **78**, 439 (1995).

- [89] J. L. Dorman, D. Fiorani, F. Giammaria, and F. Lucari, *J. Appl. Phys.* **69**, 5130 (1990).
- [90] K. Tanaka, N. Tatehata, K. Fujita, and K. Hirao, *J. Appl. Phys.*, **89**, 2213 (2001).
- [91] N. M. Dempsey *et al.*, *J. Appl. Phys.* **90**, 6268 (2001).
- [92] G. T. Fei, J. P. Barnes, A. K. Petford-Long, R. C. Doole, D. E. Hole, *J. Appl. Phys.* **35**, 916 (2002).
- [93] Gerald T. Kraus *et al.*, *J. Appl. Phys.* **82** (3), pp. 1189-1195, August 1997.
- [94] S. Visnovsky *et al.*, *J. Magn. Mater.* **122**, p. 135 (1993).
- [95] K. D. Sorge *et al.*, *IEEE Trans. Mag.*, **37**, 2197 (2001).
- [96] A. Meldrum, R. F. J. Haglund Jr., L. A. Boather, and C. W. White, *Advanced Materials* **13**, 1431 (2001).
- [97] E. Cattaruzza *et al.*, *Appl. Phys. Lett.* **73**, 1176 (1998).
- [98] S. Honda, A. Modine, T. E. Hayes, A. Meldrum, J. D. Budia, K. J. Song, J. R. Thompson, and L. A. Boather, *Nanophase and Nanocomposite Materials III*, submitted (1999).
- [99] E. Alves, C. MacHargue, R. C. Silva, C. Jesus, O. Conde, M. F. da Silva, and J. C. Soares, *Surfaces and Coating Technology* **128**, 434 (2000).
- [100] A. Morisako, N. Kohshiro, and M. Matsumoto, *J. Appl. Phys.*, **67**, 5655 (1990).
- [101] J. X. Shen, R. D. Kirkby, and D. J. Sellmyer, *J. Magn. Mater.* **81**, 107 (1989).

- [102] K. Buchanan, private communication.
- [103] K. S. Beaty *et al.*, Mater. Res. Soc. Symp. Proc. **703**, 331 (2002).
- [104] E. Hecht, *Optics*, Addison-Wesley publishing company (1987).
- [105] M. J. Freiser, IEEE Trans. Mag. **MAG-4** 152 (1968).
- [106] H. Kim, A. Grishin, and K. V. Rao, J. Appl Phys. **78**, 439 (2001).
- [107] J. P. Castera, Encyclopedia of Applied Physics **9**, 157 (1994).
- [108] W.K. Hiebert, A. Stankiewicz and M.R. Freeman, Phys. Rev. Lett. **79**, 1134 (1997).
- [109] K. D. Harris, M. J. Brett, T. J. Smy and C. Backhouse, "*Microchannel surface area enhancement using porous thin films*", J. Electrochemical society **147**, 2002-2006 (2000).
- [110] K. Robbie, S. Shafai, and M. J. Brett, "*Thin films with nanometer scale pillar microstructure*", J. Materials Research **14**, 3158-3163 (1999)
- [111] B. Dick, M. J. Brett, T. J. Smy, M. R. Freeman, M. Malac, and R. F. Egerton, "*Periodic magnetic microstructures by glancing angle deposition*", J. Vacuum Science and Technology **A18**, 1833-1844 (2000).
- [112] K. Robbie, J. C. Sit, and M. J. Brett, "*Advanced techniques for Glancing Angle Deposition*" J. Vacuum Science and Technology **B16**, 1115-1122 (1998).
- [113] M. Malac, R. F. Egerton, M. J. Brett and B. Dick, "*Fabrication of submicron regular arrays of pillars and helices*", J. Vacuum Science and Technology **17**, 2571-2674 (1998).

- [114] D. Vick, L. J. Friedrich, S. K. Dew, M. Brett, K. Robbie, M. Seto, and T. Smy, “*Self-shadowing and surface diffusion effects in obliquely deposited thin films*”, *Thin Solid Films* **339**, 88-94 (1999).
- [115] D. E. Prober, M. D. Feuer and N. Giordano, “*Fabrication of 300-Å metal lines with substrate-step techniques*”, *J. Appl. Phys.*, **37**, 94-96 (1980).
- [116] Yong Peng, Tiehan-H. Shen, and Brian Ashworth, “*Magnetic nanowire arrays: A study of magneto-optical properties*” *J. Appl. Phys.* **93** 7050-7052 (2003).
- [117] “*Circuitry engineering*”, *Electrical Engineering (EE) University of Alberta handbook*.
- [118] A. Krichevsky, M Schechter, Y. Imry, and Y. Levinson, *Phys. Rev. B* **61** (5) pp. 3723-3733 (2000).
- [119] C. W. J. Beenakker, “*Transport Phenomena in Mesoscopic Physics*” (Springer-Verlag, Berlin, 1992).

Appendix A

Glancing angle deposition (GLAD).

A.1 Motivation.

The evolutionary trend of the electronic and magnetic storage devices is well known – shrinking dimensions of all active elements. This allows higher densities of information storage and also cuts the addressing and operation times of the active elements. In the main body of the thesis we showed that cutting the feature size results in faster flux rise times (and consequently of the write time) of new recording heads. In other experiments it was found that shrinking the yoke length and applying multilayer coils work to that effect as well [15],[74],[108]. The yoke length is in turn determined by the outer diameter of the thin-film spiral coil, using a multilayer coil helps to achieve the same magnetic field value with fewer turns. An ideal geometry for a coil would be, of course helical rather than spiral, but as of now deposition would imply a complicated multi-step lithography process. The same limitation impacts the potential profitability of Magnetic Random Access Memories: the expensive multistep lithographic process forming isolated crossed wires with numerous

alignments between depositions.

In this section we suggest a new lithographic process promising to circumvent some of these difficulties. It allows one to form helical microcoils with arbitrary number of turns in just two steps of lithography, and significantly decrease the number of lithography/alignment steps required for the formation of crossed wires. This technique is not limited to magnetic sample fabrication, and can also find use in other areas of microfabrication.

The key idea of this method is based on the fact that we are living in a three-dimensional space rather than a two-dimensional one. Most lithographic techniques involve normal deposition of desired material on a substrate coated by patterned resist or shadow mask (e.g. evaporation at low pressure); diffusive coating by ions, atoms or molecules of the coating substance bombarding a substrate randomly from all direction (e.g. sputtering, high pressure evaporation); or any combination of both. In some cases the source of the deposition material (the “gun” below) is positioned at an angle to the substrate, rotating in the holder in order to avoid shadowing effects and ensure conformal coating.

However, self-shadowing of the resist is not necessarily an obstacle to achieving good results, as it can be exploited as a shadow mask to an oblique beam. The idea of oblique (glancing angle) deposition or GLAD is not new. It has been used extensively to obtain highly porous thin films [109], and to form random and regular arrays of nano-pillars and nanohelices [110]-[113]. Shadowing effects play the dominant role in the GLAD processes [114]. Oblique deposition in combination with ion-milling was also used to form metallic nano-wires with high height-to-width ratio [115].

A.2 Deposition of the crossed wires.

The manner in which shadowing can cause the substrate to “see” a different pattern that is developed on the resist is illustrated in Fig. A-1. For instance,

an array of rectangular pillars (Fig. A-1 *a*) appears in the case of crossed trenches developed in the resist (corresponding mask shown in Fig. A-1 *b*). However, when viewed at say 30° elevation from one side it appears as an array of parallel rows (Fig. A-1 *c*), and a set of parallel wires can be deposited by a gun at the position of the viewer. This array can be isolated from the rest of the deposited layers either by glancing angle, normal (90° elevation of the gun), or diffusive deposition of an insulating material. Subsequently, the substrate may be rotated 90° and a second set of wires (crossing the primary set yet isolated from them) is deposited by GLAD.

Since the deposition of several isolated layers does not require additional lithographic steps, the entire deposition can be performed without removing the sample from the vacuum chamber, preventing oxidation and other sorts of the surface contamination, thus achieving a higher quality of junctions interconnected by crossed wires. It even creates a possibility of patterned MBE growth of semiconductor materials, if one uses an MBE compatible shadow mask.

The technique is not limited to orthogonal sets of crossed wires. In the figure A-1 *d* a hexagonal mask array is shown, and a set of cylindrical pillars (A-1 *e*) effectively can be seen as three independent sets of intersecting trenches when viewed at 30° , 90° and 150° respectively (Fig. A-1 *f*), for glancing angle deposition of three sets of crossing wires (A-1 *g*). An elongated element (such as an MTJ sandwich) can be created at the intersection (exactly where it is supposed to be for MRAM applications) using the same trench pattern. First, all relevant layers for the MTJ junction are deposited at glancing angle along say, wire #1 (Fig. A-1 *g*, light gray). Then, a cap layer of the same thickness is deposited via GLAD along the wire #2 (bold gray). Note that resulting thickness of the material deposited along the wires doubles at the rhombic area of the intersection. Third, the substrate holder is turned for normal ion-milling that destroys the cap layer everywhere and the sandwich layers

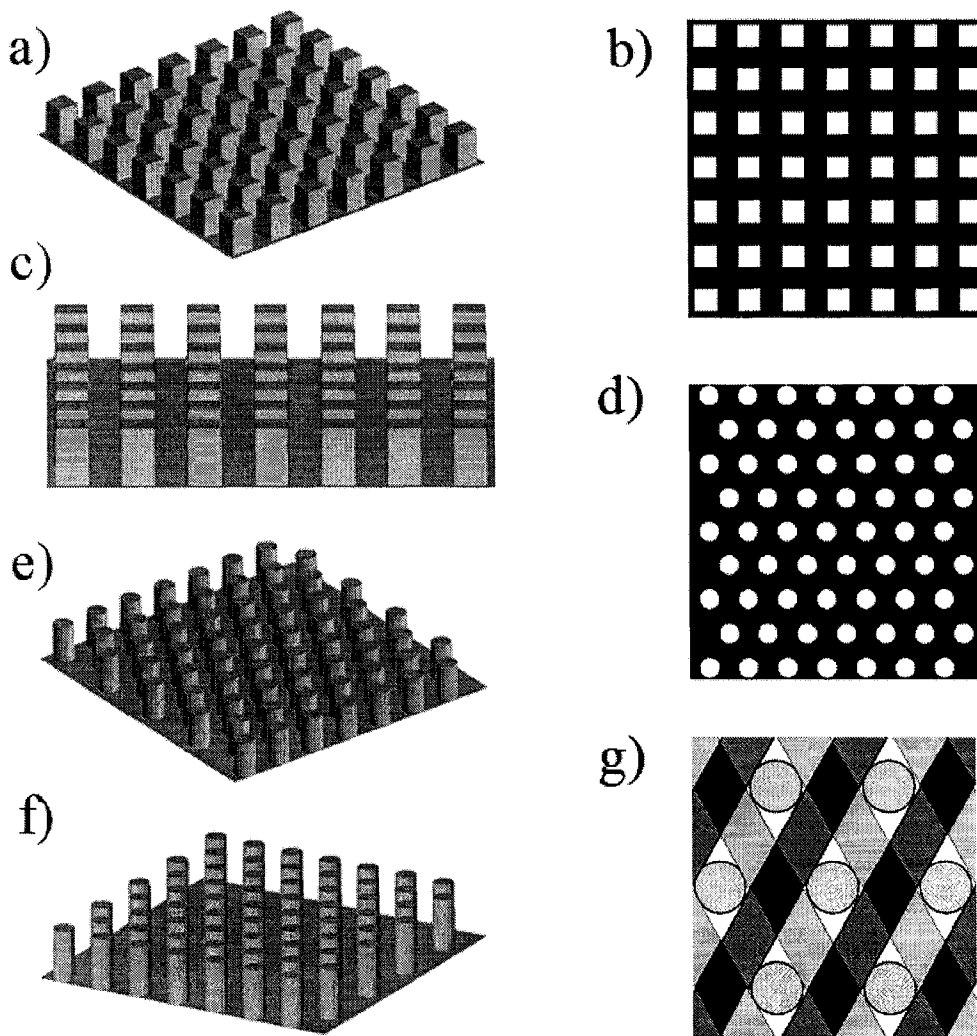


Figure A-1: (a) Model square lattice of rectangular pillars similar to the structure formed by developing crossed trenches in the resist. (b) Plan view of the same structure. (c) Micropillar array as seen from 0° azimuth and 30° elevation. (d-f) analogous projections for a hexagonal lattice of cylindrical pillars. The view in the plot (f) is from 30° azimuth, 30° elevation. (g) Typical structure of hexagonal wires as would be deposited in hexagonal array. Two sets of wires (light and bold gray) intersect forming an array of elongated rhombic elements (black).

everywhere but at the intersection. Several steps of the MRAM deposition including complex ferromagnetic element patterning can be undertaken in a single lithographic process. More complex masks can be used for formation of local islands of exposed material buried under other layers deposited by GLAD at different orientation, such as metal islands for contact pads. Again, this technique is by no means limited to MRAM applications, but can and should be used in other microfabrication processes.

Hexagonal arrays of nanopillars should not necessarily be limited to patterning by photo- or e-beam resist development. An interesting alternative is to pattern the nanopillar arrays through *self-organizing* nanopores in etched silica [116], although this remains a “long shot” for large area patterning at the current level of technology.

A.3 Thin wire deposition.

Another interesting application of glancing angle deposition process is decreasing of the minimum feature size of patterned objects beyond that set by the lithography. In general, the minimum feature size for photo- or e-beam lithography is diffraction-limited for imaging fine details on special resist. However, once the resist is developed, bombarding the substrate by much heavier ions lifts this limitation and gives an opportunity to form structures narrower than the resist window would imply. An illustration of this kind of deposition is shown in the Fig. A-2. In this example, two successive depositions result in different structure of the coating in the cases of wide (Fig. A-2 *a, c*) narrow (*b, d*) trench. In the latter case, a part of the substrate inside the resist trench remains uncoated. However, in the former case the central area of the trench is coated with the layer of double thickness, and the width of the deposition overlap depends on the deposition angle (and collimation quality), the resist thickness and the smoothness of the resist lip, but not on the trench width.

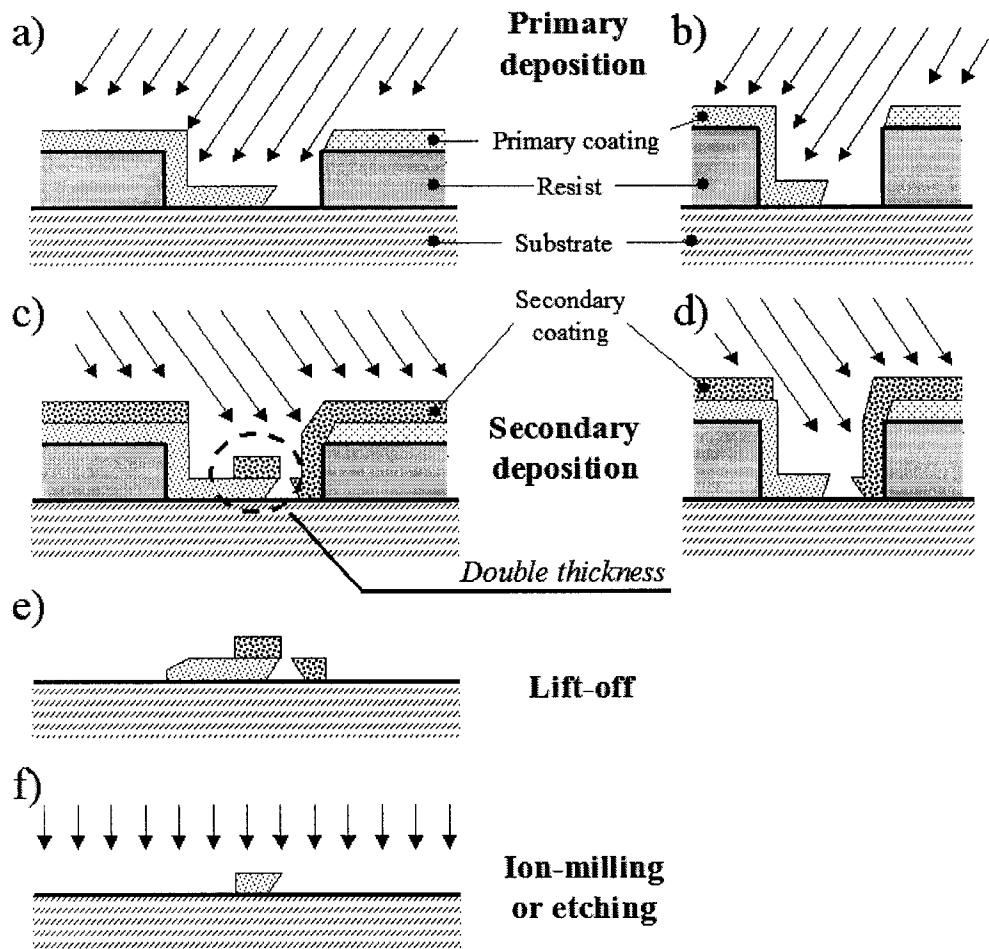


Figure A-2: Thin wire formation by GLAD. Glancing angle deposition of the first layer in the case of wide trench (a) and narrow trench (b). Second deposited layer may (c) or may not (d) overlap with the first one. In the case of the overlapping layers the lift-off results on double thickness “wire” narrower than the trench itself (e) that can be converted to a real wire by ion milling (f).

Diffraction of the atomic flux is negligible, it is just a classical shadowing forming a narrow wire at the middle of the trench. The deposited material can be subsequently etched (Fig. A-2 *f*) after lifting off the resist (Fig. A-2 *e*) in order to obtain a true nanowire. Alternatively, instead of removing the material it could be chemically treated (e.g. aluminum could be oxidized), to change its properties in the thin layers but maintain to some degree its initial properties in the capped middle area. The capping layer can also be made of a different substance.

A.4 Helical and spiral structures.

In this section we discuss the growth of yet more complex structures using GLAD, keeping in mind the possibility of direct application of helical microstructures in industry, for example in the excitation coils of recording heads. Again, the key point is that the mask “seen” by a substrate in the GLAD process may differ from the plan view of the pattern developed in the resist (Fig. A-3). In particular, a cross-section of a circular trench through the ring center has narrower wells than one viewed near to the ring edge (Fig. A-3 *a*). Thus the particle flux of GLAD condenses at the resist wall for the cross-section A-A (Fig. A-3 *b*), but can reach the substrate near the edge (cross-section B-B, Fig. A-3 *c*). It is easier to visualize in a 3-D sketch of the ring trench (Fig. A-3 *d*) shown at an angle of 50° to the surface. The only parts of the substrate (the bottom of the trench) seen in this sketch are two D-shaped segments on the sides, which are exactly where the material would be deposited in a GLAD process forming two islands of coating at the substrate. The result of a simultaneous deposition by two independent sources located at 90° azimuthal angle to each other and at 50° to the surface is shown schematically in Figure A-3 *e*. If the substrate rotates during the deposition process, each island travels along the trench climbing atop previous layers

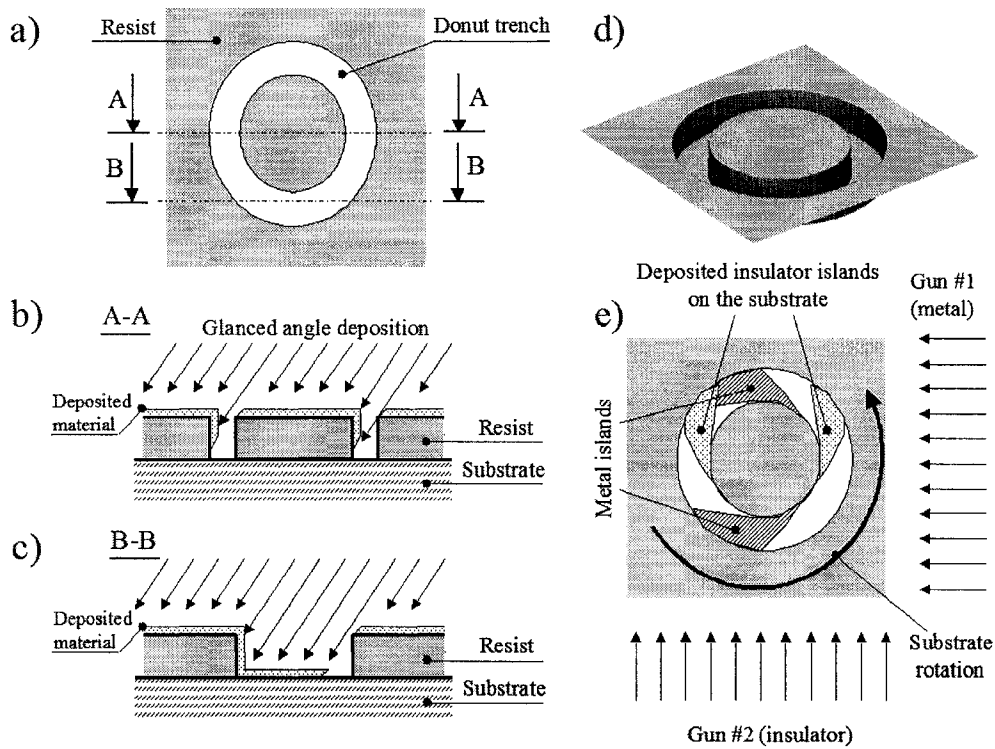


Figure A-3: (a) Plan view of the ring (donut) shaped trench in the resist. (b,c) different cross-sections of the trench and schematic view of the glancing angle deposition of a material in the trench. Molecular flux is does not reach the bottom of the trench in the middle of the donut (b), but does so closer to the edges (c). (d) 3-D view of the trench at 50° elevation angle. (e) A schematic representation of simultaneous GLAD on a rotating substrate by two independent sources.

and forming a helical (or double-helix) structure. The number of coil turns is arbitrary. Moreover, since the details of the deposition process depend only on the *angle* between the gun and the substrate and not on the position across the wafer (provided the beam is well-collimated), multiple coils can be formed on the surface of a single wafer, just as required for commercial recording head depositions where $\simeq 40,000$ heads populate a single substrate. The same argument applies to the crossed wire deposition.

Another example shows the formation of “jellyroll” rather than helical structures by GLAD, using an initial pattern of pillars. The pillars can again be made of any resist, but also can be parts of previously deposited structures such as parts of permalloy yokes of recording heads. Two guns deposit from different directions metal and insulator correspondingly (Fig. A-4 *a*) on a rotating substrate with pillar-like structures. This deposition results in spiral-like coating of the pillar walls and helical coating of the shadowed area of the substrate. The rest of the substrate and the pillar top are exposed to both guns and a film of mixed composition grows there (it can be made insulating by choosing appropriate deposition rates of the sources). When the desired number of wraps are formed, the substrate is exposed to normal ion milling (Fig. A-4 *b*) to destroy the deposited film everywhere but at the wall of the pillar. The latter survives due to the favorable aspect ratio. Now the pillar is wrapped with several layers of alternating metal and insulator spiral sheets (Fig. A-4 *c*). Making electric contacts to the inner and outer parts would complete the coil formation. This spiral coating could result in much more compact coils and consequently shorter head yoke due to the fact that the lateral size of the coil is determined by *thickness* of the layers (that easily can be brought to the nanometer range) rather than the *width* of lithographically defined spiraling wires (tens or hundreds of nanometers with a good e-beam system). This structure might also be manufacturable using a single source of aluminum at low oxygen pressure (in this case the cap layer is conductive, but

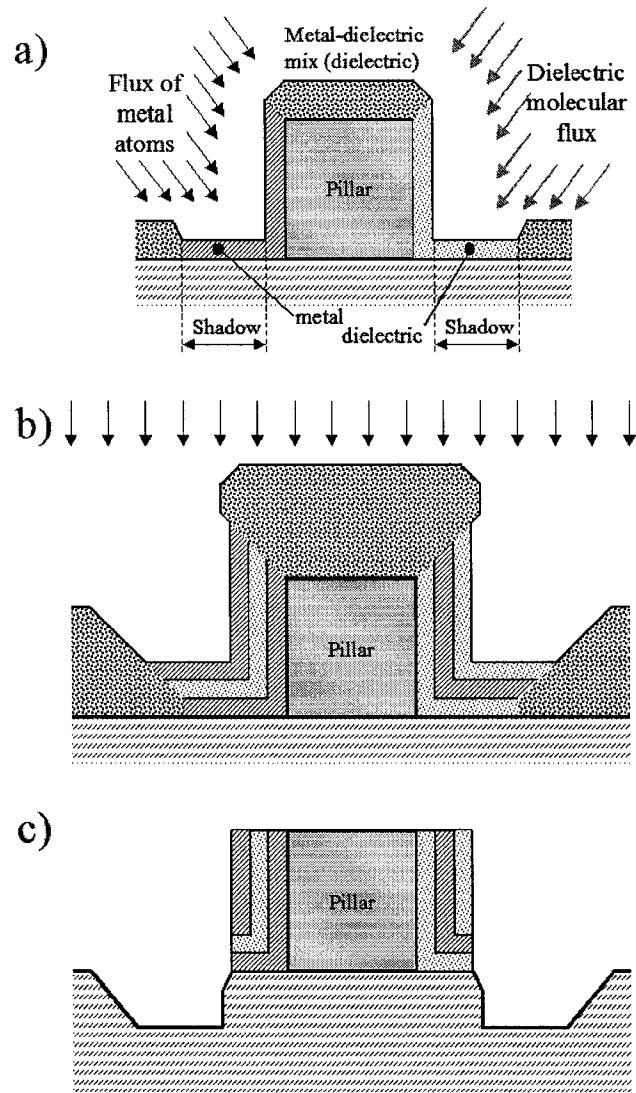


Figure A-4: (a) Two-source GLAD onto a pillar coats its walls and the shadowed area with metal or insulator; but the top of the pillar and the rest of the substrate are coated by both of them. (b) Rotating the substrate during the deposition results in spiral/helical wrapping of the pillar by metal and insulator sheets. Subsequent normal ion milling destroys the coating everywhere but at the pillar wrapping. The resulting “coil” cross-section is shown in the plot (c).

it is to be removed anyway). Alternatively, a secondary lithography step could be made before ion milling isolating the area shadowed during the deposition. The result of the milling would be a helical structure rather than a spiral pillar wrapping. In this particular case the spiral structure might be advantageous over the helical one, achieving more compact coil.

In the section A.6 we describe our attempt to observe the above effects (crossed-wire deposition, feature size reduction and pillar shadowing) experimentally.

A.5 Deposition system.

In this section we present the deposition system (Fig. A-5) used in the GLAD experiment. A vacuum-sealed stepper motor (the vacuum-tight cage is made by Tony Walford) contains a stepper motor that can index in 1.8° steps. Sample holder table is attached to the motor shaft and the substrates with developed photoresist are held at the table by tapered clamps that do not shadow glancing angle deposition. The motor axis is tilted 45° to the molecular beam direction. Remotely controlled motor indexes in $\pm 90^\circ$ steps. We would like to thank Greg Popowich for programming the remote control unit and both Greg Popowich and Don Mullin for their kind assistance with the deposition process.

A.6 Experimental results.

In order to confirm the advantages of GLAD we performed depositions of aluminum and aluminum oxide (sapphire) on sapphire substrate covered by patterned photo-resist. The particular choice of deposition materials was based on the expectation of good adhesion of aluminum and sapphire to each other and also on wide use of Al/Al₂O₃ composites in industry. Since we did not

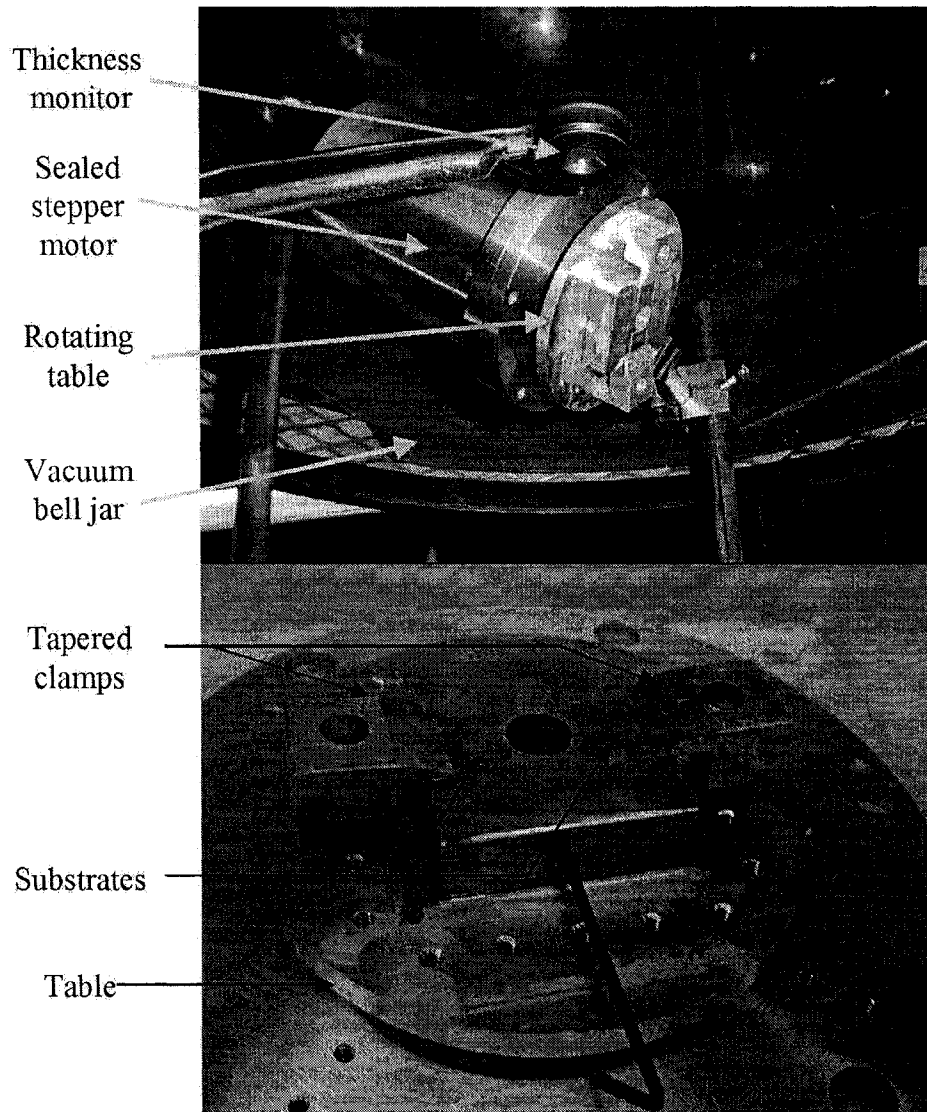


Figure A-5: (Top) assembled vacuum-tight stepper motor housing in the deposition chamber. (Bottom) The substrate holder with tapered clamps that do not impede the glancing angle deposition.

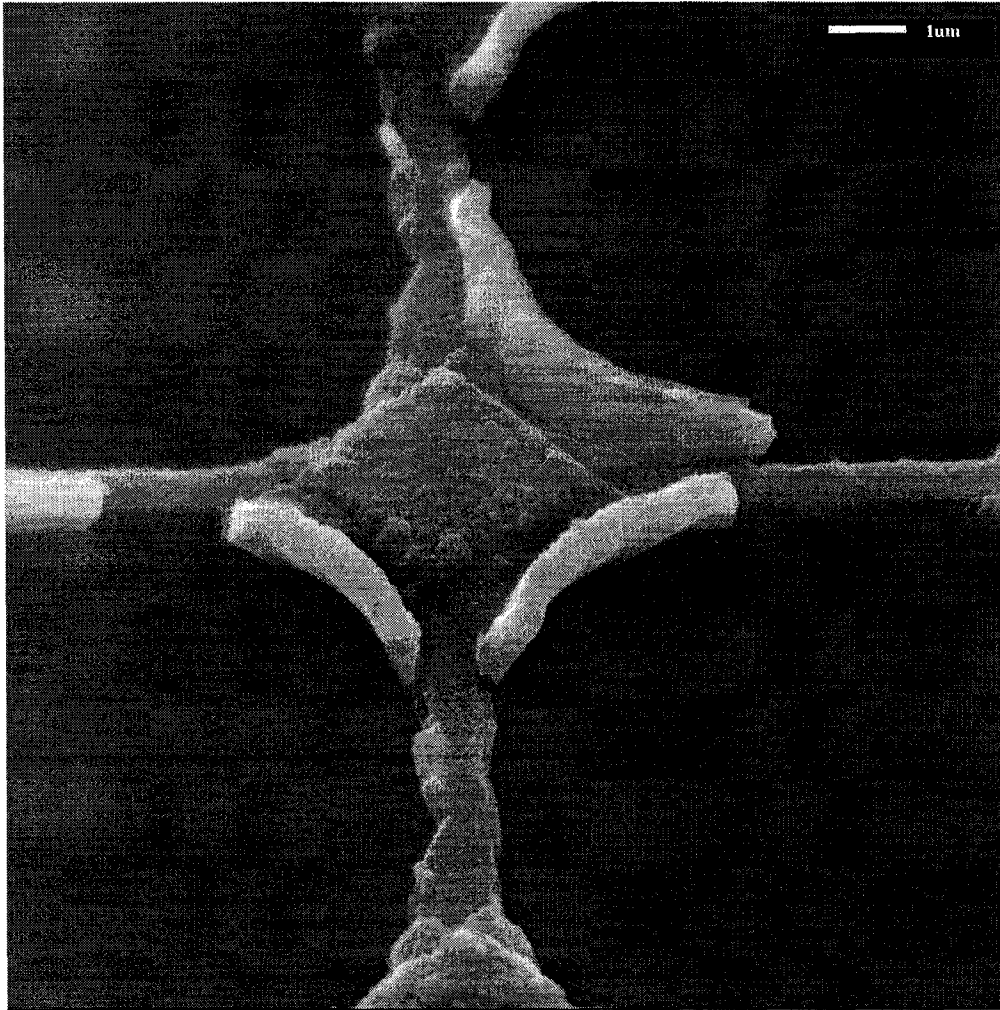


Figure A-6: Crossed wire deposition by GLAD after lift-off. The central area is elevated as the thickness of deposited material doubles there. The burrs of Al/Al₂O₃ are the result of the resist wall coating and incomplete lift-off.

have two independent evaporation guns, the layers of aluminum and sapphire were deposited successively and the substrate was rotated 90° or 180° between the depositions by a stepper-motor (see Section A.5). The lithographic mask included the following elements: (i) rectangular arrays of orthogonal crossed trenches of different width and spacing; (ii) complementary arrays of “wires” (or arrays of rectangular holes in the resist); (iii) circular pillars; (iv) complementary circular holes; (v) circular and square donut trenches and (vi) complementary circular and square donuts. We estimate the thicknesses of the resist layers on two different substrates as $1.3\ \mu\text{m}$ and $2.5\ \mu\text{m}$ respectively, based on the resist calibration graph for the particular spinning rate. The trench width varied from $2\ \mu\text{m}$ to $8\ \mu\text{m}$ in the photomask. The following deposition sequence was used:

1. Deposition of 140 nm of Aluminum (in fact it was 200 nm at a 45° deposition angle).
2. Substrate is rotated 180° . Deposition of 140 nm of Al_2O_3 .
3. Substrate is rotated 90° .
4. Repeat steps 1-3 up to a total of eight layers of coating.

This particular deposition sequence was chosen in order to ensure the helical connection between subsequently deposited layers in the square donut trenches. The substrate was subsequently examined using Scanning Electron Microscope. We are deeply indebted to George Braybrook and Dr. Dong-Chan Lee for providing the high-resolution SEM images shown below. Unfortunately the contrast between the alternating layers was too low to resolve the helical nature of the structures if it indeed is present.

A typical result of the crossed-wire deposition in the case of narrow ($2\ \mu\text{m}$) trench is shown in the Fig. A-6. Nothing reaches the substrate in the

trench perpendicular to the direction of the deposition anywhere but at the intersection. As expected (Fig. A-1 *d*), at the intersection there is a rhombic (diamond in the particular case of the square lattice) area of double thickness of deposited material. The burrs at the edges are the result of incomplete lift-off. Apart from these broken burrs it appears that both deposition and lift-off went very well, with structures firmly adhered to the substrate.

In the case of wider trenches (Fig. A-7) the atomic/molecular beam does reach the bottom of each trench causing an overlap of deposited layers. In this case there are continuous wires of double-thickness material formed at the bottom of the wider trench (Fig. A-7 *a*). Note that there are no diamond-shaped elevated areas at the trench intersections as the central area of the wider trench is exposed to the deposition at all times. On the other hand, an enlarged scan of the narrower trench (Fig. A-7 *b*) shows the lack of layer overlap in agreement with Figure A-2 *d*.

GLAD on the intersecting $2\ \mu\text{m}$ and $3\ \mu\text{m}$ trenches in $1.3\ \mu\text{m}$ -thick resist caused formation of a thin 500-600 nm double-thickness wire (Fig. A-7 *c, d*), obeying the scenario shown in Fig. A-2 *c*. Actually the trench looks more like $2\ \mu\text{m}$ since 500-600 nm of aluminum and sapphire are deposited at the wall face. The minimum feature size is reduced six-fold compared to the one that would be achievable in normal or diffusive deposition, even despite a rough top surface and consequently wavy shadowing edge. This design can certainly be scaled down and in the case of a good e-beam resist (such as PMMA) true nanowires can be built.

Figure A-8 shows the result of the GLAD on a substrate with a resist micropillar. The initial pillar diameter (before coating) is $\approx 4\ \mu\text{m}$ the resist thickness is $\approx 1.3\ \mu\text{m}$. The pillar shadow clearly forms a clover-like dip in the deposited material. The deposited Al/Al₂O₃ composite forms a mushroom-cap at the top of the pillar. Wherever the cap was removed by lift off and the resist dissolved, the deposited material contained an octagonal crater. This

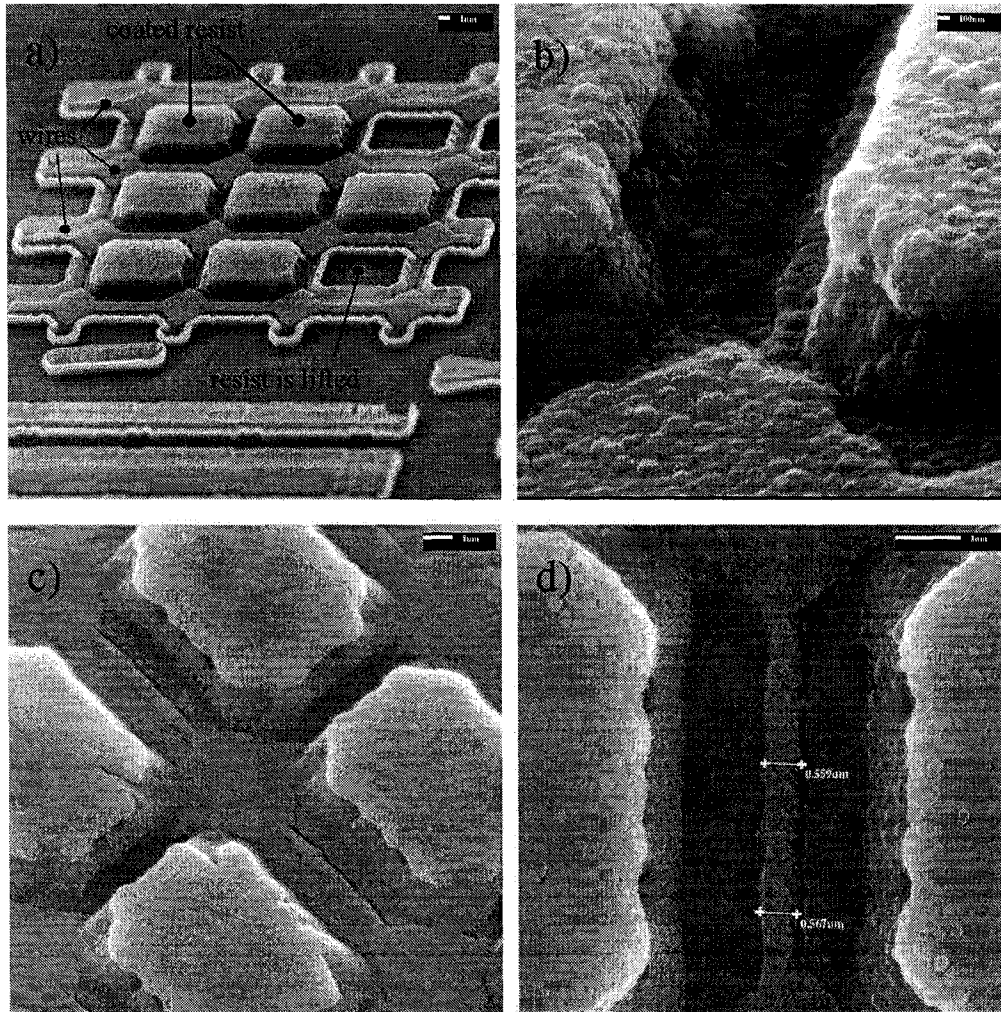


Figure A-7: Wide-trench deposition. (a) General case where one trench is wider than the other. Horizontal double-thickness wires are fully developed, while in the narrower vertical trench deposited layers do not overlap. (b) Enlarged narrow-trench area. (c) Thin wire formed in a $3\text{-}\mu\text{m}$ wide trenches. (d) The same, plan view, enlarged.

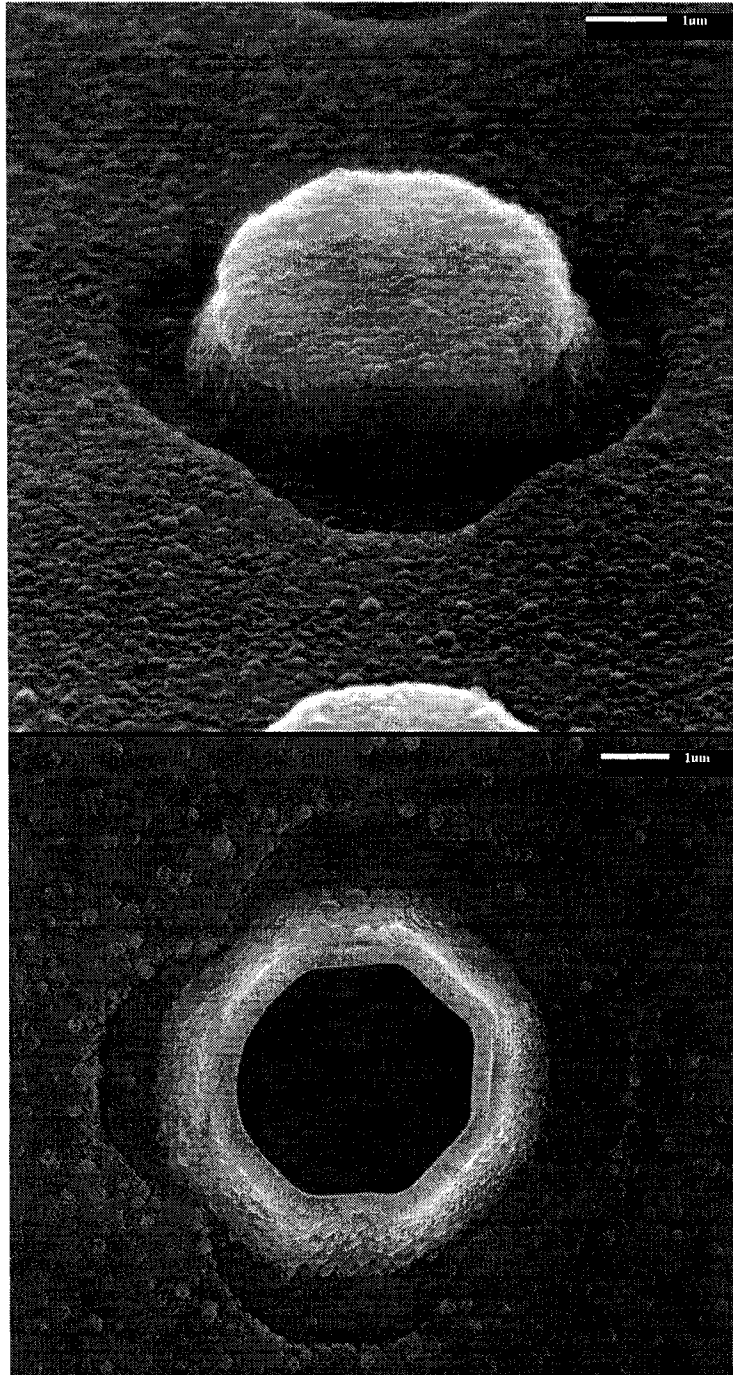


Figure A-8: (Top) A micropillar coated by Al/Al₂O₃ composite forming a mushroom-like cap at the top of the pillar. (Bottom) Similar structure, plan view. The cap is removed during lift-off. The pillar shadow causes clover-like dip in the deposited material.

octagonal shape is obviously connected to the specific conditions of our deposition: the substrate was only rotated in increments of 90° .

Finally, a complex structure formed at the bottom of the square wells in the resist by multiple shadowing is shown in the Fig. A-9. We didn't expect to find this in advance (although its formation is perfectly understandable in retrospect), and have no idea of its immediate application. However, it nicely demonstrates the complexity of the structures that can be built using GLAD. Once formed, these structures (such as semiconductor junctions) can be interconnected using GLAD again or by means of conventional lithography.

A.7 Summary.

We suggested a new lithographic process (controllable Glancing Angle Deposition on patterned resist) that we believe has certain advantages over conventional lithography. Mutually isolated crossed wires can be deposited in a single lithographic step. Consequently, the substrate does not need to be removed from the deposition chamber for re-patterning, that can contribute to its contamination. Several steps of MRAM structure deposition can be combined reducing the processing time and eventually the cost of the product.

Shadowing effects can also be used for micro- and eventually nano-scale fabrication of spiral and helical structures with arbitrary number of turns in few lithographic steps. Since the deposition process depends on the angles between the substrate and the deposition fluxes but not on the position of the structure across the wafer, multiple structures can be deposited at the same time.

The minimal feature size can be reduced beyond the resist resolution by suitable application of the deposition flux shadowing.

The test deposition conducted in our laboratory confirmed our expectations on the scenarios of the glanced angle deposition process. Various shadowing

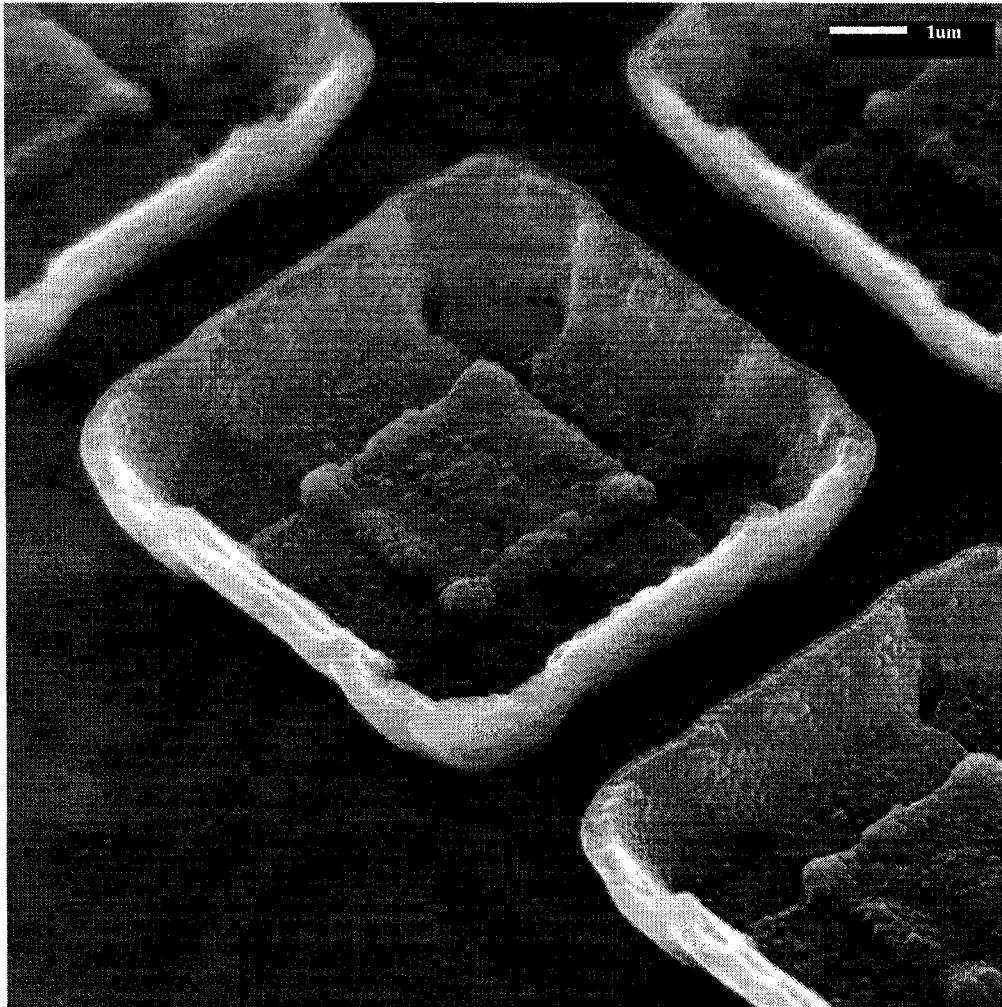


Figure A-9: A complex structure created in a square well of the resist. Different levels of material elevation are the result of the shadow overlap.

regimes observed.

A Report of Invention is in preparation.

Appendix B

Local excitation by a split-pole head

In chapter 3 we noted that the switching of one of the recording head poles (P_2) lags behind the other (P_1). In terms of the generated magnetic field it means that initially the field is not nearly longitudinal at some distance from the ABS plane of the head (emerging from one pole and returning through the other), but rather has a strong out-of-plane component (Fig. B-1). This out-of-plane component is localized laterally by the nose width of the pole (few hundred nanometers) and persists only for short period of time until the second pole “wakes up” and saturates quickly, sucking in all the flux and ensuring the desired in-plane field required for normal operation of longitudinal recording heads. During this short period, a longitudinal recording head may act effectively like a perpendicular one. It is tempting to study the effect of such localized excitation on a thin-film ferromagnetic material placed directly atop the recording head. This might mimic the performance of a soft underlayer, and thus address the question how the underlayer can affect the writing process (slow it down, in particular). On the other hand, a bulk thin film possesses strong in-plane anisotropy and is in-plane magnetized. One can ensure

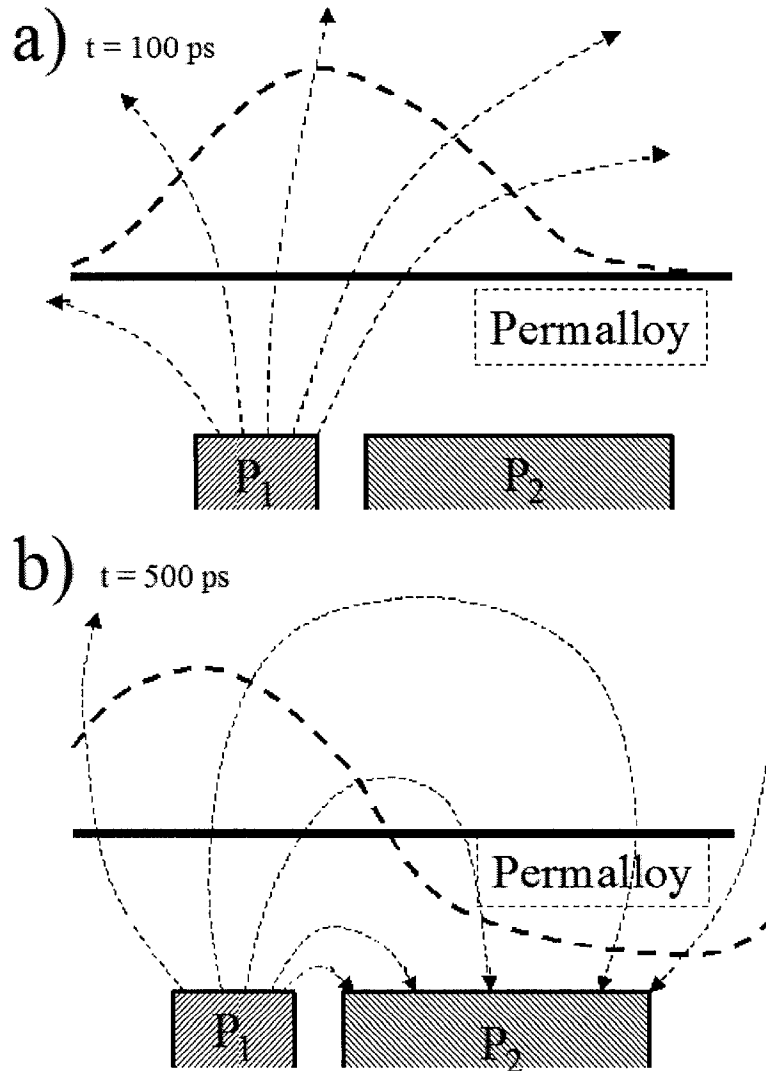


Figure B-1: Schematic field (thin dashed lines) generated by recording tip poles in the very beginning of the switching process (a) when the pole P_1 is being switched, but P_2 still hesitates; and further down the switching when the horseshoe magnet is nearly saturated (b). Thick dashed line represents the out-of-plane component of the field.

a certain direction of magnetization by applying in-plane DC bias field. When the thin film is locally perturbed by a short out-of-plane “kick”, there is an opportunity to observe spreading spin waves emanating from the center of the excitation (much like in the case of an elastic membrane hit at the center).

In order to bring the head into contact with permalloy film, we deposited a 15-nm thick $20 \times 5 \mu\text{m}$ a permalloy ($\text{Ni}_{80}\text{Fe}_{20}$) structure on a polished silicon dioxide substrate, flipped it upside down and pressed against the slider mounted on a separate glass plate. In order to keep the pieces permanently attached we put a drop of UV cement between the glass substrates. The parts were aligned such that the line connecting the poles P_1 and P_2 was parallel to the long axis of the rectangle, using an ABM mask aligner the Nanofab. The cement was polymerized with the parts under pressure using the mask aligner’s UV lamp. Unfortunately, during the aligning process the permalloy rectangle was scratched and a part of it was completely detached from the substrate. The remaining piece has a nearly rectangular shape as well, and dimensions of approximately $12 \times 5 \mu\text{m}$. This method does not result in controllable spacing and the excitation is not localized spatially, as we can see diffraction fringes suggesting at least several micrometers distance. However, we still expect it to be short in duration and relatively strong as it is generated by nearly saturated ferromagnetic pole.

The sample was imaged through the quartz substrate of the permalloy using 0.3 numerical aperture objective and 800 nm wavelength light. The entire TR-SKM layout is similar to the one shown in Figure 5-2 *b*, where the Write Wires are replaced by a recording head slider. The head is charged by a unipolar Picosecond Pulse Lab (PSPL) generator producing 10 V pulses (suitably attenuated in order to achieve 50 mA write current) of 50 ps rise time. The current in the head coils has slower rise time of ≈ 500 ps according to our garnet sensor measurements and the head shield response traces. There is no contradiction with the fact that FWHM of the out-of-plane kick is 400 ps or

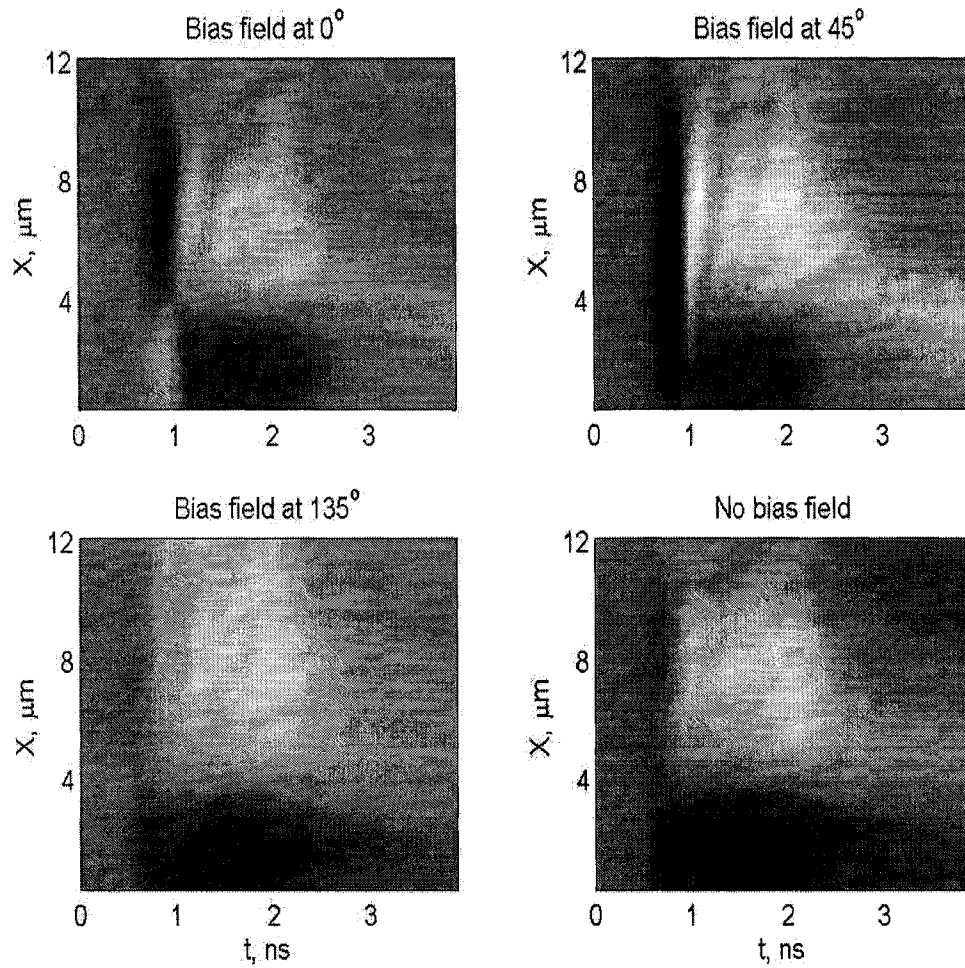


Figure B-2: Spatio-temporal scans of thin film permalloy sample excited by a separated recording head placed directly underneath it. The entire fixture is subjected to in-plane magnetic field caused by a permanent magnet. The orientation of the magnet can be changed in plane, zero degrees corresponds to the field direction from P_2 to P_1 in the ABS plane of the recording head.

even less on some occasions: this is the advantage of the differential technique, as saturating poles operate in a highly non-linear regime. In addition, in-plane DC bias field of 50 Oe can be applied by a permanent magnet at an angle ranging from -10° to 180° . Zero degrees corresponds to the direction of the bias field from the pole P_2 towards P_1 .

Spatio-temporal scans of the sample magnetization are shown in the Fig. B-2. The x -coordinate is parallel to the long axis of the sample, the grayscale represents out-of-plane magnetization (the same scale for all scans presented in Fig. B-2). Response scenarios depend on the applied magnetic field, but some features are common. First, as expected, there is a brief period of negative response between 0.7 and 1 ns time, with the exception of the 0° bias field scan where some positive signal is also observed atop the pole P_1 . Evidently, in the presence of this bias field the head is initially magnetized in the direction opposite to its final state. Second, as the head is saturated at later time, the film magnetization follows the pattern schematically shown in Fig. B-1 *b*: it has opposite polarities atop the poles of saturated horseshoe magnet. Third, the ripples of magnetization are evident, especially pronounced in the scans recorded at zero and 45° bias field.

To take a closer look at these ripples and fast initial response, we plotted the cross-section of the XT scans averaged over a few micrometers versus time. Resulting temporal scans for the bias field at 0° and 45° are shown in Figure B-3 *a* and *b* respectively. The FWHM of the initial response is between 200 and 250 ps, even shorter than our initial estimation. This is a strong result as it shows fast reaction time of the soft thin film to the out-of-plane excitation and thus the existence of the Soft Underlayer (SUL) is not likely to impede the performance of perpendicular recording heads. As for the ripples of magnetization we suggest that they are attributed to the ferromagnetic resonance. The frequency of magnetization oscillations in the Fig. B-1 *a, b* is between 2.5 and 3.5 GHz. Kittel's formula [57] for a bulk permalloy ($M_s = 800$)

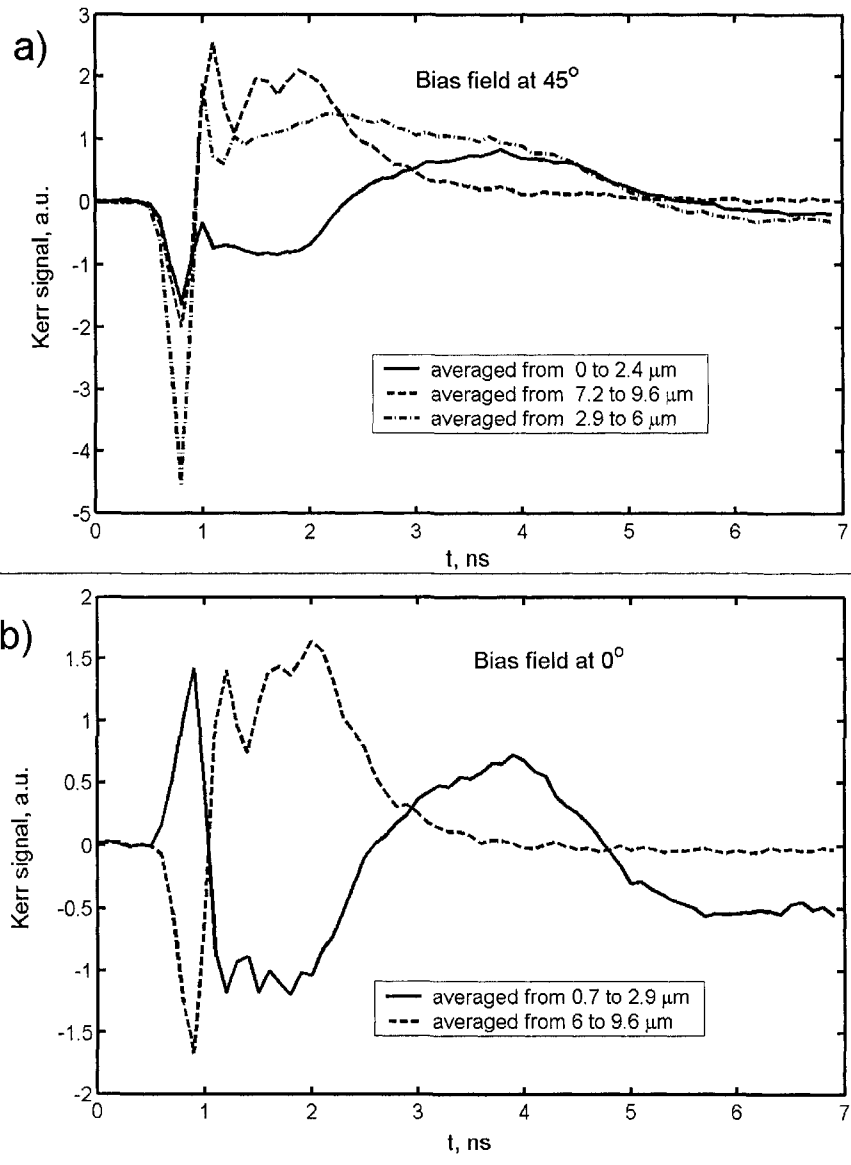


Figure B-3: "Temporal profiles" cut from the spatiotemporal scans in the Fig. B-2 by spatial averaging across indicated ranges. All traces show a strong peak of ≈ 400 ps FWHM, corresponding to the fast out-of-plane response of the P_1 pole of the recording head.

plane film and 50 Oe bias field predicts a frequency of ≈ 2.0 GHz. Taking into account the finite size of the specimen and unknown demagnetizing factors for this particular shape it is not a bad agreement.

Appendix C

Transmission lines.

C.1 General principles.

In this section we discuss a very important issue of voltage and current pulse propagation in transmission lines (such as microwave coaxial cables and strip-lines), termination of the lines and pulse combining and splitting [117]. These issues become important as the pulse risetimes and durations become comparable to or smaller than the pulse propagation time down the connecting wires and cables. To put this in perspective, a typical Picosecond Pulse Lab Generator produces a pulse of 10 ns in duration, and 50 ps of risetime. The typical propagation speed along teflon dielectric coaxial cables is approximately $2/3 c$. This means the pulse “length” is ≈ 2 m, and the reflections may distort the pulse shape if the cable length is less than 1 m (for back and forth travel of two meters). What’s more, the 50 ps risetime corresponds to a length of just 1 cm, and proper transmission lines should be brought significantly closer than this to the actual sample in order to ensure the fast risetime and proper profile of the current pulse through the sample. No material presented in this Appendix is new, we present it here for the sake of completeness: the understanding of the origin of pulse reflections is crucial for proper design of the experimental

system and for the safe operation of the equipment.

We begin with an example of an ideal lossless transmission line that can be represented as an infinite series of distributed inductances and parallel capacitors (Fig. C-1 *a*). This is a realistic representation of say, coaxial cable whose inductance and capacitance between inner and outer conductors is proportional to the cable length. Denote the inductance per unit length as L and the line stray capacitance as C . As a current pulse propagates along the wire, the line inductance causes voltage changes proportional to the current change rate:

$$\frac{\partial V}{\partial x} = -L \frac{\partial I}{\partial t} \quad (\text{C.1})$$

On the other hand, varying voltage causes displacement current through the capacitors, proportional to the voltage change rate:

$$\frac{\partial I}{\partial x} = -C \frac{\partial V}{\partial t} \quad (\text{C.2})$$

Relations (C.1),(C.2) are known as “Telegraphists equations”. Differentiating (C.1) with respect to x , (C.2) – with respect to time (or vice versa) and subtracting them from each other yields after elementary manipulations the wave equations:

$$\frac{\partial^2 V}{\partial t^2} - \frac{1}{LC} \frac{\partial^2 V}{\partial x^2} = 0 \quad (\text{C.3})$$

$$\frac{\partial^2 I}{\partial t^2} - \frac{1}{LC} \frac{\partial^2 I}{\partial x^2} = 0 \quad (\text{C.4})$$

Any function of the form $V^\pm = V(x \mp vt)$ and $I^\pm = I(x \mp vt)$ satisfies the equations (C.3,C.4) for voltage and current respectively. Superscript “+” corresponds to the right-going waves, “-” – to the left-going ones. The wave velocity v is defined as

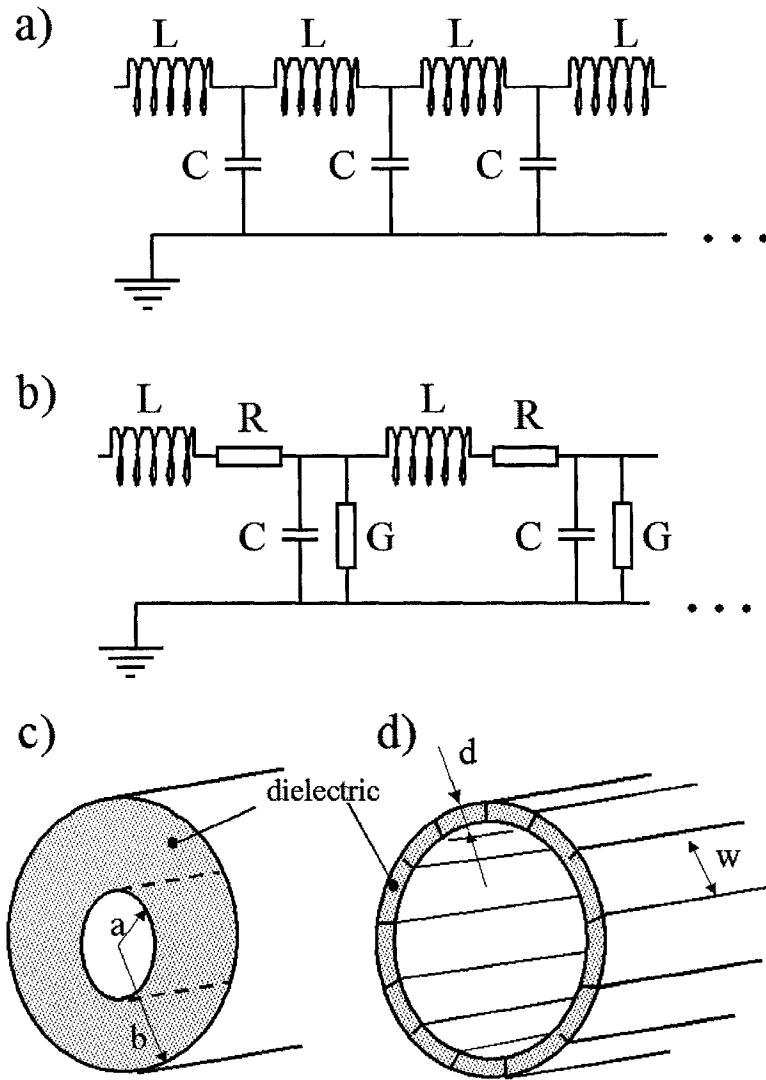


Figure C-1: (a) A schematic representation of an ideal lossless transmission line as uniformly distributed inductance and parallel capacitance. (b) Model representation of a lossy line. (c) A typical coaxial line. (d) A coaxial line with close inner and outer radii can be represented as a collection of parallel strip-lines.

$$v = \frac{1}{\sqrt{LC}} \quad (\text{C.5})$$

Now substitute V^\pm and I^\pm into equation C.1:

$$\frac{\partial V^+}{\partial x} = -L\left(-\frac{1}{\sqrt{LC}}\right)\frac{\partial I^+}{\partial t} = Z_0\frac{\partial I^+}{\partial t} \quad (\text{C.6})$$

$$\frac{\partial V^-}{\partial x} = -L\left(\frac{1}{\sqrt{LC}}\right)\frac{\partial I^-}{\partial t} = -Z_0\frac{\partial I^-}{\partial t} \quad (\text{C.7})$$

$$Z_0 \equiv \sqrt{\frac{L}{C}} \quad (\text{C.8})$$

where Z_0 (called the characteristic impedance of the line) has units of resistance.

In the case of lossy lines, wire resistance R and parallel conductance G (both – per unit length) are taken into account (Fig. C-1 b). Consider a harmonic wave of frequency ω :

$$\frac{\partial V}{\partial x} = -ZI; \quad Z = R + i\omega L \quad (\text{C.9})$$

$$\frac{\partial I}{\partial x} = -YV; \quad Y = G + i\omega C. \quad (\text{C.10})$$

Substituting into the equations C.9, C.10 voltage and current in the form $V(x, t) = V_0 \exp[i(\omega t \pm kx)]$; $I(x, t) = \mp \frac{V_0}{Z_0} \exp[i(\omega t \pm kx)]$ find that the equations are consistent if

$$ik = \sqrt{(i\omega L + R)(i\omega C + G)} \quad (\text{C.11})$$

$$Z_0 = \sqrt{\frac{i\omega L + R}{i\omega C + G}}. \quad (\text{C.12})$$

Equation (C.11) shows that both loss and dispersion take place in a real transmission line. However, in many cases of high quality coaxial cables both factors are negligible in the experiment with cables of reasonable length. Below we neglect loss and dispersion.

Consider a specific example: a coaxial line consisting of two concentric cylinders of radii a and b , with spacing filled by a dielectric constant ϵ and magnetic permeability μ (Fig. C-1 c). In this case all magnetic and electric fields are localized in the spacing between the cylinders. Both inductance and capacitance per unit length can be found from energy considerations:

$$\epsilon = \frac{Q^2}{2C} + \frac{LI^2}{2} = \int d^3r \left(\frac{\epsilon_0 \epsilon}{2} E^2 + \frac{1}{\mu_0 \mu} B^2 \right) \quad (\text{C.13})$$

$$E(r) = \frac{Q}{2\pi\epsilon_0\epsilon r}; \quad B(r) = \frac{\mu_0\mu I}{2\pi r}; \quad \text{consequently,} \quad (\text{C.14})$$

$$C = \frac{2\pi\epsilon_0\epsilon}{\ln(b/a)}; \quad L = \frac{\mu_0\mu}{2\pi} \ln \frac{b}{a}. \quad (\text{C.15})$$

For non-ferromagnetic materials magnetic permeability $\mu \approx 1$, so signal propagation speed and characteristic impedance of a coaxial cable can be estimated as:

$$v = \frac{1}{\sqrt{\epsilon_0\epsilon\mu_0\mu}} \approx \frac{c}{\sqrt{\epsilon}} \quad (\text{C.16})$$

$$Z_0 = \sqrt{\frac{\mu_0\mu}{4\pi^2\epsilon_0\epsilon}} \ln \frac{b}{a} \approx \frac{60}{\sqrt{\epsilon}} \ln \frac{b}{a} \quad (\text{C.17})$$

where $c = 1/\sqrt{\epsilon_0\mu_0}$ is the speed of light in vacuum. Note from (C.16), that the signal propagation speed in a coaxial cable doesn't depend on the inner and outer conductor radii, but only on the dielectric used. Formula (C.17) shows that scaling the coaxes does not change their characteristic impedance, only the *ratio* of the conductors' radii and the dielectric permeability are important.

However, the thinner coaxes generally exhibit higher losses. Equation (C.17) also allows estimation of the characteristic impedance of a thin double-sided stripline. Indeed, a coaxial cable of close radii a and b can be considered as a collection of parallel striplines (neglecting the fringe fields of striplines, of course, Fig. C-1 *d*). Taking a limit $a \rightarrow b$ and taking into account that the circumference of the cylinder is equal to $2\pi a$, one obtains:

$$Z_0 = \sqrt{\frac{\mu_0 \mu}{\epsilon_0 \epsilon}} \frac{d}{b} \approx \frac{38}{\epsilon} \frac{d}{w} \quad (\text{C.18})$$

where w is the stripline width, and d is the plate spacing. Characteristic impedance of the stripline is inversely proportional to the line width. Theoretically, it should be easy to cut your own transmission lines of desired impedance from a piece of double-sided circuitboard. Unfortunately, my attempts to actually do so failed: I didn't get a reasonably quality line facing strong reflections from the contact area.

In the opposite limit $b \gg a$ (just a single wire) according to the equation C.17, characteristic impedance can not be defined as the logarithm on the right hand side diverges. A single wire is not a transmission line, and in practical applications these connecting wires must be made as short as possible in order to avoid reflections and signal shape distortion. We discuss reflections in more detail in the next section.

As for the energy required to generate a pulse of duration T , it can be found as in the case of a classical circuit:

$$E = \int_0^T V^+ I^+ dt = \int_0^T \frac{V^2}{Z_0} dt \quad (\text{C.19})$$

C.2 Impedance matching.

In the previous section we discussed the wave-like signal propagation down the transmission lines. And like any wave, propagating voltage/current signals may experience reflection from irregularities such as imbedded resistors, transmission line splitting (T-junctions), line termination etc. In this section we discuss the most common scattering scenarios and possible ways to avoid reflections.

First, consider a transmission line of finite length, connected to the ground through a resistor (Fig. C-2 a). The incident voltage pulse V^+ (of arbitrary profile) arrives to the resistor from the left and is being reflected to the right as a voltage pulse V^- with an amplitude ρ . One can define the transmission amplitude as $t = V/V^+$. The voltage V across the resistor is equal to $V^+ + V^-$ as the potential at the right hand side of the resistor is zero. The current I through the resistor is equal to $I^+ + I^-$ as the line and the resistor are connected in series (the sign is correct since the current I^- represents an outgoing wave). Substituting the relations C.8 between currents and voltages yields:

$$\rho = \frac{V^-}{V^+} = -\frac{I^-}{I^+} \quad (\text{C.20})$$

$$V = V^+ + V^- \quad (\text{C.21})$$

$$I = I^+ + I^- \quad (\text{C.22})$$

$$Z = \frac{V}{I} = \frac{V^+ + V^-}{I^+ + I^-} = \frac{V^+}{I^+} \frac{1 + V^-/V^+}{1 + I^-/I^+} = Z_0 \frac{1 + \rho}{1 - \rho} \quad (\text{C.23})$$

$$\rho = \frac{Z - Z_0}{Z + Z_0}; \quad t = 1 + \rho = \frac{2Z}{Z + Z_0} \quad (\text{C.24})$$

The same reflection and transmission amplitudes would emerge if the resistor is replaced by a transmission line of characteristic impedance Z , and the derivation is completely analogous. Of course, in the latter case the pulse

energy is not absorbed but propagates down the second transmission line. Note, that for $Z = Z_0$ there is no reflection. This is called an “impedance matched” termination of the line. All energy of the pulse is absorbed in the resistor. Another important case of $Z \rightarrow \infty$ (open end termination) leads to the reflection amplitude $\rho = 1$. The pulse of full amplitude is reflected back to the source (which can be destroyed by the pulse if you are unfortunate; one of our pulsers actually was destroyed this way). In the case of a shorted line ($Z = 0$), $\rho = -1$, again the pulse of (negative) full amplitude is reflected towards the source. However, if the source can withstand this reflection, the low-impedance termination can be used to double the current running through the resistor (or the wires in the case of the TR-SKM experiment) as follows from the equations (C.22) and (C.20).

Second, consider the reflection from a resistor inserted in the transmission line (Fig. C-2 b). The voltage V_R across the resistor is now equal to $V^+ + V^- - V_t$ where V_t represents the transmission amplitude. The current is again constant along the wire. Introducing the reflection and transmission amplitudes we obtain:

$$\rho = \frac{V^-}{V^+}; \quad t = \frac{V_t}{V^+} \quad (\text{C.25})$$

$$V_R = V^+ + V^- - V_t \quad (\text{C.26})$$

$$I_R = I^+ + I^- = I_t \implies t = 1 - \rho \quad (\text{C.27})$$

$$R = \frac{V_R}{I_R} = \frac{V^+ + V^- - V_t}{I^+ + I^-} = Z_0 \frac{1 + \rho - t}{1 - \rho} \quad (\text{C.28})$$

$$\rho = \frac{R}{R + 2Z_0}; \quad t = \frac{2Z_0}{R + 2Z_0} \quad (\text{C.29})$$

There is no opportunity to achieve reflectionless propagation here. For small resistances the reflection amplitude is proportional to the resistance.

Another common source of reflections is the T-junction (Fig. C-2 c). Con-

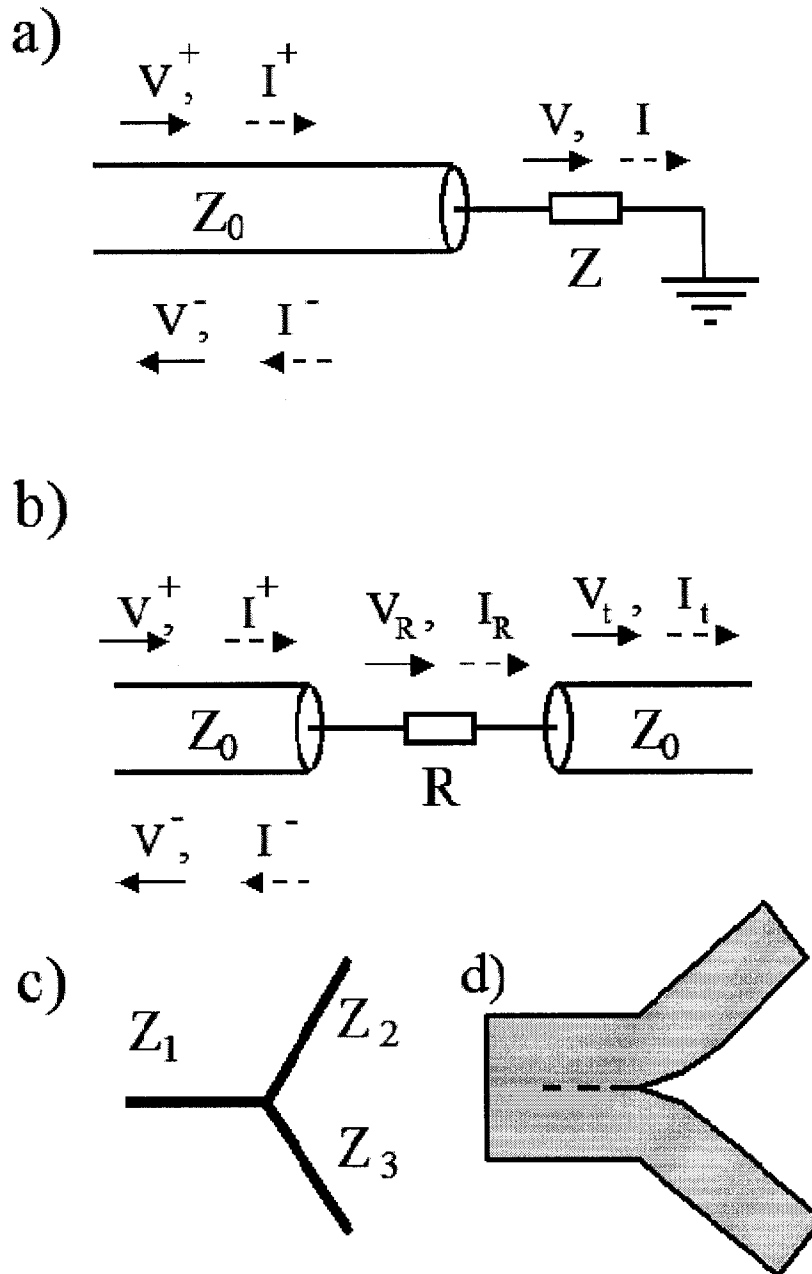


Figure C-2: (a) A transmission line of impedance Z_0 terminated through a resistor of impedance Z . (b) Scattering from a resistor of impedance Z embedded between two sections of impedance Z_0 . (c) Schematic representation of a T-junction. (d) An illustration of a smooth “adiabatic” splitting of a strip-line.

consider the most general case of such a junction where all characteristic impedances of merging lines are different. Let the channels 1,2,3 have impedances Z_1 , Z_2 , and Z_3 respectively. Then the scattering amplitude ρ_{11} corresponds to the reflection of a signal incident from the channel 1 back into the same channel, t_{21} – a scattering amplitude from channel 1 into channel 2, etc. Conducting the analysis similar to the previous cases and matching the amplitudes, yields:

$$\rho_{11} = \frac{Z_2 Z_3 - Z_1 Z_2 - Z_1 Z_3}{Z_1 Z_2 + Z_1 Z_3 + Z_2 Z_3} \quad (\text{C.30})$$

$$t_{21} = t_{31} = \frac{2Z_2 Z_3}{Z_1 Z_2 + Z_1 Z_3 + Z_2 Z_3} \quad (\text{C.31})$$

Note that transmission amplitudes are equal for the voltage pulses, but not for the current pulses. Currents split in the ratio inverse proportional to the corresponding characteristic impedances. The rest of the scattering amplitudes can be obtained from (C.30), (C.31) by cyclic permutation of the indices. If all transmission lines are equal, a negative pulse of 1/3 of the incident signal amplitude is reflected and 2/3 of the initial amplitude is scattered into each branch. Another interesting example is the case $Z_3 = Z_2 = 2Z_1$. In this case $\rho_{11} = 0$, $t_{31} = t_{21} = 1$; reflectionless splitting takes place. This result is easy to understand considering a splitting of a stripline. If fringing fields are negligible, there is a single stripline equivalent to two parallel striplines of half the width, and it does not matter where exactly the splitting takes place (Fig. C-2 *d*). According to the equation C.18, the stripline impedance is inversely proportional to its width, so half-width corresponds to double impedance as expected. Other scattering amplitudes are non-zero.

Finally, consider an impedance mismatched transmission line insert of impedance Z and finite length L in an ideal transmission line of impedance Z_0 , and find the total reflection and transmission amplitudes by summing up the

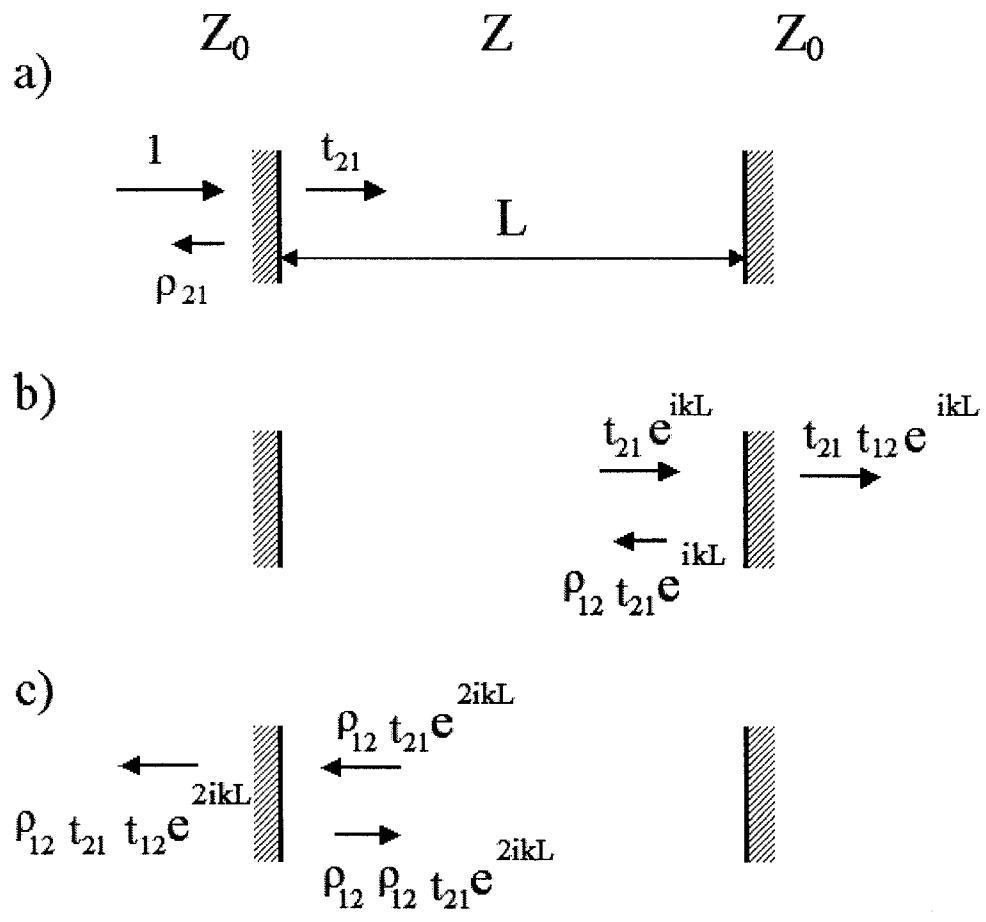


Figure C-3: An illustration of multiple reflections at two transmission line junctions.

contribution of multiple reflections [118], [119]. Assume that incident wave is proportional to e^{ikx} where k represents a wave vector of a bouncing wave inside the insert (Fig. C-3). First, the incident wave of unit amplitude is partially reflected into the first transmission line with an amplitude ρ_{21} and partially transmitted into the insert with an amplitude t_{21} (Fig. C-3 a). The amplitudes of the corresponding reflection and transmission amplitudes are given by Eq. C.24. Second the wave propagates towards the other boundary accumulating the phase e^{ikL} and is scattered there, partially penetrating into the third transmission line and partially reflected back into the second one (Fig. C-3 b). the corresponding reflection and transmission amplitudes ρ_{12} and t_{12} again can be found from the equation C.24 by interchanging Z and Z_0 . Third, the reflected part travels to the first boundary again accumulating additional the phase of e^{ikL} (Fig. C-3 c), and scatters there. Continuing the second and the third steps up to infinity and summing up the geometric series for the transmitted part yield:

$$\begin{aligned}\rho &= \rho_{21} + \frac{t_{21}\rho_{12}t_{12}e^{ikL}}{1 - \rho_{12}^2e^{2ikL}} = \frac{Z - Z_0}{Z + Z_0} \left(1 - \frac{4ZZ_0e^{2ikL}}{(Z + Z_0)^2 - (Z - Z_0)^2e^{2ikL}} \right) \quad (C.32) \\ t &= \frac{t_{21}t_{12}e^{ikL}}{1 - \rho_{12}^2e^{2ikL}} = \frac{4ZZ_0e^{ikL}}{(Z + Z_0)^2 - (Z - Z_0)^2e^{2ikL}} \quad (C.33)\end{aligned}$$

Graphs of the absolute value of the corresponding transmission amplitudes as a function of the product kL of the wave vector and the insert length for different values of the insert line impedance are shown in Figure C-4. As expected, the transmission amplitude is close to one as long as the length of the insert is much smaller than the incident signal wavelength ($kL \ll 1$). Even for a relatively strong mismatch $Z/Z_0 = 0.5$ the transmission amplitude is still decent at almost 80% of the incident wave value in the worst case (approximately 62 % of the pulse energy is transferred).

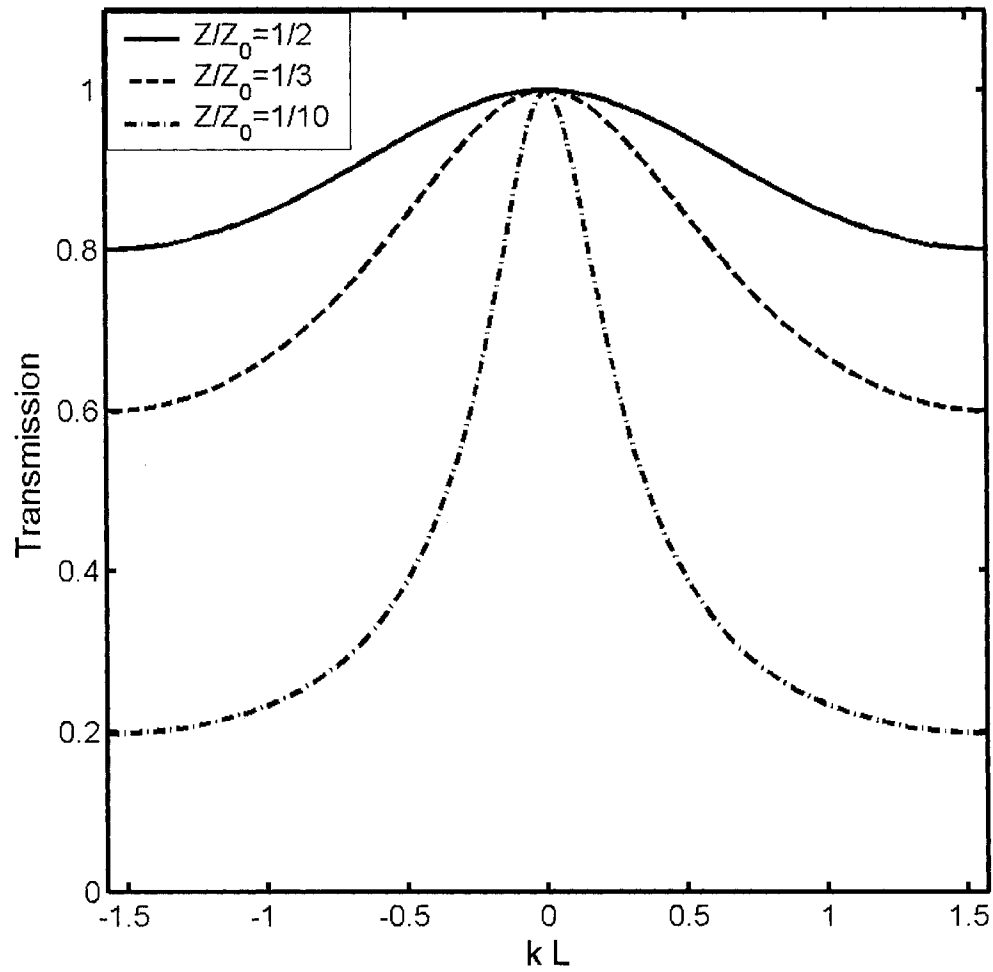


Figure C-4: Absolute values of transmission amplitudes through an impedance-mismatched insert of characteristic impedance Z as a function of the junction length, for different values of Z . The wave vector k corresponds to the bouncing wave inside the insert. All curves are periodic with a period of π .

C.3 Summary.

We presented a brief introduction to transmission line principles and the contributions of mismatched lines, T-junctions and embedded resistors to signal reflections. Using results for these fundamental building elements a wide variety of transmission line networks can be analyzed by summing up the reflection and transmission amplitudes at each block. The calculation task might be complicated, though.